Improved Instrumentation and Application of X-ray Emission Spectroscopy

Jared Abramson

A dissertation
submitted in partial fulfillment of the
requirements for the degree of

Doctor of Philosophy

University of Washington
2025

Reading Committee:
Gerald T. Seidler, Chair
Joshua Kas
Marjorie Olmstead

Program Authorized to Offer Degree:
Physics

Jared Abramson

University of Washington

Abstract

Improved Instrumentation and Application of X-ray Emission Spectroscopy

Jared Abramson

Chair of the Supervisory Committee:
Gerald T. Seidler
Department of Physics

Since its discovery x-ray fluorescence has been used to understand atomic scale phenomenon. With technological and scientific improvements x-ray fluorescence spectroscopy has become a widespread analytical technique for elemental identification and led to the development of high-resolution x-ray fluorescence spectroscopy, or x-ray emission spectroscopy (XES) which allows for an elemental selective probe of local electronic structure and ligand environment, expanding the analytical and scientific uses x-ray fluorescence. Here, I explore the applications of XES and present development of XES technique and spectrometers to further the analytical and scientific capabilities of XES. First, I present a study of cementitious materials for use in storage of nuclear waste. I show that XES is an accurate method to calculate reduction capacity through sulfur speciation and develop a new instrumental technique to improve study of small samples with XES. I incorporated this technique into a new laboratory instrument designed for high throughput analytical study of air-sensitive phosphorus samples and show the time dependent oxidation of NiP nanoparticles. Second, I examine asymmetric Rowland circle geometry for modern use in laboratory and synchrotron facilities. I collaborated on developing a new spectrometer with this capability which demonstrated the improved resolution and flexibility asymmetric geometries provide. I then present a tool designed for selection of these asymmetric geometries. Finally, I study the directionality of electronic and ligand structure of asymmetric single crystals. X-ray emission spectropolarimetry was shown to select for fluorescence from specific dipole transitions which contain information about the orbitals involved and a new technique is presented that obtains the same information by careful analysis of standard XES spectra.

Acknowledgements

I would like to thank my advisor, Professor Gerald Seidler, for all his help throughout my PhD path. I have learned so much from you as you have patiently given advice, explained topics, taught valuable skills, and shared jokes. I am honored and grateful to have you as my mentor.

Thank you to all the people in the Seidler Lab and around UW campus that have worked with me, supported me, and made my work enjoyable. A specific thank you to William Holden, Diwash Dhakal, Samantha Tetef, Anthony Gironda, Charles Cardot, and Helen Chen.

Finally thank you to my family and friends for all you have done to help me, support me, and care for me.

Table of Contents

List of Figures

Chapter 1

This allows x-rays with an energy not specified by the point-to-point spectrometer geometry to be detected leading to broadening of spectral features.

Figure 12: Different types of analyzers and analyzer arrays used in x-ray spectrometers.

Figure 13: Shown are the crystal planes, C, in bent crystal analyzers which are used to focus x-rays from the source location, S, to the detector location D on the Rowland circle. Johannson analyzers do this perfectly while Johann analyzers will have some spread in detector location for a single energy.

Figure 14: Diagram of Johann error due to the deviation of the surface of Johann type crystal analyzers from the Rowland circle.

Figure 15: Diagram showing the effect of wafer miscut in SBCAs on the detector position of diffracted x-ray fluorescence.

Chapter 2

Figure 1. Diagram of the process for secondary X-ray fluorescence from an atom, shown for Ni. An incoming primary X-ray photon scatters an electron creating a hole in an inner electron shell which is then filled by a higher energy electron emitting a secondary x-ray.

Figure 2. Transitions leading to Kα and Kβ emission for phosphorus[8].

Figure 3. Phosphorus Kα spectrum from three materials, indium phosphide, trioctylphosphine oxide, and sodium phosphate. The typical doublet profile of Kα spectra is shown for all three materials as well as a shift in energy due to oxidation state, with higher oxidation states increasing the energy[9].

Figure 4. Linear combination fit of sulfidic (lower energy) and sulfate (higher energy) reference Kα XES spectra to a S Kα XES spectra of a biochar sample to extract the oxidation state ratio[10].

Figure 5. Transitions leading to Kα and Kβ emission for 3d transition metals[8].

Figure 6. Fe Kα spectra for iron oxide, potassium hexacyanoferrate (II) and potassium hexacyanoferrate (III). The FWHM of the $K\alpha_1$ peak for these compounds decreases as the Fe spin decreases with iron oxide, potassium hexacyanoferrate (II) and potassium hexacyanoferrate (III) having four, one, and zero unpaired 3d electrons[11].

Figure 7. S Kβ spectra of three sulfur containing compounds. The main $K\beta_{1,3}$ peak at or a little below 0 eV is emission from transitions of 3p to 1s orbitals with the other important peak at about -15 eV, Kβ’, being emission from the ligand 2s orbital to sulfur 1s orbital. The energy scale is set by the $K\beta_{1,3}$ peak of Na_2SO_4. Phosphorous has the same features[12].

Figure 8. Kβ x-ray emission spectra of three manganese oxides with different Mn oxidation states. The change in 3d valence electrons with oxidation state changes is reflected in the strength of the $K\beta'$ peak and the splitting in energy of the $K\beta'$ and $K\beta_{1,3}$ peaks[13].

Figure 9. (Top) Kβ VtC for Mn samples with F, O, and N ligands showing the shift in Kβ” with ligand species. (Bottom) Kβ VtC for Mn oxides with different oxidation states. From top to bottom: $KMn^{VII}O_4$, $[Et_4N][Mn^{V}(O)(\eta^4\text{-}L)]$, $\beta\text{-}Mn^{IV}O_2$, $LiMn^{III}Mn^{IV}O_4$ and $ZnMn^{III}{}_2O_4$, $Mn^{II}O$, $Li_2Mn^{IV}O_3$. (Inset) The change in Kβ” integrated intensity with change in bond distance for the same Mn oxides[15].

Chapter 3

Figure 1: DRR spectrometer schematic with three collection cones at different photon energies that correspond to positions E1, E2, and E3 on the Rowland circle. Note how different sample positions can result in different efficiency of data collection across the face of the detector, that is, at different photon energies, due to different volumes and locations of the sample being present at different energies.

Figure 2: Illustration of the dependence of measured spectrum on sample position due to the “sampling cone” issues of Figure 1. Shown from bottom to top are spectra from a sample of HGM5-2018-2 (solid grey box) that is smaller than the total collection cone (black box). Moving from position 1 (P1) to P2 and subsequent steps are a 1.3 mm movement of the sample in the Rowland plane. A clear shift from the spectra weighing higher energies to lower energies can be seen as the sample moves across. Integrating these spectra results in a measurement that averages over sample compositional variations with equal detection efficiency at every photon energy.

Figure 3: XES spectra of all cementitious materials and the ZnS and Na_2SO_4 references. The two vertical lines correspond to the $K\alpha_1$ energies of the references.

Figure 4: Linear superposition fits to sulfide and sulfate references for the S Kα XES spectrum of a Hanford Grout Mix (HGM5), a Cast Stone, and a Blast Furnace Slag sample. A compendium of fits for all samples is presented in Figure S1.

Chapter 4

Figure S1: A compendium of XES results with fits, references, and residuals. Sample labels follow Table S1 and description in the main text.

Chapter 5

Figure 1: Dispersive Rowland refocusing (DRR) geometry with a large source off-circle. The geometry has a bent crystal analyzer at the top of the circle, a position sensitive detector on the lower left of the circle, and virtual sources on the lower right arc each with an associated

collection cone. The sample ('source' in this context) is illuminated using an X-ray source perpendicular to the circle. Note the spectral refocusing onto the detector arc and X-ray camera face.

Figure 2: (a) Front and (b) side view illustration of the double Rowland circle geometry, with accompanying CAD rendering also from (c) front and (d) side views. The P Kα and P Kβ Rowland circles share the same source location but are translated and tilted out of the plane to allow clearance for a 79.1° (2014.6 eV) and 67.6° (2137.8 eV) Bragg angle respectively. The mount of the crystal analyzers is omitted from (d) so that the analyzer orientations are more readily apparent and the stray scatter shields for the cameras are similarly omitted in this figure panel.

Figure 3: Photograph of a spectrometer placed in a glovebox with accompanying CAD rendering of the spectrometer components. Components include: (1) helium enclosure; (2) spectrometer components (see 7–13 for more details); (3) high voltage supply; (4) power source; (5) motor controller; (6) X-ray tube (hidden behind the door in the photo); (7) two Si (111) crystal analyzers and a mount; (8) sample location; (9) P Kα X-ray camera and housing; (10) P Kβ X-ray camera and housing; (11) sample mount containing a sample wheel, magnetic mount and stepper motor; (12) DRR flange; (13) helium enclosure wall. For clarity of presentation, the front window of the glovebox was removed for the photograph and the sample wheel assembly has been pulled back from the measurement position in both the photograph and the CAD.

Figure 4: X-ray camera images of the dispersed fluorescence from a Ni_2P-0h nanoparticle sample: P Kα (above) and Kβ (below). The dispersive direction is horizontal, with lower to higher energy moving left to right. The vertical direction shows the out of plane dimensions, where minor curvature is observed from geometric effects causing photons to be bent towards lower energy. The pixel intensity shown is from a CMOS sensor's analog to digital converter and is different from photon count because of sensor gain.

Figure 5: Linear superposition fit of the P Kα spectrum for an aged Ni_2P nanophase sample to phosphide (Ni_2P-bulk) and phosphate ($Ni_3(PO_4)_2$) references. (a) Fits using the reference spectra as directly measured. (b) Fits after the reference spectra have been broadened by 0.2 eV to compensate for a range of local environments, see the text for discussion. A compendium of fits for all air exposure times, using both broadened and unbroadened references, is presented in Fig. SI-2.

Figure 6: P Kα data for the Ni_2P-0h nanoparticles exposed to air for differing lengths of time, and two reference samples, Ni_2P-bulk and $Ni_3(PO_4)_2$. Typical total measurement times for an ensemble of seven nanophase samples (averaged to give the results shown) is 9 hours, ~80 minutes per sample. Panel (a) shows the spectra offset with vertical guides, shaded bands, for the $K\alpha_1$ peaks of the phosphide and phosphate reference compounds. Panel (b) shows the same spectrum overlaid. Note that the apparent isosbestic point is ~2014.25 eV, supporting the use of a simple two-phase decomposition onto reference compounds.

Chapter 6

Chapter 7

stage. (c) The motorized azimuthal (φ) degree of freedom allows for tilt-free correction of crystal miscut and for automated asymmetric operation.

Figure 5: (a) Symmetric spectrometer operation at $\theta_B = 65°$ in XAFS mode. (b) Asymmetric spectrometer operation at the same θ_B with $\alpha = 25°$, placing the source diametrically from the optic resulting in a monochromatic diffracted beam with no Johann broadening.

Figure 6: Polar plots in (α, ϕ) for calculated and measured reflections. (a) Calculated values of selected asymmetric reflections of a Si(551) analyzer. (b) Experimental data for Si(551) SBCA obtained by sampling phi-alpha space values at a fixed Bragg angle. (c) Calculated values of asymmetric Si(211) reflections. (d) Experimental data for Si(211) SBCAs. A threshold on reflection intensity was implemented to remove background in experimental data.

Figure 7: (Left) Diagram of the energy range achievable operating symmetrically with the Si SBCAs commonly used for transition metal XAS and XES: $\boldsymbol{G}_0$ = (100), (110), (111), (211), (331), (533), (551). The vertical gray lines indicate emission lines and the vertical black dashed lines indicate K-edges between 4 and 10 keV. (Right) Diagram of the energy range achievable operating asymmetrically with a Si(551) SBCA. Duplicate reflections, those that cover the exact same energy range at the same Bragg angle are omitted for clarity.

Figure 8: Emission lines measured asymmetrically with a Si(551) analyzer, arranged in order of ascending energy, presented with no background subtraction. The Bragg angle required to select the nominal energy of the emission line is given for each scan.

Figure 9: (a) XRT ray traced simulation of a Si(551) operated symmetrically far from backscatter, demonstrating Johann error as lower diffracted energies on the left and right sides of the crystal. (b) The same photon energy when using the asymmetric $\boldsymbol{G}_{hkl}$ = (553) reflection with the same analyzer. The crystal is optically near backscatter, resulting in elimination of Johann error.

Figure 10: Symmetric and asymmetric energy response functions corresponding to Fig. 9 (a) and (b), demonstrating the reduction of Johann error.

Figure 11: K$\beta_{1,3}$ emission spectra of (a) Cu and (b) Zn. Spectra were collected using the Si(551) SBCA symmetrically and with the most optimal asymmetric plane. Further from backscatter, the symmetric reflection analyzer response function broadens due to Johann error. On the other hand, the asymmetric reflection response function is narrow because of a mechanical analyzer angle, θ_M, close to 90°.

Figure 12: Cu K XANES measured using a Si(551) analyzer symmetrically and $\boldsymbol{G}_{hkl}$ = (553) reflection asymmetrically, compared to synchrotron results. At 8978.9 eV, $\theta_B = \theta_M = 65.2°$ symmetrically whereas $\theta_B = 77.5$ and $\theta_M = 92.5°$. The asymmetric configuration eliminates Johann error by operating mechanically at near backscatter. Masking the edges of the analyzer removes Johann broadening in the symmetric case, whereas masking in the asymmetric case

shows no appreciable difference in energy resolution. Spectra are offset for clarity of presentation.

Figure 13: (a) Ni K XAFS measured using a Si(551) analyzer symmetrically and with the $\boldsymbol{G}_{hkl}$ = $(55\bar{1})$ reflection asymmetrically, compared to synchrotron results. Both spectra show agreement with synchrotron data. Spectra are offset for clarity of presentation. (b) The background subtracted EXAFS oscillations.

Figure 14: The asymmetric configuration implemented for HERFD-XANES measurements. Note the longer source-detector chord length (blue arrows), allowing greater flexibility in special sample environments and less size constraints than a symmetric counterpart.

Figure 15: Zn HERFD-XANES measured with $\boldsymbol{G}_{hkl}$ = (642) of a Si(211) SBCA.

Figure 16: Elastic lines measured using a Si(211) analyzer asymmetrically $\boldsymbol{G}_{hkl}$ = (642), demonstrating Johann error elimination and narrowing of the analyzer response function when operated asymmetrically.

Figure 17: XRS of graphite showing elastic, inelastic, and XRS features of C K-edge. Measured with Si(211) using $\boldsymbol{G}_{hkl}$ = (642). The analyzer was mechanically at backscatter with a Bragg angle of 79.1°. The elastic peak FWHM is approximately 1.3 eV.

Chapter 8

Figure 1: Diagram of asymmetric operation from the reference frame of the SBCA. θ_{B} is the Bragg angle, α is the angle between the crystal plane normal to the SBCA surface (which reflection the crystal was cut for, G_0) and the reflection plane being used for asymmetric operation, G_{hkl}, and θ_{M} is the angle between the SBCA surface and the incident X-rays.

Figure 2: Pole plot demonstrating other reciprocal lattice vectors, G_{hkl}, available from the Si (211) SBCA. The radial direction is α, the angle of the reciprocal lattice vector with respect to [211], and the azimuthal direction is φ, the rotation angle of the system about the [211] direction. We show G_{hkl} with Miller indices in the range ±12, with only selected points labeled for clarity of presentation.

Figure 3: Two options for studying the Cu $K\beta_{1,3}$ fluorescence. (a) Symmetric operation of a Si (551) SBCA; (b) asymmetric operation of a Si (551) SBCA using the Si (553) diffraction plane.

Figure 4: Descriptions of the five main use cases for the `hklhop` package. The two main functions in the package are `hkl_selection` and `crystal_selection`.

Figure 5: Predicted energy dispersion across the SBCA face for Si (642) reflections from symmetric and two asymmetric configurations: (a) using the (642) G_{hkl} symmetrically having θ_{B} and θ_{M} of 81.40 deg. (b) using the (642) G_{hkl} from a Si (551) SBCA having θ_{B} of 81.40 deg. and θ_{M} of 94.70 deg. (c) using the (64−2) G_{hkl} from a Si (551) SBCA having θ_{B} of 81.40

deg. and θ_M of 107.48 deg. The larger broadening seen for the (642) symmetric and (64−2) asymmetric configuration is due to the inferior θ_M.

Figure 6: Bar charts generated by an auxiliary function of the package, bar_chart, displaying the energy ranges of the Si (100), Si (211), Si (551), and Si (642) SBCAs when used asymmetrically. The *y*-axis of each graph shows accessible crystal planes for ~4–10 keV.

Chapter 9

Figure 1: The polarized dipole $p \rightarrow s$ emission spectra and final states of our toy system described by Eq. 4. Only final state configurations with a spin down electron in the d_{xy} orbital are calculated. The top row shows the spectra for different dipole transition operators (x, y, and z). The middle row shows the expectation value of the total system $\langle S^2 \rangle$ operator for the final states. The last row shows the singlet configuration corresponding to the p core hole created by each of the dipole transition operators.

Figure 2: The polarized dipole $p \rightarrow s$ emission spectra for a final state described by Eq. 4, but with two electrons pinned into the same d_{xy} orbital. The top row shows the emission spectra for each polarization and the bottom row shows the singlet configuration of each final state.

Figure 3: (a) $LiVCuO_4$ crystal structure. (b) Face down view on the a-b plane of square planar Cu-O chains.

Figure 4: (a) $DyNiC_2$ crystal structure. (b) Face down view on the b-c plane of distorted square planar Ni-C chains.

Figure 5: Rowland Circle geometry for unpolarized, (a), and partially polarized, (b), CtC and VtC Kβ XES measurements. For each geometry the first SBCA is for Cu measurements and the second is for Ni measurements.

Figure 6: Cu foil Kβ x-ray emission spectra taken at high (orange) and low (green) Bragg angle.

Figure 7: The calculated ratio of reflectance of x-rays with polarization parallel to the Rowland plane (R_p) verse perpendicular to the Rowland plane (R_s) as a function of Bragg angle for the SBCA. The minimum and maximum Bragg angles for the unpolarized (red) and partially polarized (green) XES spectra are marked.

Figure 8: (a) $LiVCuO_4$ single crystal sample. (b) $DyNiC_2$ single crystal sample. (c) $DyNiC_2$ sample shown positioned in the spectrometer sample environment for *z*-polarized, *y*-directed (σ_z, I_y) XES spectra.

Figure 9: Kβ XES scans of the $LiVCuO_4$ single crystal sample as it is stepped across the entrance slit and the summation of these scans. A vertical gray dashed line marks the center

position of the K$\beta_{1,3}$ peak, found by a fit to the summation. This energy is used to apply a Bragg angle correction to the sample spectra, positioning it correctly in energy relative to a Cu foil reference spectra.

Figure 10: (left) $LiVCuO_4$ Cu and (right) $DyNiC_2$ Ni Kβ CtC-XES. (a, b) Unpolarized emission at high Bragg angle from radiation propagating along the *x* (blue), *y* (red), and *z* (brown) directions. (c, d) polarized spectra extracted from the directional spectra in (a, b) with polarizations along the *x* (purple), *y* (green), and *z* (orange) directions. Difference plots are shown at the bottom of each subplot and are calculated by subtracting the average spectra from each curve. Note the polarization dependence in the Kβ' feature for $LiVCuO_4$.

Figure 11: (left) $LiVCuO_4$ Cu and (right) $DyNiC_2$ Ni VtC-XES. (a, b) Measured unpolarized emission from radiation propagating along the *x*, *y*, and *z* directions as defined by the coordinate systems in Section 2.5. (c, d) Measured partially polarized emission, where each spectrum is dominated by a single polarization axis, albeit with poorer energy resolution. (e, f) Extracted polarized spectra. (g, h) Calculated polarized emission, including both electric dipole and quadrupole components.

Figure 12: Radiation pattern of dipole and quadrupole transitions between different *l*, *m* orbitals. (a) and (b) show dipole transitions from the p_z and p_x to *s* orbitals respectively while (c) and (d) show quadrupole transition from the d_{z2} and d_{xy} to *s* orbitals. The shape of the radiation patterns are equivalent to oscillating charges with spatial distributions that are consistent with the lobes of positive and negative phases from each atomic orbital.

Figure 13: FEFF calculated Cu VtC spectra and DOS from LiVCuO4. (a) Polarized x-ray emission with the quadrupole component averaged over directions perpendicular to the polarization axes. (b) Isotropic emission separated into dipole (red) and quadrupole (blue) components. (c) The p-projected density of states. (d) The d-projected density of states.

Figure 14: FEFF calculated Ni VtC spectra and DOS from DyNiC2. (a) Polarized x-ray emission with the quadrupole component averaged over directions perpendicular to the polarization axes. (b) Isotropic emission separated into dipole (red) and quadrupole (blue) components. (c) The p-projected density of states. (d) The d-projected density of states.

List of Tables

Chapter 3

Chapter 4

Chapter 7

Chapter 8

Chapter 9

Chapter 1 – X-ray Emission Spectroscopy Introduction

1. X-ray Fluorescence History

1.1 X-ray Fluorescence Discovery

In late 1895 Wilhelm Roentgen was studying electrical discharge in Crookes tubes, a type of cathode beam vacuum tube, and observed that even when visible and ultraviolet light wasn't allowed out of the Crookes tube a spare barium platinocyanide screen, which was known to fluoresce when exposed to electromagnetic radiation, lit up nearby. Roentgen concluded that some other type of radiation was being produced causing the screen to fluoresce and reported his discovery of x-rays, named X for an unknown variable[1]. Roentgen's further study of these new rays[2], particularly what materials they pass through, led him to discover that they penetrated weakly through hard dense materials, like metals or bones, but penetrated through many other materials more easily, including soft tissue. Using this fact he took an x-ray image of his wife's hand, illuminating the bones and rings, which was the first analytical use of x-rays[3] (Fig. 1).

Figure 1. X-ray taken by Wilhelm Roentgen of his wife's hand a few weeks after his first discovery of this new type of electromagnetic radiation, x-rays[3].

Following Roentgen's discovery and using a similar Crooke's tube x-ray source, Charles Barkla investigated some of the first known properties of interactions between these mysterious x-rays and various materials[4]. Barkla did so with a hardened x-ray beam, where low energy x-rays have been removed, aimed at a target material. He observed the radiation resulting from the x-ray interaction with the target material, which he dubbed secondary radiation as opposed to primary radiation from the source, and found three types; scattered primary x-rays from the source, electrons scattered from the target material, and x-rays emitted from the target material at different energy from the primary beam.

Of importance to this work is the secondary radiation of x-rays emitted by the target material after interacting with the source beam. Barkla found that the target was absorbing the primary x-ray and then emitting a new x-ray at a different energy, a process dubbed x-ray fluorescence, which is the namesake and used in x-ray fluorescence spectroscopy. In his study Barkla discovered that different materials had x-ray fluorescence of different energies and within a single material he discovered two types of x-ray fluorescence which he labeled K and L fluorescence lines and were later shown to be fluorescence from filling an 1*s* or 2*p* electron shell hole respectively[5-8].

1.2 X-ray Fluorescence Development and Analysis

Around the same time the father and son duo of William and Lawrence Bragg studied the interactions of x-rays with crystalline solids by x-ray diffraction expanding on the work of Laue and colleges who showed that x-rays were waves[9, 10]. Lawrence Bragg showed that the x-ray diffraction patterns could be explained when treating the crystal as a set of planes of atoms separated by a distance *d*, referred to henceforth as the *d*-spacing, due to interference of reflected x-rays scattered from successive planes[11]. Bragg's Law (Eq. 1) successfully explain the x-ray diffraction patterns they observed and determine conclusively the crystal structures of NaCl, KCl, KBr, KI, and diamond[12, 13].

$$n\lambda = 2d\sin\theta \quad (1)$$

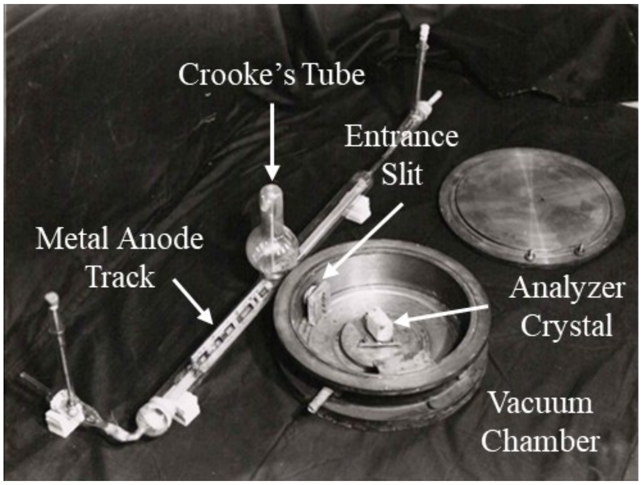

Figure 2.[14] Picture of Henry Moseley's spectrometer which is located in the History of Science Museum at Oxford University. A Crooke's tube and sample rail are shown tangent to the outside of the vacuum chamber which produce fluorescence dependent of which metal anode is used. The vacuum chamber, the round metallic piece shown, has a crystal in the center to perform Bragg reflection, diffracting the fluorescence at an energy dependent angle onto the photosensitive film placed on the inside of the vacuum chamber.

Incorporating Bragg's law into x-ray devices, Henry Moseley developed a new spectrometer to study the interaction of x-rays and materials[15]. Moseley's spectrometer, shown in Fig. 2, was based on G.W.K. Kaye's design[16] and has the same working principle as modern spectrometers. A Crooke's tube generates an x-ray beam with a metal anode chosen specifically for the study. This x-ray beam will have a broad bremsstrahlung but also strong fluorescence from the characteristic emission of the metal anode. The x-ray beam passes through an entrance slit into a vacuum chamber where it hits the analyzer crystal, potassium ferrocyanide in Moseley's case, and is diffracted to hit a photosensitive film on the inner surface of the vacuum chamber. The position the diffracted fluorescence illuminates the film allows for an energy determination by Bragg's law.

Using his spectrometer, Moseley performed some of the first groundbreaking x-ray fluoresces (XRF) experiments with the ability to resolve finer details in the K and L fluorescence that Barkla had first observed. Particularly, he resolved the K fluorescence line into what we now call Kα and Kβ fluorescence arising from 2p→1s and 3p→1s electron transitions, respectively[17, 18]. Moseley studied XRF spectra from close to forty elements observing their different fluorescence lines on a consistent energy scale thanks to his spectrometer, Fig. 3. He found that there was a proportionality between the square root of the emitted frequency (energy) of fluorescence and an integer value which primarily followed the ordering of the periodic table at the time. This held true for each fluorescence line, although with a different proportionality constant, and taken together with the just emerged Bohr-Rutherford model of the nuclear atom, Moseley concluded that these integers were the atomic charge of the nucleus of the element. In addition to confirming and tweaking the ordering of the periodic table, Moseley identified four locations in the periodic table of undiscovered elements, all of which were later found[17, 18].

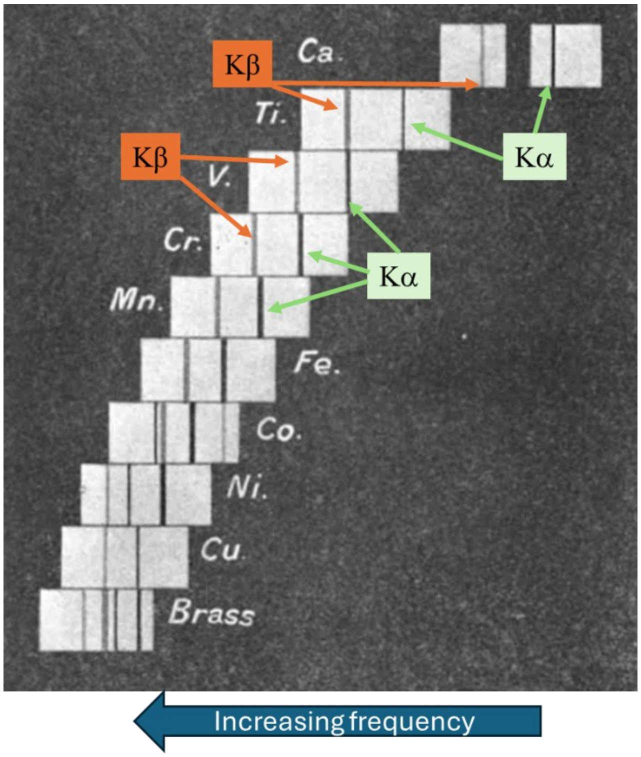

Figure 3. (Adapted from Moseley[17]) Selection of data Moseley published of Kα and Kβ fluorescence from a variety of metals. Using these spectra he developed Moseley's law relating the square root of the fluorescence frequency to the atomic number of the element.

Building on Moseley's work, Manne Siegbahn used an improved spectrometer to continue the study of the K and L spectral lines but with ~1000x greater resolution due to a slew of improvements to the instrumentation, instrument characterization, and instrument usage[19, 20]. This enabled him to identify more features of the known spectral lines, for example seeing the splitting of the $K\alpha_1$, $2p_{3/2}\rightarrow 1s$, and $K\alpha_2$, $2p_{1/2}\rightarrow 1s$ [21-26], and identify new spectral lines, known as the N and M lines[27-30]. This finer picture allowed Siegbahn to develop an understanding of the electronic orbitals and confirm some recent quantum mechanical calculations. He also developed a full set of notations for electron transitions that is still used today in x-ray spectroscopy, displayed in Fig. 4.

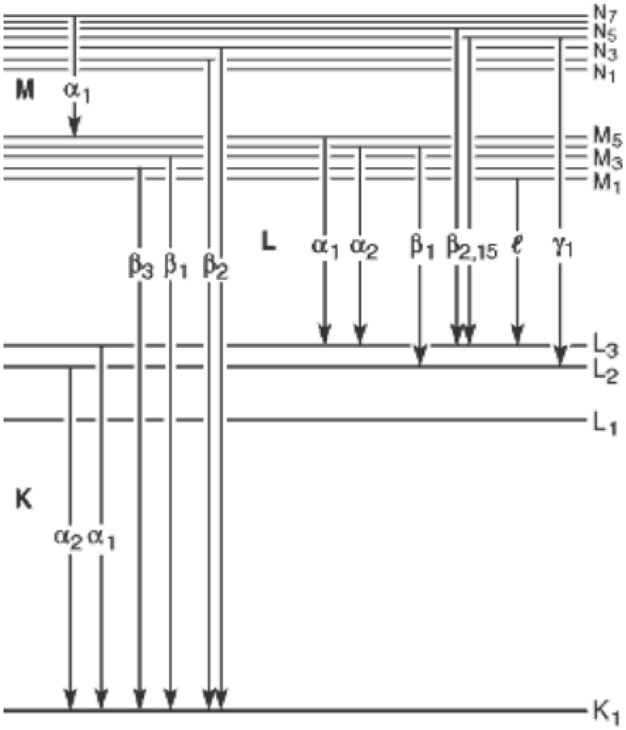

Figure 4. Transitions for the main types of x-ray fluorescence with the notation developed by Manne Siegbahn.

In the many years that have passed since these early spectroscopy experiments of Moseley and Siegbahn the resolution of XRF has further increased leading to a new descriptor of high resolution XRF for when the resolution is on the order of the core hole lifetime broadening, x-ray emission spectroscopy (XES). Core hole lifetime broadening in x-ray spectroscopy occurs due to the finite lifetime of the core hole, created in the absorption of a primary x-ray, before the atom fluoresces. Due to the energy-time representation of the Heisenberg uncertainty principle this lifetime leads to uncertainty in energy resulting in broadening of spectral lines by a Lorentzian line shape, typically between half to a few eV. When instrumental resolution is on the order of core-hole lifetime broadening, the broadening becomes a dominant factor in spectral line shape and XES is said to be performed.

This development of XES was led by many new x-ray sources, analyzer crystals materials and geometries, and x-ray detectors being developed and used in groundbreaking work which, in addition to increased resolution, increased efficiency and applicability. Of importance here, cylindrically and spherically bent crystal analyzers (CBA and SBCA respectively) have enabled Rowland geometries for X-ray spectroscopy to become the dominant approach, although von Hamos geometries have also seen considerable success. As the later chapters in this dissertation use Rowland geometries, I will focus on it here.

2 X-ray Spectrometers

2.1 Rowland Circle Geometry

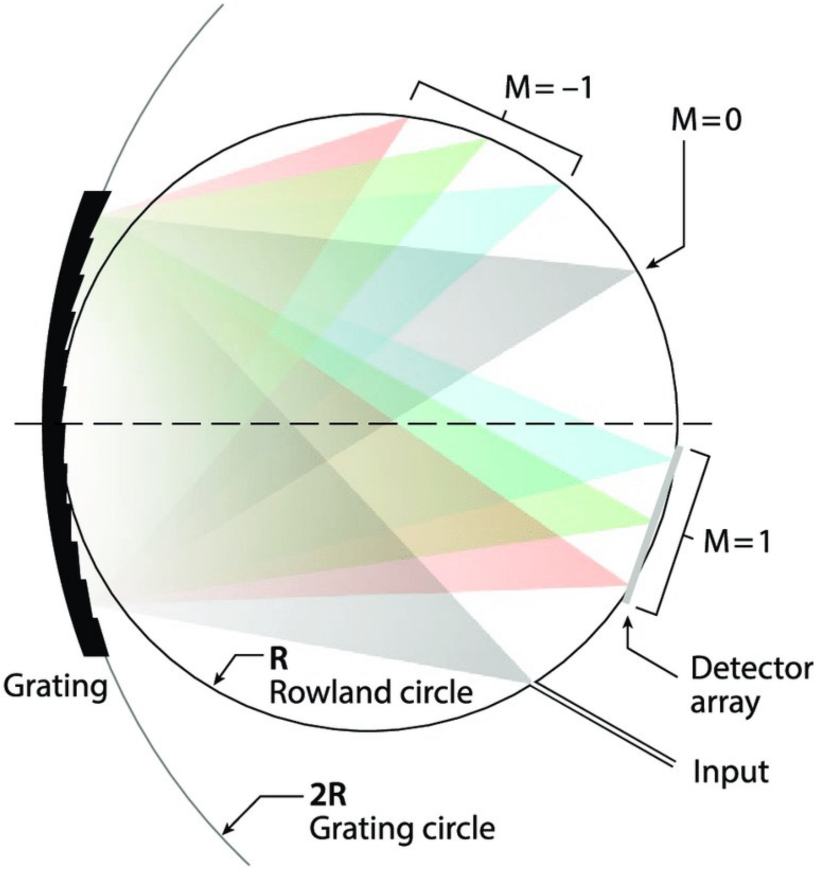

Figure 5. (From Cataldo[31]) Diagram of Rowland geometry for optical wavelengths. The primary light beam (grey) enters the Rowland circle and is diffracted by the grating with a angular dispersion dependent on the energy of the photon.

Flat gratings and lenses have been used to diffract light and focus it to perform various types of optical spectroscopies since the 1600s. In 1883 Henry Rowland's invention of a 'ruling engine' enabled him to reproducibly move a diamond tip very small distances and allowed him to etch gratings on a concave surface with the required precision for spectroscopic use for the first time[32]. This brought a new wave of spectroscopic techniques as the curved gratings allow for higher resolution spectroscopy to be performed without the use of lenses since the gratings diffracted and focused light from one location to another. Rowland defined what is now known as Rowland circle geometry, a virtual circle (the Rowland circle) on which the source, center of a diffractive grating, and detector lie, see Fig. 5. Importantly the curvature of the diffractive grating is twice the curvature of the Rowland circle, which when combined with the fact that incident and outgoing angle of diffracted light with respect to surface normal are wavelength dependent, lead geometrically to the diffracted light having point-to-point focus on the Rowland circle, Fig. 5.

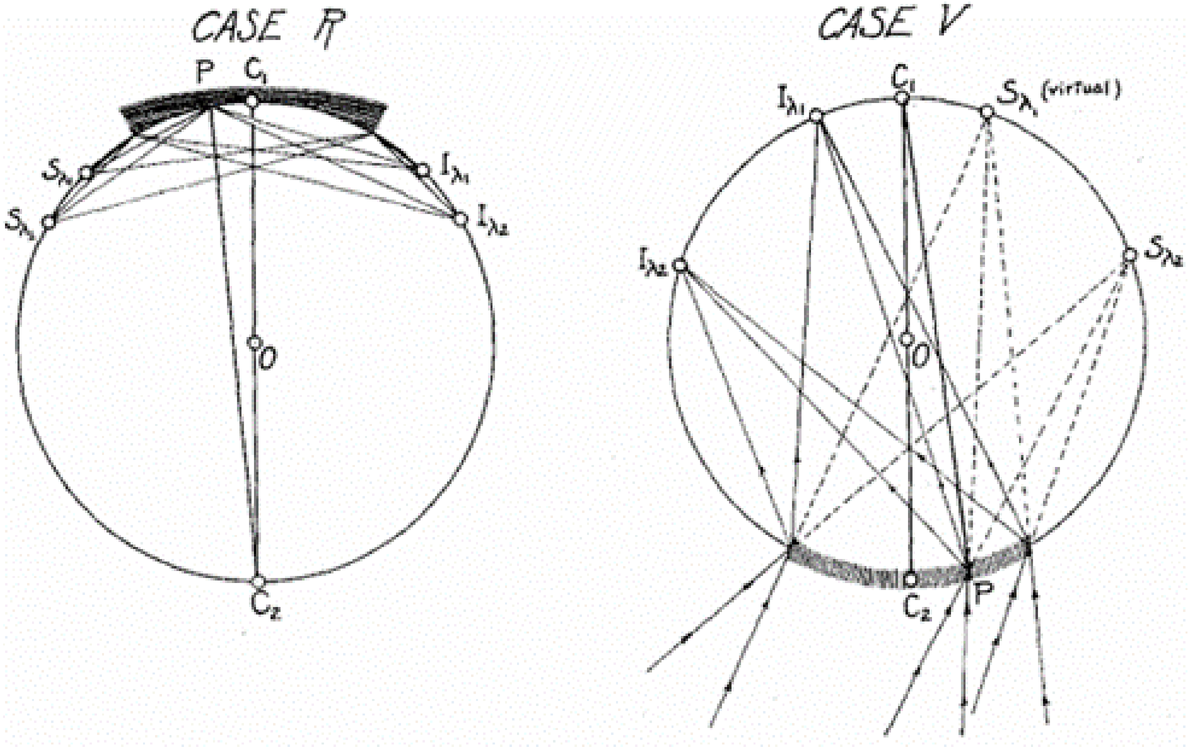

Figure 6. (From DuMond and Kirkpatrick[33]) Diagrams of the adaptation of the Rowland circle geometry to x-ray spectroscopy using crystal planes as a grating. The crystal planes can effectively be used in two geometries, either perpendicular or parallel to the Rowland circle radius.

As x-ray spectroscopy was beginning, a limiting problem was the intensity of detected radiation. To improve this Jesse DuMond and Harry Kirkpatrick investigated if the Rowland circle, which had previously only been used for optical wavelengths, could be applied to x-rays to result in greater intensity. They observed that theoretically a flexible crystal, ex. mica, could be bent into the shape of Rowland gratings while maintaining the conditions for Bragg reflection allowing the use of the Rowland circle geometry with x-ray diffraction[33]. DuMond and Kirkpatrick observed two ways to do so, with either the crystal planes of the x-ray grating approximately parallel, Case V, or perpendicular, Case R, to the radius of the Rowland circle, Fig. 6. In Case V x-rays come from a source behind the crystal and outside the Rowland circle which can be traced to virtual source locations on the Rowland circle. In Case R x-rays come from a real source on the Rowland circle. In both cases x-rays are diffracted according to Bragg's law to land at a point *I* depending on wavelength. Case R, with the crystal planes perpendicular to the Rowland circle radius, is used exclusively in this work and therefore will be the only geometry discussed.

Using the Rowland circle geometry with a circular mosaic of small flat crystals in this geometry DuMond and Kirkpatrick obtained the point-to-point focusing capabilities and increasing intensity of the Rowland circle, while still having the energy dispersion of Bragg reflection to maintain good energy resolution. This is shown geometrically in Fig. 7 where x-rays from a point source, which sits on the Rowland circle, will hit the analyzer at all points making the same angle, θ_B, with the crystal diffraction planes due to the Rowland geometry. θ_B is called the Bragg angle. According to Bragg's law, Eq. 1, x-rays of a specific wavelength will diffract off the analyzer symmetrically, focusing to a point where the detector is placed. This gives an efficient, energy selective way of collecting x-ray fluorescence from a source.

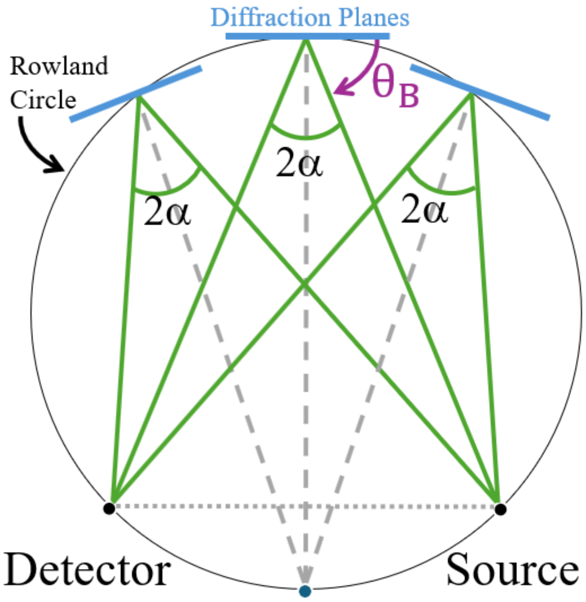

Figure 7. (Adapted from Seidler et. al.[34]) Diagram of the Rowland circle geometry. Any x-rays from the source that hit the Rowland circle and are diffracted according to Bragg's law at an angle θ_B to the tangent will focus on the detector location.

2.2 Rowland Circle Spectrometers

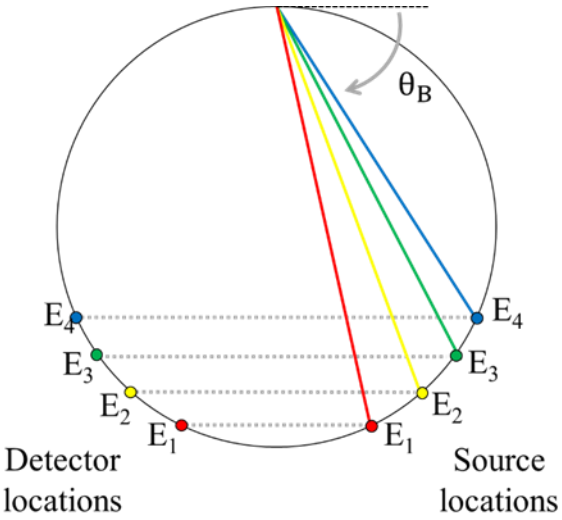

Figure 8. (From Seidler et. al.[34]) Diagram of point-to-point operation of a Rowland circle spectrometer. Each source point on one side of the Rowland circle has a corresponding detector point on the opposite side with the pair specifying an energy determined by the Bragg angle.

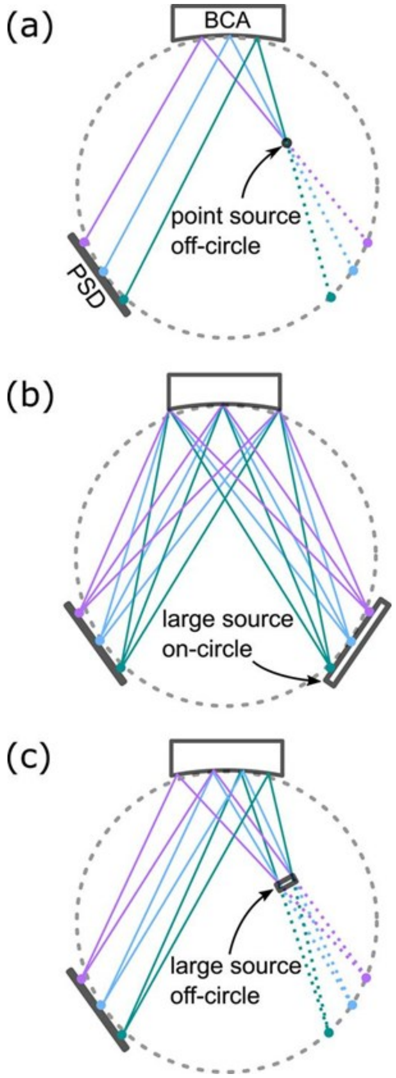

Figure 9. (From Holden[35]) Diagram of three dispersive Rowland geometries for XES. See text for discussion.

The Rowland circle geometry can be operated two ways to perform XES.

The first is point-to-point operation where the source and detector locations pick out a single energy based on the Bragg angle as described above. By simultaneously shifting the source and detector positions to access different energies, Fig. 8, and counting the number of photons detected at each angle the desired XES spectra can be measured.

The second is a dispersive operation with a stationary source and a position sensitive detector (PSD). In dispersive operation a whole spectrum is simultaneously measured with each position on the PSD corresponds to a different Bragg angle and therefore energy. There are three general configurations; point source off circle, Fig. 9a, large source on circle, Fig. 9b, and large source off circle, Fig. 9c. With a point source off circle virtual sources can be traced back to the Rowland circle at different angles, corresponding to different energies by Bragg's Law, each hitting different locations on the PSD. This provides excellent resolution but poor intensity as well as susceptibility to analyzer inconsistencies as each energy only is diffracted by a small portion of the analyzer. With a large source on-circle different parts of the sample contribute for each energy. The whole analyzer diffracts each energy providing good intensity but is very susceptible to any sample variations. Finally with a large source off-circle virtual sources can again be traced back to the Rowland circle. For each energy a portion of the sample and analyzer contributes with the exact proportion depending on the sample size. This maintains the good resolution and intensity of the other cases without worrying about sample or analyzer inhomogeneities. This is the geometry used in later chapters and is named the dispersive Rowland refocusing (DRR) geometry[35].

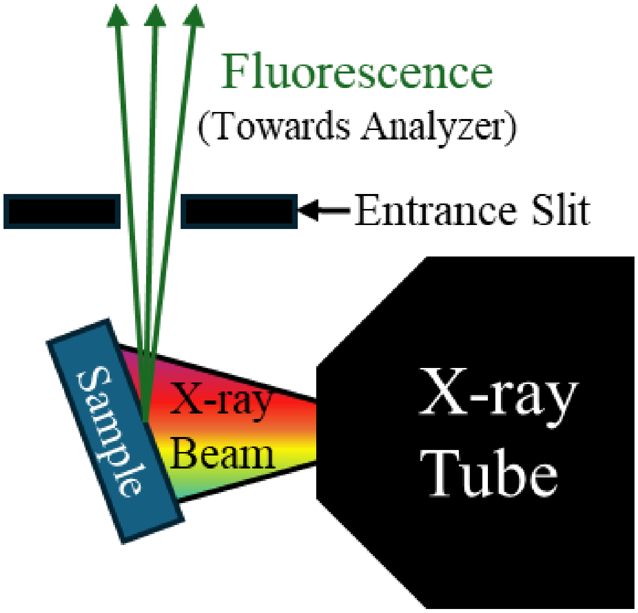

Figure 10. Diagram of a standard source for laboratory XES. The polychromatic x-ray beam illuminates the sample causing it to fluoresce, some of which will pass through an entrance slit towards the analyzer.

The source for these spectroscopic configurations in the laboratory consists of either a sample, which is caused to fluoresce for DRR, or an entrance slit with the fluorescing sample behind it for point-to-point operation. Shown in Fig. 10 is a standard laboratory source configuration for point-to-point spectroscopy where the fluorescence is caused by a polychromatic conical beam from an x-ray tube which passes through an entrance slit placed on the Rowland circle. At a synchrotron when fluorescence is instead caused by a focused monochromatic beam the same general source configuration is used but without an entrance slit. The inclusion or lack of an entrance slit is due to a desire to limit source size broadening. The source has an effective width which is the in-plane size of the fluorescing sample as seen by the diffracting analyzer, Fig. 11. This width will span point-to-point energy positions above and below the intended energy which will still be detected and cause broadening of the measured spectrum. For large samples with an unfocused beam this can be a large effect, but using a focused beam or entrance slit constrains the effective source width.

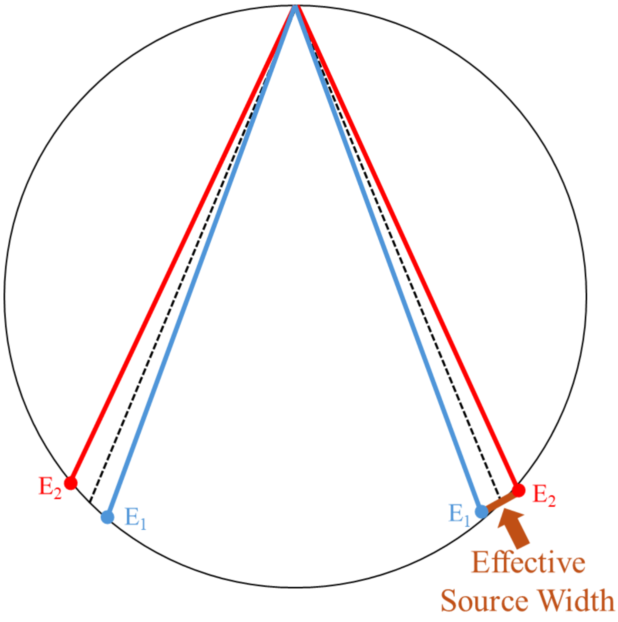

Figure 11. Diagram showing source size broadening. The effective source width, size of the source as seen by the analyzer, spans a range of energy locations on the Rowland circle: E_1 to E_2. This allows x-rays with an energy not specified by the point-to-point spectrometer geometry to be detected leading to broadening of spectral features.

The source configuration for a specific experiment is chosen to maximize the measured sample fluorescence intensity while minimizing source size error. The intensity is primarily determined by the power of the x-ray source but secondarily by the sample geometry both in size and orientation with respect to the x-ray source. Geometries are chosen to maximize the x-ray beam power incident on the sample and the fluorescence incident on the analyzer.

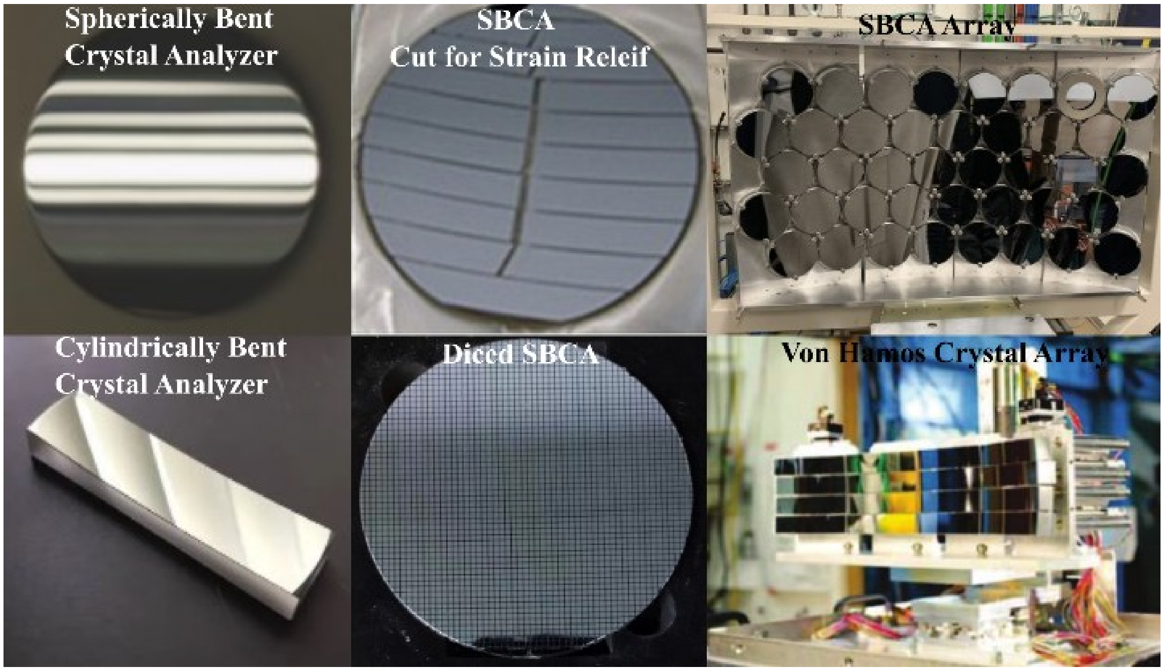

Figure 12. [36-40] Different types of a analyzers and analyzer arrays used in x-ray spectrometers.

The analyzers used in these Rowland circle operations can take a variety of geometries and compositions chosen for specific studies and uses, see Fig. 12 for examples. Analyzers will be chosen with a material composition, typically Si, Ge, quartz, sapphire, or $LiNbO_3$, and crystal orientation normal to the surface, ex. [111] to give a specific *d*-spacing which allows access to a specific energy range according to Bragg’s law. In this work the analyzers are used individually but they can also be placed into an array to increase the solid angle subtended and therefore increase the collection efficiency of the spectrometer. Finally, analyzers will have some curvature, either flat, cylindrically bent or spherically bent. If the analyzers are bent, they will either be Johann or Johannson type, see Fig. 13.

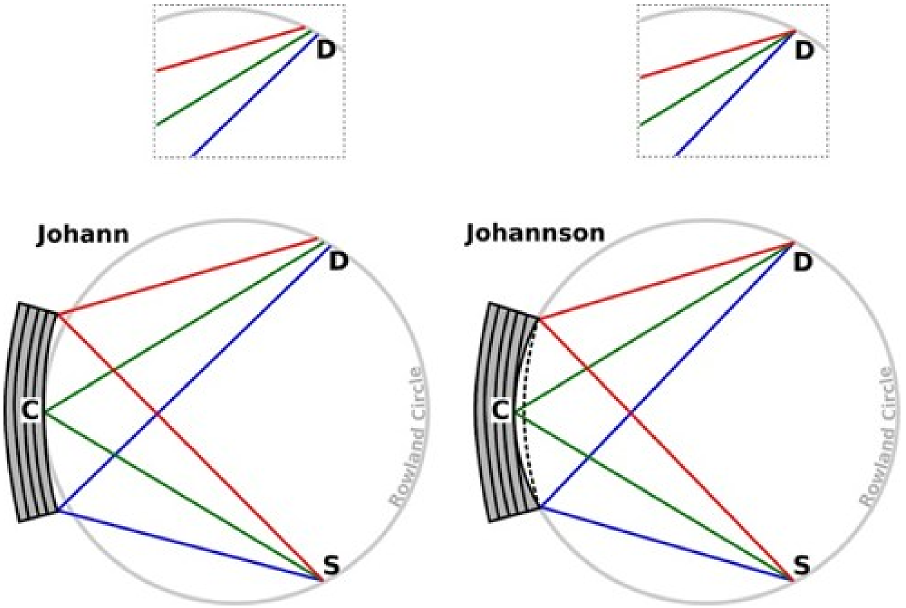

Figure 13. (From Kowalska et. al.[41]) Shown are the crystal planes, C, in bent crystal analyzers which are used to focus x-rays from the source location, S, to the detector location D on the Rowland circle. Johannson analyzers do this perfectly while Johann analyzers will have some spread in detector location for a single energy.

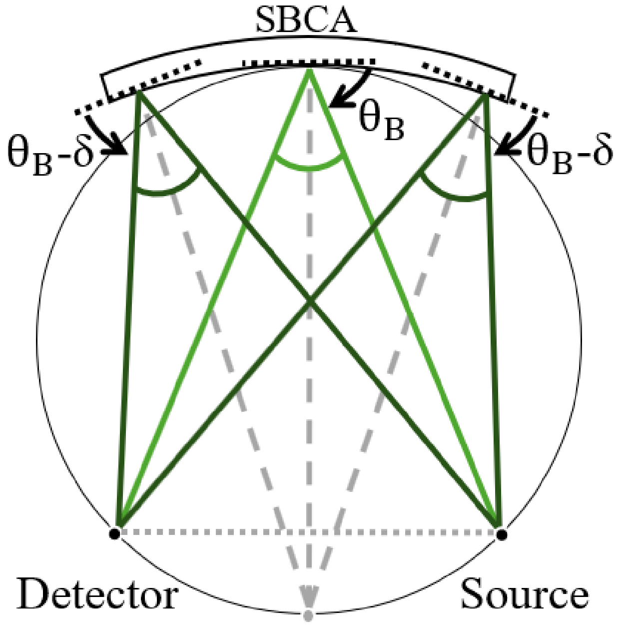

Figure 14. Diagram of Johann error due to the deviation of the surface of Johann type crystal analyzers from the Rowland circle.

Bent crystal analyzers, both Johann and Johannson, start as flat crystals cut or grown along a crystallographic plane. Then the crystals are curved to a radius twice that of the Rowland circle they will be used for and bonded to a substrate to hold that shape. Johann analyzers are complete after this step, having the correct geometry for Rowland operation and crystal structure enabling x-ray diffraction to perform XES. But since a Johann crystal analyzer has a radius twice that of the Rowland circle it's surface only lies on the Rowland circle at its center, deviating more from the Rowland circle further out from the center you are, Fig. 13. This deviation results in x-rays at one source location being at slightly different Bragg angles, and therefore energy, when diffracted from the center verses the edge of the analyzer, Fig. 14. This leads to a broadening of spectral features and is called Johann error.

This error can be minimized in a few ways. Operationally by working at large Bragg angles close to backscatter the Bragg angle deviation between the center and edge of the analyzer is minimized, see Chen et. al[42]. Mechanically the edge of the analyzer can be masked leaving the center of the analyzer, where the Johann error is smaller, exposed; although this comes with the downside of a lower count rate. Systematically to remove the Johann error a Johannson analyzer can be used.

Johannson analyzers are made initially the same a Johann analyzers but with an extra step after curving the crystal of grinding the analyzer surface to match the radius of the Rowland circle, Fig. 13. This results in the analyzer crystal planes having twice the radius of the Rowland circle, keeping diffraction the same, but the surface of the analyzer now lays atop the Rowland circle. Consequently x-rays will diffract with the same Bragg angle from any part of the analyzer, resulting in no Johann error.

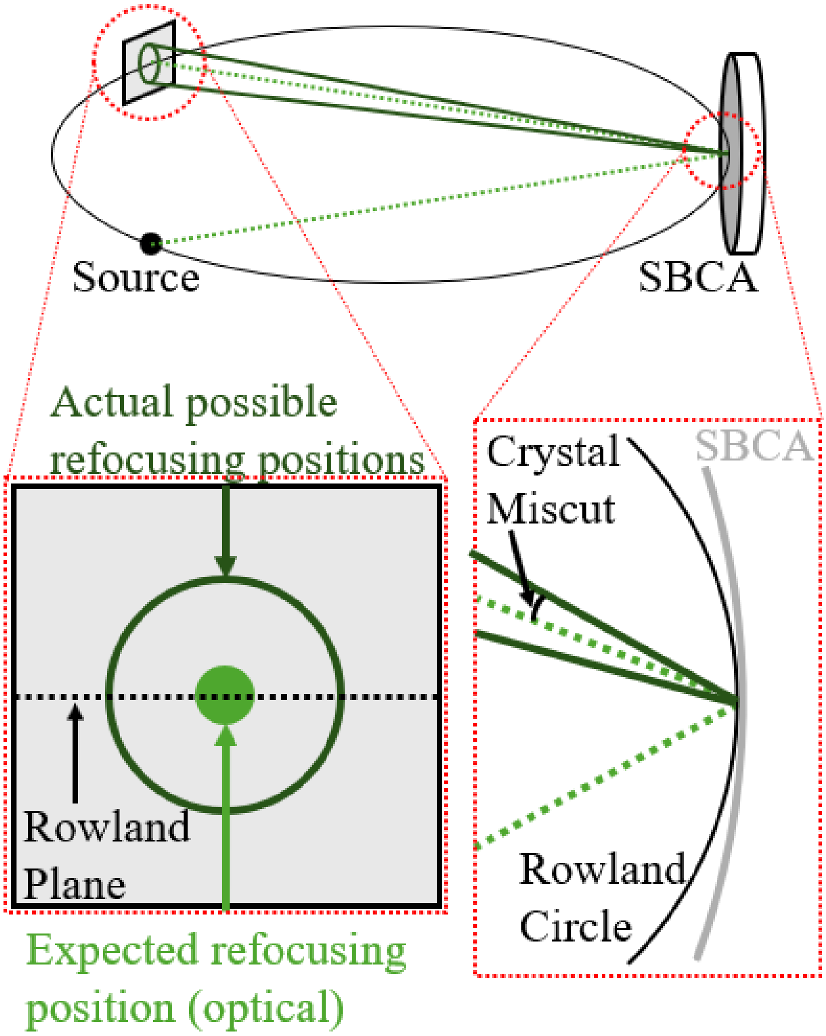

Figure 15. (From Seidler et. al.[34]) Diagram showing the effect of wafer miscut in SBCAs on the detector position of diffracted x-ray fluorescence.

While crystal analyzers are made with a specified crystallographic plane parallel to the crystal surface, in practice the crystal plane will not be perfectly parallel to the analyzer surface and the angular difference, usually on a scale of hundredths to tenths of a degree, is called crystal miscut, Fig. 15. This crystal miscut leads to diffracted photons not hitting the Rowland circle at the calculated detection position, given the *d*-spacing and Bragg angle, but instead on a circle around it. This crystal miscut is corrected by first rotating the crystal so the diffracted x-rays are in the Rowland plane and then adding an offset to the detector angle position relative to the Bragg angle so the diffracted x-rays are incident on the detector[43].

The diffracted radiation off the crystal analyzers is observed by various types of detectors. The two used for the work here are single pixel silicon drift detectors (SDDs) for point-to-point spectrometers and CMOS camera position-sensitive detectors[35] for DRR spectrometers. Both have a similar underlying principle of converting an incoming x-ray into an electrical signal proportional to the energy of the x-ray. The SDDs have no position sensitivity with a single pixel but have excellent energy resolution and noise suppression. The CMOS detectors have a large pixel array enabling position sensitivity along with energy detection and, while comparatively worse, still have acceptable resolution and noise suppression.

References

1. W. C. Röntgen, *Nature* 1896, **53**, 274–276.
2. W. C. Röntgen, *Archives of the Roentgen Ray*, 1899, **3**, 80-88.
3. W. C. Röntgen, "Hand with Rings", 1895
4. C. G. Barkla, *Philosophical Magazine*, 1903, **5**, 685-698.
5. C. G. Barkla, *Philosophical Magazine*, 1908, **15**, 288-296.
6. C. G. Barkla, *Philosophical Magazine*, 1910, **20**, 370-379.
7. C. G. Barkla, *Philosophical Magazine*, 1916, **31**, 257-260.
8. C. G. Barkla and C. A. Sadler, *Philosophical Magazine*, 1907, **14**, 408-422.
9. W. Friedrich and P. Knipping, *Sitz.ber. Bayer. Akad. Wiss.,*, 1912, 311-322.
10. W. Friedrich, P. Knipping and M. Laue, *Annalen Der Physik*, 1913, **41**, 971-988.
11. W. Bragg, *Proceedings of the Cambridge Philosophical Society*, 1913, **17**, 43-57.
12. W. H. Bragg and W. L. Bragg, *Proceedings of the Royal Society of London. Series A, Containing Papers of a Mathematical and Physical Character*, 1913, **89**, 277-291.
13. W. L. Bragg, *Proceedings of the Royal Society of London. Series A, Containing papers of a mathematical and physical character*, 1913, **89**, 248-277.
14. Moseley's X-ray spectrometer and his mother's pocket diary, https://www.hsm.ox.ac.uk/moseleys-x-ray-spectrometer-and-pocket-diary#listing_580741_0).
15. H. G. J. Moseley and C. G. Darwin, *Philosophical Magazine*, 1913, **26**, 210-232.
16. G. W. C. Kaye and J. J. Thomson, *Philosophical Transactions of the Royal Society of London. Series A, Containing Papers of a Mathematical or Physical Character*, 1909, **209**, 123-151.
17. H. G. J. Moseley, *Philosophical Magazine*, 1913, **26**, 1024-1034.
18. H. G. J. Moseley, *Philosophical Magazine*, 1914, **27**, 703-713.
19. M. Siegbahn, *Philosophical Magazine*, 1916, **32**, 494-496.
20. M. Siegbahn and E. Friman, *Physikalische Zeitschrift*, 1916, **17**, 176-178.
21. M. Siegbahn, *Nature*, 1916, **96**, 676-676.
22. M. Siegbahn and E. Friman, *Philosophical Magazine*, 1916, **32**, 39-49.
23. M. Siegbahn and E. Friman, *Annalen Der Physik*, 1916, **49**, 611-615.
24. M. Siegbahn and E. Friman, *Annalen Der Physik*, 1916, **49**, 616-U612.
25. M. Siegbahn and W. Stenstrom, *Physikalische Zeitschrift*, 1916, **17**, 318-319.
26. M. Siegbahn and W. Stenstrom, *Physikalische Zeitschrift*, 1916, **17**, 48-51.
27. M. Siegbahn, *Philosophical Magazine*, 1919, **37**, 601-612.
28. M. Siegbahn, *Philosophical Magazine*, 1919, **38**, 639-646.
29. M. Siegbahn, *Zeitschrift Fur Physik*, 1922, **9**, 68-80.
30. M. Siegbahn and V. Dolejsek, *Zeitschrift Fur Physik*, 1922, **10**, 159-168.
31. G. Cataldo, *Development of ultracompact, high-sensitivity, space-based instrumentation for far-infrared and submillimeter astronomy*, Massachusetts Institute of Technology, 2015.
32. H. A. Rowland, *The London, Edinburgh, and Dublin Philosophical Magazine and Journal of Science*, 1883, **16**, 197-210.

33. J. W. M. DuMond and H. A. Kirkpatrick, *Review of Scientific Instruments*, 1930, **1**, 88-105.
34. G. T. Seidler, A. J. Gironda, J. E. Abramson, C. Cardot, Y. Chen and D. Dhakal, unpublished work.
35. W. M. Holden, O. R. Hoidn, A. S. Ditter, G. T. Seidler, J. Kas, J. L. Stein, B. M. Cossairt, S. A. Kozimor, J. H. Guo, Y. F. Ye, M. A. Marcus and S. Fakra, *Review of Scientific Instruments*, 2017, **88**, 073904
36. XRStech, https://xrstech.com/x-ray-crystal-analyzers-2/).
37. X. Gao, S. Q. Gu, Q. Gao, Y. Zou, Z. Jiang, S. Zhang, X. J. Wei, H. S. Yu, G. D. Sheng, P. Q. Duan and Y. Y. Huang, *X-Ray Spectrometry*, 2013, **42**, 502-507.
38. R. Alonso-Mori, J. Kern, D. Sokaras, T. C. Weng, D. Nordlund, R. Tran, P. Montanez, J. Delor, V. K. Yachandra, J. Yano and U. Bergmann, *Rev Sci Instrum*, 2012, **83**, 073114.
39. Z. Y. Guo, Q. S. Diao, Y. J. Zhang, X. Jia, S. X. Jin, X. L. Gan, H. Zhang, Y. Tian, Q. F. Han, H. J. Qian, K. Ishii and W. Xu, *X-Ray Spectrometry*, 2024, **54**, 247-253.
40. LUXIUM Solutions, https://www.luxiumsolutions.com/applications/x-ray-analyzers-synchrotrons).
41. J. K. Kowalska, F. A. Lima, C. J. Pollock, J. A. Rees and S. DeBeer, *Israel Journal of Chemistry*, 2016, **56**, 803-815.
42. Y. Chen and G. T. Seidler, unpublished work.
43. G. T. Seidler, D. R. Mortensen, A. J. Remesnik, J. I. Pacold, N. A. Ball, N. Barry, M. Styczinski and O. R. Hoidn, *Review of Scientific Instruments*, 2014, **85**.

Chapter 2 – X-ray Emission Spectra

1. X-ray Fluorescence

The process of x-ray fluorescence, shown in Fig. 1, starts when an atom in an initial relaxed electronic state absorbs an x-ray photon that excites a bound electron into a higher electron orbital or into the continuum. This leaves a hole with the atom in an intermediate state. The hole is filled by an electron from a higher orbital resulting (with some probability) in a fluorescence x-ray whose energy is equal to the difference in the orbital energies. These orbital energies can take on different values depending on the atomic and environmental conditions. They can be calculated and discussed through the initial and final state wave functions with a Hamiltonian of the form in Eq. 1[1]. H_{EL} represents the single electron energy level. An example of the H_{EL} is given in Eq. 2 for emission from a $2p$ electron filling a $1s$ hole in a 3d transition metal element. $\varepsilon_d n_d$, $\varepsilon_{2p} n_{2p}$, and $\varepsilon_{1s} n_{1s}$ represent the $3d$, $2p$, and $1s$ energy levels respectively. $H_{multiplet}$ in Eq. 1 represents multiplet couplings from multipole terms of orbital interactions such as $2p$-$3d$ exchange interaction, $3d$-$3d$ Coulomb interaction, or spin-orbit coupling. H_{CF} represents the crystal-field effects from ligand bond splitting of valence level orbitals.

$$H = H_{EL} + H_{multiplet} + H_{CF} \quad (1)$$

$$H_{EL} = \varepsilon_d n_d + \varepsilon_{2p} n_{2p} + \varepsilon_{1s} n_{1s} \quad (2)$$

Following the notation of Siegbahn, x-ray fluorescence is labeled by a capital Latin script letter, a Greek lowercase letter, and an Arabic numeral which generally represent, respectively, the orbital of the hole in the intermediate state, the orbital of the electron which fills it in the final state and the subshell of that same electron. This work will address K-emission XES which follows after initial excitation in the $1s$ orbital.

X-ray fluorescence is very commonly used for element identification by low-resolution spectrometers[2-4]. Here, we focus on high-resolution studies of XRF that are capable of resolving information about oxidation state and local chemical environment. Such studies, as mentioned in more detail in Chap. 1, are commonly called ‘X-ray Emission Spectroscopy’ (XES).

Comprehensive treatments of x-ray emission spectroscopy are given in Glatzel and Bergmann[5] and DeGroot and Kotani[6, 7]. We summarize here some key points for context for the subsequent chapters that report experimental results.

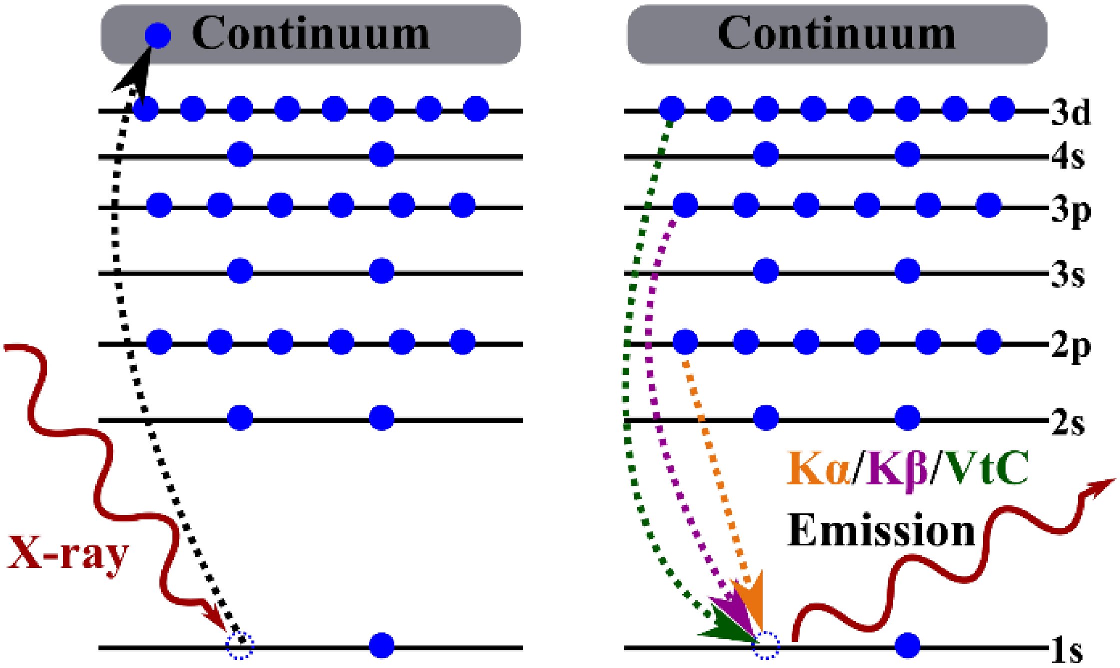

Figure 1. Diagram of the process for secondary X-ray fluorescence from an atom, shown for Ni. An incoming primary X-ray photon scatters an electron creating a hole in an inner electron shell which is then filled by a higher energy electron emitting a secondary x-ray.

2. Kα XES

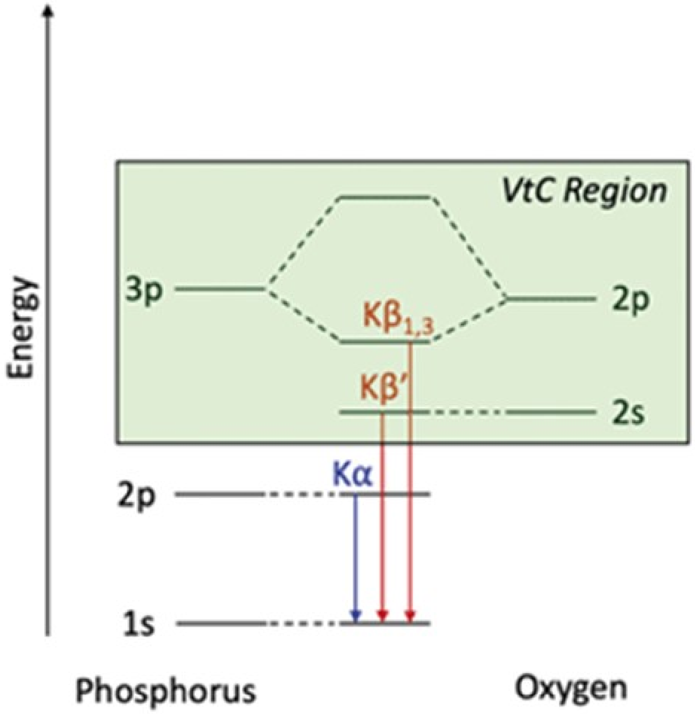

Figure 2. Transitions leading to Kα and Kβ emission for phosphorus[8].

Kα x-ray emission comes from an electron in the 2*p* orbital filling the 1*s* hole as shown in Fig. 1. It has two main features, $K\alpha_1$ and $K\alpha_2$ coming from an electron filling the hole from the $2p_{3/2}$ and $2p_{1/2}$ subshells which have distinct energies due to spin-orbit splitting of the 2*p* orbital. There is equal probability of any non-interacting electron in the 2*p* orbital filling the 1*s* hole but due to the occupation of the $2p_{3/2}$ subshell being twice the occupation of the $2p_{1/2}$, $K\alpha_1$ emission is about twice as intense as $K\alpha_2$. This intensity difference along with the inherent broadenings of x-ray emission, such as core hole lifetime and experimental broadenings, like source size or Johann error, lead to Kα XES having a typical doublet profile, see Fig. 3. When electron-electron interactions cannot be ignored this typical doublet profile is slightly distorted as in Fig. 6.

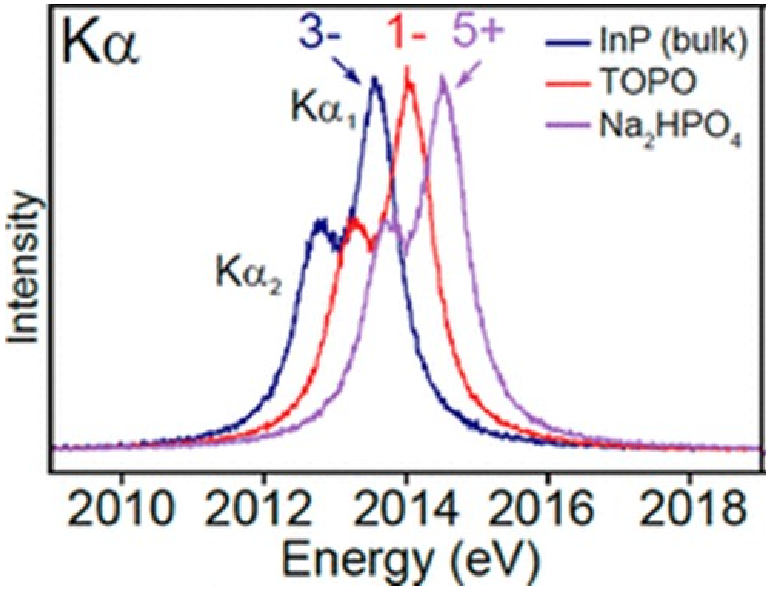

Figure 3. Phosphorus Kα spectrum from three materials, indium phosphide, trioctylphosphine oxide, and sodium phosphate. The typical doublet profile of Kα spectra is shown for all three materials as well as a shift in energy due to oxidation state, with higher oxidation states increasing the energy[9].

Kα XES for third row main group (Group 3) elements, like sulfur and phosphorus in this work, arise from the intermediate state of $1s^12p^6$ transitioning to a final state of $1s^22p^5$, see Fig. 2. Due to Group 3 elements having a relatively simple electronic structure the Hamiltonian will be dominated by the H_{EL} term; with only $3p$ valence electrons, which do not couple with the $2p$ orbital, there are no multiplet effects and with Kα being a core-to-core (CtC) emission process there are no crystal field terms. The Kα doublet profile therefore remains constant with only shifts in energy depending on the oxidation state of the atom, see Fig. 3. These energy shifts are due to the change in nuclear screening felt by the $2p$ electron orbital due to the $3p$ electrons. As the screening of the nucleus decreases with an increase in oxidation state, all electrons are more tightly bound to the nucleus but electrons closer to the nucleus feel a greater effect, increasing the energy separation of the $2p$ and $1s$ orbitals. This oxidation state dependent energy shift along with the constant spectral profile leads to Kα emission being an excellent analytical tool for finding sulfur or phosphorus oxidation state distributions by fitting reference spectra with known oxidation states to a sample spectrum with unknown or mixed sample oxidation state, Fig. 4.

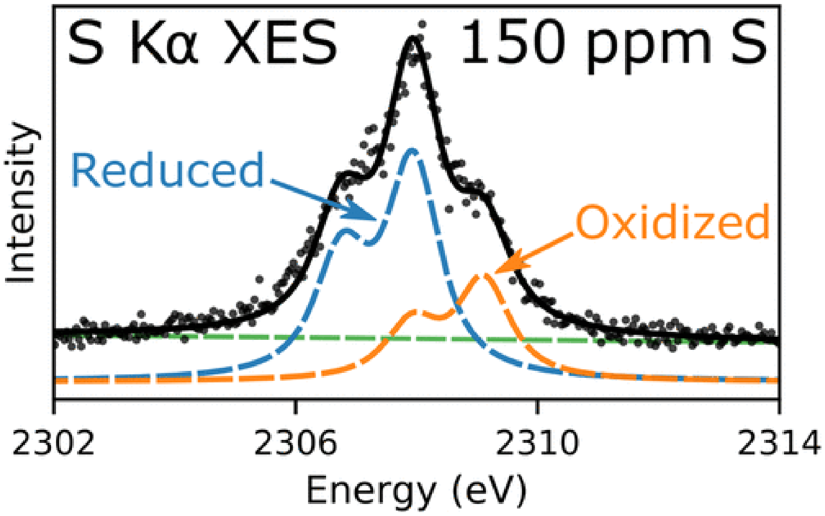

Figure 4. Linear combination fit of sulfidic (lower energy) and sulfate (higher energy) reference Kα XES spectra to a S Kα XES spectra of a biochar sample to extract the oxidation state ratio[10].

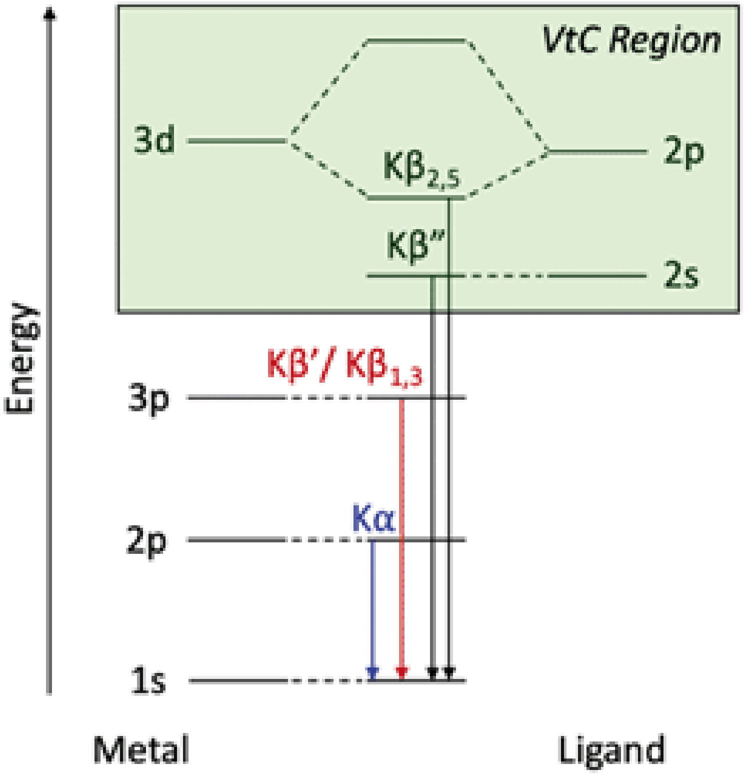

Figure 5. Transitions leading to Kα and Kβ emission for 3d transition metals[8].

Kα XES from 3d transition metals (3d TM) is more complicated due to the presence of 3d valence electrons, Fig. 5. The atomic-like intermediate state is a core hole is $1s^1 2p^6 3d^n$ but in real materials the presence of a ligand causes a more complicated intermediate state $1s^1 2p^6 3d^n$ + $1s^1 2p^6 3d^{n+1}\underline{L}$, where $\underline{L}$ represents a ligand hole state with energy $\varepsilon_{3d} - \varepsilon_{2p}$. Due to the lowered energy, the atom will have predominantly $1s^1 2p^6 3d^{n+1}\underline{L}$ character when ligands are present, as they are in this work, and the state is simplified to just $1s^1 2p^6 3d^{n+1}\underline{L}$. The final state will be $1s^2 2p^5 3d^{n+1}\underline{L}$. The Kα doublet shape for 3d TM isn't constant due to exchange interactions between the 2p and 3d levels leading to a nonzero $H_{multiplet}$ term. Depending on the metal-ion spin state, i.e. number of unpaired 3d electrons, the ideal, atomic-like $K\alpha_1$ emission is split into more lines. This changes the FWHM as shown in Fig. 6, with a higher spin state having a larger FWHM, although this effect plateaus at very high spin states as 3d electrons will cross over back to the ligand 2p orbitals. The $K\alpha_2$ emission line is similarly affected but has an additional broadening compared to the Kα_1 due to the Coster-Kronig effect, where the final state $2p_{1/2}$ hole is filled by a $2p_{3/2}$ electron.

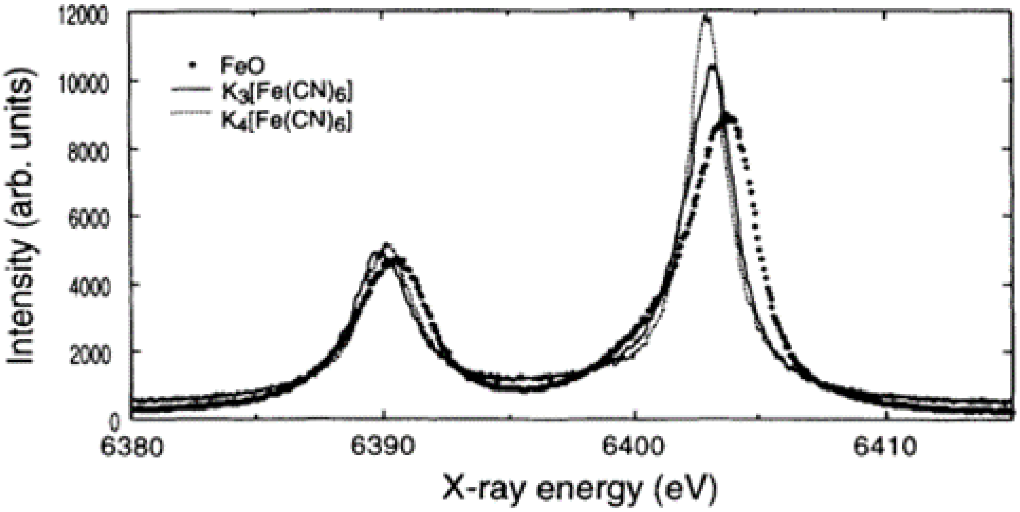

Figure 6. Fe Kα spectra for iron oxide, potassium hexacyanoferrate (II) and potassium hexacyanoferrate (III). The FWHM of the Kα_1 peak for these compounds decreases as the Fe spin decreases with iron oxide, potassium hexacyanoferrate (II) and potassium hexacyanoferrate (III) having four, one, and zero unpaired 3d electrons[11].

3 Kβ XES

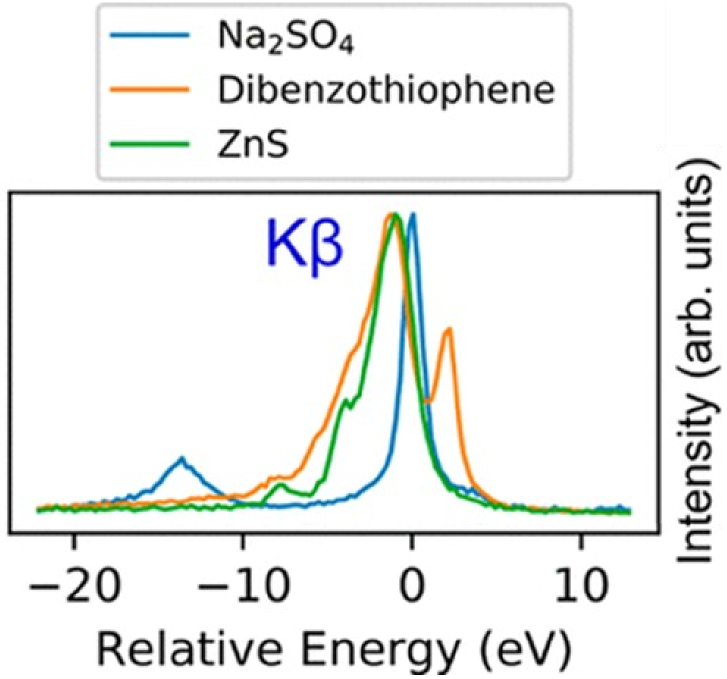

Figure 7. S Kβ spectra of three sulfur containing compounds. The main $K\beta_{1,3}$ peak at or a little below 0 eV is emission from transitions of 3p to 1s orbitals with the other important peak at about -15 eV, Kβ', being emission from the ligand 2s orbital to sulfur 1s orbital. The energy scale is set by the $K\beta_{1,3}$ peak of Na_2SO_4. Phosphorous has the same features[12].

Kβ x-ray emission results from the decay of a $3p$ electron to a $1s$ orbital hole, Fig. 1 and Fig. 5. The main feature is $K\beta_{1,3}$ which includes emission from both $3p_{3/2}$ and $3p_{1/2}$ orbitals which, unlike Kα, cannot be separated due to the weak spin-orbit coupling of the $3p$ orbital. Other features in the Kβ spectrum are dependent on the atom and its local environment, as we now will discuss.

For Group 3 elements, like phosphorus and sulfur, Kβ XES is a valence-to-core XES (VtC-XES) and therefore reflect the valence band electronic structure and the bonding environment, Fig. 2. Instead of transitions from atomic orbitals to fill the $1s$ hole, there are transitions from molecular orbitals (MOs) mixing Group 3 $3p$ and ligand orbitals to varying degrees and resulting in a Hamiltonian with a nonzero H_{CF} term. The specific MOs that form and the amount of *3p* and ligand character depends on the chemical bonding. This makes VtC-XES a direct tool for studying Group 3 valence electronic structure and chemical bonding.

A few features are common in most Group 3 Kβ spectra and will be discussed here. The $K\beta_{1,3}$ mainline comes from MOs with some ligand 2*p* character in σ-bonds and is the strongest feature due to the large overlap of the orbitals in this type of bonding. In addition to the $K\beta_{1,3}$ mainline there are three common satellite features: Kβ'', $K\beta_x$, and Kβ'. The Kβ'' satellite peak is just above the $K\beta_{1,3}$ peak in energy, as in dibenzothiophene in Fig. 7, and comes from mixing of ligand 2*p* and Group 3 3*p* from π-bonding; this feature is typically weaker than the $K\beta_{1,3}$ due to the smaller orbital overlap. The $K\beta_x$ satellite peak just below the $K\beta_{1,3}$ peak in energy, see ZnS in Fig. 7 (-8eV), comes from hybridization of ligand 2*p* or 2*s* with Group 3 3*p* when the ligand is protonated, lowering the energy of select MOs. The Kβ' peak, prominent in Na_2SO_4 at -15 eV in Fig. 7, comes from MOs with mainly ligand 2*s* character. Due to its separation from the Kβ mainline and its orbital character being primarily ligand it is a very useful indicator of ligand speciation.

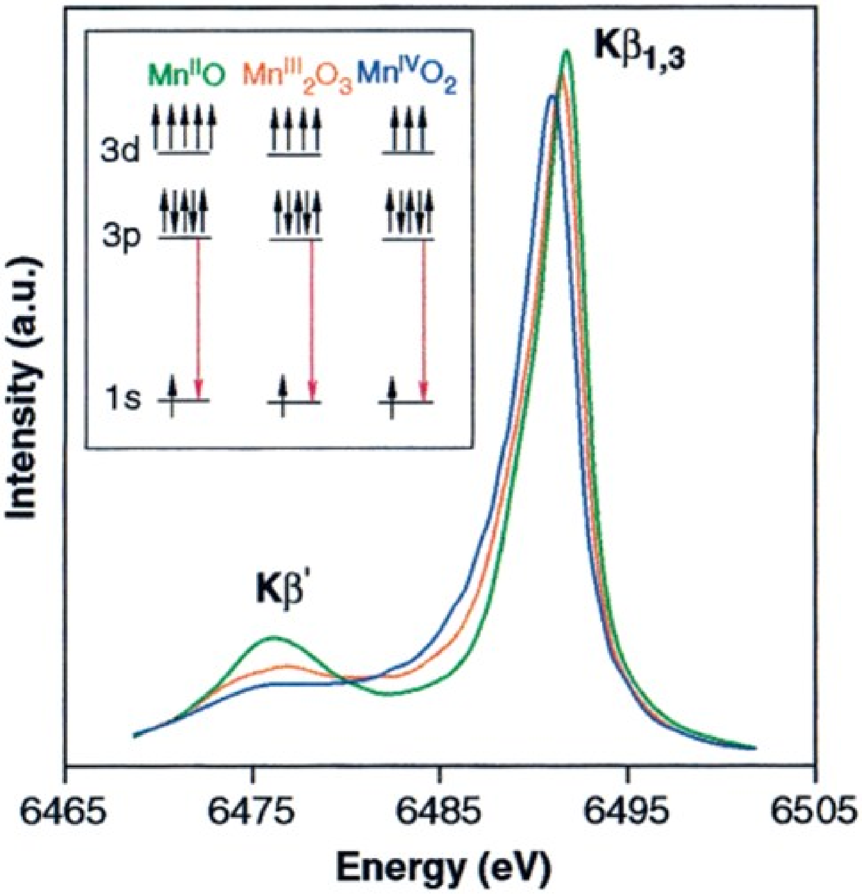

Figure 8. Kβ x-ray emission spectra of three manganese oxides with different Mn oxidation states. The change in 3d valence electrons with oxidation state changes is reflected in the strength of the Kβ' peak and the splitting in energy of the Kβ' and Kβ$_{1,3}$ peaks[13].

3d TM Kβ CtC-XES, generally just called Kβ XES, comes from intermediate states of $1s^1 3p^6 3d^{n+1}\underline{L}$ transitioning into final states of $1s^2 3p^5 3d^{n+1}\underline{L}$. Due to the strong (3*p*,3*d*) exchange coupling the multiplet effects of this interaction lead to a new feature, the Kβ' satellite peak. In the final state of 3d TM Kβ fluorescence, if the spin of the unpaired 3*d* electrons and 3*p* hole are parallel it results in Kβ' or antiparallel for Kβ$_{1,3}$. Due to the exchange interaction of parallel spins being stronger, the Kβ' satellite appears at lower energy compared to the Kβ$_{1,3}$ peak. Additionally the separation between the Kβ$_{1,3}$ peak and Kβ' satellite and the Kβ' satellite intensity increase with more unpaired 3*d* electrons since more unpaired 3*d* electrons results in a larger (3*p*,3*d*) exchange interaction. In this way the Kβ$_{1,3}$ and Kβ' splitting, and more easily the

Kβ' intensity, can be used as an indicator of oxidation state and/or metal-ion spin state as in Fig. 8 where a larger Mn oxidation state leads to fewer Mn 3*d* electrons and therefore smaller peak splitting and a smaller Kβ' feature. Other effects like the crystal field, 3*d* spin orbit coupling and Jahn-Teller distortions are present and lead to more multiplet peaks, and therefore changes to the FWHM, but are much weaker and not discussed here.

3d TM Kβ VtC-XES comes from transitions of MOs with 3*d* character into the 1*s* hole, i.e., intermediate states of $1s^1 3p^6 3d^{n+1}\underline{L}$ transitioning into final states of $1s^2 3p^6 3d^n\underline{L}$. Due to dipole selection rules these transitions from 3*d* MOs are very weak but strongly reflect the ligand *s* and *p* orbitals involved in bonding. There are two main features in 3d TM Kβ VtC-XES, Kβ'' and $K\beta_{2,5}$. The $K\beta_{2,5}$ peaks arise from transitions from MOs with ligand 2*p* character and appear just below the Fermi level. The Kβ'' peaks are from MOs with ligand 2*s* character and appear at lower energy compared to $K\beta_{2,5}$ by the energy difference in binding energies between ligand *s* and ligand *p* orbitals. This makes the Kβ'' peak an indicator, with some limitations[14], of the ligand speciation as shown in the upper part of Fig. 9, where three VtC spectra for different Mn compounds with either F, O or N ligands have a distinct Kβ'' energy. The Kβ'' peak is also very sensitive to ligand to metal bond distance due to the localization of the ligand 2*s* orbital which causes the intensity to decrease quickly with increased bond distance. An example is shown in the bottom and inset of Fig. 9 where VtC spectrum of different Mn oxides, all having Mn-O bonds, show a large change in intensity of the Kβ'' peak which when plotted against the Mn-O bond distance reveals a roughly ,exponential trend.

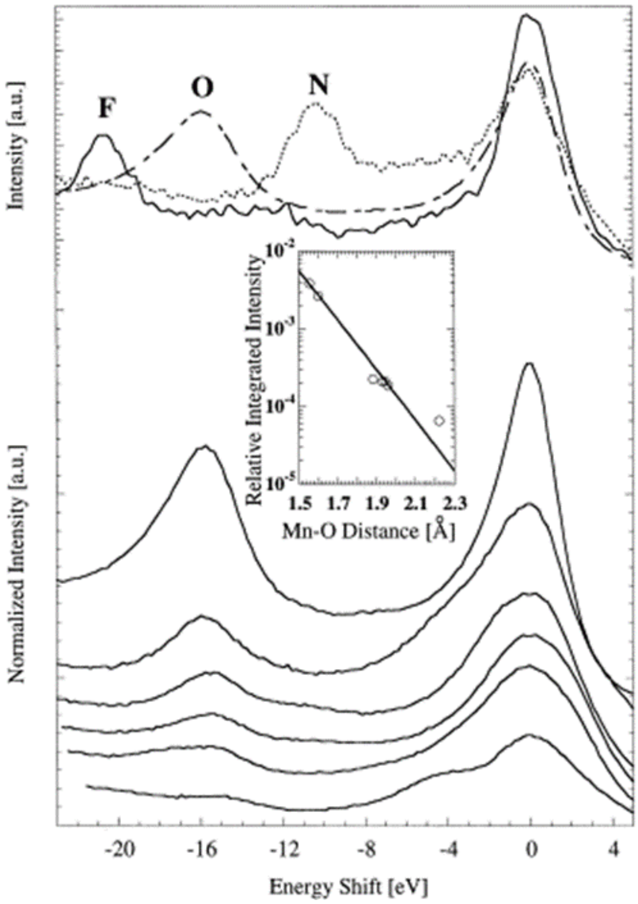

Figure 9. (Top) Kβ VtC for Mn samples with F, O, and N ligands showing the shift in Kβ'' with ligand species. (Bottom) Kβ VtC for Mn oxides with different oxidation states. From top to bottom: $KMn^{VII}O_4$, $[Et_4N][Mn^{V}(O)(\eta^4\text{-}L)]$, β-$Mn^{IV}O_2$, $LiMn^{III}Mn^{IV}O_4$ and $ZnMn^{III}{}_2O_4$, $Mn^{II}O$, $Li_2Mn^{IV}O_3$. (Inset) The change in Kβ'' integrated intensity with change in bond distance for the same Mn oxides[15].

References

1. X. Wang, F. M. F. de Groot and S. P. Cramer, *Physical Review B*, 1997, **56**, 4553-4564.
2. D. Friebel, M. W. Louie, M. Bajdich, K. E. Sanwald, Y. Cai, A. M. Wise, M. J. Cheng, D. Sokaras, T. C. Weng, R. Alonso-Mori, R. C. Davis, J. R. Bargar, J. K. Norskov, A. Nilsson and A. T. Bell, *Journal of the American Chemical Society*, 2015, **137**, 1305-1313.
3. A. Horta, B. Malone, U. Stockmann, B. Minasny, T. F. A. Bishop, A. B. McBratney, R. Pallasser and L. Pozza, *Geoderma*, 2015, **241**, 180-209.
4. A. M. W. Hunt and R. J. Speakman, *Journal of Archaeological Science*, 2015, **53**, 626-638.
5. P. Glatzel and U. Bergmann, *Coordination Chemistry Reviews*, 2005, **249**, 65-95.
6. A. K. F. de Groot, *Core Level Spectroscopy of Solids*, CRC Press, 1st edn., 2008.
7. F. de Groot, *Coordination Chemistry Reviews*, 2005, **249**, 31-63.
8. Z. Mathe, O. M. Stepanic, S. Peredkov and S. DeBeer, *Chemical Science*, 2021, **12**, 7888-7901.
9. J. L. Stein, W. M. Holden, A. Venkatesh, M. E. Mundy, A. J. Rossini, G. T. Seidler and B. M. Cossairt, *Chemistry of Materials*, 2018, **30**, 6377-6388.
10. W. M. Holden, G. T. Seidler and S. Cheah, *Journal of Physical Chemistry A*, 2018, **122**, 5153-5161.
11. J. Kawai, C. Suzuki, H. Adachi, T. Konishi and Y. Gohshi, *Physical Review B*, 1994, **50**, 11347-11354.
12. W. M. Holden, E. P. Jahrman, N. Govind and G. T. Seidler, *The Journal of Physical Chemistry A*, 2020, **124**, 5415-5434.
13. J. Messinger, J. H. Robblee, U. Bergmann, C. Fernandez, P. Glatzel, H. Visser, R. M. Cinco, K. L. McFarlane, E. Bellacchio, S. A. Pizarro, S. P. Cramer, K. Sauer, M. P. Klein and V. K. Yachandra, *Journal of the American Chemical Society*, 2001, **123**, 7804-7820.
14. S. N. MacMillan, R. C. Walroth, D. M. Perry, T. J. Morsing and K. M. Lancaster, *Inorganic Chemistry*, 2015, **54**, 205-214.
15. U. Bergmann, C. R. Horne, T. J. Collins, J. M. Workman and S. P. Cramer, *Chemical Physics Letters*, 1999, **302**, 119-124.

Chapter 3 - An Exploration of Benchtop X-ray Emission Spectroscopy for Precise Characterization of the Sulfur Redox State in Cementitious Materials

Originally published as: J. Abramson, N. Avalos, A. Bourchy, S. Saslow, G. T. Seidler. *X-ray Spectrometry* 2021 Vol. 51 Issue 2 Page 151. J. Abramson wrote and conducted the majority of this work.

The evolution of sulfur chemistry in cements is best known in the bailiwick of failure mechanisms via sulfate attack but is equally important for its contributions to the reduction capacity of cementitious materials often used for immobilizing nuclear waste streams destined for long-term storage, e.g., cementitious waste forms (CWF). The total reduction capacity of CWFs, encompassing contributions from both S and Fe reductants, and its implications toward radionuclide immobilization is most often studied by destructive wet chemistry methods requiring acid digestion in the presence of Ce(IV) and subsequent titration and colorimetric interpretation. Here, we investigate a similarly analytical but nondestructive alternative, benchtop high resolution wavelength-dispersive x-ray fluorescence spectroscopy, most commonly known as x-ray emission spectroscopy (XES), for probing the bulk sulfur oxidation state distribution. We present here an initial investigation of S XES, including an improved experimental protocol for lab XES of inhomogeneous samples, both as a complement to the Ce(IV) test and for new scientific opportunities that it enables for observing changes in sulfur *chemistry. We discuss future improvements and opportunities, including: (1) the practical challenges associated with coordinating XES and Ce(IV) liquid extraction for a more comprehensive perspective on reduction capacity and for a high-precision evaluation of uncertainties in the Ce(IV) test; and (2) new opportunities, due to the nondestructive nature of XES, for controlled evolution studies aimed at elucidating specific chemical responses of CWFs exposed to invasive gas or liquid species or to accelerated aging by radiative dose or thermal treatment.*

1. Introduction

The retention of toxic metals and radionuclides of concern within cementitious waste forms (CWFs) can be improved with the addition of strong reductants to cement dry blends (e.g., blast furnace slag (BFS) and sodium sulfide)[1]. For instance, technetium-99 (^{99}Tc), most often present in its oxidized form as pertechnetate ($Tc(VII)O_4^-$) in nuclear waste streams, is less soluble in its reduced Tc(IV) state, e.g., as ^{99}Tc oxides ($TcO_2 \cdot nH_2O$) and sulfides (Tc_2S_7).[2] Therefore, the conversion of redox-sensitive contaminants to a less soluble species by the addition of reductants has been widely explored as a valuable method to decrease their likelihood of leaching from the CWF and into the environment surrounding the containment media.[1, 3, 4] Also, the use of a variety of reductants that can sustain reducing conditions over the life cycle of CWFs would delay the re-oxidation of contaminants and their subsequent release. For this reason, the ability to quantify the reduction capacity of CWFs, their dry mix ingredients, and any additives for boosting the reducing capacity of a CWF is central to both monitoring existing CWFs and the development of improved materials that delay contaminant release via redox processes.

The Ce(IV) method is a common analytical tool for determination of the total (non-element-specific) reduction capacity of cementitious materials and has been used in several CWF development studies.[1, 5-7] Specifically, a reduction capacity is calculated by determining the difference between the initial oxidizing equivalents in the Ce(IV) solution and the reducing equivalents of Fe(II) required to neutralize excess Ce(IV) after reacting the solution with the CWF sample for several days.[1] Because the Ce(IV) solution is 10% H_2SO_4 and is highly acidic (pH ranges from 0-1), this facilitates the dissolution of most of the sample (crushed to a particle size < 2 mm) with the aim of providing a measure of total reductive capacity, with contributions from ferrous iron oxides, sulfides, and other reductants for CWFs. This approach is different from the sibling Cr(VI) method, which uses a neutral (pH 7) solution to target reduction capacity contributions from the exposed sample surface. However, there are several caveats to using the Ce(IV) and Cr(VI) methods. Both methods require the partial destruction of the sample to maximize oxidant exposure to reductants in the sample, though sample dissolution is more severe when using the highly acidic Ce(IV) method. Second, titration of the Ce(IV) leachate with 20 mM ammonium ferrous sulfate until the solution turns/remains a lilac color relies on the analysts' best judgment, which creates room for human error. Lastly, these methods are labor intensive, requiring approximately 20 person-hours for the analysis of 15 specimens based on the tests performed herein. These issues highlight the importance of finding a non-destructive benchtop capability that can quantitatively address total reduction capacity.

However, the fact that the Ce(IV) method measures a total reductive capacity at all is already limiting from the perspective of understanding the detailed chemical evolution within the CWF. As one example, we propose that there should be special benefit to tracking the evolving sulfur oxidation state, and hence its contribution to reductive capacity, within these CWFs due to the ability for sulfides to form less soluble phases compared to other reductants. For instance, CWFs that are capable of reducing ^{99}Tc to a less soluble phase with sulfides [Tc(VII)O_4^- to a Tc(IV) sulfide] retain ^{99}Tc better than CWFs that form Tc(IV) oxides instead. The formation of Tc(IV) sulfide in CWFs is favorable because a multi-step release pathway is required to revert this phase to its mobile Tc(VII) species [Tc(IV) sulfide → Tc(IV) oxide → Tc(VII)O_4^-], therefore slowing the oxidation and release process.[2, 6] However, as reduction capacity is lost with time, contaminants like ^{99}Tc within CWFs are at increased risk for oxidation and subsequent release to the surrounding environment. As such, the ability to nondestructively monitor and quantify the sulfur-related reduction capacity in CWFs as they age offers a valuable tool for assessing CWF performance and predicting future environmental risks due to contaminant release.

Given that the relevant chemical question is the quantification and monitoring of the redox state and hence reductive capacity of specific elements, one can naturally consider whether x-ray absorption near edge structure (XANES) could play a role. XANES indeed sees extensive use to address the question of oxidation state distributions and more generally the mineral chemistry of species in CWFs,[8-10] but for the present case of modest S concentrations in a cementitious matrix S K-edge XANES requires synchrotron x-ray access, which does not fit our goal of a high-access, analytical method for evaluating S-contributed reduction capacity. Furthermore, the reliability of oxidation state distributions inferred by XANES is necessarily limited by the ability to define extremely relevant reference standards.[11] In complex, multiphase systems with numerous redox active phases and interfaces, such as most cementitious materials, the selection of reference compounds for, e.g., using principal component analysis to infer oxidation state ratios, is nontrivial and may well be extremely cement-system specific.

It is interesting to instead consider a related route that admittedly forgoes much of the detailed structural information that is available from XANES but retains and can considerably simplify extraction of simple oxidation state distribution information. Specifically, instead of looking at the spectrum of x-rays absorbed we instead consider the spectrum of x-rays emitted by S in cementitious materials. This technique, x-ray fluorescence (XRF) and more specifically wavelength dispersive x-ray fluorescence (WD-XRF) where emitted x-rays are diffracted by a crystal analyzer, has seen use in the last half century to monitor S content and speciation of various materials, oil, minerals, and plant tissue among others[12-17]. More recently WD-XRF has been employed to look at cementitious materials and sulfate attack of cements[18, 19], and in these studies that pursued the question of oxidation state the photon energy resolution was unable to separate the $K\alpha_1$ and $K\alpha_2$ peaks. Consequently, estimations for oxidation state were somewhat sensitive to assumptions about relevant reference compounds because of the weak dispersion of fluorescence line energies even within a nominal classical oxidation state, as has been demonstrated with higher-resolution S WD-XRF studies over several decades[20-32].

Here, we take the next step and perform such a higher resolution WD-XRF study wherein we follow the habit in the synchrotron x-ray community to call the technique x-ray emission spectroscopy (XES), a label that is reserved for when the energy resolution becomes comparable to the intrinsic broadening due to the core-hole lifetime of the photoexcited species. Unlike XANES, which requires synchrotron access when the species of interest is dilute, nonresonant XES can be performed with lab-based equipment even for relatively dilute systems[11, 33, 34]. We find that the sulfur content in several cementitious materials relevant for CWFs is sufficient for relatively rapid in-house measurement of the S $K\alpha$ XES, and that the resulting spectra can be fit with high precision to reference standards when allowing an additional fit parameter for small shifts in the nominal $K\alpha_1$ location due to chemical effects within the same nominal oxidation state[21, 22].

Looking to the future, this opens several venues. First, the nondestructive nature of the measurement allows for simple and accelerated aging studies, or for studies investigating more aggressive chemical changes due to exposure to O_2, CO_2, SO_4^{2-}, or H_2. Second, if issues surrounding the high variability of elemental compositions in the constituent dry mixes of the CWF can be addressed, then S-specific reductive capacities can be inferred from the measured sulfide/sulfate ratios, so that the combination with the Ce(IV) method will then allow isolation of the relative S-specific and Fe-specific reductive capacities with only benchtop methods.

2. Methods

2.1 Materials

Cement dry and additive ingredients – Fly ash (FA), which qualifies as class C and F, was provided by the Centralia, Washington power plant.[35] Grade 100 blast furnace slag (BFS) and Type I/II ordinary portland cement (OPC) were both supplied by Lafarge North America Inc (Seattle, Washington State, USA). Two sources of BFS and OPC were used across the cements studied in this work: BFS-new is from material received after 2018, whereas BFS-old is material used for cements formulated in 2018 only. OPC-new material impacts only the 2020 cement formulations, whereas OPC-old is material used in all formulations before 2020. PowerPozz ™ metakaolin, used to formulated geopolymer-based CWFs, was purchased from Advanced Cement Technologies (Washington State, USA) and the potassium metal sulfide II (KMS-2) getter was synthesized according to a previously published procedure[36]. For the purpose of this study, KMS-2 was evaluated as a high-sulfide benchmark material and has been investigated as a CWF additive for improving reduction and immobilization of ^{99}Tc[37].

Fresh and Aged Cement Specimens - Different cement formulations were analyzed in this study to evaluate how reduction capacity (presented as fraction sulfide) changes as a function of time using XES (described later). Cement formulations were also analyzed using the Ce(IV) method to determine total reduction capacity (presented as μeq/g,) in attempt to separate S and Fe contributions in combination with XES. Hanford Grout Mix 5 (HGM-5) is a baseline CWF formulation used currently for disposal activities at the Hanford Site nuclear waste reservation in South Eastern Washington.[38] The HGM-5 formulation has a low reducing capacity, consisting of a dry ingredient mix containing 75 wt% FA and 25 wt% OPC and mixed at a water-to-dry-mix (wdm) ratio of 0.29. The second formulation, Cast Stone (CS), is a more reducing formulation that has been the focus of Hanford waste form development efforts over the past decade.[35, 38-40] CS consists of 45 wt% FA, 8 wt% OPC and 47 wt% BFS mixed at a wdm ratio of 0.45. Finally, a geopolymer formulation containing 70 wt% BFS, 17 wt% metakaolin and 13 wt% anhydrous solids from the activating solution, e.g., Na_2O and SiO_2, and mixed with water at a wdm ratio of 0.60 was also studied. For archived cementitious material that have been exposed to ambient conditions over time (between 1 to 2 years), selected specimens are identified in Table 1 and preparation details may be found for archived samples in the respective cited literature.[38, 41]

Grout Fabrication (HGM5-2020 and CS-2020 specimens) – New CS and HGM-5 grout formulations were fabricated for the purpose of providing an early age CWF for this study. Specific dry ingredient and double deionized water (DDI) amounts for fabrication of each formulation is listed in Table 2. A pre-determined amount of DDI was added to a plastic 0.1 L Nalgene beaker. Then, grout dry ingredients (previously weighed and homogenized by hand in a plastic bag) were added into the beaker and mixed by hand for 3 minutes or until no visible chunks were present. The resultant slurry was then poured into plastic 2” x 4” forms for curing for 28 days at room temperature and >80% relative humidity conditions. At the end of 28 days, the cured CWF was removed from the mold and stored at ambient conditions with a damp paper towel sustaining a humid environment for approximately 6-months.

Dry Ingredient Mixtures for CS and HGM5 Formulations – It is important to note that two dry ingredient mixtures were analyzed for the CS and HGM5 formulations. One set was taken from left over dry ingredients used to make CS and HGM5 CWFs used in studies performed in 2018 (HGM5-2018-Dry Mix and CS-2018-Dry Mix).[38] The second set was prepared in 2021 for the purpose of this study using the source materials used to formulate all CWFs after 2018 (HGM5-2020-Dry Mix and CS-2020-Dry Mix). As noted earlier, between 2018 and 2019, a new batch of BFS was acquired (BFS-new). As the primary contributor of reducing agents, this change in BFS source material will play a key role in the results discussion. Additionally, a new source of OPC was acquired in February 2020 (OPC-new).

Specimen name	Report
*HGM5-2018	Asmussen et. al 2019
HGM5-2019	Saslow et al. 2021
**HGM5-2020	Unpublished
*CS-2018	Asmussen et. al 2019
CS-2019	Saslow et al. 2021
**CS-2020	Unpublished
Geopolymer-2019	Saslow et al. 2021

* Approximately 0.1 g of homogenized dry mix material from this formulation year was used for Ce(IV) dry ingredient mix analysis (Samples CS-2018-Dry Mix and HGM5-2018-Dry Mix).

** Approximately 0.1 g of homogenized dry mix material was reserved prior to fabrication for use in preparing dry ingredient mix pellets for XES analysis.

Table 1: Archived cementitious specimen sources, see Saslow, et al.[41], and Asmussen, et al.[38], for details.

Pellet preparation - Grout specimens listed in Table 2 were milled to a powder for 5 minutes. Pellets (~100 mg up to 400 mg) from materials listed in Table SI-1 were made using a manual hydraulic press (Carver Laboratory press) with a die size of 13 mm in diameter. Approximately 10 wt% cellulose was used for select materials in Table SI-1 to improve pellet binding. For the HGM5 and CS 2018 and 2020 samples, triplicate pellets (sample names ending in -1, -2, and -3) were prepared to assess reproducibility of the XES and or Ce(IV) analytical methods.

Specimen Name	**wdm**	**FA (g)**	**OPC (g)**	**BFS (g)**	**DDI (g)**
HGM5-2020	0.29	64.8	21.6	-	25.0
CS-2020	0.45	25.0	4.4	26.2	25.0

Table 2: Freshly made cementitious specimen ingredients. Column description: wdm = 'water to dry mix'; FA = 'fly ash', OPC = 'ordinary Portland cement'; BFS = 'blast furnace slag'; DDI = 'double deionized water'.

2.2 S Kα X-ray Emission Spectroscopy (XES)

Sulfur Kα XES spectra were obtained from the prepared cementitious pellets and sulfide and sulfate reference compounds using an updated version of the laboratory S XES spectrometer previously reported in Holden, et al. [42] Briefly, this instrument achieves better than 1-eV energy resolution via a Si (111) cylindrically bent analyzer on a 10-cm diameter Rowland circle. The x-ray illumination on the sample is large (~1 cm^2) and a CMOS x-ray camera [43] placed tangent to the Rowland circle completes the 'Dispersive Rowland Refocusing' (DRR) geometry. [42] An average Bragg angle of 58.9 degrees ensures that the correct energy range is projected onto the detector plane. This spectrometer has been previously used for studies of oxidation state and more complex electronic structure for sulfur and phosphorus compounds showing excellent agreement with synchrotron results, including for the reference compounds used here and cited below[11, 21, 44, 45].

All measurements were performed using an unfocused, commercial X-ray tube (model VF-50 with Pd anode, from Varex, Inc.) operated at 50 W tube power (25 kV and 2 mA). The sample space is held at ~100mTorr vacuum. The instrument was allowed to stabilize for at least an hour with the tube at the desired power before data collection to prevent any thermal drift. To ensure consistency of energy scale calibration across the entire effort, for each group of samples we also measured the same two reference materials, i.e., crystalline ZnS (MTI Corp.) and Na_2SO_4 powder (Fisher Chemical, sealed in an 8-μm wall thickness polyimide pouch). The overall energy scale itself was set by the S $K\alpha_1$ emission of ZnS at 2307.69 eV[22].

It is useful here to motivate and explain a change in sample measurement protocol that was inspired by the possibility of spatially inhomogeneous materials. A schematic of the dispersive Rowland refocusing (DRR) spectrometer together with the collection cones from different energy points is given in Figure 1. Sample inhomogeneity will result in a biasing of the overall shape of the spectrum due to the collection cones seeing different parts of the inhomogeneous sample. Similarly, see Figures 1(a) – 1(c), if the sample is smaller than the total collection cone width and not positioned correctly then the efficiencies of collection at different energies will depend on the sample position. This is illustrated in Figure 2 by the progression in spectral shapes due to the 'cone-crossing' of a small cementitious sample, HGM5-2018-1. In past studies with DRR spectrometers[11, 21, 44, 45] we have used large samples that we anticipate would be strongly *homogeneous*, and simply centered the sample in the collection cones. Here, we sweep the sample through the collection cones, taking short scans as the sample is stepped through the cones, and sum the resulting position-dependent spectra. This gives equal weight at all detected energies to all positions on the face of the sample. We propose that this method, which does extend total measurement time by ~2x, should always be used when there is any uncertainty in sample homogeneity.

Total measurement times were 3-5 hours for each cementitious sample, divided into short 3 min scans where the sample was stepped through the analyzer collection cones, as described above. The resulting, summed spectra were integral normalized with a linear background subtraction. In these studies, and in studies of similar samples where the sample was held stationary, there was no evidence of x-ray beam damage.

The spectra were analyzed to find the fractions of sulfide and sulfate moieties in each cementitious sample. This was done using a least squares fit of the spectra to a linear superposition of the pure sulfide reference, ZnS, and pure sulfate reference, Na_2SO_4. For each fit, a small energy shift was allowed independently for each of the sulfide and sulfate reference spectra. This is necessary because of the nonzero chemical sensitivity of the Kα energies within compounds of the same nominal oxidation state.[21, 22] The limitations of this 'two endpoint' approach, i.e., ignoring possible intermediate oxidation states, is discussed in section III.

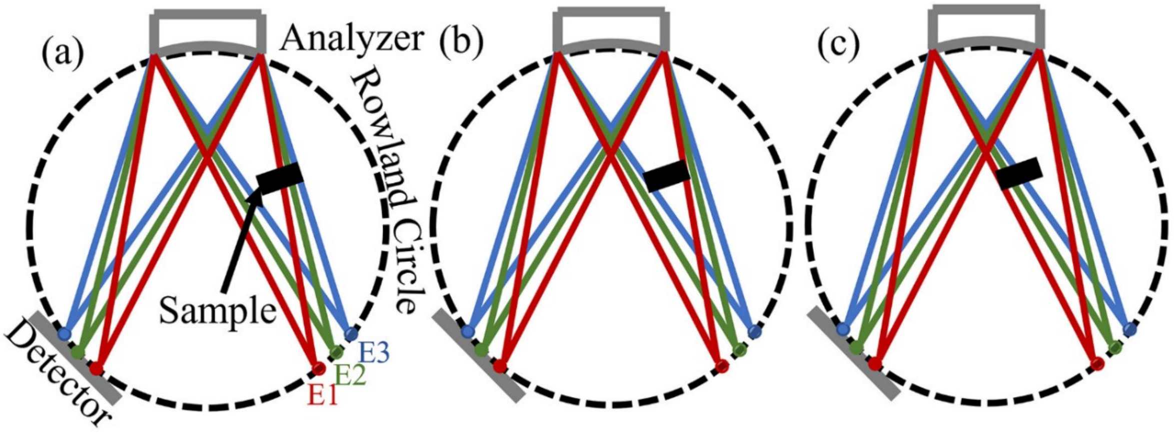

Figure 1: DRR spectrometer schematic with three collection cones at different photon energies that correspond to positions E1, E2, and E3 on the Rowland circle. Note how different sample positions can result in different efficiency of data collection across the face of the detector, i.e., at different photon energies, due to different volumes and locations of the sample being present at different energies.

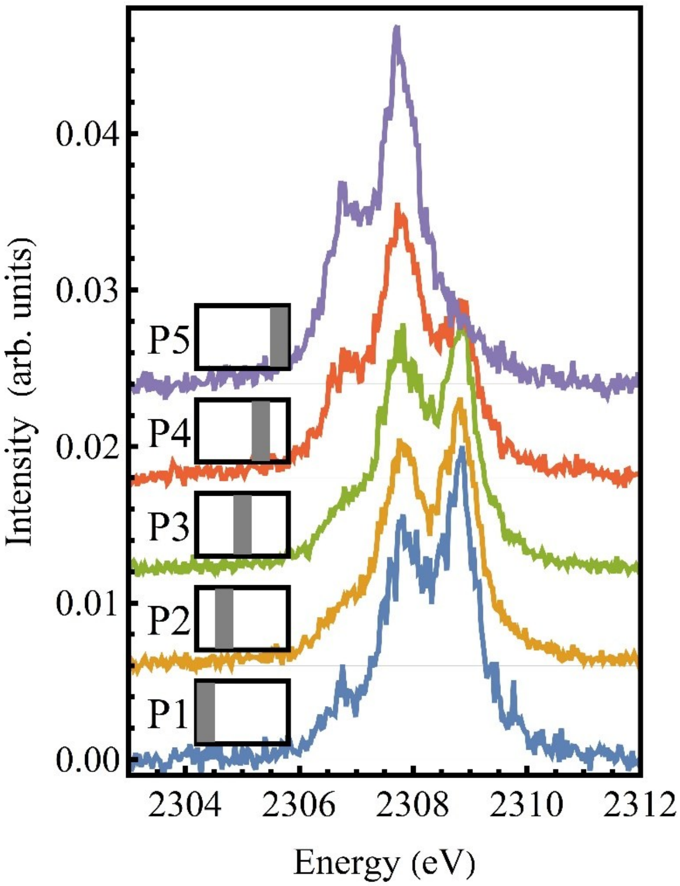

Figure 2: Illustration of the dependence of measured spectrum on sample position due to the 'sampling cone' issues of Fig. 1. Shown from bottom to top are spectra from a sample of HGM5-2018-2 (solid grey box) that is smaller than the total collection cone (black box). Moving from position 1 (P1) to P2 and subsequent steps are a 1.3mm movement of the sample in the Rowland plane. A clear shift from the spectra weighing higher energies to lower energies can be seen as the sample moves across. Integrating these spectra results in a measurement that averages over sample compositional variations with equal detection efficiency at every photon energy.

2.3 Ce(IV) method

Directions for all solution preparation and total reductive capacity measurements are described in work by Um, et al.1 Specifically, reagent grade (NH4)2Fe(SO4)2 x 6H2O and (NH4)4Ce(SO4)4 x 2H2O were purchased from Sigma-Aldrich and used to make the 20 mM Fe(II) and 40 mM Ce(IV) solutions, respectively. Concentrated (98%) H2SO4 was obtained from Fisher chemical. Ferroin indicator solution was purchased from Fluka Analytical. The concentration of Fe(II) in the 20 mM Fe(II) solution was calibrated with a 100 mM Ce(IV) standard from Fluka Analytical prior to the conduction of reduction capacity measurements.

Grout sample specimens were first milled and sieved to a size fraction of < 2 mm. Powdered cement ingredients were used as provided by the supplier. Crushed grout specimens were then contacted with a 40 mM Ce(IV) solution, also consisting of 10% concentrated H2SO4, at a solution to solid ratio of 30 mL: 1 g and placed on an orbital shaker at 40 rpm for 4 days. At the end of the reaction period, solid-containing solutions were filtered using a 0.45 μm Nalgene vacuum filter. For the powdered ingredients, solutions were centrifuged for 10 min at 2000 rpm prior to filtering (Table SI-2). Then, ferroin solution was added at a ratio of 1:100 to the filtrate sample being titrated. The final solution was titrated using a burette that dispensed 20 mM Fe(II) solution until the solution turned a lilac or faint pink color. Titrations were performed in triplicate.

3. Results and Discussion

3.1 Sulfur oxidation states in cementitious materials

The S Kα XES spectra for all the cementitious materials along with the ZnS (top-most curve) and Na_2SO_4 (bottom most curve) references are shown in Figure 3. Each curve shows a K$\alpha_{1,2}$ doublet due to spin-order splitting, where the Kα_1 at higher energy is due to $2p^{3/2}$ → 1s transitions, while the Kα_2 is due to $2p^{1/2}$ → 1s transitions, and consequently has roughly half as much intensity because of the relative populations of the $2p^{3/2}$ and $2p^{1/2}$ orbitals.

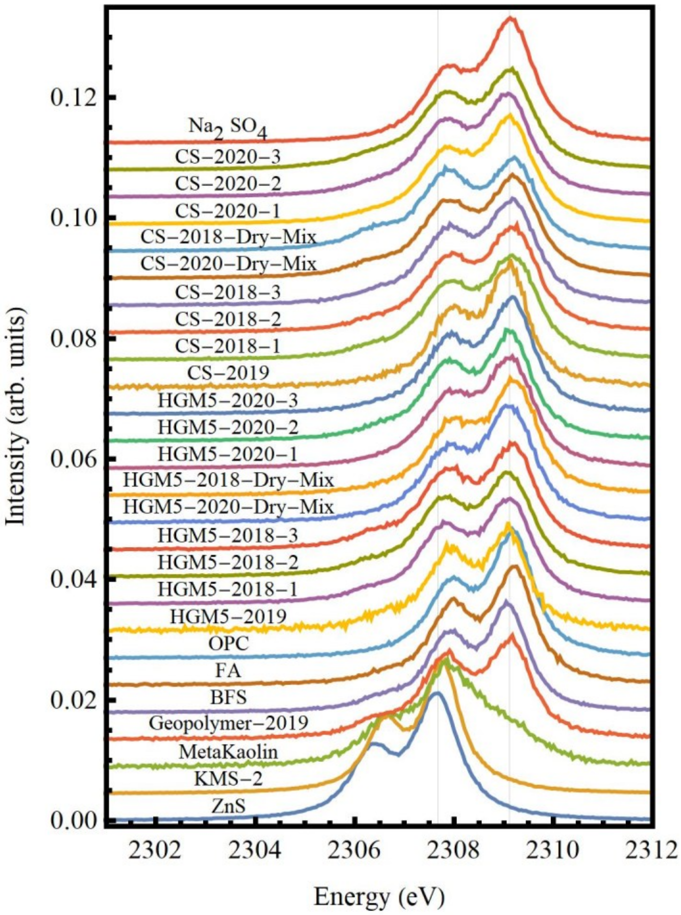

Figure 3: XES spectra of all cementitious materials and the ZnS and Na_2SO_4 references. The two vertical lines correspond to the Kα_1 energies of the references.

The expected dominance of sulfate-containing phases in the cementitious materials and their main ingredients is apparent from the general strength of the sulfate doublet in their spectra. Some representative fits to a superposition of sulfide and sulfate contributions are shown in Figure 4, where the sulfide contribution can be seen changing the shape of what would otherwise be the $K\alpha_2$ line from a sulfate moiety and adding a small lower-energy shoulder at ~2306.5 eV. These inferred sulfide fractions as well as the shifts to the reference spectra for each fit component (due to chemical effects[22]) are given in Table 3. Some notable outliers are KMS-2 and OPC-old which have sulfide fractions of 0.99 and 0.0099, respectively, meaning that they contain sulfur as purely sulfide or sulfate. Additionally, metakaolin had an unusual spectral shape which led it to a poor fit using the two reference spectra. This is most likely due to the presence of other sulfur oxidation states, such as from sulfoxides[21]. Previous XANES studies of some BFS materials[8, 10] show a significant contribution from sulfoxide moieties, although we see no evidence for them in our BFS-new measurements.

As shown in Table 3, XES sulfide fraction measurements from multiple samples sourced from the same batch of materials (CS-2018, CS-2020, HGM5-2018, and HGM5-2020 replicates 1-3) generally showed excellent reproducibility, with some exception for CS-2020. The general trends in the sulfide fractions also make sense for the individual CWF dry ingredients. When comparing the three dry ingredients used to formulate CS and HGM5 CWFs, the BFS has the largest sulfide fraction (0.16 S^{2-}), followed by mildly reducing FA (0.091 S^{2-}), and finally OPC (0.0099 S^{2-}). As BFS is often added to CWF formulations to increase reducing capacity of the immobilizing matrix, and with common reductants in BFS being FeS and CaS,[6, 9] this general trend agrees with the literature.

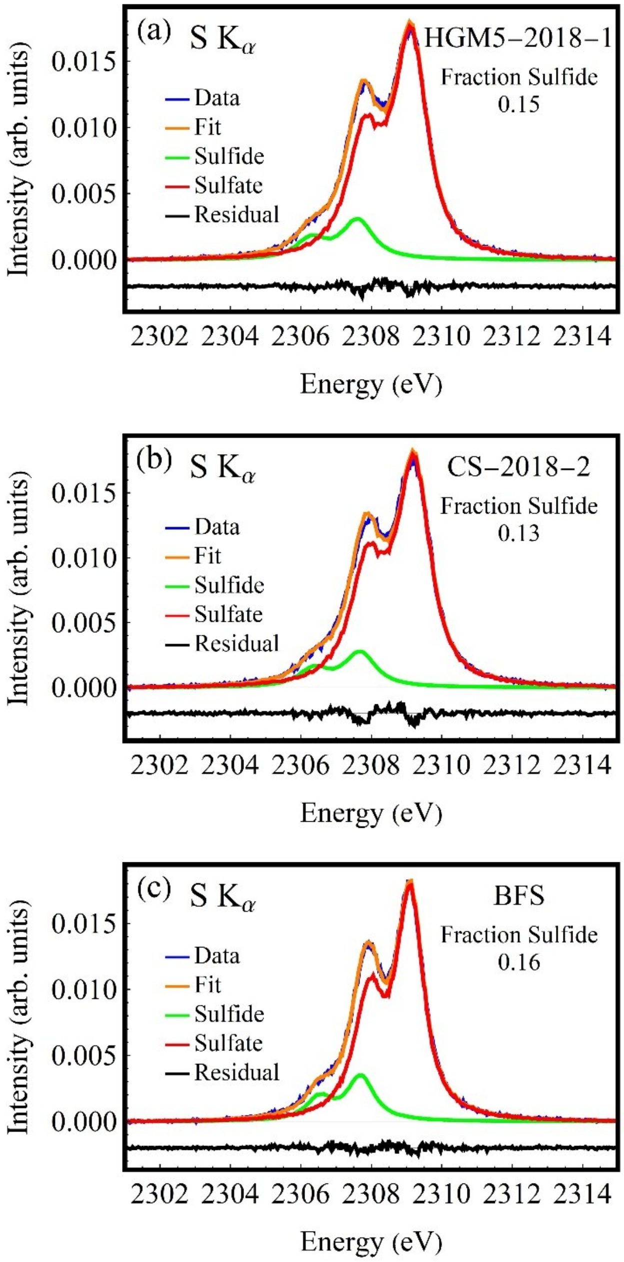

Figure 4: Linear superposition fits to sulfide and sulfate references for the S Kα XES spectrum of a Hanford Grout Mix (HGM5), a Cast Stone, and a Blast Furnace Slag sample. A compendium of fits for all samples is presented in Fig. SI-1.

A look at the trends across formulation years for Cast Stone samples and its dry mixes at first reveals some unexpected results. Following the logic that reduction capacity deteriorates with time, one would expect to measure the highest sulfide fraction in the dry mix material and then lower sulfide fractions with each passing year as the cured CWF ages. In this study, 0.17 and 0.23 sulfide fractions were measured for the CS dry mixes (CS-2020-Dry Mix and CS-2018-Dry Mix), which was comprised of BFS, OPC, and FA sources left over from the 2020 and 2018 formulation efforts. After approximately 6 months of aging, the sulfide fraction decreased to 0.11 ± 0.03 (CS-2020 1-3), and then in 2019 (corresponding to 1 year of aging), this sulfide fraction plummeted to 0.050. However, the sulfide fraction then increased to 0.14 ± 0.03 for CS aged 2 years (CS-2018 1-3). Upon further investigation into this sulfide fraction disparity, we again note that a new batch of BFS was acquired between 2018 and 2019 formulation campaigns. And while both batches of BFS acquired meets ASTM C989/C989M-18a requirements for Grade 100 BFS, including a maximum sulfide content of 2.5 wt%, the true amount of sulfide is likely significantly different across these two BFS source batches (which account for 47 wt% of dry ingredients added) based on these XES measurements[46]. This is supported by the higher sulfide fraction measured in the CS-2018-Dry Mix material of 0.23. Finally, if we consider that the sulfide fraction decreased by up to 71% after aging mixed 2020 CS material for two years, then one would expect a sulfide fraction less than 0.07 in the CS-2018 sample, which is the original sulfide fraction in the CS-2018-Dry Mix less 71%. Yet, the CS-2018 sulfide fraction is 0.14, suggesting that the source materials used to formulate these CWFs impacts not only the reducing capacity, but also the rate at which these CWFs age and oxidize.

Sample	Fraction Sulfide	Shift of Sulfide (ZnS) Reference (eV)	Shift of Sulfate (Na_2SO_4) Reference (eV)
CS-2020-Dry Mix	0.17	0.04	-0.07
CS-2020-1	0.079	0.17	0.055
CS-2020-2	0.11	0.14	0.0934
CS-2020-3	0.15	0.15	0.047
CS-2019	0.050	-0.19	-0.01
CS-2018-Dry Mix	0.23	0.064	-0.056
CS-2018-3	0.14	-0.04	-0.04
CS-2018-2	0.13	-0.03	-0.06
CS-2018-1	0.14	-0.02	-0.06
HGM5-2020-Dry Mix	0.038	-0.11	0.01
HGM5-2020-1	0.034	-0.062	0.039
HGM5-2020-2	0.088	0.018	0.030
HGM5-2020-3	0.027	0.055	-0.0012
HGM5-2019	0.21	-0.04	-0.00
HGM5-2018-Dry Mix	0.013	0.0040	-0.062
HGM5-2018-3	0.17	-0.01	-0.04
HGM5-2018-2	0.16	0.07	0.03
HGM5-2018-1	0.15	0.05	0.03
OPC-old	0.0099	-0.12	-0.03
FA	0.091	-0.19	-0.06
BFS-new	0.16	0.03	0.00
Geopolymer-2019	0.22	-0.02	0.02
Metakaolin	0.62	-0.22	0.18
KMS-2	0.99	-0.03	0.10

Table 3: XES fit results of fraction sulfide and energy shifts of sulfide and sulfate references.

The sulfide fraction differences that can occur across different batches of the same classified cementitious ingredients, also explains the unlikely trend in sulfide fractions across the HGM-5 CWFs and the measured dry mixes. Simply, the HGM-5 dry mixes have sulfide fractions equal to 0.038 HGM5-2020-Dry Materials and 0.013 HGM5-2018-Dry Materials, whereas the 2020, 2019 and 2018 cured CWFs have sulfide fractions equal to 0.050 ± 0.03, 0.21 and 0.16 ± 0.01, respectively. Aside from the up to one order of magnitude jump in sulfide content between the starting materials and the aged CWFs, there are two key points to make: (1) BFS is not added to the HGM-5 formulation, therefore the majority of the reducing capacity will come from FA (accounting for 75 wt% of dry ingredients), which was determined to have a lower sulfide fraction (0.100), and (2) FA has a maximum SO_3 content of 5% according to ASTM C618-19, with no designation for sulfide content, likely due to comparatively much lower contributions to the FA material[47]. It is also important to note that there is likely even some variability in sulfide fraction across the OPC materials, considering the 0.025 increase in sulfide in 2020 using the OPC-new material compared to the 2018 mix using OPC-old material.

At the time of this study, it was not possible to quantify the sulfide fraction of the exact starting materials used for each CS and HGM-5 formulation year. As such, the unexpected trends (or lack thereof) in the XES sulfide data as a function of CWF age underscores the importance of measuring the sulfide fraction of all new starting materials used in CWFs in future studies.

3.2 Future Directions: Comparison to Ce(IV) and New Possibilities for Longitudinal Studies

Looking to the future, the ability to infer sulfur contributions to the reduction capacity of cementitious materials would have clear benefit, perhaps especially when integrated with the Ce(IV) test via prior knowledge of the total sulfur content in the CWF. For most CWFs, it is expected that S and Fe are the two dominant species contributing to reduction capacity. As the Ce(IV) test is sensitive to the total reduction capacity, the combination of the Ce(IV) test with benchtop S Kα XES has the potential to separate the S and Fe contributions with high-access analytical methods. We report here only a first attempt at such an integration, finding promise for the approach but (substantially) a need for a finer determination of S and Fe compositions to make a meaningful combination of the two methods.

The sulfide fraction, *x*, can be converted to a sulfur reduction capacity by

$$\mathrm{S}\left(\frac{\mu\mathrm{eq}}{\mathrm{g}}\right) = \frac{\mathrm{x} * \mathrm{S\ mass\ fraction\ in\ sample}\left(\frac{\mathrm{g}}{\mathrm{g}}\right) * 8\ \times 10^{6}\ \left(\frac{\mu\mathrm{eq}}{\mathrm{mol}}\right)}{\mathrm{S\ atomic\ mass}\ \left(\frac{\mathrm{g}}{\mathrm{mol}}\right)} \qquad \text{Eq. 1}$$

Note the importance of knowledge of the S mass fraction in the sample for this conversion. A head-to-head comparison of the Ce(IV) results, the S reduction capacity inferred from XES, and the theoretical maximum reduction capacities for Fe, S, and full samples *based on the average Fe and S compositions reported in the literature*,[1, 7, 48] are presented in Table 4. While there is an overall order-of-magnitude agreement, there are numerous inconsistencies in Table 4. These include cases where the inferred S reduction capacity from XES is larger than the total reduction capacity from the Ce(IV) test, or where the deficit between the inferred S reduction capacity and the Ce(IV) total reduction capacity is too large to be accommodated by even the theoretical Fe reduction capacity, i.e., if all Fe was Fe(II) – which it certainly is not. Although S Kα XES is sensitive only to the first few microns of sample while the Ce(IV) method is sensitive to the bulk, we note that XES sample pellets were made from well mixed powders and that spectra from the interior and surface were identical. The most likely explanations for these discrepancies come from (1) incomplete dissolution of the sample used in the Ce(IV) method that undervalues the total reduction capacity and, (2) the notorious inhomogeneity of industrial cementitious materials[8, 10, 49-51]. Large sample-to-sample variation in these relatively low mass fraction constituents (S and Fe) is not only possible but actually rather likely when comparing measurements across formulation time series where consistent materials sources were not used. In turn, this would result in large systematic errors in the inferred S reduction capacity from XES (see Eq. 1) or the theoretical maximum reduction capacities in Table 4 without thorough characterization of the starting materials.

	Based on Measurements and Knowledge of Composition		Based Solely on Composition			Estimated Composition*	
Sample	**Ave. Ce(IV) Total Reduction Capacity**	**Sulfide Reduction Capacity (XES)**	**Calculated Fe Maximum Reduction Capacity**	**Calculated S Maximum Reduction Capacity**	**Calculated Maximum Total Reduction Capacity**	**Fe**	**S**
	(eq/g)			(eq/g)		(mg/kg)	
HGM5-2018	354	174**	515	1114	1629	28740	4465
HGM5-2019	120	175	515	1114	1629	28740	4465
HGM5-2020	128	55**	515	1114	1629	28740	4465
HGM5-2018-Dry Mix	99	14	515	1114	1629	28740	4465
HGM5-2020-Dry Mix	-	28	515	1114	1629	28740	4465
CS-2018	617	195**	292	1528	1820	16305	6122
CS-2019	320	61	292	1528	1820	16305	6122
CS-2020	394	173**	292	1528	1820	16305	6122
CS-2018-Dry Mix	633	351	292	1528	1820	16305	6122
CS-2020-Dry Mix	-	266	292	1528	1820	16305	6122
Geopolymer-2019	449	405	104	1843	1946	5784	7384
Metakaolinite	38	90	358	125	483	20000	500
BFS-new	777	522	114	3369	3483	6340	13500
FA	327	82	750	818	1568	41900	3280
OPC-old	93	33	405	3292	3697	22600	13200

Table 4: (left) Comparison of total reduction capacity from the Ce(IV) test and the sulfide reduction capacity inferred from XES. (right) Theoretical maximum reduction capacities from Fe, S, and both together, for each sample. The several discrepancies in the table are discussed in the text and are likely due to the use of literature average values for S and Fe content, rather than sample- specific measurement. Please note that HGM5-2020-Dry Mix and CS-2020-Dry Mix specimens were not analyzed using the Ce(IV) method. For this reason, no measurement under *Ave. Ce(IV) Total Reduction Capacity* is provided.

*Based on element analysis reported for dry ingredients in Saslow et al. 2018[52]

**Average values calculated from measurements of triplicate sub-samples of the source material.

There are three main considerations that need to be investigated in the future to understand, and hopefully resolve, these disagreements: (1) the S and Fe contents should be explicitly measured on the comparison samples, or at a minimum on the common (well mixed) parent materials; (2) the escape length of S Kα photons in the present samples is only 2 – 4 μm, strongly suggesting that a protocol be developed to measure many samples and/or a flowing powder to average over a more reliably representative sample volume; and (3) it would be valuable to combine S XES determination of S reduction potential with an analogous Fe K-edge XANES determination for a complete spectroscopic measurement of reduction potential in a sample with finely known S and Fe content, and then compare that result with Ce(IV) to get a bound on operator error in the colorimetric titration of the Ce(IV) test.

Before concluding, it is interesting to consider the future application of benchtop characterization of S Kα oxidation state (without needing to continue to reduction capacity) in cementitious materials, and CWFs in particular. First, from a purely spectroscopic perspective, it would be beneficial to include S Kβ measurements, as those have higher sensitivity to moieties intermediate between nominally pure sulfide and sulfate[21]. Moving on to science outcomes, numerous applications, such as for CWF of heavy elements or for concrete secondary containment walls in deep geological repositories[49, 52-54], require safety assessments relevant for long timelines[38, 55]. Yet longitudinal studies of cementitious materials under relevant environmental conditions or without using aging accelerants, e.g., wet/dry cycling, CO_2, O_2 temperature, and humidity, benchmarked against true age cement metrics remain limited[56-58].

In this context, nondestructive testing of the same sample, even if a small sample volume, has clear value exactly because of the removal of sample-to-sample compositional variation. S Kα XES studies of model CWFs under natural and accelerated aging conditions would allow a precise study of the evolution of the sulfur redox chemistry and its evolution under both representative conditions and those more accessible and realistic for research programs. Standardizing aging methods for different cements, which includes a conversion from cement sulfur chemistry (sulfide content) to an approximate true age of the cement, would improve confidence in how cementitious materials will behave long-term and the associated risk assessments.

Such studies could, for example, also be performed in anoxic environments or with other specialized conditions that best mimic conditions in specific application spaces. For instance, exposure to H_2, radiation fields, steel corrosion products, and or elevated temperatures would be ideal for understanding the impact deep geologic repository conditions may have on the cement used in engineered barriers of varying distance from disposed waste. Beyond understanding the evolving sulfur redox chemistry within the cements under these varying environmental conditions, there would be clear benefit to including such information in a multi-modal studies with other cementitious properties as a function of age, e.g., compressive strength, saturated permeability, and mineralogical transformations, that will also impact long-term repository performance.

4. Conclusions

We report measurement of the S Kα x-ray emission spectroscopy from a broad range of cementitious materials having immediate relevance for cementitious waste forms (CWF) for immobilization of radionuclides or other heavy elements. These nondestructive, benchtop measurements can, with sufficient knowledge of sample composition, be used to quantify the sulfur contribution to the CWF's total reduction capacity. This approach to quantifying reduction capacity offers a nondestructive alternative to the destructive Ce(IV) titration test method with added element specificity for targeted tracking of chemical processes known to impact CWF performance. Other future applications include especially longitudinal study of the S redox chemistry as a function of direct and accelerated aging of CWFs in environments relevant for storage conditions and facilities.

Acknowledgements: This research was supported by the Laboratory Directed Research and Development (LDRD), Nuclear Process Science Initiative (NPSI) and Earth Systems Science Overhead funds at Pacific Northwest National Laboratory (PNNL). PNNL is a multiprogram national laboratory operated for the U.S. Department of Energy (DOE) by Battelle Memorial Institute under Contract no. DE-AC06-76RLO-1830. This research was also partially supported by the U.S. National Science Foundation, Division of Chemistry, under grant CHE-1904437. We acknowledge Matt R. Asmussen for his support.

References

1. Um, W.; Yang, J. S.; Serne, R. J.; Westsik, J. H., Reductive capacity measurement of waste forms for secondary radioactive wastes. *Journal of Nuclear Materials* **2015,** *467*, 251-259.
2. Pearce, C. I.; Icenhower, J. P.; Asmussen, R. M.; Tratnyek, P. G.; Rosso, K. M.; Lukens, W. W.; Qafoku, N. P., Technetium Stabilization in Low-Solubility Sulfide Phases: A Review. *Acs Earth and Space Chemistry* **2018,** *2*, (6), 532-547.
3. Wang, G. H.; Um, W.; Kim, D. S.; Kruger, A. A., Tc-99 immobilization from off-gas waste streams using nickel-doped iron spinel. *Journal of Hazardous Materials* **2019,** *364*, 69-77.
4. Um, W.; Chang, H. S.; Icenhower, J. P.; Lukens, W. W.; Serne, R. J.; Qafoku, N. P.; Westsik, J. H.; Buck, E. C.; Smith, S. C., Immobilization of 99-Technetium (VII) by Fe(II)-Goethite and Limited Reoxidation. *Environmental Science & Technology* **2011,** *45*, (11), 4904-4913.
5. Atkins, M.; Glasser, F. P.; Kindness, A., Cement Hydrate Phases: Solubility At 25C. *Cement and Concrete Research* **1992,** *22*, 241-246.
6. Lukens, W. W.; Bucher, J. J.; Shuh, D. K.; Edelstein, N. M., Evolution of technetium speciation in reducing grout. *Environmental Science & Technology* **2005,** *39*, (20), 8064-8070.
7. Roberts, K. A.; Kaplan, D. I. *Reduction Capacity of Saltstone and Saltstone Components*; SRNL-STI-2009-00637; November 30, 2009.
8. Arail, Y.; Powell, B. A.; Kaplan, D. I., Sulfur speciation in untreated and alkali treated ground-granulated blast furnace slag. *Science of the Total Environment* **2017,** *589*, 117-121.
9. Allen, P. G.; Siemering, G. S.; Shuh, D. K.; Bucher, J. J.; Edelstein, N. M.; Langton, C. A.; Clark, S. B.; Reich, T.; Denecke, M. A., Technetium speciation in cement waste forms determined by X-ray absorption fine structure spectroscopy. *Radiochimica Acta* **1997,** *76*, (1-2), 77-86.
10. Roy, A., Sulfur speciation in granulated blast furnace slag: An X-ray absorption spectroscopic investigation. *Cement and Concrete Research* **2009,** *39*, (8), 659-663.
11. Holden, W. M.; Seidler, G. T.; Cheah, S., Sulfur Speciation in Biochars by Very High Resolution Benchtop K alpha X-ray Emission Spectroscopy. *Journal of Physical Chemistry A* **2018,** *122*, (23), 5153-5161.
12. Alexander, G. V., DETERMINATION OF ZINC, COPPER, AND IRON IN BIOLOGICAL TISSUES-AN X-RAY FLUORESCENCE METHOD. *Analytical Chemistry* **1962,** *34*, (8), 951-&.
13. Birks, L. S.; Gilfrich, J. V., X-RAY-FLUORESCENCE ANALYSIS OF CONCENTRATION AND VALENCE STATE OF SULFUR IN POLLUTION SAMPLES. *Spectrochimica Acta Part B-Atomic Spectroscopy* **1978,** *33*, (7), 305-310.
14. Chubarov, V.; Amosova, A.; Finkelshtein, A., X-ray fluorescence determination of sulfur chemical state in sulfide ores. *X-Ray Spectrometry* **2016,** *45*, (6), 352-356.
15. Denoyer, E. R.; Siegel, L. A., DETERMINATION OF SULFUR, NICKEL AND VANADIUM IN FUEL AND RESIDUAL OILS BY X-RAY-FLUORESCENCE SPECTROMETRY. *Analytica Chimica Acta* **1987,** *192*, (2), 361-366.

16. Hennings, S.; Plessow, A., Distinction and quantification of inorganic sulfur species including thiosulfate by X-ray fluorescence (WD-XRF). *X-Ray Spectrometry* **2018,** *47*, (2), 144-152.
17. Li, Z. L.; Yu, R. Q.; Shi, L. M.; Jun, X.; Zhang, M.; Wang, Q. G., VALENCE-STATE SPECIATION OF SULFUR BY X-RAY-FLUORESCENCE SPECTROMETRY AND KALMAN FILTERING. *Analytica Chimica Acta* **1991,** *248*, (1), 257-261.
18. Chubarov, V. M.; Amosova, A. A.; Finkelshtein, A. L., Determination of iron and sulfur valence state in coal ashes by wavelength-dispersive X-ray fluorescence spectrometric technique. *Spectrochimica Acta Part B-Atomic Spectroscopy* **2020,** *163*.
19. Cruz-Hernandez, Y.; Chrysochoou, M.; Wille, K., Wavelength dispersive X-ray fluorescence method to estimate the oxidation reaction progress of sulfide minerals in concrete. *Spectrochimica Acta Part B-Atomic Spectroscopy* **2020,** *172*.
20. Furuya, K.; Kato, Y.; Kikuchi, T.; Gohshi, Y., STATE ANALYSIS OF SULFUR IN COAL AND COAL FLY-ASH BY DOUBLE-CRYSTAL X-RAY-FLUORESCENCE SPECTROMETRY. *Mikrochimica Acta* **1983,** *2*, (3-4), 263-270.
21. Holden, W. M.; Jahrman, E. P.; Govind, N.; Seidler, G. T., Probing Sulfur Chemical and Electronic Structure with Experimental Observation and Quantitative Theoretical Prediction of K alpha and Valence-to-Core K beta X-ray Emission Spectroscopy. *Journal of Physical Chemistry A* **2020,** *124*, (26), 5415-5434.
22. Mori, R. A.; Paris, E.; Giuli, G.; Eeckhout, S. G.; Kavcic, M.; Zitnik, M.; Bucar, K.; Pettersson, L. G. M.; Glatzel, P., Electronic Structure of Sulfur Studied by X-ray Absorption and Emission Spectroscopy. *Analytical Chemistry* **2009,** *81*, (15), 6516-6525.
23. Qi, Q. W.; Furuya, K.; Fukushima, S.; Iida, A.; Gohshi, Y., CHEMICAL-STATE ANALYSIS OF SULFUR AND PHOSPHORUS IN BIOLOGICAL SAMPLES BY X-RAY-FLUORESCENCE. *Biological Trace Element Research* **1987,** *13*, 383-392.
24. Parratt, L. G., Effects of chemical binding on the x-ray K alpha(1) (2) doublet lines of sulphur studied with a two-crystal spectrometer. *Physical Review* **1936,** *49*, (1), 14-16.
25. Petric, M.; Bohinc, R.; Bucar, K.; Nowak, S. H.; Zitnik, M.; Kavcic, M., Electronic Structure of Third-Row Elements in Different Local Symmetries Studied by Valence-to-Core X-ray Emission Spectroscopy. *Inorganic Chemistry* **2016,** *55*, (11), 5328-5336.
26. Sato, T.; Takahash.Y; Yabe, K., AN X-RAY EMISSION SPECTROSCOPIC INVESTIGATION OF CHEMICAL BOND OF SULFUR .I. PEAK SHIFT OF KALPHA AND NUMBER OF VALENCE ELECTRONS OF SULFUR ATOM IN COMPOUNDS. *Bulletin of the Chemical Society of Japan* **1967,** *40*, (2), 298-+.
27. Takahashi, Y.; Yabe, K., AN X-RAY EMISSION SPECTROSCOPIC INVESTIGATION OF CHEMICAL BOND OF SULFUR .3. PROFILE OF SKBETA BAND IN SULFUR COMPOUNDS. *Bulletin of the Chemical Society of Japan* **1969,** *42*, (11), 3064-+.
28. Takahashi, Y.; Yabe, K.; Sato, T., AN X-RAY EMISSION SPECTROSCOPIC INVESTIGATION OF CHEMICAL BOND OF SULFUR .2. NUMBER OF VALENCE ELECTRONS OF SULFUR ATOM IN ORGANIC COMPOUNDS. *Bulletin of the Chemical Society of Japan* **1969,** *42*, (9), 2707-+.
29. Yarmoshenko, Y. M.; Trofimova, V. A.; Dolgih, V. E.; Korotin, M. A.; Kurmaev, E. Z.; Aguiar, J. A.; Ferreira, J. M.; Pavao, A. C., X-RAY-EMISSION SPECTRA AND VALENCE

STATE OF SULFUR-ATOMS OF YBA2 (CUO)(1-X)(NIS)(X) (3)O-4-DELTA. *Journal of Physics-Condensed Matter* **1995,** *7*, (1), 213-218.

30. Yarmoshenko, Y. M.; Trofimova, V. A.; Elokhina, L. V.; Kurmaev, E. Z.; Butorin, S.; Cloots, R.; Ausloos, M., SULFUR OXYGEN SUBSTITUTION IN YBA2CU3O6+XSY ANALYZED BY MEANS OF X-RAY-EMISSION SPECTROSCOPY. *Physica C* **1993,** *211*, (1-2), 29-35.

31. Yarmoshenko, Y. M.; Trofimova, V. A.; Elokhina, L. V.; Kurmaev, E. Z.; Butorin, S.; Cloots, R.; Ausloos, M.; Aguiar, J. A.; Lobatchevskaya, N. I., POSSIBILITY OF SULFUR-OXYGEN SUBSTITUTION IN YBA2CU3O6+XSY ANALYZED BY MEANS OF X-RAY-EMISSION SPECTROSCOPY. *Journal of Physics and Chemistry of Solids* **1993,** *54*, (10), 1211-1214.

32. Yasuda, S.; Kakiyama, H., CHEMICAL EFFECTS IN X-RAY K-ALPHA AND K-BETA EMISSION-SPECTRA OF SULFUR IN ORGANIC-COMPOUNDS. *Spectrochimica Acta Part a-Molecular and Biomolecular Spectroscopy* **1979,** *35*, (5), 485-493.

33. Jahrman, E. P.; Seidler, G. T.; Sieber, J. R., Determination of Hexavalent Chromium Fractions in Plastics Using Laboratory-Based, High-Resolution X-ray Emission Spectroscopy. *Analytical Chemistry* **2018,** *90*, (11), 6587-6593.

34. Seidler, G. T.; Mortensen, D. R.; Remesnik, A. J.; Pacold, J. I.; Ball, N. A.; Barry, N.; Styczinski, M.; Hoidn, O. R., A laboratory-based hard x-ray monochromator for high-resolution x-ray emission spectroscopy and x-ray absorption near edge structure measurements. *Review of Scientific Instruments* **2014,** *85*, (11), 113906.

35. Saslow, S. A.; Um, W.; Russell, R. L.; Wang, G.; Asmussen, R. M.; Sahajpal, R. *Updated Liquid Secondary Waste Grout Formulation and Preliminary Waste Form Qualification*; PNNL-26443; RPT-SWCS-009 Rev 0 830403000; United States, 2017.

36. Neeway, J. J.; Asmussen, R. M.; Lawter, A. R.; Bowden, M. E.; Lukens, W. W.; Sarma, D.; Riley, B. J.; Kanatzidis, M. G.; Qafoku, N. P., Removal of TcO4- from Representative Nuclear Waste Streams with Layered Potassium Metal Sulfide Materials. *Chemistry of Materials* **2016,** *28*, (11), 3976-3983.

37. Asmussen, R. M.; Pearce, C. I.; Miller, B. W.; Lawter, A. R.; Neeway, J. J.; Lukens, W. W.; Bowden, M. E.; Miller, M. A.; Buck, E. C.; Serne, R. J.; Qafoku, N. P., Getters for improved technetium containment in cementitious waste forms. *Journal of Hazardous Materials* **2018,** *341*, 238-247.

38. Asmussen, R. M.; Saslow, S. A.; Neeway, J. J.; Westsik, J. H.; Rod, K. A.; Lonergan, C. E.; Johnson, B. *Development and Characterization of Cementitious Waste Forms for Immobilization of Granular Activated Carbon, Silver Mordenite, and HEPA Filter Media Solid Secondary Waste*; PNNL-28545; 2019.

39. Serne, R.; Westsik, J.; Williams, B.; Jung, H.; Wang, G. *Extended leach testing of simulated LAW cast stone monoliths*; PNNL-24297 Rev 1 830403000; PNNL: 2015.

40. Um, W.; Williams, B. D.; Snyder, M. M. V.; Wang, G. *Liquid Secondary Waste Grout Formulation and Preliminary Waste Form Qualification* PNNL-26443; RPT-SWCS-009 Rev 0 830403000; 2016.

41. Saslow, S.; Asmussen, M.; Smith, G. L.; Reid, D.; Malbrouki, R.; Swanberg, D. J. In *Cementitious Waste Form Development for Treatment of Liquid Secondary Wastes – 21038*,

Proceedings of the 47th Annual Waste Management Conference (WM2021), Reducing Risk Through Sound Technical Solutions, Phoenix, AZ. , March 8-12, 2021; Phoenix, AZ. , 2021.
42. Holden, W. M.; Hoidn, O. R.; Ditter, A. S.; Seidler, G. T.; Kas, J.; Stein, J. L.; Cossairt, B. M.; Kozimor, S. A.; Guo, J. H.; Ye, Y. F.; Marcus, M. A.; Fakra, S., A compact dispersive refocusing Rowland circle X-ray emission spectrometer for laboratory, synchrotron, and XFEL applications. *Review of Scientific Instruments* **2017,** *88*, (7), 073904.
43. Holden, W. M.; Hoidn, O. R.; Seidler, G. T.; DiChiara, A. D., A color x-ray camera for 2-6 keV using a mass produced back illuminated complementary metal oxide semiconductor sensor. *Review of Scientific Instruments* **2018,** *89*, (9), 093111.
44. Stein, J. L.; Holden, W. M.; Venkatesh, A.; Mundy, M. E.; Rossini, A. J.; Seidler, G. T.; Cossairt, B. M., Probing Surface Defects of InP Quantum Dots Using Phosphorus K alpha and K beta X-ray Emission Spectroscopy. *Chemistry of Materials* **2018,** *30*, (18), 6377-6388.
45. Mitra, K. L. W.; Chang, C. H.; Hanrahan, M. P.; Yang, J. Y.; Tofan, D.; Holden, W. M.; Govind, N.; Seidler, G. T.; Rossini, A. J.; Velian, A., Surface Functionalization of Black Phosphorus with Nitrenes: Identification of P=N Bonds by Using Isotopic Labeling. *Angewandte Chemie-International Edition* **2021,** *60*, (16), 9127-9134.
46. Standard Specification for Slag Cement for Use in Concrete and Mortars. In *ASTM C989 / C989M-18a*, West Conshohocken, PA, 2018.
47. Standard Specification for Coal Fly Ash and Raw or Calcined Natural Pozzolan for Use in Concrete. In *ASTM C618-19*, West Conshohocken, PA, 2019.
48. Westsik, J. H.; Piepel, G. F.; Lindberg, M. J.; Heasler, P. G.; Mercier, T. M.; Russell, R. L.; Cozzi, A.; Daniel, W. E.; Eibling, R. E.; Hansen, E. *Supplemental Immobilization of Hanford Low-Activity Waste: Cast Stone Screening Tests*; PNNL-22747; 2013.
49. Ma, B.; Charlet, L.; Fernandez-Martinez, A.; Kang, M. L.; Made, B., A review of the retention mechanisms of redox-sensitive radionuclides in multi-barrier systems. *Applied Geochemistry* **2019,** *100*, 414-431.
50. Ma, B.; Fernandez-Martinez, A.; Madé, B.; Findling, N.; Markelova, E.; Salas-Colera, E.; Maffeis, T. G. G.; Lewis, A. R.; Tisserand, D.; Bureau, S.; Charlet, L., XANES-Based Determination of Redox Potentials Imposed by Steel Corrosion Products in Cement-Based Media. *Environmental Science & Technology* **2018,** *52*, (20), 11931-11940.
51. Ma, B.; Fernandez-Martinez, A.; Wang, K.; Madé, B.; Hénocq, P.; Tisserand, D.; Bureau, S.; Charlet, L., Selenite Sorption on Hydrated CEM-V/A Cement in the Presence of Steel Corrosion Products: Redox vs Nonredox Sorption. *Environmental Science & Technology* **2020,** *54*, (4), 2344-2352.
52. Dauzeres, A.; Le Bescop, P.; Sardini, P.; Coumes, C. C. D., Physico-chemical investigation of clayey/cement-based materials interaction in the context of geological waste disposal: Experimental approach and results. *Cement and Concrete Research* **2010,** *40*, (8), 1327-1340.
53. De Windt, L.; Spycher, N. F., Reactive Transport Modeling: A Key Performance Assessment Tool for the Geologic Disposal of Nuclear Waste. *Elements* **2019,** *15*, (2), 99-102.
54. Ewing, R. C.; Whittleston, R. A.; Yardley, B. W. D., Geological Disposal of Nuclear Waste: a Primer. *Elements* **2016,** *12*, (4), 233-237.
55. Chung, C. W.; Urn, W.; Valenta, M. M.; Sundaram, S. K.; Chun, J.; Parker, K. E.; Kimura, M. L.; Westsik, J. H., Characteristics of Cast Stone cementitious waste form for

immobilization of secondary wastes from vitrification process. *Journal of Nuclear Materials* **2012,** *420*, (1-3), 164-174.
56. Torres, E.; Turrero, M. J.; Garralon, A.; Cuevas, J.; Fernandez, R.; Ortega, A.; Ruiz, A. I., Stable isotopes applied to the study of the concrete/bentonite interaction in the FEBEX in situ test. *Applied Geochemistry* **2019,** *100*, 432-443.
57. Vehmas, T.; Montoya, V.; Alonso, M. C.; Vasicek, R.; Rastrick, E.; Gaboreau, S.; Vecernik, P.; Leivo, M.; Holt, E.; Fink, N.; Mouheb, N. A.; Svoboda, J.; Read, D.; Cervinka, R.; Vasconcelos, R.; Corkhill, C., Characterization of Cebama low-pH reference concrete and assessment of its alteration with representative waters in radioactive waste repositories. *Applied Geochemistry* **2020,** *121*, 104703.
58. Wei, J. Q.; Meyer, C., Degradation rate of natural fiber in cement composites exposed to various accelerated aging environment conditions. *Corrosion Science* **2014,** *88*, 118-132.

Chapter 4 - Supplemental Information: An Exploration of Benchtop X-ray Emission Spectroscopy for Precise Characterization of the Sulfur Redox State in Cementitious Materials

Originally published as: J. Abramson, N. Avalos, A. Bourchy, S. Saslow, G. T. Seidler. *X-ray Spectrometry* 2021 Vol. 51 Issue 2 Page 151. J. Abramson wrote and conducted the majority of this work.

Table SI-1 Pellet preparation from powdered materials

Specimen Name	Specimen Mass (g)	Cellulose Mass (g)	Total Pellet Mass (g)
HGM5-2018-1	0.1005	-	0.1005
HGM5-2018-2	0.1005	-	0.1005
HGM5-2018-3	0.0995	-	0.0995
HGM5-2019	0.3713	-	0.3713
HGM5-2020-1	0.1081	-	0.1081
HGM5-2020-2	0.1035	-	0.1035
HGM5-2020-3	0.1024	-	0.1024
HGM5-2020-Dry Mix	0.0959	0.0096	0.1004
HGM5-2018-Dry Mix	0.170	0.040*	0.210
[2]CS-2018-1	0.1000	~ 0.0097	0.1000
[2]CS-2018-2	0.0995	~ 0.0097	0.0995
[2]CS-2018-3	0.0996	~ 0.0097	0.0996
CS-2019	0.3639	-	0.3639
CS-2020-1	0.1070	-	0.1070
CS-2020-2	0.1034	-	0.1034
CS-2020-3	0.1028	-	0.1028
CS-2020-Dry Mix	0.0875	0.0086	0.0933
CS-2018-Dry Mix	0.231	-	0.231
Geopolymer-2019	0.3801	-	0.3801
FA	0.2441	0.1007	0.3448
BFS-new	0.3907	-	0.3907
OPC-old	0.3697	-	0.3697
KMS-2	0.3098	-	0.3098
Metakaolin	0.1169	-	0.1169

[2] Approximately 0.2998g of the CS-2018 specimen was mixed with 0.0292g of cellulose (10 wt%). Then, the homogenized material was divided in 3 parts (of approximately 0.1 g) to make 3 pellets total.

*Pellet was made from dry material at University of Washington and BN binder was used

Table SI-2: Preparation of specimens for reduction capacity measurements using the Ce(IV) method.

Specimen Name	Specimen Mass (g)	40 mM Ce(IV) (mL)
HGM5-2018	0.99	30
HGM5-2019	1.01	30
HGM5-2020	1.01	30
[2]HGM5-2018-Dry Mix	0.494	15
CS-2018	1.01	30
CS-2019	1.01	30
CS-2020	1.00	30
[2]CS-2018-Dry Mix	0.500	15
Geopolymer-2019	1.01	30
[1]FA	1.00	30
[1]BFS-new	1.01	30
[1]OPC-old	1.01	30
[1]Metakaolinite	1.01	30

[1] Solutions were centrifuged following the 4 day reaction period in 40 mM Ce(IV)

[2] Dry mix prepared with BFS-old and/or OPC-old source materials used to formulate CWFs in 2018

Figure SI-1 (below and following pages): A compendium of XES results with fits, references, and residuals. Sample labels follow Table SI-1 and description in the main text.

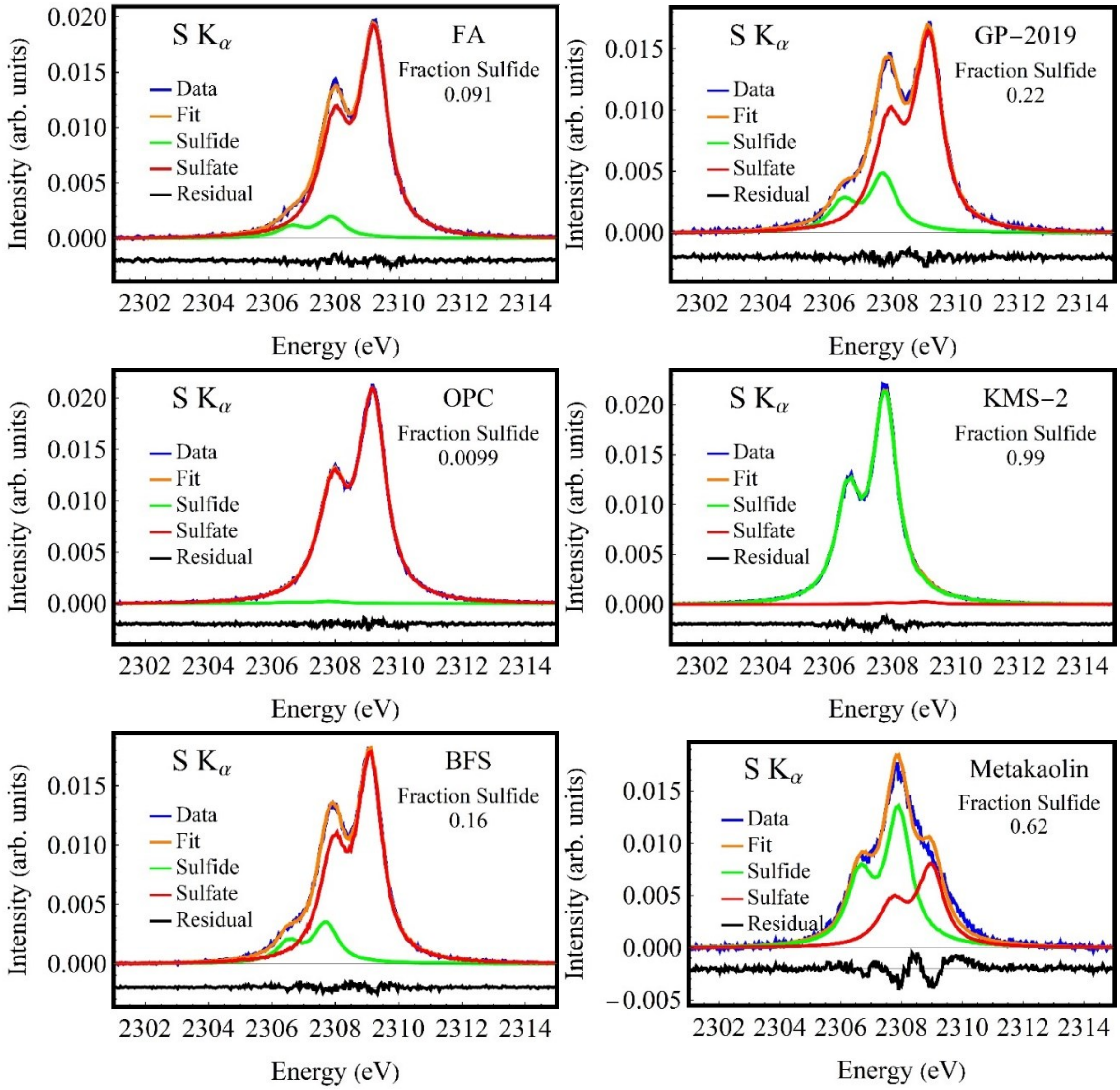

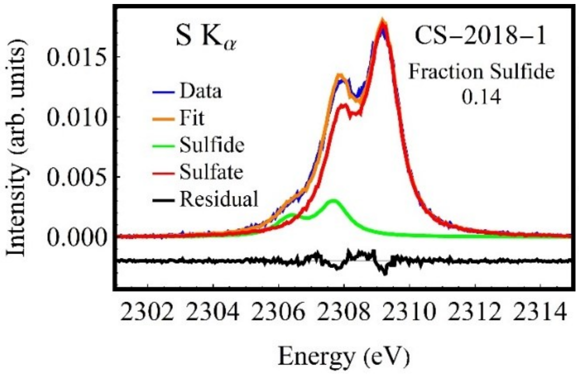
S K_α
CS−2018−1
Fraction Sulfide
0.14
Data
Fit
Sulfide
Sulfate
Residual
Intensity (arb. units)
0.015
0.010
0.005
0.000
2302 2304 2306 2308 2310 2312 2314
Energy (eV)

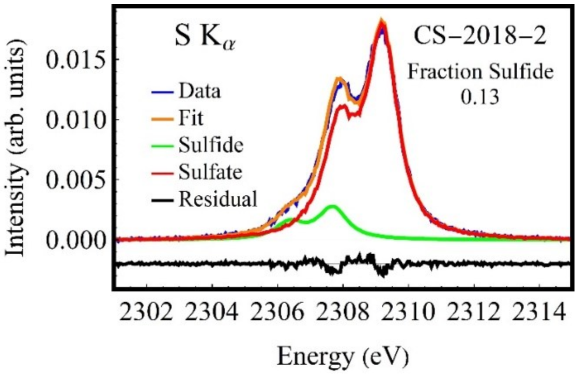
S K_α
CS−2018−2
Fraction Sulfide
0.13
Data
Fit
Sulfide
Sulfate
Residual
Intensity (arb. units)
0.015
0.010
0.005
0.000
2302 2304 2306 2308 2310 2312 2314
Energy (eV)

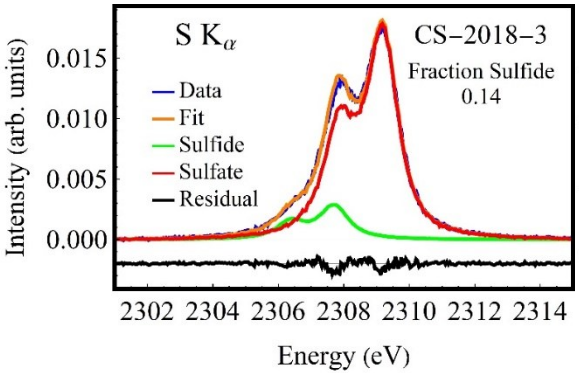
S K_α
CS−2018−3
Fraction Sulfide
0.14
Data
Fit
Sulfide
Sulfate
Residual
Intensity (arb. units)
0.015
0.010
0.005
0.000
2302 2304 2306 2308 2310 2312 2314
Energy (eV)

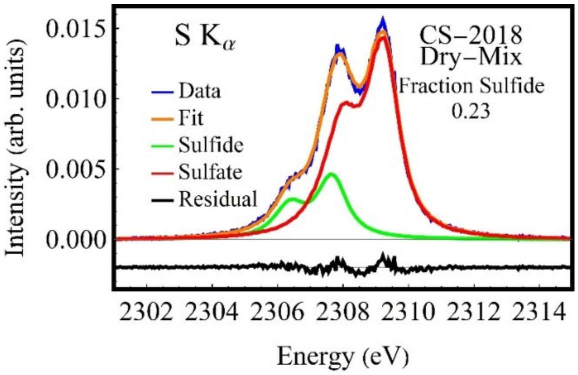
S K_α
CS−2018
Dry−Mix
Fraction Sulfide
0.23
Data
Fit
Sulfide
Sulfate
Residual
Intensity (arb. units)
0.015
0.010
0.005
0.000
2302 2304 2306 2308 2310 2312 2314
Energy (eV)

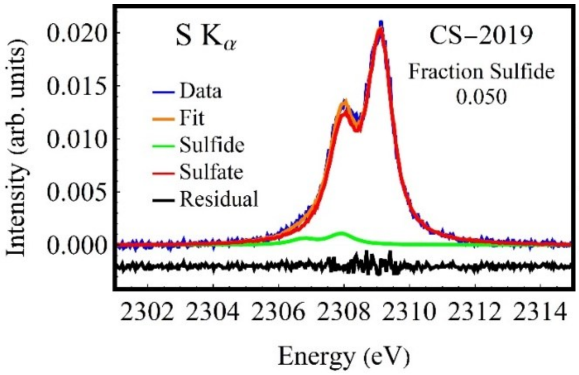
S K_α
CS−2019
Fraction Sulfide
0.050
Data
Fit
Sulfide
Sulfate
Residual
Intensity (arb. units)
0.020
0.015
0.010
0.005
0.000
2302 2304 2306 2308 2310 2312 2314
Energy (eV)

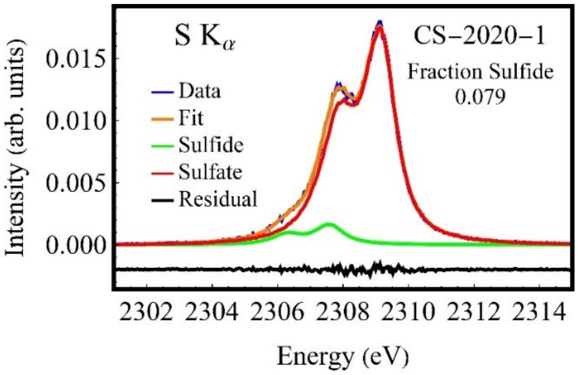
S K_α
CS−2020−1
Fraction Sulfide
0.079
Data
Fit
Sulfide
Sulfate
Residual
Intensity (arb. units)
0.015
0.010
0.005
0.000
2302 2304 2306 2308 2310 2312 2314
Energy (eV)

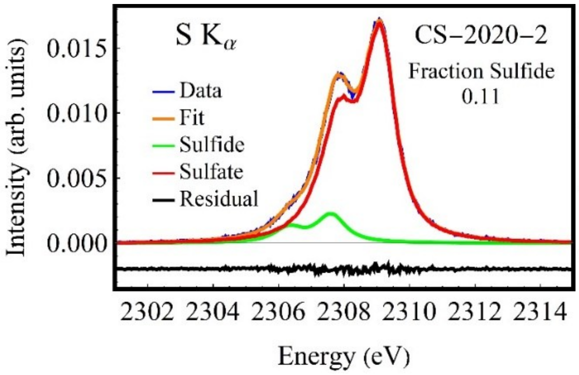
S K_α
CS−2020−2
Fraction Sulfide
0.11
Data
Fit
Sulfide
Sulfate
Residual
Intensity (arb. units)
0.015
0.010
0.005
0.000
2302 2304 2306 2308 2310 2312 2314
Energy (eV)

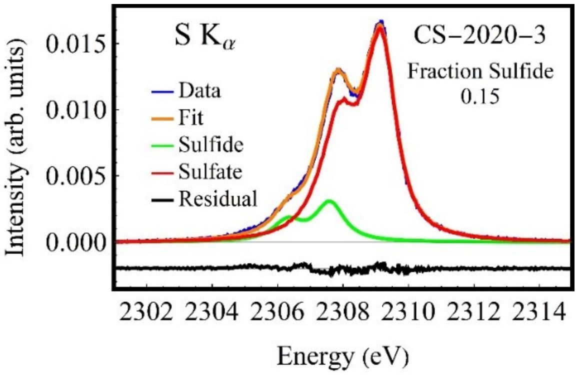
S K_α
CS−2020−3
Fraction Sulfide
0.15
Data
Fit
Sulfide
Sulfate
Residual
Intensity (arb. units)
0.015
0.010
0.005
0.000
2302 2304 2306 2308 2310 2312 2314
Energy (eV)

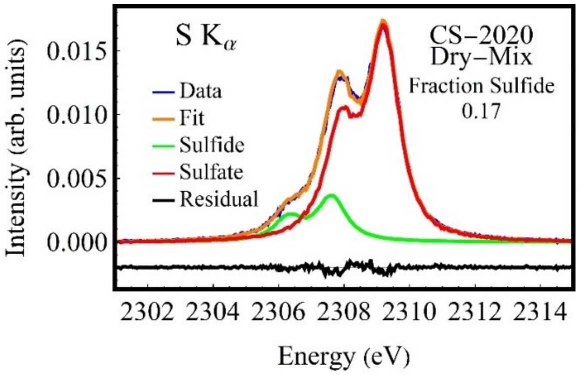
S K$_\alpha$
CS−2020
Dry−Mix
Fraction Sulfide
0.17
Data
Fit
Sulfide
Sulfate
Residual
Intensity (arb. units)
0.000
0.005
0.010
0.015
2302 2304 2306 2308 2310 2312 2314
Energy (eV)

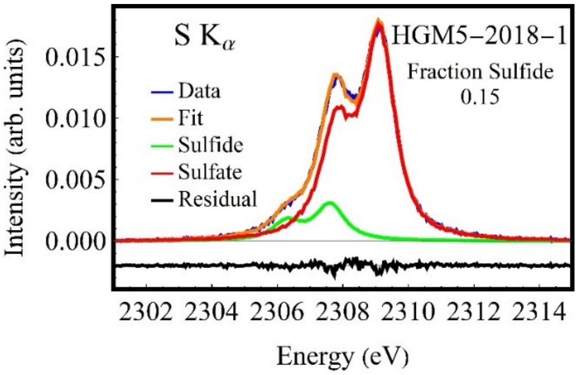
S K$_\alpha$
HGM5−2018−1
Fraction Sulfide
0.15
Data
Fit
Sulfide
Sulfate
Residual
Intensity (arb. units)
0.000
0.005
0.010
0.015
2302 2304 2306 2308 2310 2312 2314
Energy (eV)

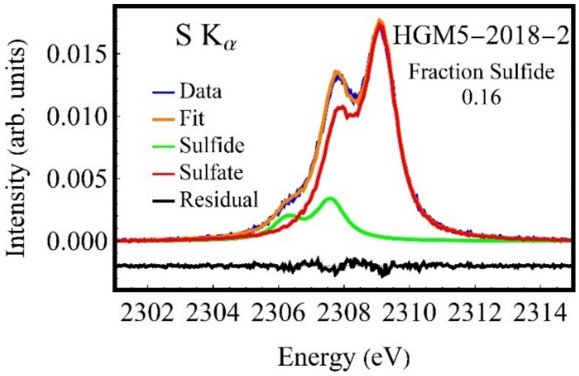
S K$_\alpha$
HGM5−2018−2
Fraction Sulfide
0.16
Data
Fit
Sulfide
Sulfate
Residual
Intensity (arb. units)
0.000
0.005
0.010
0.015
2302 2304 2306 2308 2310 2312 2314
Energy (eV)

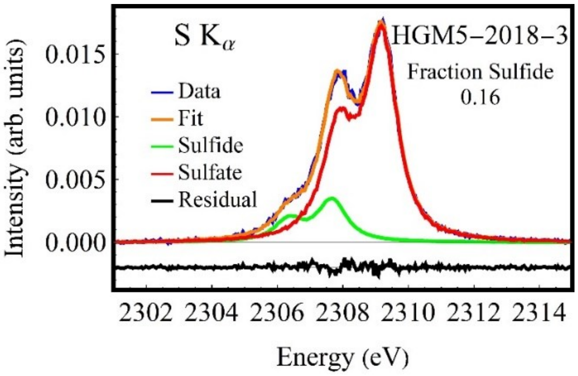
S K$_\alpha$
HGM5−2018−3
Fraction Sulfide
0.16
Data
Fit
Sulfide
Sulfate
Residual
Intensity (arb. units)
0.000
0.005
0.010
0.015
2302 2304 2306 2308 2310 2312 2314
Energy (eV)

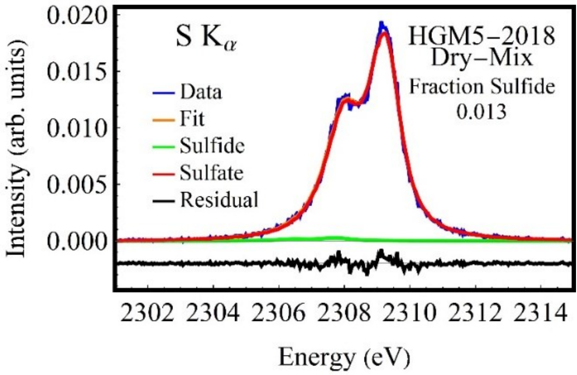
S K$_\alpha$
HGM5−2018
Dry−Mix
Fraction Sulfide
0.013
Data
Fit
Sulfide
Sulfate
Residual
Intensity (arb. units)
0.000
0.005
0.010
0.015
0.020
2302 2304 2306 2308 2310 2312 2314
Energy (eV)

3

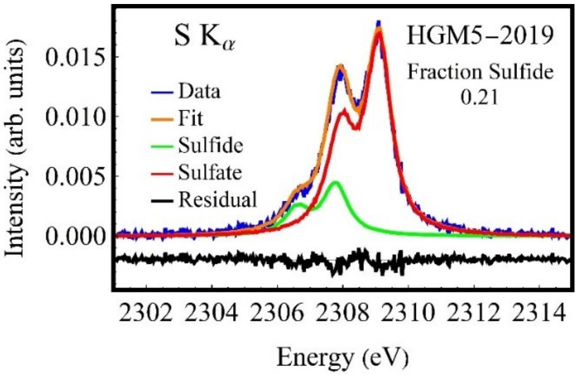
S K$_\alpha$
HGM5−2019
Fraction Sulfide
0.21
Data
Fit
Sulfide
Sulfate
Residual
Intensity (arb. units)
0.000
0.005
0.010
0.015
2302 2304 2306 2308 2310 2312 2314
Energy (eV)

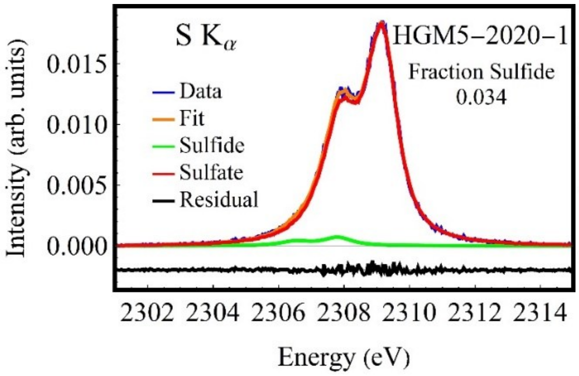
S K$_\alpha$
HGM5−2020−1
Fraction Sulfide
0.034
Data
Fit
Sulfide
Sulfate
Residual
Intensity (arb. units)
0.000
0.005
0.010
0.015
2302 2304 2306 2308 2310 2312 2314
Energy (eV)

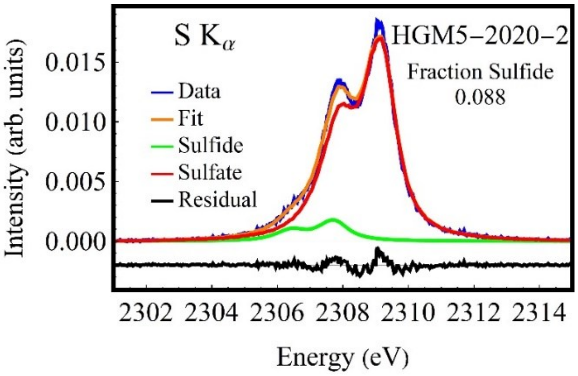
S K$_\alpha$
HGM5−2020−2
Fraction Sulfide
0.088
Data
Fit
Sulfide
Sulfate
Residual
Intensity (arb. units)
0.000
0.005
0.010
0.015
2302 2304 2306 2308 2310 2312 2314
Energy (eV)

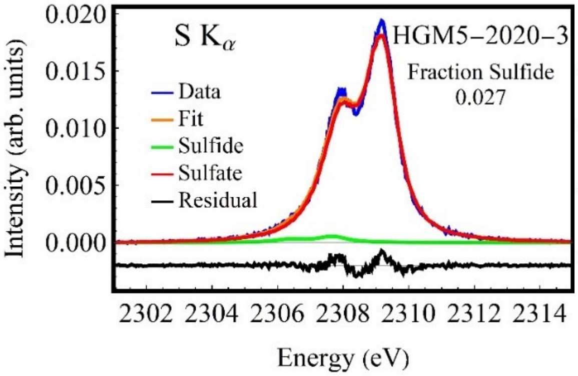
S Kα
HGM5−2020−3
Fraction Sulfide
0.027
Data
Fit
Sulfide
Sulfate
Residual
Intensity (arb. units)
0.020
0.015
0.010
0.005
0.000
2302
2304
2306
2308
2310
2312
2314
Energy (eV)

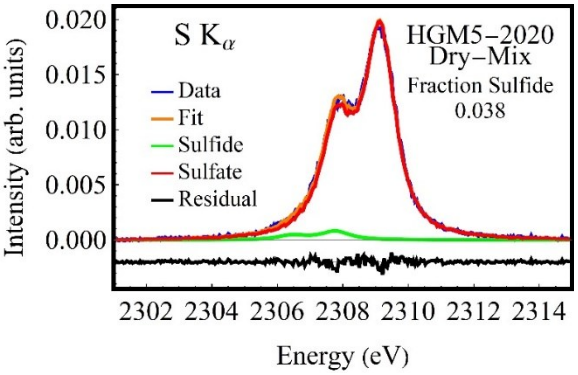
S Kα
HGM5−2020
Dry−Mix
Fraction Sulfide
0.038
Data
Fit
Sulfide
Sulfate
Residual
Intensity (arb. units)
0.020
0.015
0.010
0.005
0.000
2302
2304
2306
2308
2310
2312
2314
Energy (eV)

Chapter 5 - Laboratory X-ray Emission Spectrometer for Phosphorus Kα and Kβ Study of Air-Sensitive Samples

Originally published as: J. Abramson, W. Holden, R. Rivera-Maldonado, A. Velian, B. Cossairt, G. Seidler. *Journal of Analytical Atomic Spectrometry* 2023 Vol. 38 Page 1125-1134.

J. Abramson wrote and conducted the majority of this work.

The analytical chemistry of phosphorus-containing materials is often impeded by the long measurement times and relatively large sample masses needed for ^{31}P NMR spectroscopy, by the scarcity and access limitations of synchrotron beamlines operating in the energy range of the P K-edge, by the challenges posed by species interconversion during liquid extraction, and by the considerable air-sensitivity typical of many phosphorus-containing materials and nanophases. To this end, we report the design and operation of a new laboratory-based spectrometer to simultaneously perform P Kα and Kβ X-ray emission spectroscopy (XES) while being housed in a research-grade controlled-atmosphere glovebox. Demonstration studies on nickel phosphide nanophases illustrate the importance of air-free XES and the value of simultaneous Kα and Kβ spectroscopy for identifying the P oxidation state and for investigating nanoscale influences on valence level electronic structure.

1. Introduction

Phosphorus is well known for its numerous biological functions and importance in nutrition [1-5], but is seeing strong contemporary interest for applications of black phosphorus and phosphorene [6-9] in addition to a steadily growing body of research on the catalytic properties of metal phosphides [8, 10-13]. Phosphorus-31 nuclear magnetic resonance (^{31}P NMR) spectroscopy has been a workhorse technique used, e.g., to study phosphorus chemistry in water and soil health [14-16] and also transition metal catalyst structure [17, 18]. However, ^{31}P NMR spectroscopy requires relatively large sample mass and suffers from long measurement times. An alternative, which is also element-specific and extremely local, is x-ray absorption spectroscopy (XAS). Synchrotron XAS strongly interrogates P electronic structure and environment but suffers from a poor fit with routine analytical application, the relatively few synchrotron beamlines operating in the energy range of the P K-edge, and the scarcity of such beamlines equipped with research-grade gloveboxes to support the extreme air-sensitivity of many P-rich compounds [19-21]. Synchrotron x-ray emission spectroscopy (XES) also informs P electronic structure and is performed at synchrotron beamlines to great effect [19, 21-24], but shares the above limitations of synchrotron XAS.

Recent work has, however, emphasized that some of the above issues surrounding access can be addressed with high-throughput laboratory XES for analytical application [25-30]. This includes laboratory-based study of the P Kα and Kβ XES of several systems [21, 29, 31, 32] with successful determination of oxidation state distribution, ligand identity, and bonding of various phosphorus compounds. Improved measurement times and smaller sample masses when compared to ^{31}P NMR spectroscopy have also been reported [29].

Building on these prior developments and addressing the added complexity of air-sensitivity of P-rich systems, we report here the design and commissioning of a new laboratory-based XES spectrometer that simultaneously measures the P Kα (core-to-core) and P Kβ (valence-to-core) XES while permanently installed in a research-grade controlled-atmosphere glovebox. This instrument uses the small footprint 'Dispersive Rowland Refocusing' (DRR) geometry[33] seen to have synchrotron-level performance across many studies despite the use of only a low-powered, low-brilliance conventional x-ray tube source [25, 33, 34]. We propose that the integration of compact laboratory based XES instruments with controlled atmosphere gloveboxes holds high scientific and analytic potential, well beyond the present case of phosphorus.

2. Spectrometer Design

The general layout for each of the two tandem spectrometers follows the (DRR) geometry discussed in Holden, et al [33]. As shown in Fig. 1, a finite sized sample inside the Rowland circle is illuminated by an unfocused x-ray beam source – the Rowland circle location is defined by the position and radius of curvature of the cylindrical analyzer optic. The optics and other key components of the two Rowland circles are shown in Fig. 2a and Fig. 2b. Computer aided design (CAD) renderings of the double spectrometer are shown in Fig. 2c and 2d. In Fig. 3, a photograph of the installed system and a CAD rendering showing the spectrometer and sample handling wheel are presented with components labeled.

The largest component is the controlled-atmosphere glovebox (M. Braun Complete Labstar Pro Glovebox System). This system has a hinged, removable front window to simplify spectrometer installation and maintenance. The spectrometer enclosure is a stainless-steel vacuum chamber (LACO Technologies) with inner dimensions 23 cm x 30 cm x 30 cm and 6.35-mm wall thickness, component 1 in Fig. 3. This enclosure acts as both a helium gas enclosure and as the primary radiation safety enclosure. There are multiple small KF-style flanges for helium gas handling and electrical feedthroughs. The sample is directly illuminated by x-rays from an air-cooled tube source (Varex VF-80 with a Pd anode) having a maximum electron beam power of 100W at 35kV accelerating potential (Spellman high-voltage supply, hardware-limited to 35 kV to simplify radiation shielding). This system provides a diverging, unfocused beam of combined bremsstrahlung and fluorescence radiation from a Pd anode. The x-ray tube is attached to the outside of a flange, Fig. 3 component 12 labeled 'DRR flange', which holds the other DRR elements and is fastened to the spectrometer enclosure.

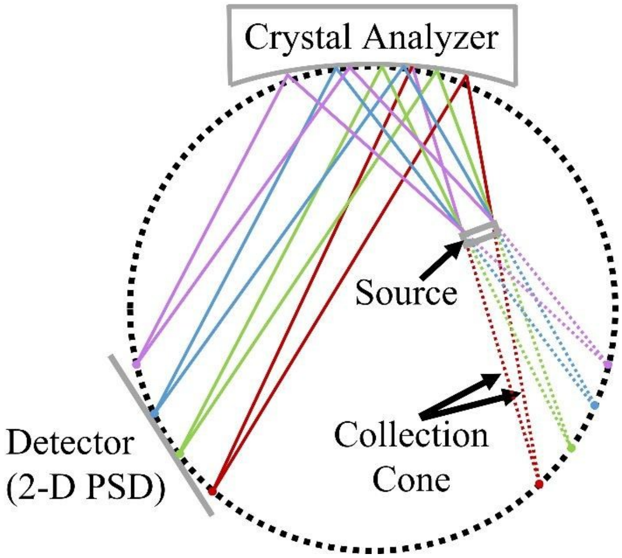

Figure 1. Dispersive Rowland Refocusing (DRR) geometry with a large source off-circle. The geometry has a bent crystal analyzer at the top of the circle, a position sensitive detector on the lower left of the circle, and virtual sources on a lower right arc each with an associated collection cone. The sample ('source' in this context) is illuminated by an X-ray source perpendicular to the circle. Note the spectral refocusing onto the detector arc and x-ray camera face.

Fluorescence from the sample can be diffracted by either of two 10-cm radius, cylindrically bent, Si (111) Johann analyzers (XRS Tech). These analyzers are positioned in separate DRR geometries of corresponding 10-cm diameter Rowland circles which are tilted and rotated with respect to each other, see Fig. 2 and component 7 in Fig. 3. The analyzers are 20 mm wide (in the Rowland planes) by 8 mm tall (perpendicular to Rowland planes) and positioned at a 79.1° (2014.6eV) and 67.6° (2137.8eV) Bragg angle for phosphorus Kα and Kβ, respectively. Due to energy broadening caused by the relatively low Bragg angle for phosphorus Kβ, the edges of the Kβ crystal analyzer are masked with aluminum foil leaving only the central ~4 mm exposed. The analyzers are held in a 3-D printed plastic mount that registers to the DRR flange by dowel pins to ensure correct positioning.

The diffracted fluorescence is detected by one of two energy-resolving x-ray cameras which have been previously reported [35], components 9 and 10 in Fig. 3. The x-ray camera detectors are mounted using 3-D printed plastic pieces registered against the DRR flange. The detectors are commercially available CMOS-based devices (IDS Imaging Development Systems Inc.) that have been modified by removing the image sensor glass cover to allow direct illumination of the CMOS sensor's active region by ~2 keV photons. The Kα detector is a UI-382LE camera with a Sony IMX 290 detector (1936 pixels x 1096 pixels) while the Kβ detector is a UI-3882LE camera with a Sony IMX 178 detector (3088 pixels x 2076 pixels). The 2.9-µm and 2.4- µm pixel sizes for the Sony IMX 290 and Sony IMX 178, respectively, correspond to energy broadenings of ~0.01 eV for Kα and ~0.02 for Kβ on our 10-cm Rowland circle. Given the small energy spacing between pixel-defined bins compared to the relevant core-hole broadening and minimum instrumental broadening due to the Si (111) Darwin width, we rebin all spectra on an 0.05 eV grid.

The sample mount assembly includes a 10-position sample wheel (component 11 in Fig. 3), attached by a small magnetic kinematic mount to a NEMA 11 bipolar stepper motor. Sample exchange is performed by first pulling the sample mount assembly away from the source via the linear slide rail and then detaching the sample wheel at the kinematic mount. This arrangement allows for easier installation and removal of samples inside of the glovebox, where manipulation is made more challenging by thick gloves.

3. Methods

3.1. Reference Sample Preparation

Nickel phosphide references were used to test the spectrometer and run the commissioning studies. Disodium hydrogen phosphate reference was used to set the energy scale by matching peaks to known energies [36], see Fig. SI-1. Pellets were made by pressing an approximately 1:1 mass ratio of commercial reference powders, Ni_2P (98%, Millipore-Sigma) or $Ni_3(PO_4)_2$ (98%, Alfa Aesar) or Na_2HPO_4 (98%, Millipore-Sigma), and BN powder (98%, Millipore-Sigma) into a 13-mm diameter die. These reference pellets were cut into approximately 10 mm x 5 mm x 1 mm sized pieces to fit in the spectrometer without collisions. Pellets were dried under vacuum at 80°C overnight prior to use in the glovebox.

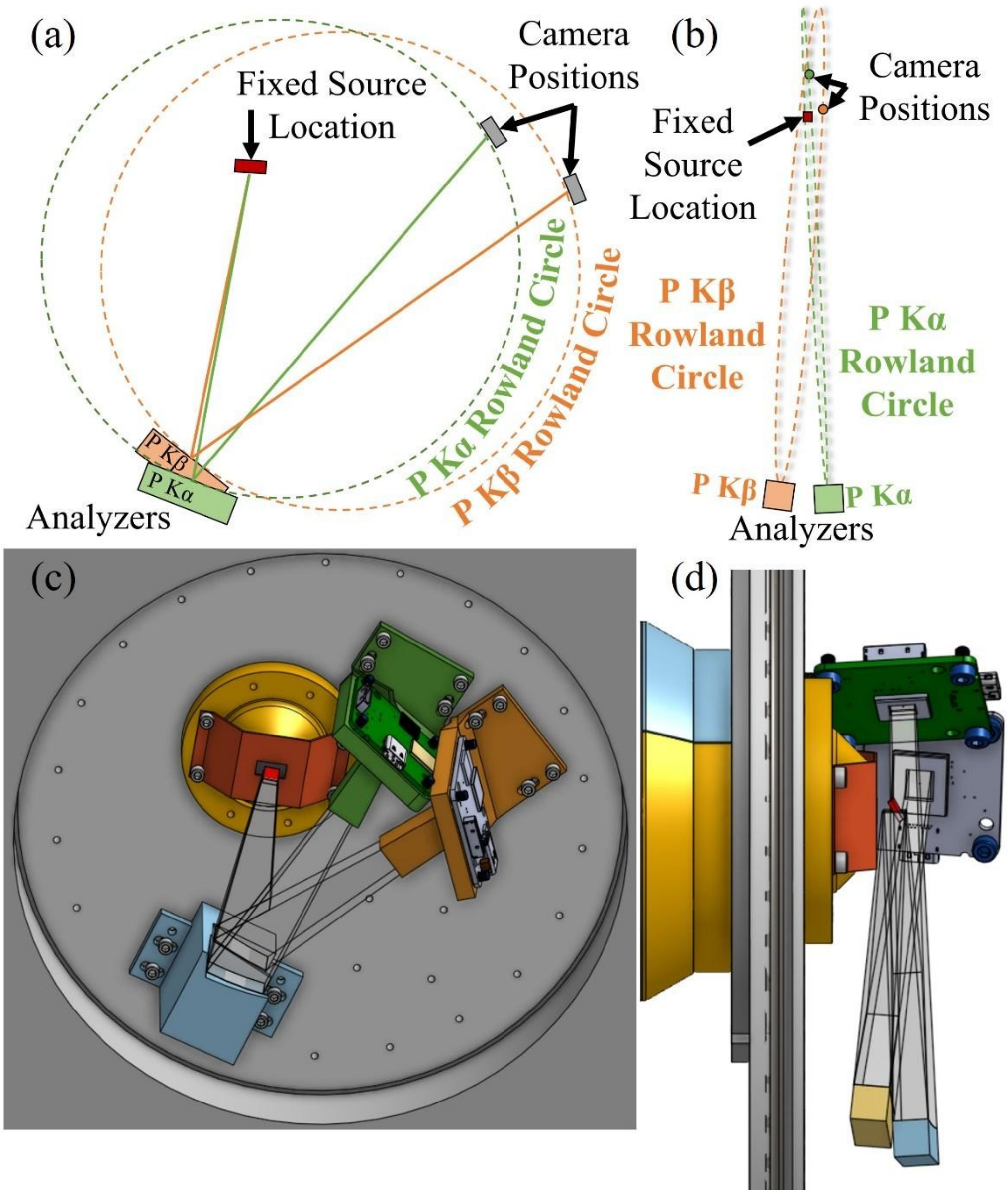

Figure 2. (a) Front and (b) side view illustration of the double Rowland circle geometry, with accompanying CAD rendering also from (c) front and (d) side views. The P Kα and P Kβ Rowland circles share the same source location but are translated and tilted out of plane to allow clearance for a 79.1° (2014.6eV) and 67.6° (2137.8eV) Bragg angle respectively. The mount of the crystal analyzers is omitted from Fig. 2d so that the analyzer orientations are more readily apparent and the stray scatter shields for the cameras are similarly omitted in that figure panel.

3.2 Ni_2P Nanoparticle Synthesis

All glassware was dried at 160 °C overnight prior to use. All manipulations were performed using standard Schlenk techniques or inside a nitrogen atmosphere glovebox unless stated otherwise. nickel (II) chloride (98%, Millipore-Sigma) was dried at 100°C under vacuum overnight before being stored in a nitrogen glovebox for use. Oleylamine (90% Technical Grade, Millipore-Sigma), pentane, and toluene were dried over CaH_2, distilled, and stored over 4 Å sieves in a nitrogen glovebox. Tris(diethylamino)phosphine (97%, Millipore-Sigma), 2-propanol (99.5% Anhydrous, Millipore-Sigma), and acetonitrile (99.8% Anhydrous, Millipore-Sigma) was stored in a nitrogen glovebox and used as received.

To synthesize the Ni_2P nanoparticles in toluene, nickel (II) chloride (472 mg, 3.6 mmol) was quickly transferred from a glovebox to a 3-neck round bottom flask connected to a Schlenk line before the reaction vessel was purged and refilled with dry N_2 three times. Then oleylamine (24 mL) was quickly transferred from the glovebox to the reaction flask via syringe. The solution was heated to 120 °C using a thermal probe inserted into a thermal well in contact with solution and degassed for approximately one hour. Afterwards, heat was turned off, and the solution was placed under active N_2 flow and allowed to cool to approximately 70 °C.

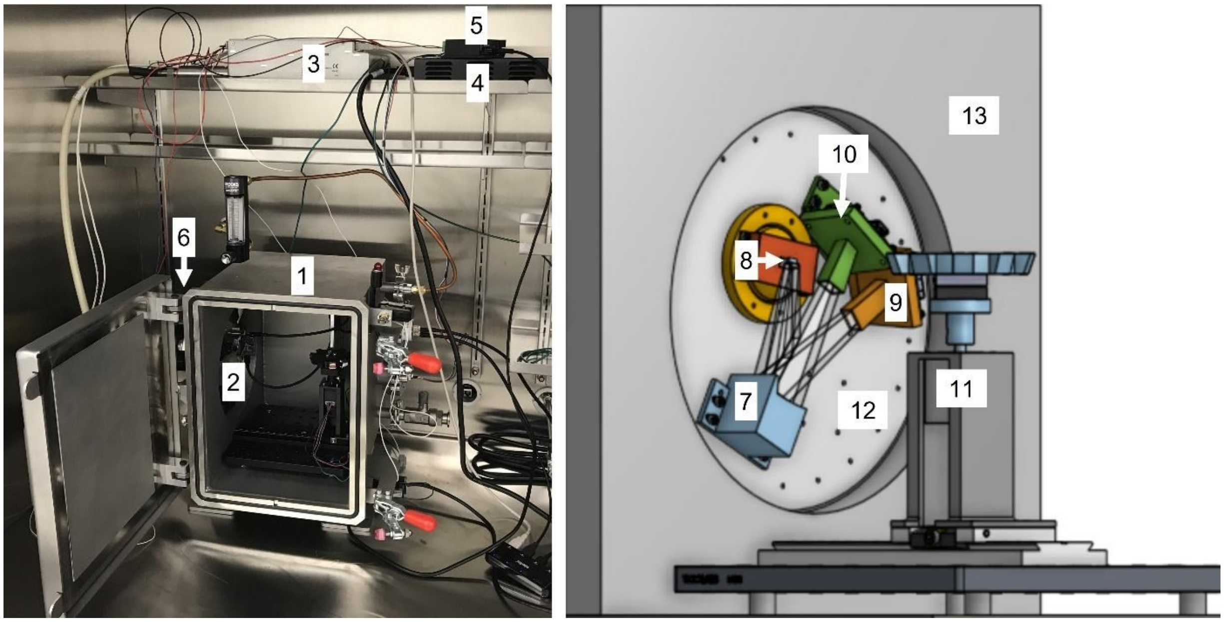

Figure 3. Photograph of the spectrometer placed in a glovebox with accompanying CAD rendering of the spectrometer components. Components include: (1) Helium enclosure; (2) spectrometer components (see 7-13 for more detail); (3) High voltage supply; (4) Power source; (5) Motor controller; (6) X-ray tube (hidden behind door in photo); (7) Two Si (111) crystal analyzers and mount; (8) Sample location; (9) P Kα x-ray camera and housing; (10) P Kβ x-ray camera and housing; (11) Sample mount containing sample wheel, magnetic mount and stepper motor; (12) DRR flange; (13) Helium enclosure wall. For clarity of presentation, the front window of the glovebox was removed for the photograph and the sample wheel assembly has been pulled back from the measurement position in both the photograph and the CAD.

Tris(diethylamino)phosphine (4.0 mL, 14 mmol) was then quickly transferred from the glovebox and injected into the reaction flask. The solution was heated to 250 °C and held for 1 hour prior to being cooled to near room temperature. Finally, the condenser columns and rubber septum were replaced with a glass stopper and t-adapter while flowing an overpressure of N_2 before being transferred into the glovebox through 15 fast cycles of evacuation and refill in the glovebox antechamber.

The nanoparticle solution was purified by centrifugation at 7830 rpm for 15 min with a 1:10 volume ratio of solution to 2-propanol. This was followed three times by decanting the supernatant, dissolving the solid pellet in minimal pentane, again adding a 10x volume ratio of 2-propanol, and centrifuging at 7830 rpm for 15 min. Finally, the supernatant was decanted, minimal toluene was used to dissolve the solid pellet, a 1:4 volume ratio for solvent:antisolvent was used with acetonitrile as the antisolvent, and the solution was centrifuged at 7830 rpm for 15 min. The supernatant was decanted and the remaining solid was dissolved in pentane and dried under vacuum.

With the above synthesis completed, a concentrated solution of Ni_2P nanoparticles in toluene was drop cast on Si (100) wafers (Ted Pella). Seven replicate samples were made and mounted onto the sample wheel. The as-prepared samples are referred to as Ni_2P-0h (meaning zero hours of air exposure), and are subsequently renamed based on air exposure time as Ni_2P-1h, etc.

For the different air exposure times, nanoparticle samples were unmounted from the sample wheel and removed from the glovebox for needed incremental air exposures to achieve the desired cumulative air exposure. Then they were reloaded into the glovebox and remounted in the spectrometer.

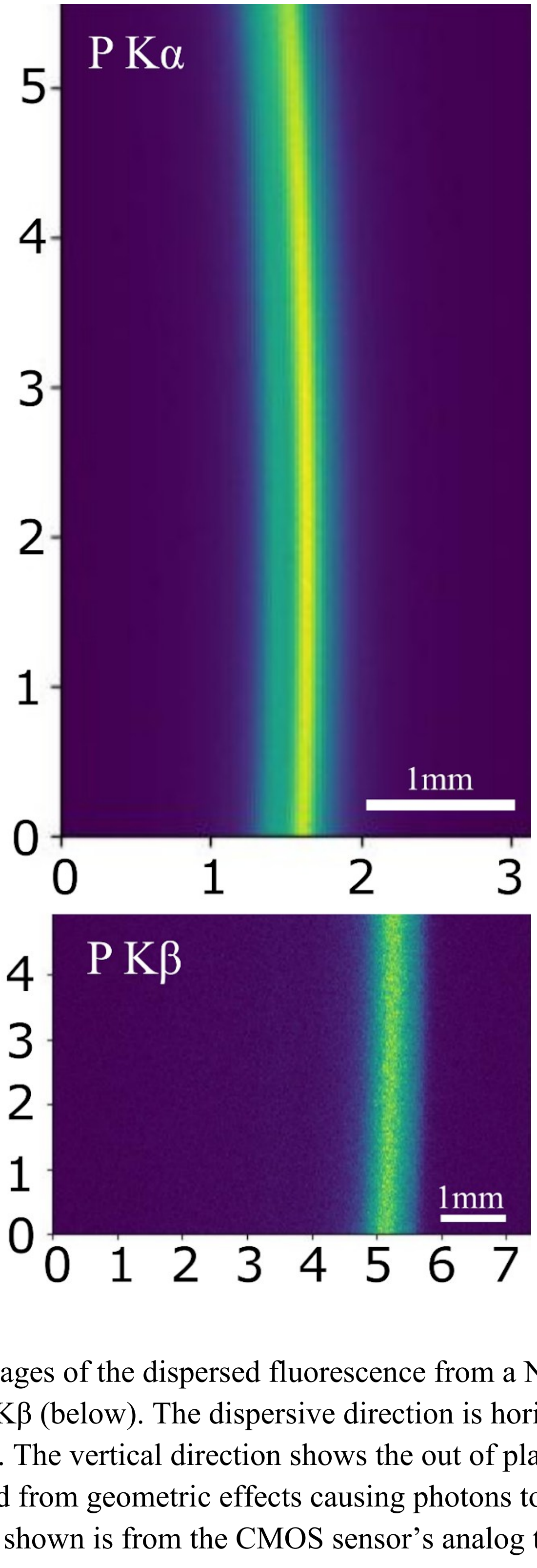

Figure 4. X-ray camera images of the dispersed fluorescence from a Ni_2P-0h nanoparticle sample: P Kα (above) and Kβ (below). The dispersive direction is horizontal, lower to higher energy moving left to right. The vertical direction shows the out of plane dimension, where minor curvature is observed from geometric effects causing photons to be bent towards lower energy. The pixel intensity shown is from the CMOS sensor's analog to digital converter and is different from photon count because of sensor gain.

3.3 Measurement protocols

All measurements were performed at ~100W x-ray tube power, i.e., at 2.8-mA tube current and 35-kV accelerating potential. The instrument is allowed to thermalize for at least half an hour at the desired power before data collection – no spectral drift is observed between chronologically early and late scans. Prior to data acquisition, the spectrometer enclosure is flushed with helium gas for about 15 minutes until the counts for a reference sample plateau.

To minimize potential errors from finite sample size, sample homogeneity, or analyzer irregularities, we follow the methods of Abramson, et al. [25]. This is done by taking short two-minute camera exposures at each position while stepping individual samples by ~0.44 mm through the illumination region and summing the resulting spectra. This gives equal weight at all detected energies to all positions on the face of the sample regardless of size or concentration. Using this protocol, P Kα and Kβ spectra were collected as x-ray camera images for nanoparticle samples exposed to air for various amounts of time, and reference compounds. Data was taken twice at each position on seven replicate samples for a total collection time of ~80 minutes per replicate sample during which Kα and Kβ are collected simultaneously. This was repeated for each air exposure time.

Control software for the instrument is written in Python, and the user interface is presented in Jupyter. Users specify a sample map with each entry containing a name, sample wheel position, and integration time. Then, calling names given in the sample map, a list of scans is set up to run automatically with x-ray camera images saved for each scan.

The camera images for one sample are summed over the sample wheel movement to form a single image, Fig. 4 shows summed representative x-ray camera images for the dispersed fluorescence from a Ni_2P-0h nanoparticle. In this image the energy dispersive direction is horizontal, and the vertical direction shows the out of plane divergence. The curvature of the fluorescence on the camera face is due to the cylindrical analyzer geometry and is parameterized using a second order polynomial fit to the center-of-masses calculated for each row after Gaussian filtering. The coefficients for this polynomial are used to assign each pixel of the detector to an energy bin, and the intensities with each such label are summed to produce the spectrum (processing software courtesy of easyXAFS LLC [35]). The energy scale is then set by measurement of Na_2HPO_4, having $K\alpha_1$ and $K\beta_{1,3}$ energies at 2014.55 eV and 2137.80 eV, respectively, based on Petric et. al.[36].

The spectra of all seven replicate samples at each time point were summed. $K\alpha$ spectra were background subtracted by a linear background calculated using the first and last 2 eV of the spectra, and then integral normalized. $K\beta$ spectra were background subtracted by a linear background calculated using the first and last 5 eV of the measurement, and then normalized using the associated $K\alpha$ integral to put them on an approximate mole-weighted scale.

3.4 Analysis Techniques

Linear superposition fitting was performed in Mathematica for the Ni_2P nanoparticle $K\alpha$ spectra, using the Ni_2P-Bulk and $Ni_3(PO_4)_2$ reference spectra as end points. The energy of the endpoint spectra was allowed to shift in order to accommodate the small differences in $K\alpha$ energies known to occur within one, nominal, oxidation state [36]. These shifts averaged 0.013 eV for the phosphide reference and 0.10 eV for the phosphate reference.

3.5 Electronic Structure Calculation

The FEFF10 real-space multiple-scattering code [37, 38] was used to calculate the XES using self-consistent potentials (SCP), full-multiple-scattering (FMS), and Hedin-Lundqvist self-energy corrections. The use of FEFF10 for valence-to-core XES calculation has been discussed previously, such as in Mortensen, et al [39]. The cluster sizes used in the calculations were 6 Å for both the SCP and FMS calculations. For the bulk calculation, the structure was taken as the hexagonal crystal structure [40] with space group p-62m. The Kβ XES was then calculated for each of the two inequivalent sites in the unit cell and stoichiometrically averaged to obtain the total Kβ XES spectrum. To approximate the surface Kβ XES spectrum of the nanoparticle, a 9 Å cluster was cut from the bulk, and the spectra of all surface P atoms were averaged.

4. Results and Discussion

To begin, we show in Fig. 5 a representative averaged sample fit of Ni_2P-24h, using a linear superposition fitting to phosphide (Ni_2P-Bulk) and phosphate ($Ni_3(PO_4)_2$) reference compound endpoints. In the top panel, the fit is done with no broadening of the two endpoint reference spectra, and the residual shows clear discrepancies indicating a weakness of the model. This isn't unexpected, as the nanophase materials have inhomogeneity from both their surface truncation (even if there are no surface adsorbates or other complications) and from the presence of an amorphous layer at the surface [41]. These effects are discussed further in the following paragraphs. Because of this inhomogeneity, we include 0.2 eV broadening of the reference spectra to allow for small differences in the Kα energies from slightly different local environments. The resulting fit, shown in the bottom panel of Fig. 5, is much improved. Fits for the entire aging sequence are shown in Fig. SI-2. In general, we find a statistical error in the fraction phosphide of 0.01 or less from the standard error determined from the seven replicate samples at each time point, see Table SI-1 and Table SI-2 for replicate fraction phosphide, standard deviation, and standard error. We also estimate a systematic error of the fitting of ±0.02 due to uncertainties in the use of the broadened-fit model.

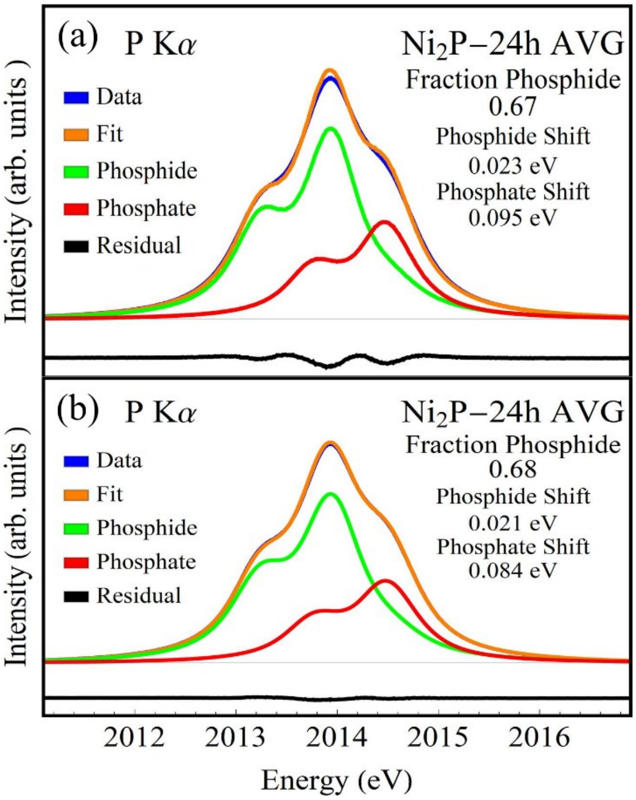

Figure 5. Linear superposition fit of the P Kα spectrum for an aged Ni2P nanophase sample to the phosphide (Ni_2P-Bulk) and phosphate ($Ni_3(PO_4)_2$) references. (a) Fits using the reference spectra as directly measured. (b) Fits after the reference spectra have been broadened by 0.2eV to compensate for a range of local environments, see the text for discussion. A compendium of fits for all air exposure times, using both broadened and unbroadened references, is presented in Fig. SI-2.

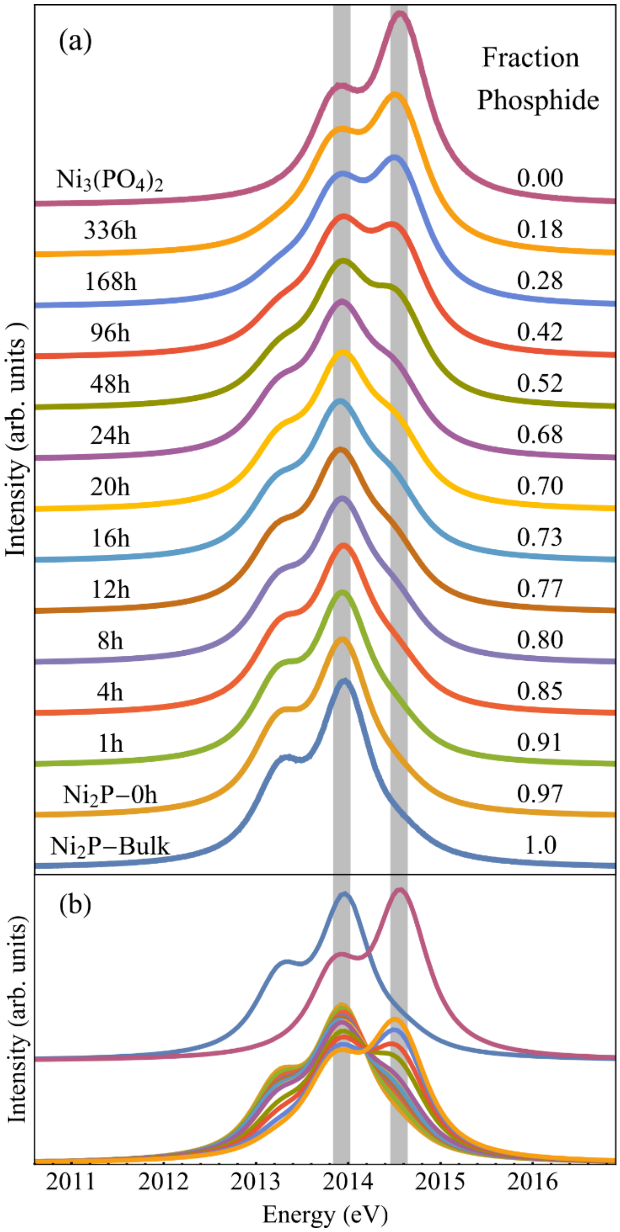

Figure 6. P Kα data for the Ni_2P-0h nanoparticles exposed to air for differing lengths of time, and two reference samples, Ni_2P-Bulk and $Ni_3(PO_4)_2$. Typical total measurement times for the ensemble of seven nanophase samples (averaged to give the results shown) is 9 hours, ~80 minutes per sample. Panel (a) shows the spectra offset with vertical guides, shaded bands, for the $K\alpha_1$ peaks of the phosphide and phosphate reference compounds. Panel (b) shows the same spectra overlayed. Note the apparent isosbestic point ~2014.25 eV, supporting the use of a simple two-phase decomposition onto reference compounds.

Next, in Fig. 6 we show P Kα data for Ni_2P nanoparticles that have been exposed to air for differing lengths of time, the phosphide reference, Ni_2P-Bulk, and the phosphate reference, $Ni_3(PO_4)_2$. The reference spectra show the typical Kα line shape, i.e., two peaks ($K\alpha_1$ and $K\alpha_2$) with a roughly 2:1 peak intensity ratio and a small trough in between indicating excellent energy resolution, fully comparable to work at a synchrotron facility. This can be seen, for example, when comparing our Na_2HPO_4 spectra, used for energy calibration and shown in SI-1, to synchrotron spectra from Petric et. al.[36]. Additionally, the reference spectra show the expected trend in energy shift with oxidation state.

The air-exposed, replicate-averaged Ni_2P nanoparticle spectra, to varying degrees, no longer show just two distinct $K\alpha_1/K\alpha_2$ peaks, indicating a mixed P oxidation state. The increase in intensity at 2014.55 eV paired with the decrease in intensity at 2013.80 eV (the two gray energy bands in Fig. 6) indicates a shift to a larger percentage of highly oxidized P upon increased air exposure. Fig. 6b shows the Ni_2P nanoparticle spectra have an approximate isosbestic point suggesting that the transition in P oxidation is a simple two-phase mixture. Given this, linear combination fitting of the Ni_2P nanoparticle spectra was performed to obtain a value for the fraction of P which has not been oxidized, listed in Fig. 6a as fraction phosphide.

In Fig. 7 we show Kβ spectra for the Ni_2P nanoparticles and references; again, this is collected simultaneously with the Kα results shown in Fig. 6. The Kβ reference spectra show all the expected features with high energy resolution: main $K\beta_{1,3}$ peak, oxygen ligand $K\beta'$ peak for $Ni_3(PO_4)_2$, and $K\beta''$ side peak for Ni_2P-Bulk. These reference Kβ spectra agree with previous phosphate and phosphide results [29, 36, 42]. The Ni_2P nanophase Kβ spectra, interestingly, show both similarities and differences with respect to the reference compounds. This is particularly notable when comparing the Ni_2P-Bulk reference to Ni_2P-0h nanoparticle sample -- the Ni_2P-0h

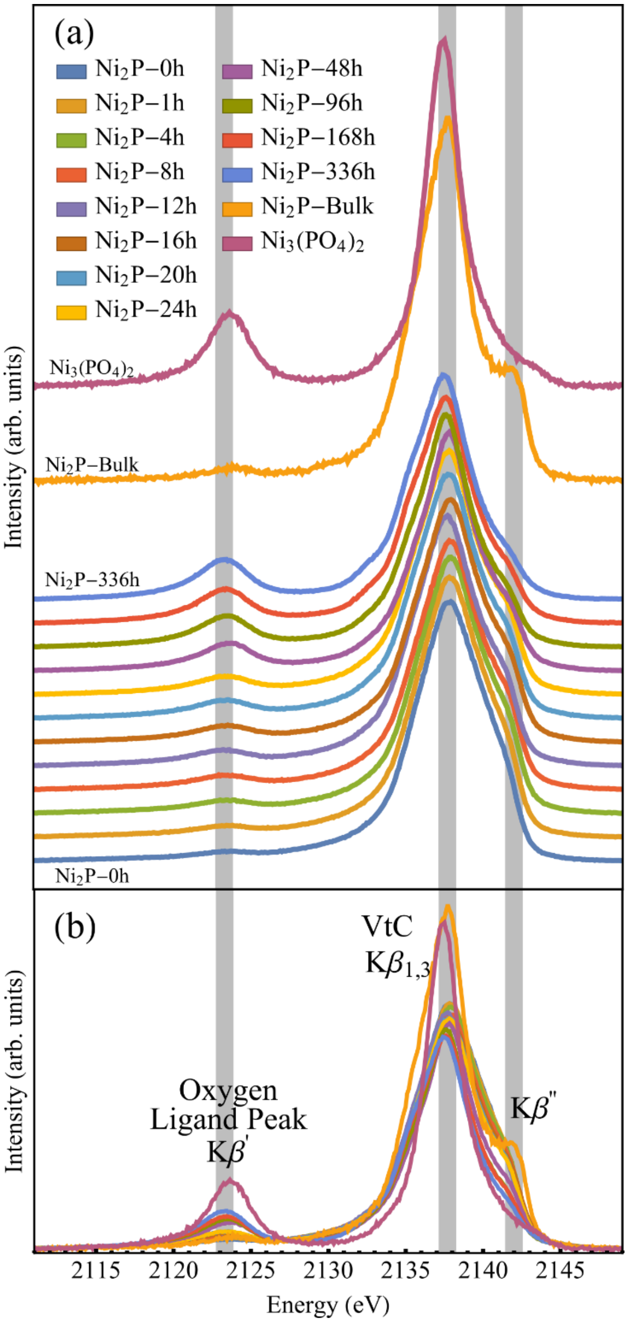

Figure 7. P Kβ spectra for the aging sequence of Ni_2P nanoparticles and the two reference samples, Ni_2P-Bulk and $Ni_3(PO_4)_2$. Note that as the air exposure time of the samples increases, there is a subtle shift in the main $K\beta_{1,3}$ peak and satellite $K\beta''$ peak, in addition to a steady increase in the intensity of the oxygen ligand peak.

nanoparticle sample contains only about 4% phosphate from the P Kα fitting and, therefore, our initial expectation was that the Kβ spectra of the nanophase would agree well with that of the bulk Ni_2P.

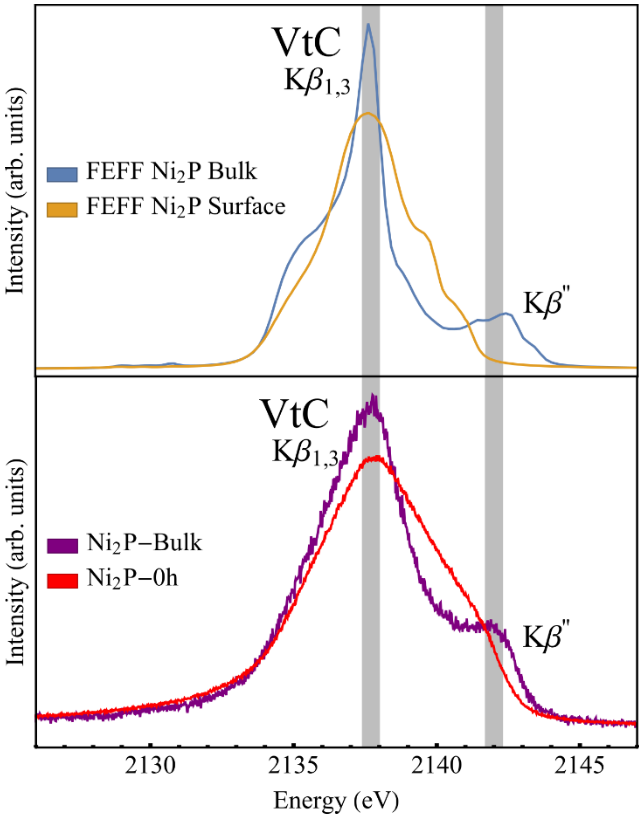

Figure 8. FEFF calculations for Ni_2P Bulk and Ni_2P Surface materials shown with data for Ni_2P-Bulk and Ni_2P nanoparticles, Ni_2P-0h. The differences between the bulk and surface theoretical spectra are in qualitative agreement with the deviations between the (macroscopic) crystalline Ni_2P-Bulk reference and the Ni_2P-0h spectra.

The main difference is the spectral line shape of the main $K\beta_{1,3}$ peak (~2137.80 eV), both in terms of its greater width and the decreased prominence of the $K\beta''$ side peak (~2142.00 eV). It is important to remember, however, that the nanoparticles have a mean diameter of only 5 nm and, further, that transmission electron microscopy (TEM) typically shows a disordered

Ni- and P- containing layer at the surface. Comparing average sizes of nanoparticles obtained by analyzing TEM images (~5 nm in diameter) and average crystallite domain sizes obtained by applying the Scherrer equation to peaks in the diffractogram (~4 nm in diameter) demonstrates that the surface layer is approximately 0.5 nm. Surface amorphization is seen in other studies as well [43-46], including one which estimated the disordered surface layer thickness of Ni_2P nanoparticles to be between 0.55 nm and 0.75 nm depending on surface facet terminations [41]. While it is not possible to model this disordered phase without additional information about its composition, the general effect of the nanoparticle surface, compared to bulk, on electronic structure can be modeled. In Fig. 8 we show the predicted bulk and near-surface contributions for an idealized crystalline Ni_2P nanoparticle. The general character of the deviation between the bulk Ni_2P and the native nanophase Ni2P-0h is in reasonable agreement between data and theory – the $K\beta''$ side peak shifts to lower energy and the main $K\beta_{1,3}$ peak broadens.

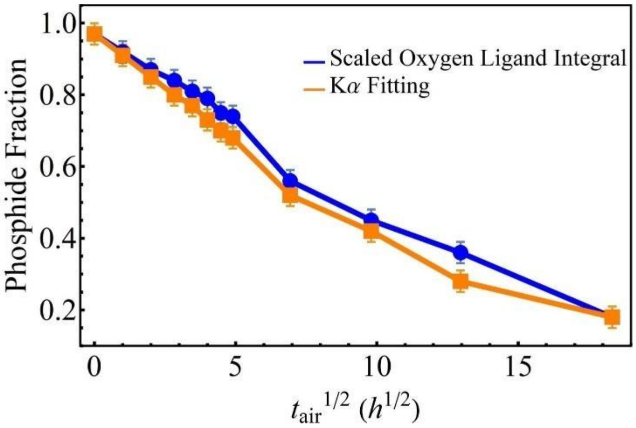

Figure 9. The phosphide fraction extracted from fits to Kα and from scaling of the oxygen ligand integral in Kβ (see the text), as a function of the square root of air exposure time, $t_{air}^{1/2}$. Both plots show a negative trend with increasing air exposure in rough agreement with a diffusion-limited model of oxidation.

Hence, while we can perform a simple linear superposition analysis of the Kα spectra to extract an estimate of P oxidation, no similar analysis is possible with the Kβ spectra, apparently due to electronic and structural differences near the surface of the nanoparticles. That being said, the Kβ data does show an increased presence of P-O bonds (i.e. higher oxidation state P) with longer air exposure via the increasing strength of the oxygen ligand peak, Kβ' at ~2124 eV.

The increased air exposure of the Ni_2P nanoparticle samples show a consistent increase in phosphate character across both Kα and Kβ spectra. In Fig. 9. We show the phosphide fraction, derived from fitting the Kα spectra to the references (as above) and a scaled representation of the integral of the oxygen ligand peak in the Kβ spectra, both plotted against the square root of air exposure time. Although the intensity of the ligand integral should be roughly proportional to the occurrence of P-O bonding, the absence of a valid fully-oxidized reference compound because of nanoscale effects discussed above, along with the effects of extreme sensitivity to oxygen ligand 2s energy and bond length [47], makes it impossible to assign a phosphide fraction metric to the ligand peak integral intensity on its own basis. Hence, the ligand integral results are scaled by the Kα-derived phosphide fractions at the 0 h and 336 h extrema -- the resulting general agreement is clear. The roughly linear trend as a function of the square root of air exposure time hints at a diffusion-limited model of P oxidation in the Ni_2P nanoparticles.

5. Conclusions

We report the design and performance of a new x-ray emission spectrometer that simultaneously measures P Kα and Kβ XES while being housed in a research grade, controlled atmosphere glovebox. A commissioning study of the gradual oxidation of Ni_2P nanoparticles due to air exposure showed excellent energy resolution and short acquisition times for both P Kα and Kβ XES. This system is housed in a shared user facility and provided with a user-friendly scripting interface. We anticipate that this system will see a wide range of future applications on air-sensitive P-rich materials while also serving as a proof-of-principle for future laboratory XES systems in research-grade gloveboxes.

Acknowledgements

The research was funded by the University of Washington Molecular Engineering Materials Center under U.S. National Science Foundation award DMR-1719797 and also by the U.S. National Science Foundation under award CHE-1904437. Jared Abramson acknowledges support from the University of Washington Clean Energy Institute and Rivera-Maldonado would like to thank the ARCS Foundation for additional funding.

References

1. Alori, E.T., B.R. Glick, and O.O. Babalola, *Microbial Phosphorus Solubilization and Its Potential for Use in Sustainable Agriculture.* Frontiers in Microbiology, 2017. **8**. 971
2. Lopez-Arredondo, D.L., et al., *Phosphate Nutrition: Improving Low-Phosphate Tolerance in Crops*, in *Annual Review of Plant Biology, Vol 65*, S.S. Merchant, Editor. 2014. p. 95-123.
3. Menezes-Blackburn, D., et al., *Opportunities for mobilizing recalcitrant phosphorus from agricultural soils: a review.* Plant and Soil, 2018. **427**(1-2): p. 5-16
4. Veneklaas, E.J., et al., *Opportunities for improving phosphorus-use efficiency in crop plants.* New Phytologist, 2012. **195**(2): p. 306-320
5. Yaakob, M.A., et al., *Influence of Nitrogen and Phosphorus on Microalgal Growth, Biomass, Lipid, and Fatty Acid Production: An Overview.* Cells, 2021. **10**(2). 393
6. Li, B.S., et al., *Black Phosphorus, a Rising Star 2D Nanomaterial in the Post-Graphene Era: Synthesis, Properties, Modifications, and Photocatalysis Applications.* Small, 2019. **15**(8). 1804565
7. Liu, H., et al., *Semiconducting black phosphorus: synthesis, transport properties and electronic applications.* Chemical Society Reviews, 2015. **44**(9): p. 2732-2743
8. Pang, J.B., et al., *Applications of Phosphorene and Black Phosphorus in Energy Conversion and Storage Devices.* Advanced Energy Materials, 2018. **8**(8). 1702093
9. Xu, Y.J., et al., *Recent progress in black phosphorus and black-phosphorus-analogue materials: properties, synthesis and applications.* Nanoscale, 2019. **11**(31): p. 14491-14527
10. Liu, W.L., H.Q. Zhi, and X.B. Yu, *Recent progress in phosphorus based anode materials for lithium/sodium ion batteries.* Energy Storage Materials, 2019. **16**: p. 290-322
11. Rahman, M.Z., et al., *2D phosphorene as a water splitting photocatalyst: fundamentals to applications.* Energy & Environmental Science, 2016. **9**(3): p. 709-728
12. Shi, R., et al., *Black/red phosphorus quantum dots for photocatalytic water splitting: from a type I heterostructure to a Z-scheme system.* Chemical Communications, 2019. **55**(83): p. 12531-12534
13. Wu, Y., et al., *The Promise and Challenge of Phosphorus-Based Composites as Anode Materials for Potassium-Ion Batteries.* Advanced Materials, 2019. **31**(50). 1901414
14. Garcia-Oliva, F., et al., *Severe wildfire hinders renewal of soil P pools by thermal mineralization of organic P in forest soil: Analysis by sequential extraction and P-31 NMR spectroscopy.* Geoderma, 2018. **309**: p. 32-40
15. Huang, R.X. and Y.Z. Tang, *Speciation Dynamics of Phosphorus during (Hydro)Thermal Treatments of Sewage Sludge.* Environmental Science & Technology, 2015. **49**(24): p. 14466-14474
16. Schmieder, F., et al., *Phosphorus speciation in a long-term manure-amended soil profile - Evidence from wet chemical extraction, P-31-NMR and P K-edge XANES spectroscopy.* Geoderma, 2018. **322**: p. 19-27
17. Andrews, P., et al., *Highly active homogeneous nickel catalysts for alkene dimerisation: crystal strucure* $[Ni(\eta^3\text{-}C_3H_5)(PPh_3)Br]$ *and in situ characterisation of* $AlEt_3$*-activated* $[Ni(\eta^3\text{-}C_3H_5)(PPh_3)Br]$ *by nuclear magnetic resonance and extended X-ray absorption fine structure spectroscopy.* Journal of the Chemical Society-Dalton Transactions, 1994(9): p. 1337-1347

18. Liu, C., et al., *Topological construction of phosphorus and carbon composite and its application in energy storage.* Energy Storage Materials, 2019. **20**: p. 343-372
19. Sahkouri, M., et al., *Glovebox-integrated XES and XAS station for in situ studies in tender x-ray region.* Electronic Structure, 2020. **2**(4). 047001
20. Scheinost, A.C., et al., *ROBL-II at ESRF: a synchrotron toolbox for actinide research.* Journal of Synchrotron Radiation, 2021. **28**: p. 333-349
21. Li, M.S., et al., *New Insights into the High-Performance Black Phosphorus Anode for Lithium-Ion Batteries.* Advanced Materials, 2021. **33**(35). 2101259
22. Petric, M., et al., *Electronic Structure of Third-Row Elements in Different Local Symmetries Studied by Valence-to-Core X-ray Emission Spectroscopy.* Inorganic Chemistry, 2016. **55**(11): p. 5328-5336
23. Petric, M. and M. Kavčič, *Chemical speciation via X-ray emission spectroscopy in the tender X-ray range.* Journal of Analytical Atomic Spectrometry, 2016. **31**(2): p. 450-457
24. Mathe, Z., et al., *Phosphorus Kβ X-ray emission spectroscopy detects non-covalent interactions of phosphate biomolecules in situ.* Chemical Science, 2021. **12**(22): p. 7888-7901
25. Abramson, J.E., et al., *An exploration of benchtop X-ray emission spectroscopy for precise characterization of the sulfur redox state in cementitious materials.* X-Ray Spectrometry, 2022. **51**(2): p. 151-162
26. Holden, W.M., G.T. Seidler, and S. Cheah, *Sulfur Speciation in Biochars by Very High Resolution Benchtop K alpha X-ray Emission Spectroscopy.* Journal of Physical Chemistry A, 2018. **122**(23): p. 5153-5161
27. Jahrman, E.P., G.T. Seidler, and J.R. Sieber, *Determination of Hexavalent Chromium Fractions in Plastics Using Laboratory-Based, High-Resolution X-ray Emission Spectroscopy.* Analytical Chemistry, 2018. **90**(11): p. 6587-6593
28. Malzer, W., et al., *A laboratory spectrometer for high throughput X-ray emission spectroscopy in catalysis research.* Review of Scientific Instruments, 2018. **89**(11): p. 113111
29. Stein, J.L., et al., *Probing Surface Defects of InP Quantum Dots Using Phosphorus K alpha and K beta X-ray Emission Spectroscopy.* Chemistry of Materials, 2018. **30**(18): p. 6377-6388
30. Zimmermann, P., et al., *Modern X-ray spectroscopy: XAS and XES in the laboratory.* Coordination Chemistry Reviews, 2020. **423**. 213466
31. Mitra, K.L.W., et al., *Surface Functionalization of Black Phosphorus with Nitrenes: Identification of P=N Bonds by Using Isotopic Labeling.* Angewandte Chemie-International Edition, 2021. **60**(16): p. 9127-9134
32. Tetef, S., et al., *Informed Chemical Classification of Organophosphorus Compounds via Unsupervised Machine Learning of X-ray Absorption Spectroscopy and X-ray Emission Spectroscopy.* The Journal of Physical Chemistry A, 2022. **126**(29): p. 4862-4872
33. Holden, W.M., et al., *A compact dispersive refocusing Rowland circle X-ray emission spectrometer for laboratory, synchrotron, and XFEL applications.* Review of Scientific Instruments, 2017. **88**(7): p. 073904. 073904
34. Holden, W.M., et al., *Probing Sulfur Chemical and Electronic Structure with Experimental Observation and Quantitative Theoretical Prediction of K alpha and Valence-to-Core K beta X-ray Emission Spectroscopy.* Journal of Physical Chemistry A, 2020. **124**(26): p. 5415-5434

35. Holden, W.M., et al., *A color x-ray camera for 2-6 keV using a mass produced back illuminated complementary metal oxide semiconductor sensor.* Review of Scientific Instruments, 2018. **89**(9): p. 093111. 093111

36. Petric, M., et al., *Chemical State Analysis of Phosphorus Performed by X-ray Emission Spectroscopy.* Analytical Chemistry, 2015. **87**(11): p. 5632-5639

37. Kas, J.J., et al., *Advanced calculations of X-ray spectroscopies with FEFF10 and Corvus.* Journal of Synchrotron Radiation, 2021. **28**: p. 1801-1810

38. Rehr, J.J. and R.C. Albers, *Theoretical approaches to x-ray absorption fine structure.* Reviews of Modern Physics, 2000. **72**(3): p. 621-654

39. Mortensen, D.R., et al., *Benchmark results and theoretical treatments for valence-to-core x-ray emission spectroscopy in transition metal compounds.* Physical Review B, 2017. **96**(12). 125136

40. Larsson, E., *An X-ray investigation of Ni-P system and crystal structures of NiP and NiP_2.* Arkiv for Kemi, 1965. **23**(3-4): p. 335-&

41. Papawassiliou, W., et al., *Crystal and electronic facet analysis of ultrafine Ni2P particles by solid-state NMR nanocrystallography.* Nature Communications, 2021. **12**(1): p. 4334

42. Sugiura, C., *X-Ray Emission Spectra and Electronic Structures of Red Phosphorus, 3d Transition-Metal Phosphides and III–V Compounds.* Journal of the Physical Society of Japan, 1995. **64**(7): p. 2510-2523

43. Wang, J., A.C. Johnston-Peck, and J.B. Tracy, *Nickel Phosphide Nanoparticles with Hollow, Solid, and Amorphous Structures.* Chemistry of Materials, 2009. **21**(19): p. 4462-4467

44. Moreau, L.M., et al., *Defining Crystalline/Amorphous Phases of Nanoparticles through X-ray Absorption Spectroscopy and X-ray Diffraction: The Case of Nickel Phosphide.* Chemistry of Materials, 2013. **25**(12): p. 2394-2403

45. Mundy, M.E., et al., *Aminophosphines as Versatile Precursors for the Synthesis of Metal Phosphide Nanocrystals.* Chemistry of Materials, 2018. **30**(15): p. 5373-5379

46. Murphy, I.A., et al., *Covalent Functionalization of Nickel Phosphide Nanocrystals with Aryl-Diazonium Salts.* Chemistry of Materials, 2021. **33**(24): p. 9652-9665

47. MacMillan, S.N., et al., *Ligand-Sensitive But Not Ligand-Diagnostic: Evaluating Cr Valence-to-Core X-ray Emission Spectroscopy as a Probe of Inner-Sphere Coordination.* Inorganic Chemistry, 2015. **54**(1): p. 205-214

Chapter 6 - Supplemental Information: Laboratory X-ray Emission Spectrometer for Phosphorus Kα and Kβ Study of Air-Sensitive Samples

Originally published as: J. Abramson, W. Holden, R. Rivera-Maldonado, A. Velian, B. Cossairt, G. Seidler. *Journal of Analytical Atomic Spectrometry* 2023 Vol. 38 Page 1125-1134.

J. Abramson wrote and conducted the majority of this work.

Replicate 5 Phosphide Fraction	Replicate 6 Phosphide Fraction	Replicate 7 Phosphide Fraction	Standard Deviation	Standard Error
0.93	0.94	0.94	0.010	0.0038
0.88	0.89	0.89	0.011	0.0043
0.83	0.82	0.82	0.0073	0.0028
0.78	0.77	0.77	0.0049	0.0019
0.76	0.74	0.74	0.0083	0.0031
0.72	0.71	0.70	0.0073	0.0028
0.69	0.68	0.67	0.0073	0.0028
0.69	0.66	0.65	0.012	0.0047
0.54	0.52	0.50	0.016	0.0060
0.44	0.41	0.38	0.024	0.0090
0.32	0.28	0.26	0.026	0.0097
0.23	0.20	0.19	0.018	0.0069

Table SI-1 Ni2P nanophase sample replicate phosphide fraction determined from fitting to reference spectra (Ni2P-Bulk and Ni3(PO4)2), standard deviation and standard error. See Fig. SI-2 for plots of fits.

Replicate 5 Phosphide Fraction	Replicate 6 Phosphide Fraction	Replicate 7 Phosphide Fraction	Standard Deviation	Standard Error
0.97	0.97	0.96	0.0081	0.0030
0.91	0.91	0.91	0.0088	0.0033
0.85	0.85	0.85	0.0053	0.0020
0.81	0.80	0.79	0.0064	0.0024
0.77	0.76	0.76	0.0070	0.0026
0.74	0.72	0.72	0.0076	0.0029
0.71	0.69	0.68	0.0090	0.0034
0.70	0.67	0.66	0.014	0.0052
0.54	0.52	0.49	0.018	0.0069
0.43	0.40	0.36	0.027	0.010
0.30	0.26	0.24	0.026	0.0097
0.20	0.17	0.16	0.018	0.0069

Table SI-2 Ni_2P nanophase sample replicate phosphide fraction determined from fitting to 0.2 eV broadened reference spectra (Ni_2P-Bulk and $Ni_3(PO_4)_2$), standard deviation and standard error. See Fig. SI-2 for plots of fits.

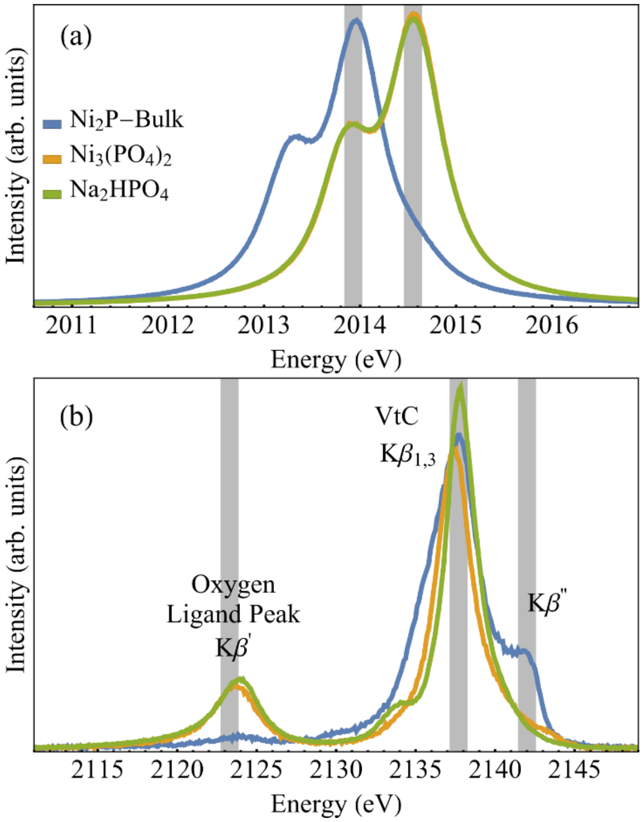

Figure SI-1: P Kα and Kβ reference spectra, Ni_2P-Bulk and $Ni_3(PO_4)_2$, with Na_2HPO_4 reference spectra. The Na_2HPO_4 spectra was used to set the energy scale, see text for details.

Figure SI-2 (below and following pages): A compendium of P Kα XES results with fits, references, and residuals for all Ni_2P nanophase samples after summing replicate spectra. In each case the left column is the fit with the original, unbroadened references, while the right column uses the slightly broadened reference spectra discussed in the text.

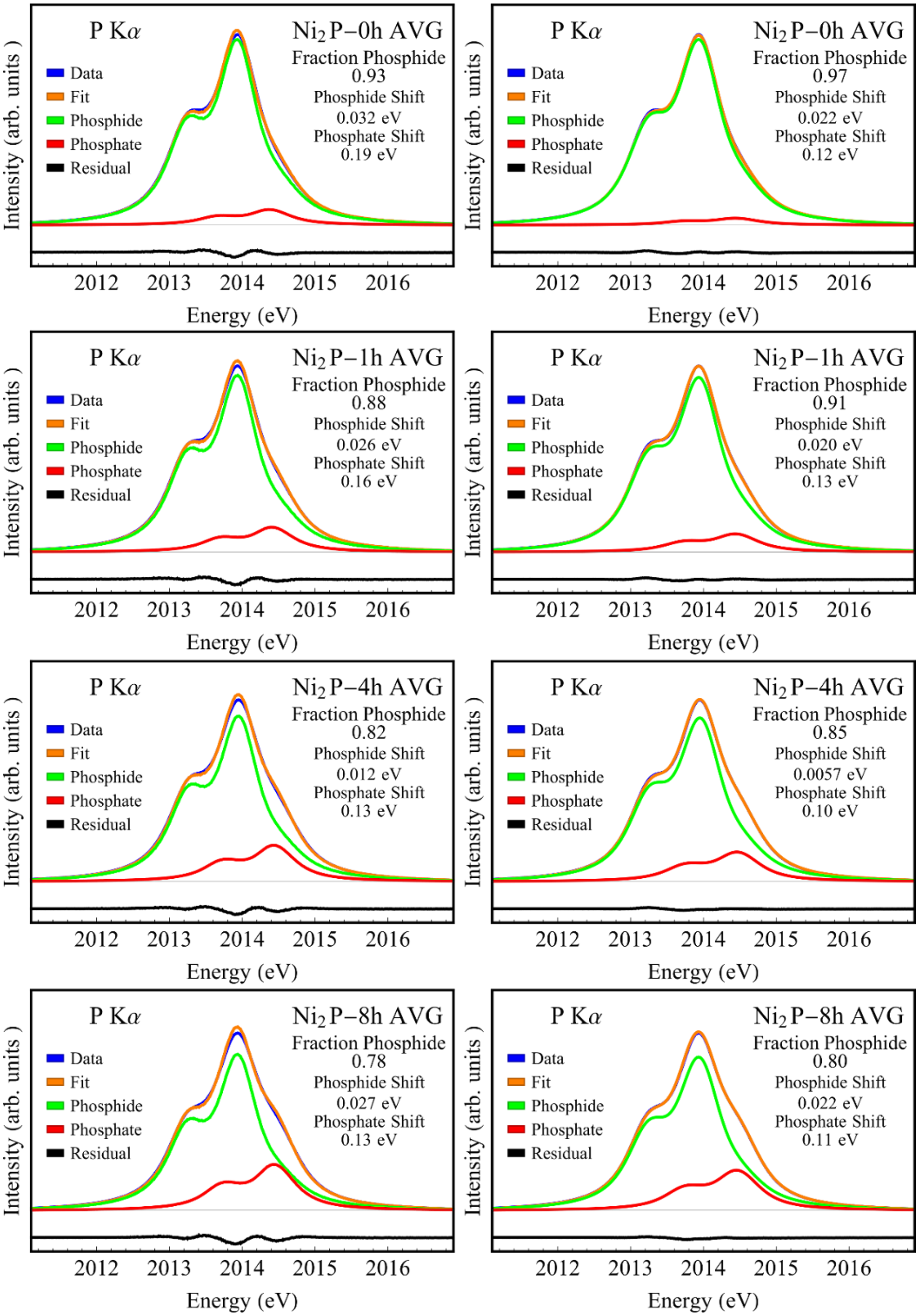

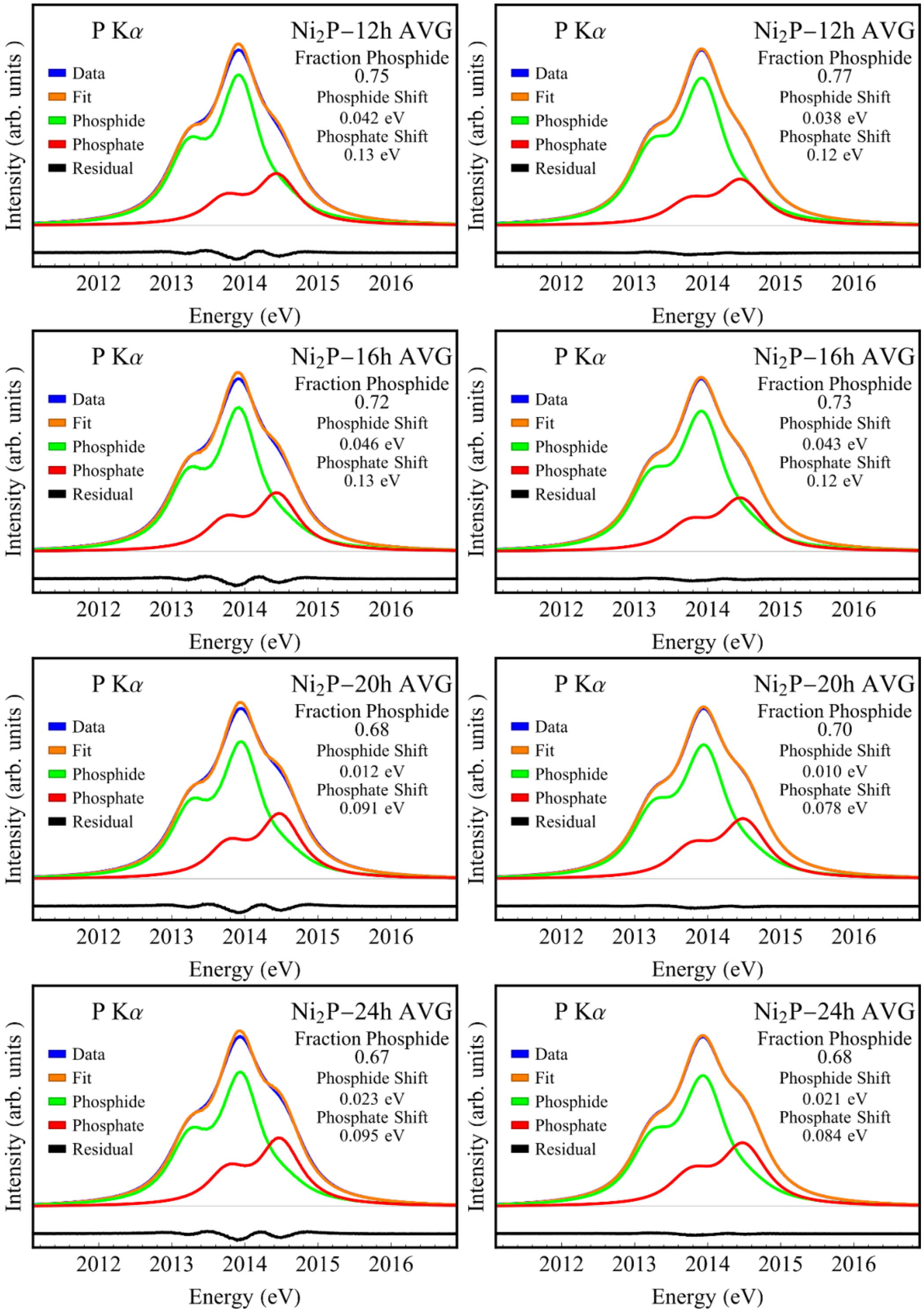
P Kα
Ni$_2$P−12h AVG
Fraction Phosphide
0.75
Phosphide Shift
0.042 eV
Phosphate Shift
0.13 eV
Data
Fit
Phosphide
Phosphate
Residual
Intensity (arb. units)
2012
2013
2014
2015
2016
Energy (eV)
P Kα
Ni$_2$P−12h AVG
Fraction Phosphide
0.77
Phosphide Shift
0.038 eV
Phosphate Shift
0.12 eV
Data
Fit
Phosphide
Phosphate
Residual
Intensity (arb. units)
2012
2013
2014
2015
2016
Energy (eV)
P Kα
Ni$_2$P−16h AVG
Fraction Phosphide
0.72
Phosphide Shift
0.046 eV
Phosphate Shift
0.13 eV
Data
Fit
Phosphide
Phosphate
Residual
Intensity (arb. units)
2012
2013
2014
2015
2016
Energy (eV)
P Kα
Ni$_2$P−16h AVG
Fraction Phosphide
0.73
Phosphide Shift
0.043 eV
Phosphate Shift
0.12 eV
Data
Fit
Phosphide
Phosphate
Residual
Intensity (arb. units)
2012
2013
2014
2015
2016
Energy (eV)
P Kα
Ni$_2$P−20h AVG
Fraction Phosphide
0.68
Phosphide Shift
0.012 eV
Phosphate Shift
0.091 eV
Data
Fit
Phosphide
Phosphate
Residual
Intensity (arb. units)
2012
2013
2014
2015
2016
Energy (eV)
P Kα
Ni$_2$P−20h AVG
Fraction Phosphide
0.70
Phosphide Shift
0.010 eV
Phosphate Shift
0.078 eV
Data
Fit
Phosphide
Phosphate
Residual
Intensity (arb. units)
2012
2013
2014
2015
2016
Energy (eV)
P Kα
Ni$_2$P−24h AVG
Fraction Phosphide
0.67
Phosphide Shift
0.023 eV
Phosphate Shift
0.095 eV
Data
Fit
Phosphide
Phosphate
Residual
Intensity (arb. units)
2012
2013
2014
2015
2016
Energy (eV)
P Kα
Ni$_2$P−24h AVG
Fraction Phosphide
0.68
Phosphide Shift
0.021 eV
Phosphate Shift
0.084 eV
Data
Fit
Phosphide
Phosphate
Residual
Intensity (arb. units)
2012
2013
2014
2015
2016
Energy (eV)

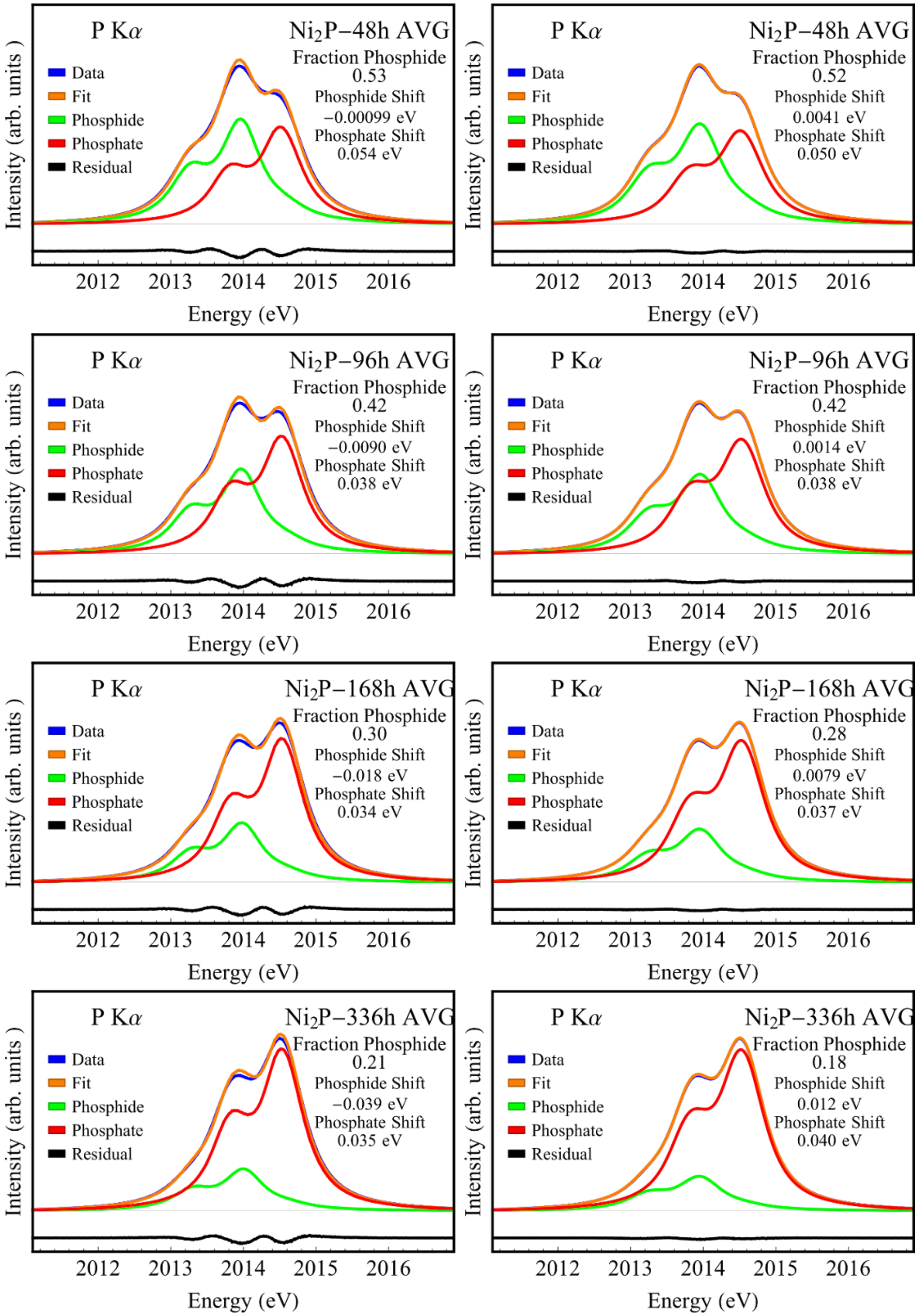
P Kα
Ni$_2$P−48h AVG
Fraction Phosphide
0.53
Phosphide Shift
−0.00099 eV
Phosphate Shift
0.054 eV
P Kα
Ni$_2$P−48h AVG
Fraction Phosphide
0.52
Phosphide Shift
0.0041 eV
Phosphate Shift
0.050 eV
P Kα
Ni$_2$P−96h AVG
Fraction Phosphide
0.42
Phosphide Shift
−0.0090 eV
Phosphate Shift
0.038 eV
P Kα
Ni$_2$P−96h AVG
Fraction Phosphide
0.42
Phosphide Shift
0.0014 eV
Phosphate Shift
0.038 eV
P Kα
Ni$_2$P−168h AVG
Fraction Phosphide
0.30
Phosphide Shift
−0.018 eV
Phosphate Shift
0.034 eV
P Kα
Ni$_2$P−168h AVG
Fraction Phosphide
0.28
Phosphide Shift
0.0079 eV
Phosphate Shift
0.037 eV
P Kα
Ni$_2$P−336h AVG
Fraction Phosphide
0.21
Phosphide Shift
−0.039 eV
Phosphate Shift
0.035 eV
P Kα
Ni$_2$P−336h AVG
Fraction Phosphide
0.18
Phosphide Shift
0.012 eV
Phosphate Shift
0.040 eV
Data
Fit
Phosphide
Phosphate
Residual
Intensity (arb. units)
Energy (eV)
2012
2013
2014
2015
2016

Chapter 7 - Asymmetric Rowland Circle Geometries for Spherically Bent Crystal Analyzers in Laboratory and Synchrotron Applications

Originally published as: A. Gironda, J. Abramson, Y. Chen, M. Solovyev, G. Sterbinsky, G. T. Seidler. *Journal of Analytical Atomic Spectrometry* 2024 Vol. 39 Page 1375-1387. J. Abramson was a key contributor to the development, experimentation and writing of this work.

Spherically bent crystal analyzers (SBCAs) are the dominant high-resolution hard x-ray optic in the ongoing rebirth of laboratory-based x-ray absorption fine structure (XAFS) and x-ray emission spectroscopy (XES) as well as in synchrotron methods such as high energy resolution fluorescence detection (HERFD) and non-resonant x-ray Raman scattering (XRS). In the overwhelming majority of cases, SBCAs are implemented in a 'symmetric' configuration on the Rowland circle, wherein the diffracting crystal plane is nominally coincident with the analyzer surface. We report here comprehensive investigations of 'asymmetric' operation of SBCA on the Rowland circle, wherein the diffracting crystal plane is not coincident with the optical surface of the analyzer. First, we have developed a laboratory spectrometer for XAFS and XES that is specialized for asymmetric SBCA operation. We find several benefits, including the capacity to use a single SBCA over a very wide energy range via 'hkl hopping' and the frequent ability to eliminate Johann error, the most prevalent energy-broadening mechanism when using SBCA symmetrically on the Rowland circle. Second, we expand these ideas to synchrotron

facilities with a demonstration study of HERFD and XRS where asymmetric operation also provided advantage. Our results suggest that large-array systems for HERFD augmented with an additional mechanical degree of freedom could streamline user operation and also indicate benefits to XRS in the asymmetric configuration, where larger solid angle, larger sample-to-detector distance, and decreased Johann error can be achieved simultaneously.

1. Introduction

Spherically bent crystal analyzers (SBCAs), specifically those with Johann-type profiles[1], are hard x-ray optics that provide a useful combination of large collection solid angle and fine energy resolution. This has resulted in their extensive use in the ongoing rebirth of laboratory-based x-ray absorption fine structure (XAFS) and x-ray emission spectroscopy (XES)[2–10] in addition to their historical and continued use as workhorse optics for high-resolution photon-in photon-out x-ray spectroscopy at synchrotron facilities.[11–18] With infrequent but valuable exceptions[19–22], such applications have been in a 'symmetric' Rowland circle configuration wherein the diffracting plane is nominally coincident with the surface of the SBCA diffracting wafer.

Here, we propose that asymmetric operation of SBCA on the Rowland circle is an underutilized opportunity. The basic parameters for asymmetric Rowland circle operation are defined in Fig. 1. In the Figure, note the asymmetry angle α, the need for a 'mechanical' analyzer angle θ_M, and the inequality of the chord lengths ρ and *d* when $\alpha \neq 0$. The usual theorem for equality of inscribed angles still holds when $\alpha \neq 0$ so that the optic still functions as a monochromator in the Rowland plane, barring Johann error which will be discussed in

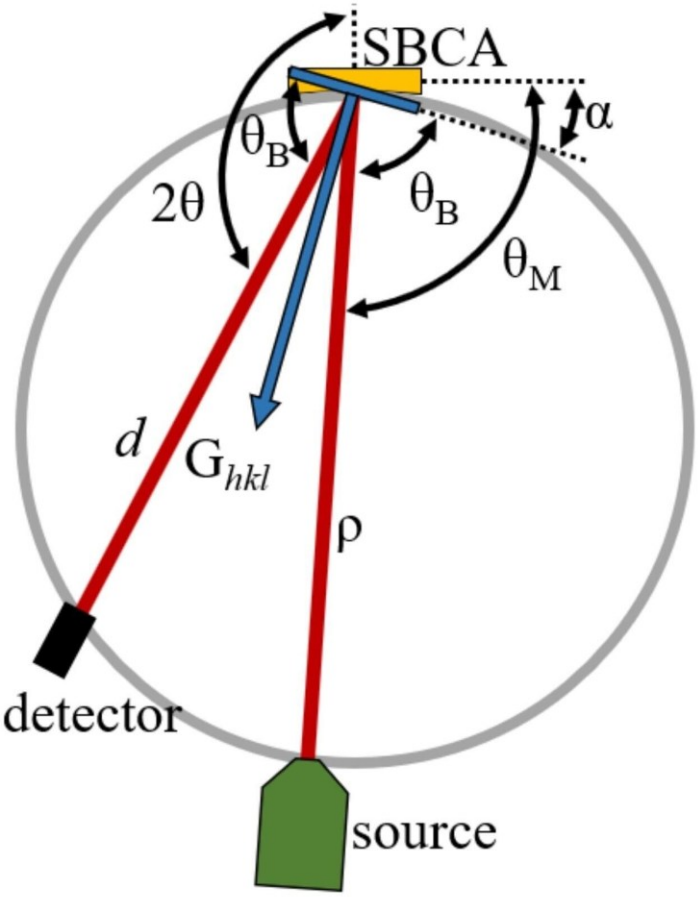

Figure 1: Diagram of spectrometer components during asymmetric operation in the reference frame of the SBCA. α denotes the angle between the diffracting plane for the reflection $\mathbf{G}_{hkl}$ and the plane at the optic's surface (nominally normal to the reciprocal lattice vector $\mathbf{G}_0$). Note the chord lengths *d* and ρ differ when $\alpha \neq 0$.

detail later. Out-of-plane astigmatism at large α can become considerable, but we find that is not a significant limitation on energy resolution. It is not difficult to derive the dependence of the parameters in Fig. 1 on the Bragg angle, θ_B, and α, specifically

$$\begin{aligned} \rho &= D\sin(\theta_B + \alpha) \\ d &= D\sin(\theta_B - \alpha) \qquad \text{Eqs. (1)} \\ 2\theta &= 2\theta_B \\ \theta_M &= \theta_B + \alpha \end{aligned}$$

where *D* is the diameter of the Rowland circle or equivalently the radius of curvature of the Johann SBCA.

With this background established, we address the potential advantages of asymmetric operation as a central principle in spectrometer design. We denote by $\mathbf{G}_0$ the reciprocal lattice vector normal to the wafer surface and assume the wafer miscut is small. Choosing $\mathbf{G}_0$ is equivalent to choosing which wafer material and orientation to use in the optic, and it determines the useful energy range in symmetric operation -- Bragg angles below 60 deg generally suffer degraded energy resolution due to Johann error and source-size broadening. While analyzer harmonics sometimes enable high-resolution access to a few distinct energy ranges[23], both laboratory instruments and synchrotron facilities typically fabricate or acquire a suite of SBCAs having a variety of $\mathbf{G}_0$ vectors.

Asymmetric operation modifies these considerations. Any single crystal has a multitude of additional crystal planes at various angles to the surface. Each allowed reflection capable of diffraction in an asymmetric configuration gives an additional useful energy range dependent on its own *d*-spacing. Hence, as a first advantage, we show below that asymmetric operation of a single SBCA can permit high-resolution performance for photon energies from 5 keV through 10 keV and beyond with no gaps in the energy range. The good performance of many different reflections of various Miller indices (*hkl*) from a single analyzer is a major result of the present study, and we find it appropriate to introduce the term '*hkl* hopping' when a monochromator jumps between different Miller indices of a single SBCA to adjust energy range or to improve energy resolution, which we now address.

The second advantage of asymmetric operation is the minimization or even elimination of Johann error for SBCAs; prior work by Suortti and others for curved analyzers on the Rowland circle as well as asymmetric applications in other fields and other classes of optics motivates and supports this inquiry[21,22,24–35]. Briefly, Johann analyzers possess a radius of curvature for the diffracting wafer that is equal to the diameter of the desired Rowland circle. This yields the necessary suface orientations but results in small displacements between the wafer surface and the Rowland circle at the analyzer edges with corresponding errors in the Bragg angle upon moving away from the analyzer center. There is consequently a characteristic low energy tail in the analyzer's energy response function[36].

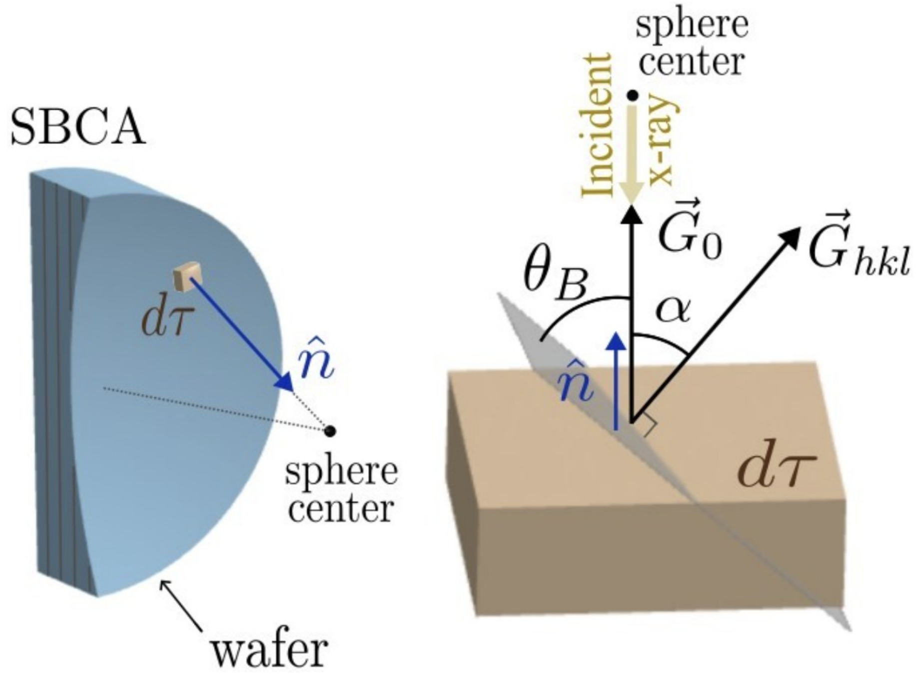

Figure 2: An infinitesimal single crystal element (right) of a spherically bent crystal analyzer (left), demonstrating a geometric argument for the elimination of Johann error in asymmetric Rowland geometries when the source is close to the sphere-center of the SBCA curved wafer.

The underlying principle for suppression of Johann error via asymmetric operation is illustrated in Fig. 2. As shown, consider the special case where all incident x-rays have an incoming path exactly normal to each infinitesimal crystallite that makes up the SBCA surface, i.e., the special case where a point source is located at the sphere center of the curved analyzer wafer surface. The key observation is that for every point on the analyzer surface, the angle between an arbitarily chosen reciprocal lattice vector $\mathbf{G}_{hkl}$ and the incident x-ray is the same everywhere on the surface. Hence, in this special case the Bragg angle is the same at every point on the surface and Johann error from the lack of coincidence between the edges of the analyzer and the Rowland circle is eliminated. More generally, asymmetric operation allows operation with the source *closer to* the sphere center than is often possible symmtrically, and hence with dereased Johann error. We illustrate this later with XANES and XES measurements.

Finally, a third benefit comes from those special geometries that are expected to fully eliminate Johann error, as described by Fig. 2. Non-resonant x-ray Raman scattering (XRS), i.e., the non-resonant inelastic x-ray scattering from semi-core levels, gives a hard x-ray analog to electron energy loss spectroscopy and allows x-ray spectroscopy on low-energy shells while using high-energy photons. This capability has seen sufficient demand that several dedicated facilities have been constructed at synchrotron facilities[37–41]. However, the extremely small cross-section for inelastic scattering from the semi-core levels makes all XRS spectrometers subject to severe competition between the collection solid angle and the energy resolution. The best practice to date has been to use banks of 1-m SBCA as close as possible to a backscatter geometry in symmetric Rowland operation, together with considerable diligence to reject background scatter[12,14,17,18]. That being said, achieving highest energy resolution still requires analyzer masking to reduce Johann error; in some cases, small off-circle broadening is accepted as a compromise that aids with clearance between detector and the beam spot on the sample[13]. The more recently available 0.5-m SBCA having four times the solid angle of the older 1-m SBCA have not been used for XRS because their larger angular size results in far larger Johann error *in symmetric operation*. On the other hand, the Johann-rejection strategy of Fig. 2 provides a possible path toward simultaneously attaining large solid angle, fine energy resolution, and large clearance between sample and detector. XRS measurements are performed in so-called inverse-scanning mode where a single energy is chosen for the outgoing (analyzed) photon while the incident monochromator is scanned to create the necessary range of energy losses: *the spectrometer must have low Johann error at only a single energy*.

In this paper we address all three of these proposed benefits. We describe a new laboratory-based XAFS and XES hard x-ray spectrometer specifically designed to enable easy exploration of asymmetric Rowland geometries. With this instrument we demonstrate *hkl* hopping over a broad energy range and also demonstrate the minimization of Johann error through choice of the favorable special geometry with the source near the spherical center of the analyzer. These benefits also appear in our preliminary synchrotron studies, where we use asymmetric reflections to access the otherwise inconvenient Zn Kα_1 for high-energy resolution fluorescence detection (HERFD) x-ray absorption spectroscopy and also use an optimal asymmetric configuration for XRS via an 0.5-m radius SBCA. This ensemble of results across laboratory and synchrotron venues supports the hypothesis that asymmetric operation of SBCA has been underutilized and suggests directions for further inquiry.

2. Laboratory Spectrometer Design and Operation

We now present the six main spectrometer systems in order: the x-ray enclosure, x-ray sources, the detector and its subassembly, the optic, the motorization of the primary Rowland circle degrees of freedom, the additional motorized degree of freedom used to rotate many different desired reflections into the Rowland plane, and the overall control software.

The spectrometer is housed in a steel enclosure, approximately 1.8-m wide by 1.5-m deep by 1.3-m tall. The slightly oversized enclosure provides ample space for special sample environments in the future such as a cryostat or additional equipment such as a potentiostat for *operando* electrochemical measurements. The computer-aided design (CAD) rendering in Fig.

3 shows the design of the spectrometer and its key components in Rowland circle geometries configured for XAFS and XES measurements in Fig. 3 (a) and (b), respectively. In XAFS mode (Fig. 3 (a)), a 100 W X-ray source (Varex VF-80 Pd-anode tube) with variable width entrance slits to adjust apparent source size is placed on-circle via manual slide. In XES mode (Fig. 3 (b)), a 3 kW X-ray source (Varex OEG-76H W-anode tube) with a preliminary 1 mm fixed-width entrance slit on the sample enclosure is placed on-circle via manual slide. A kinematic feature at the fixed source location ensures precise placement of radiation entrance slits on circle. A 100 W x-ray tube with a tungsten anode, but otherwise identical to the XAFS-mode source, was used for commissioning in XES measurements (not shown in the figure).

The detector is a silicon drift detector (SDD) with 150 mm^2 area sensing element (KETEK AXAS M-1) mounted on a motorized linear stage (Velmex XSlide) to adjust the detector-analyzer chord length. The optics are 0.5-m radius of curvature SBCAs (XRS Tech). The chord lengths and angular positioning of the detector and optic are motorized. The optic and detector subassemblies are concentrically mounted on the θ and 2θ rotation stages, respectively, of a repurposed goniometer from a commercial X-ray diffraction instrument (Bruker D8 Advance). The θ and 2θ stages of the goniometer are independent, allowing for the α offsets required in asymmetric operation. The entire goniometer-detector-optic subassembly is mounted on a motorized linear stage (Velmex tandem BiSlide) to adjust source-analyzer chord length, ρ.

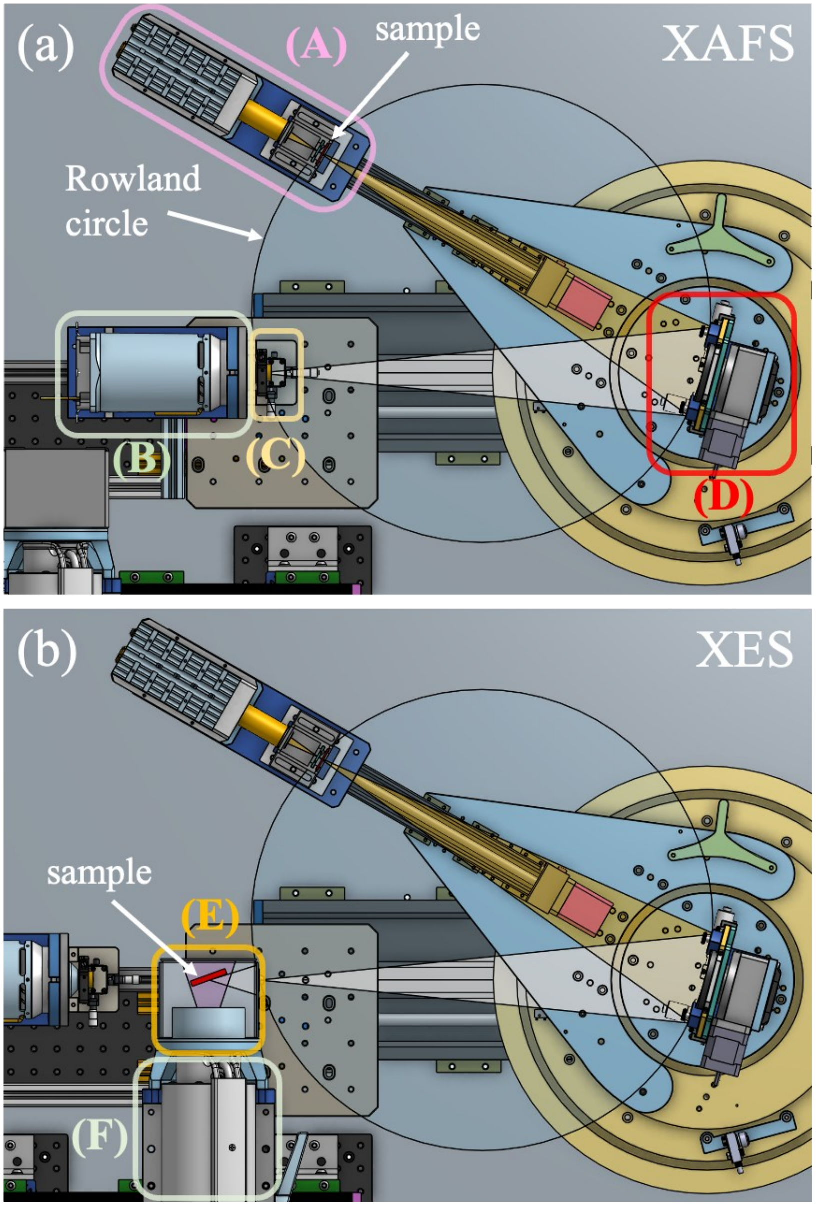

Figure 3: Top-view CAD renderings of the spectrometer configured for **(a)** XAFS and **(b)** XES measurements. The key components are outlined with boxes and labelled as follows: (A) detector, (B) 100 W XAFS source, (C) Adjustable-width XAFS entrance slit, (D) crystal analyzer and optic tower, (E) XES sample enclosure and entrance slit, and (F) 3 kW XES source.

For automated asymmetric operation, an additional motorized degree of freedom we refer to as the ‘clock angle’ or φ is required in the optic subassembly. This additional degree of freedom also enables motorized tilt-free correction of crystal miscut.[42] CAD renderings of the optic cartridge, the full optic tower assembly, and the φ rotation stage and direction are shown in the three panels of Fig. 4. The cartridge mounts concentrically on a small, motorized rotation stage (Velmex B5990TS). The fine adjustment *x*-*y* stage at the base of the optic tower aligned the optic on the rotation axis of the goniometer during spectrometer commissioning.

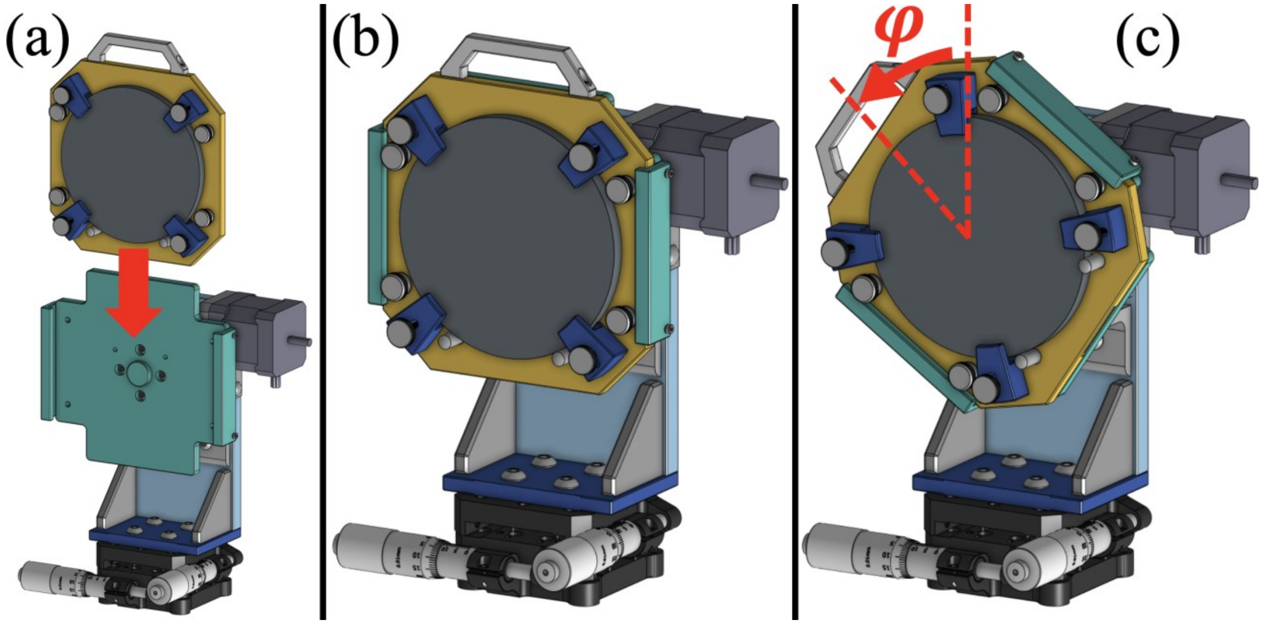

Figure 4: **(a)** An optic cartridge is loaded into the optic tower subassembly. **(b)** The fully assembled motorized optic tower which concentrically indexes the crystal on a motorized rotation stage. **(c)** The motorized azimuthal (φ) degree of freedom allows for tilt-free correction of crystal miscut and for automated asymmetric operation.

Recalling from the introduction the requirements for asymmetric Rowland configurations, the spectrometer achieves these geometries by using independent rotation and linear stages. Representative symmetric and asymmetric configurations are shown in CAD renderings in Fig.

5. Specifically, Fig. 5(a) shows a typical symmetric operation at an unfavorable θ_B far from backscatter, whereas Fig. 5(b) shows an asymmetric configuration at the same θ_B but satisfying the condition of $\theta_B + \alpha = 90$ deg, the configuration that is expected to eliminate Johann error, recall Fig. 2. It is important to note Fig. 5(a) and (b) could be at radically different energies because of the different d-spacings for $\mathbf{G}_0$ and $\mathbf{G}_{hkl}$. The purpose of the Figure is to demonstrate the difference in geometries in these different diffracting conditions. Note that the chord lengths between source-and-analyzer and analyzer-and-detector become unequal when $\alpha \neq 0$.

The spectrometer control software consists of two main components. First, a library of routines was written in Python (Jupyter) to generate ASCII files with component-by-component instructions for each step in any desired spectrometer scan. Second, LabView software was written to interpret the scan definition files and execute the desired measurements by commanding the motors and reading the detector. The LabView software can define measurement projects that perform sequences of measurements each parametrized by a different scan definition file including for successive scans using different $\mathbf{G}_{hkl}$. For both XAFS and XES, the energy is scanned by stepping the crystal angle $\theta_M$and satisfying the Rowland circle geometry at a particular Bragg angle by driving the ρ, detector, and 2θ stages.

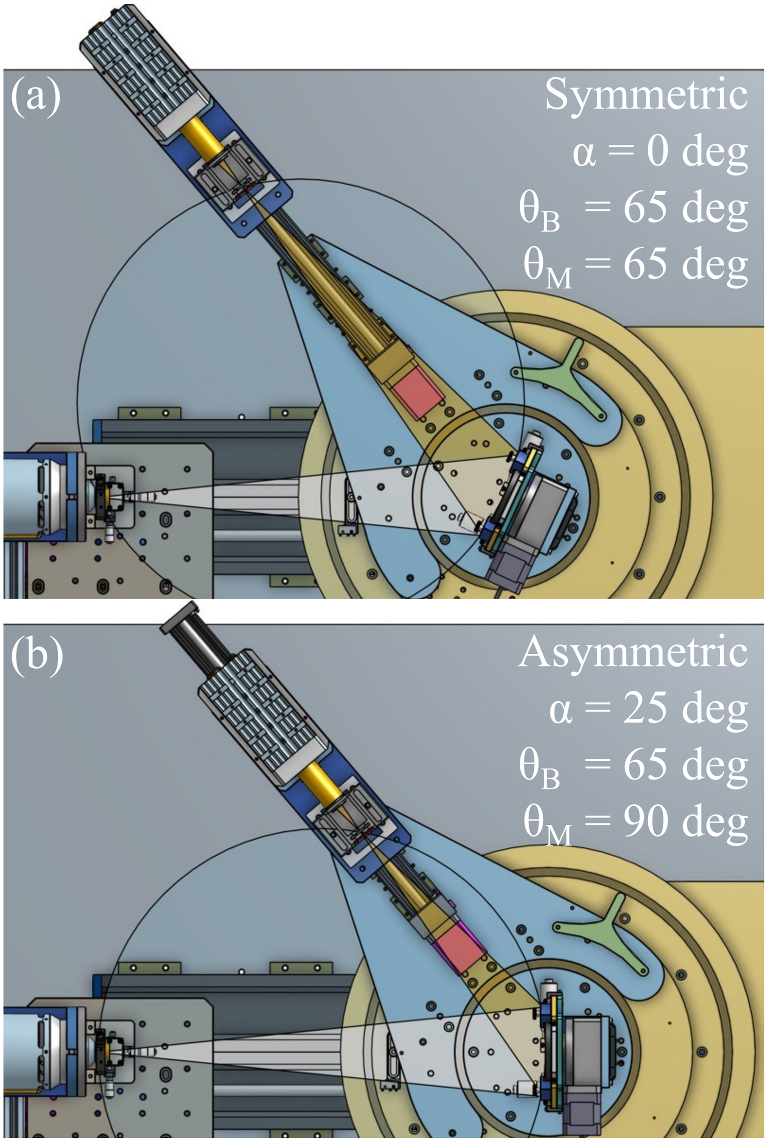

Figure 5: **(a)** Symmetric spectrometer operation at θ_B = 65 deg in XAFS mode. **(b)** Asymmetric spectrometer operation at the same θ_B with α = 25 deg, placing the source diametrically from the optic resulting in a monochromatic diffracted beam with no Johann broadening.

3. Methods

Ray tracing simulations are generated using the xrt Python package[43]. The ray tracing calculations use a 250-μm by 250-μm area source and a 100-mm diameter, 0.5-m SBCA in both symmetric and asymmetric Rowland circle configurations, thus approximating the experimental conditions. Calculations for the location of asymmetric reflections and their resulting energy ranges were performed in home-written software in Python (Jupyter).

XES and XAFS measurements were taken with the laboratory-based instrument described in Section II using only a 100 W source in both configurations. Studies were selected to demonstrate instrument capabilities to characterize the advantages of asymmetric operation. For XAFS, standard metal reference foils of Cu and Ni (EXAFS Materials) were used. To demonstrate the extended energy range afforded by asymmetric operation, a multi-component transition metal oxide sample was prepared for XES. Equal masses of V_2O_3, MnO, FeO, NiO, CuO, ZnO, and $SrTiO_3$ were dry milled together to homogeneously mix the sample. The multi-component powder was enclosed in a polyimide pouch for XES study.

XRS and HERFD-XANES measurements were performed at sector 25-ID of the Advanced Photon Source. This used a Si(111) double crystal monochromator and a set of Kirkpatrick-Baez mirrors to achieve an approximately 100 μm by 100 μm spot size on the sample. The monochromator was not detuned, and the resulting expected energy resolution is 1.2 - 1.3 eV at 8700 eV. An Eiger S 500K camera (Dectris Corp.) was used to measure the x-rays analyzed by the SBCA (XRS Tech) and an SDD (Hitachi, Vortex) was used to measure total fluorescence yield in the HERFD study. The HERFD sample was a ZnO film with embedded Ge nanocrystals, prepared by sequential sputtering of ZnO and Ge targets under reactive ZnO growth conditions[44]. The XRS sample was an 0.9-mm diameter cylinder of randomly oriented graphite in a low-Z binder (mechanical pencil lead). For both studies the incident flux was ~$3\text{x}10^{12}$ ph/sec.

4. Results and Discussion

4.1 The Asymmetric Rowland Geometry in the Laboratory

We begin by illustrating a central motivation of asymmetric operation, i.e., the large number of crystal planes that are available and the consequently wide energy range that can be accessed with fine energy resolution for a single SBCA. See Fig. 6. In panel (a) we show the calculated locations for a large number of asymmetric reflections for a Si(551) analyzer in terms of the asymmetry angle α (radial direction in the polar plot) and the clock angle φ (azimuthal direction in the polar plot). Note that the $\mathbf{G}_0$=(551) reflection itself is at the center of the polar plot. In panel (b) we show an experimental survey of the (α, φ) space at θ_B= 82 deg and find excellent agreement with the calculations of panel (a). In addition, as shown by the color scale indicating the dominant energy detected at a given location, we observe that a very large energy range can likely be patched together by *hkl*-hopping between different asymmetric configurations. This type of study is readily performed in the laboratory because of the very broad bremsstrahlung spectrum of x-ray tubes. Panels (c) and (d) show analogous calculations and experimental results for a Si(221) analyzer. Miller indices in panels (b) and (d) were identified by consistency between the theoretical (α, φ) polar plot with all allowed reflections and the results of converting the observed energy of an experimental reflection to the sum of squared indices by Bragg's law.

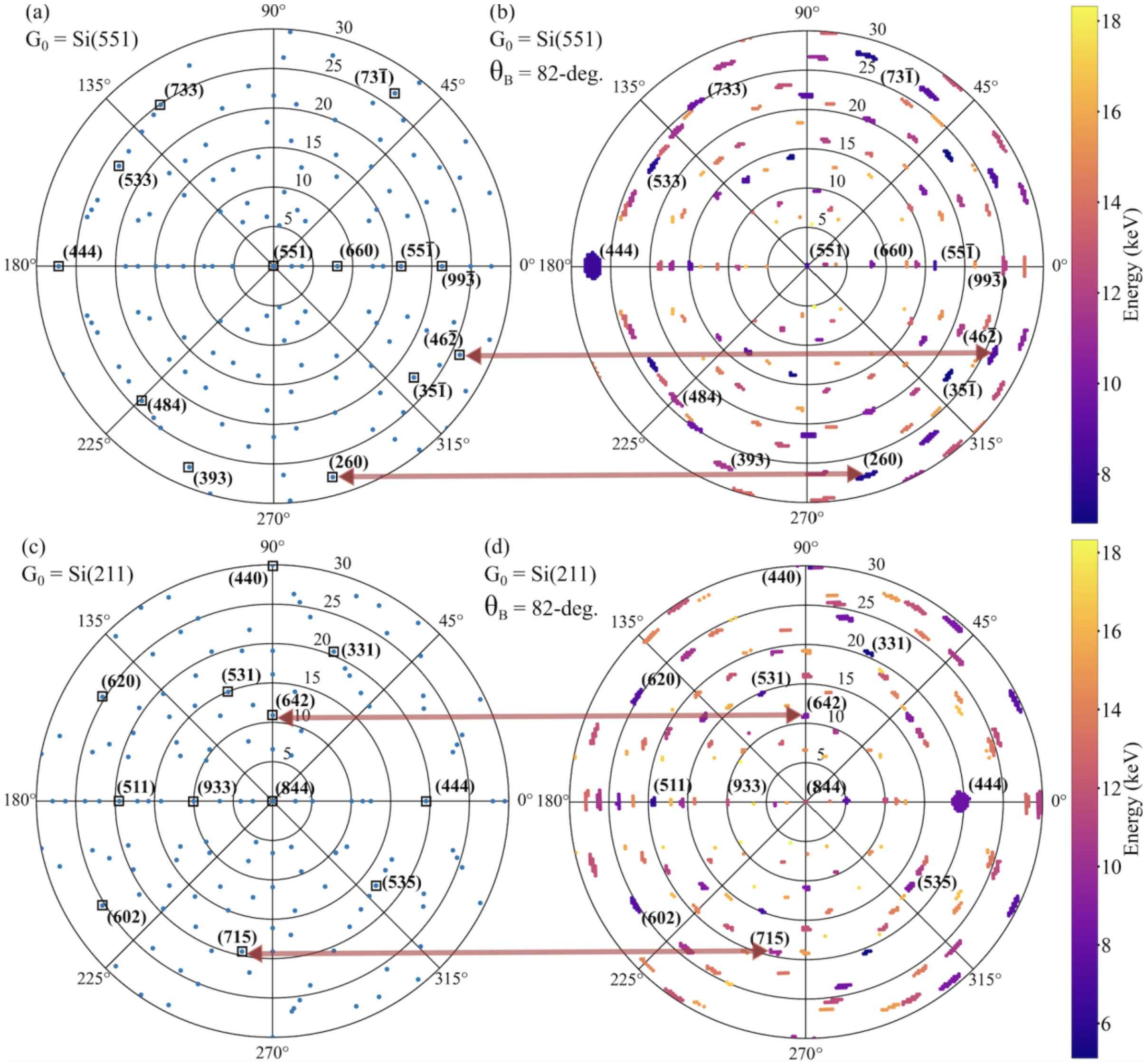

Figure 6: Polar plots in (α, ϕ) for calculated and measured reflections. (a) Calculated values of selected asymmetric reflections of a Si(551) analyzer. (b) Experimental data for Si(551) SBCA obtained by sampling phi-alpha space values at a fixed Bragg angle. (c) Calculated values of asymmetric Si(211) reflections. (d) Experimental data for Si(211) SBCAs. A threshold on reflection intensity was implemented to remove background in experimental data.

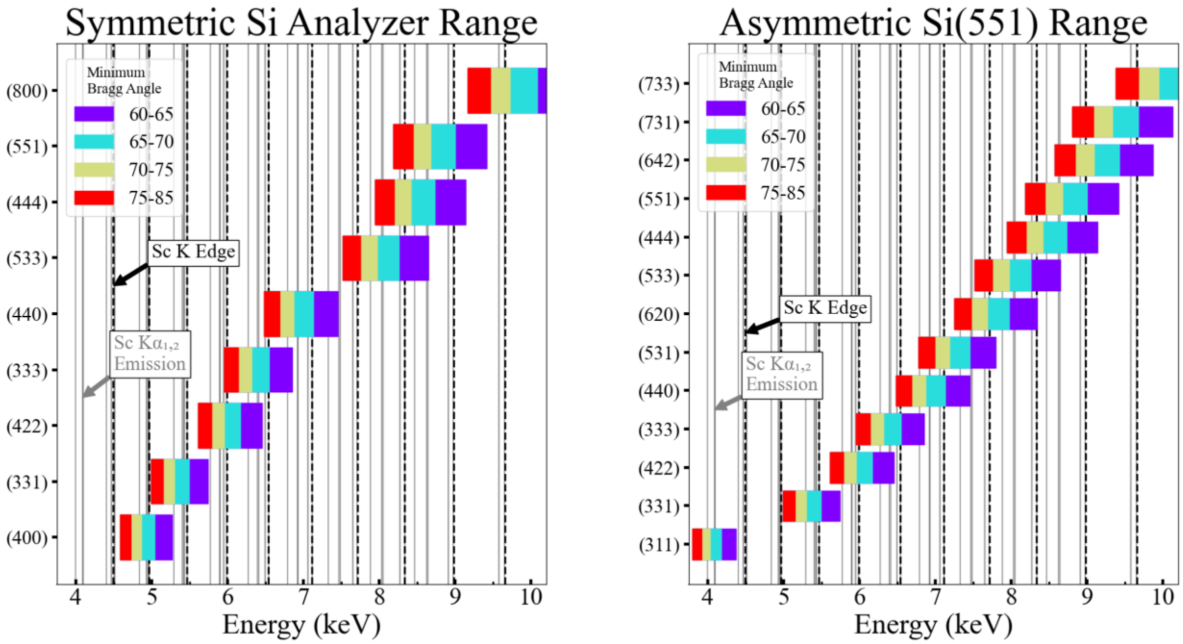

Figure 7: (Left) Diagram of the energy range achievable operating symmetrically with the Si SBCAs commonly used for transition metal XAS and XES: $\mathbf{G}_0$ = (100), (110), (111), (211), (331), (533), (551). The vertical gray lines indicate emission lines and the vertical black dashed lines indicate K-edges between 4 and 10 keV. (Right) Diagram of the energy range achievable operating asymmetrically with a Si(551) SBCA. Duplicate reflections, those that cover the exact same energy range at the same Bragg angle are omitted for clarity.

In both Fig. 6 (b) and (d) an azimuthal smearing is seen in the experimental results at large values of α near the borders of the pole plots. When at large asymmetries the chord length *d* from the SBCA to the detector becomes much smaller than the vertical radius of curvature of the analyzer, resulting in a significant vertical (perpendicular to the Rowland plane) extension and enlargement of the sagittal defocusing of the analyzed x-rays. The loss of intensity that occurs when the analyzed beam height is larger than the active diameter of the spectrometer's SDD is a confounding factor that leads to a trade-off between analyzed flux and the experimental convenience of asymmetric operation.

In Fig. 7 we compare the energy ranges of a conventional suite of SBCA operating symmetrically and the accessible diffraction planes of a single SBCA operated asymmetrically. This is investigated for the energy range of absorption edges and emission lines of the 3*d* transition metals. A comprehensive energy range is possible with a single analyzer operating asymmetrically and a suitable reflection is nearly always available that is close to the special condition (with the source moderately close to the analyzer spherical center) for a given emission or absorption edge. Hence, both a large energy range and high energy resolution should be expected with the Si(551) analyzer studied in the right panel of Fig. 7. We emphasize that there are complicated trade-offs between energy range coverage and analyzed flux (due to the vertical extent of the analyzed beam, described above), and we do not claim that Si(551) is necessarily optimal, although it does illustrate a favorable case for the argument being made here.

We next access a series of planes of the Si(551) SBCA on the amalgam XES, see Fig. 8. We measure Kα, Kβ, and valence-to-core (VTC) emission *en masse* with a single analyzer, demonstrating an expanded energy range through *hkl* hopping. The optimal reflections for the study are given in the left-hand side of Table 1; the experimental reflections used modestly differ in some cases. Fifteen emission lines spanning ~5 keV to ~14 keV were collected across seven elemental species using nine unique diffraction planes from the Si(551) analyzer. By comparison, under symmetric operation at useful Bragg angles the Si(551) crystal has an energy range of only ~8.2 – 9.3 keV and the same emission measurements would require a considerable number of separate Si optics, even if somewhat inferior Bragg angles were employed.

Table 1. Optimal asymmetric reflections for $\mathbf{G}_0$ = Si(551) and best symmetric counterparts for 3*d* transition metal XES, where both Si and Ge analyzers are considered for the symmetric case. For each emission line, the configuration expected to have the least Johann error is given in bold.

Emission	Energy (eV)	$\mathbf{G}_{hkl}$	θ_B (deg.)	α (deg.)	θ_M (deg.)	Best Si Symmetric Analyzer	θ_B (deg.)	Best Ge Symmetric Analyzer	θ_B (deg.)
V Kβ	5428	$(33\bar{1})$	66.47	21.31	**87.78**	(331)	66.47	(422)	81.49
Mn Kα	5900	(422)	71.44	23.84	**95.28**	(422)	71.44	(511) or (333)	74.81
Mn Kβ	6492	(333)	66.04	27.21	93.25	(440)	84.06	(531)	**86.94**
Fe Kα	6405	(333)	67.85	27.21	**95.06**	(511) or (333)	67.85	(440)	75.42
Fe Kβ	7059	(531)	73.11	13.97	**87.08**	(531)	73.11	(620)	79.04
Ni Kα	7480	(620)	74.87	27.67	**102.54**	(620)	74.87	(533)	73.87
Ni Kβ	8267	$(55\bar{1})$	80.49	16.1	**96.59**	(551) or (711)	80.49	(642)	82.7
Cu Kα	8046	(444)	79.45	27.21	106.66	(444)	**79.45**	(551) or (711)	76.55
Cu Kβ	8904	(731)	80.03	21.61	101.64	(731) or (553)	**80.03**	(800)	79.91
Zn Kα	8637	(642)	81.57	13.34	**94.91**	(642)	81.57	(553) or (731)	77.04
Zn Kβ	9570	(733)	77.56	24.95	102.51	(733)	77.56	(555) or (751)	**82.57**
Sr Kα	14,161	(884)	75.35	11.42	**86.77**	(777) or (11 5 1)	77.77	(991)	81.09
Sr Kβ	15,825	(12 6 2)	78.13	18.25	**96.38**	(13 3 3) or (995)	80.53	(13 5 3) or (11 9 1)	80.6

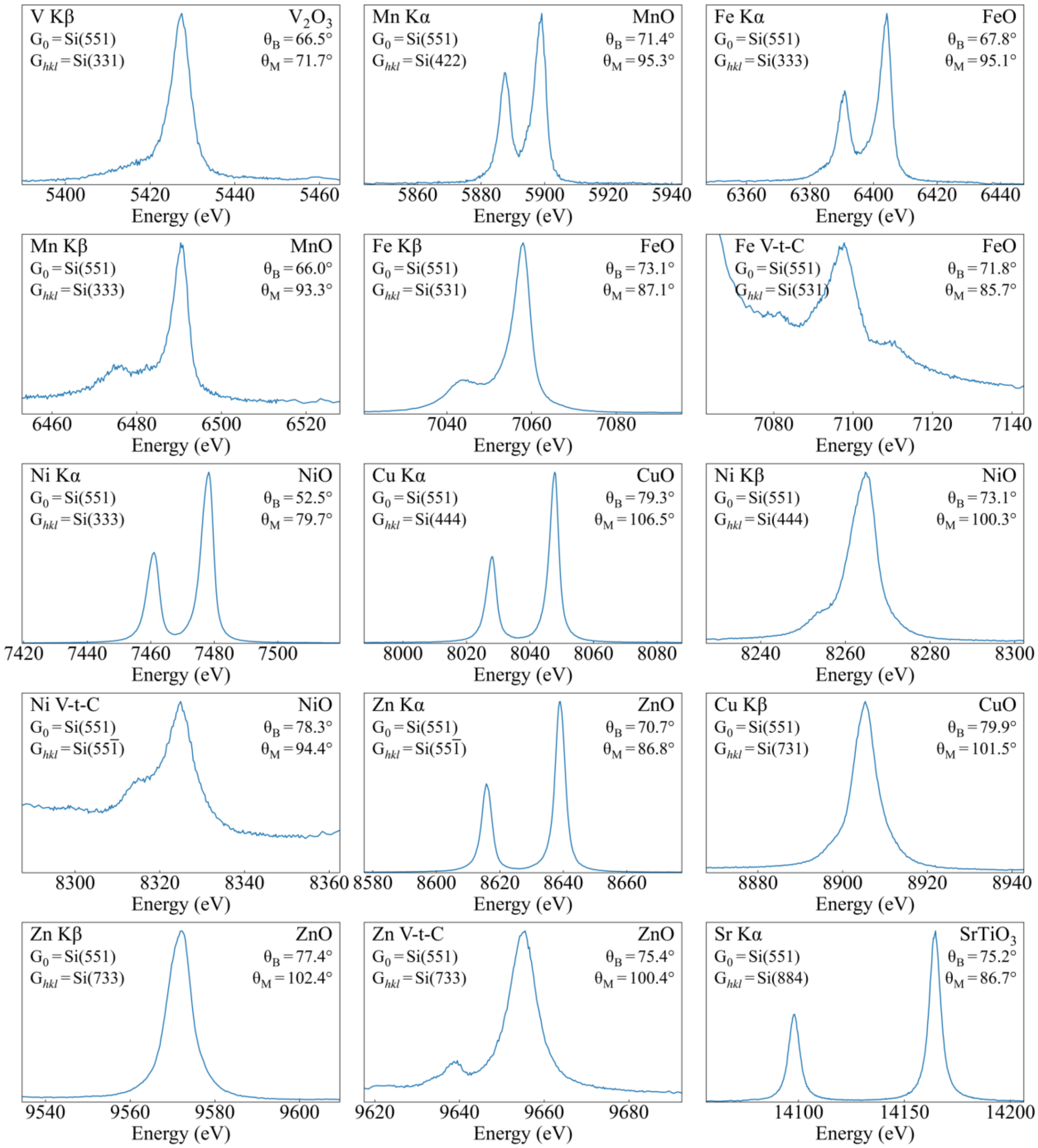

Figure 8: Emission lines measured asymmetrically with a Si(551) analyzer, arranged in order of ascending energy, presented with no background subtraction. The Bragg angle required to select the nominal energy of the emission line is given for each scan.

Having established the comprehensive advantage of a greatly increased energy range, we now address the proposed second benefit of asymmetric operation: an enhanced energy resolution compared to symmetric cases through elimination of Johann error when $\theta_B + \alpha = \theta_M \sim 90$ deg. Ray tracing simulations in Fig. 9 show the reduction of Johann error when

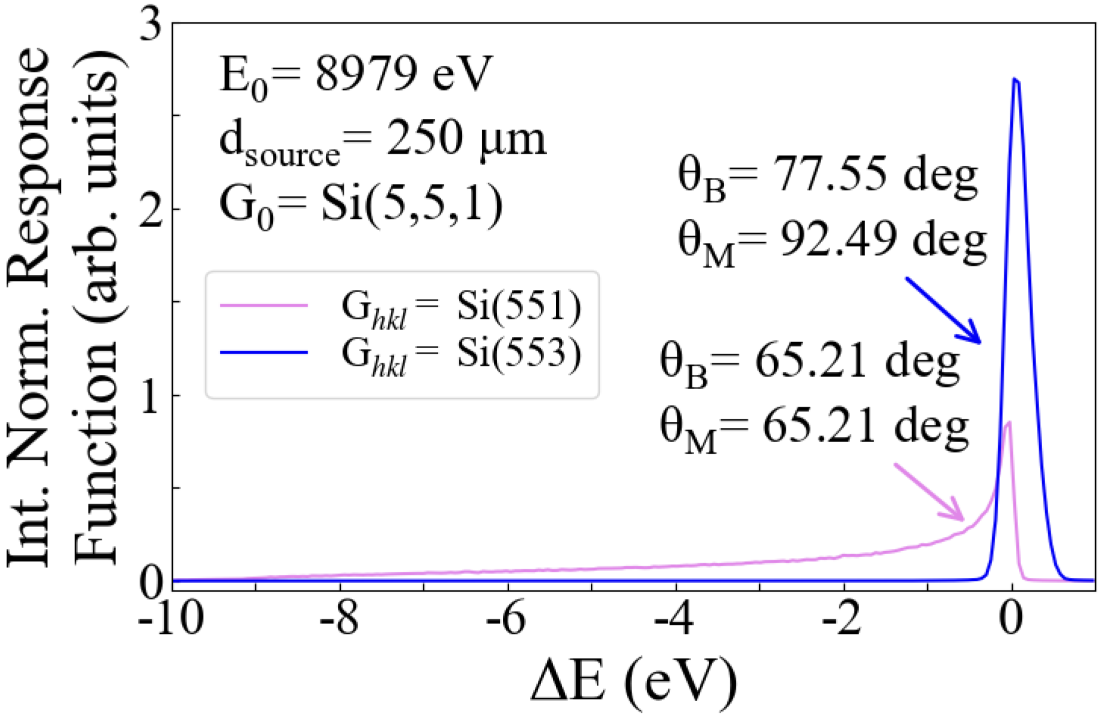

Figure 10: Symmetric and asymmetric energy response functions corresponding to Fig.9 (a) and (b), demonstrating the reduction of Johann error.

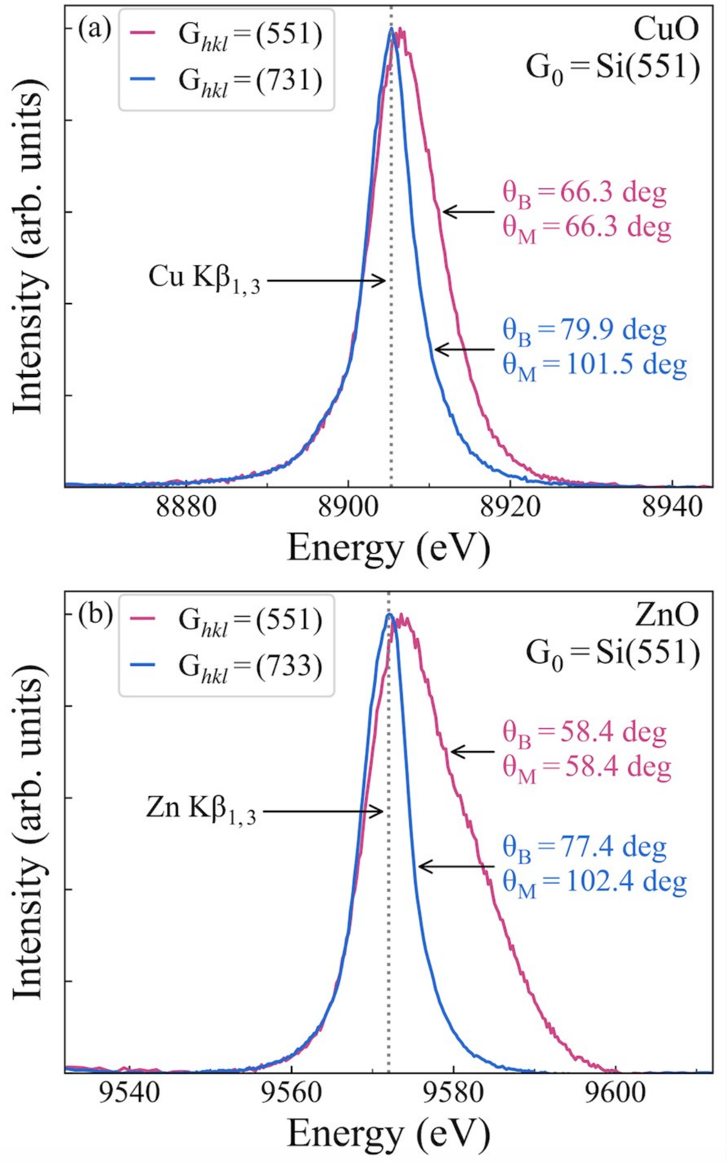

Figure 11: K$\beta_{1,3}$ emission spectra of (a) Cu and (b) Zn. Spectra were collected using the Si(551) SBCA symmetrically and with the most optimal asymmetric plane. Further from backscatter, the symmetric reflection analyzer response function broadens due to Johann error. On the other hand, the asymmetric reflection response function is narrow because of a mechanical analyzer angle, θ_M, close to 90 deg.

approaching this special condition. Fig. 9 (a) shows an equatorial full-range broadening of ~9 eV at the analyzer edge of an SBCA at $\theta_B = 65$ deg. Fig. 9 (b), at the same photon energy,

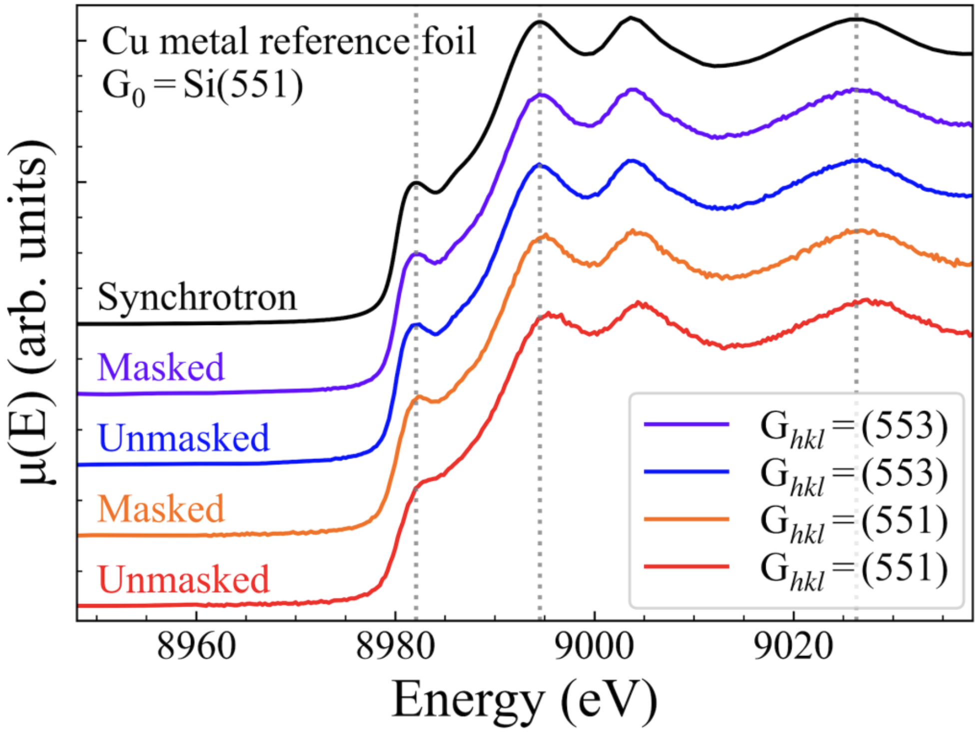

Figure 12: Cu K XANES measured using a Si(551) analyzer symmetrically and $\mathbf{G}_{hkl} = (553)$ reflection asymmetrically, compared to synchrotron results. At 8978.9 eV, $\theta_B = \theta_M = 65.2$ deg symmetrically whereas $\theta_B = 77.5$ and $\theta_M = 92.5$ deg. The asymmetric configuration eliminates Johann error by operating mechanically at near backscatter. Masking the edges of the analyzer removes Johann broadening in the symmetric case, whereas masking in the asymmetric case shows no appreciable difference in energy resolution. Spectra are offset for clarity of presentation.

shows less than 10% as much broadening (with an opposite sign) for $\theta_B = 77.5$ deg and $\alpha = 14.9$ deg.

The ray tracing results show the availability of an asymmetric plane at the same energy as its conventional symmetric counterpart but with improved energy resolution via reduction of

Johann broadening. This is further illustrated in Fig. 10, which shows the energy response functions corresponding to cases (a) and (b) of Fig. 9. The general consideration that Johann error is smallest when the source is near to the SBCA sphere center is also investigated in Table 1, where the most favorable cases with respect to this condition are shown in bold for each emission line. The asymmetric option from even the single favorable case of a Si(551) analyzer are always quite close to the best choices among Si or Ge analyzers used symmetrically and is generally better by this metric.

To show this Johann error reduction in practice, Cu and Zn Kβ XES on the amalgam sample were measured using both (somewhat unfavorable) symmetric and (rather favorable) asymmetric configurations. Fig. 11(a) and (b) shows significant difference in the width and symmetry of the characteristic emission. The symmetric spectrum is broadened with a tail primarily because of Johann error, as well as some contribution from source size broadening. Asymmetric reflections with θ_M near backscatter have improved energy resolution through elimination of Johann error. The effect is more evident in Fig. 11(b) as the symmetric Zn measurement is far from backscatter at $\theta_B = 58$ deg, so broadening is more pronounced. The standard deviation of the energy response function calculated via ray tracing in the asymmetric

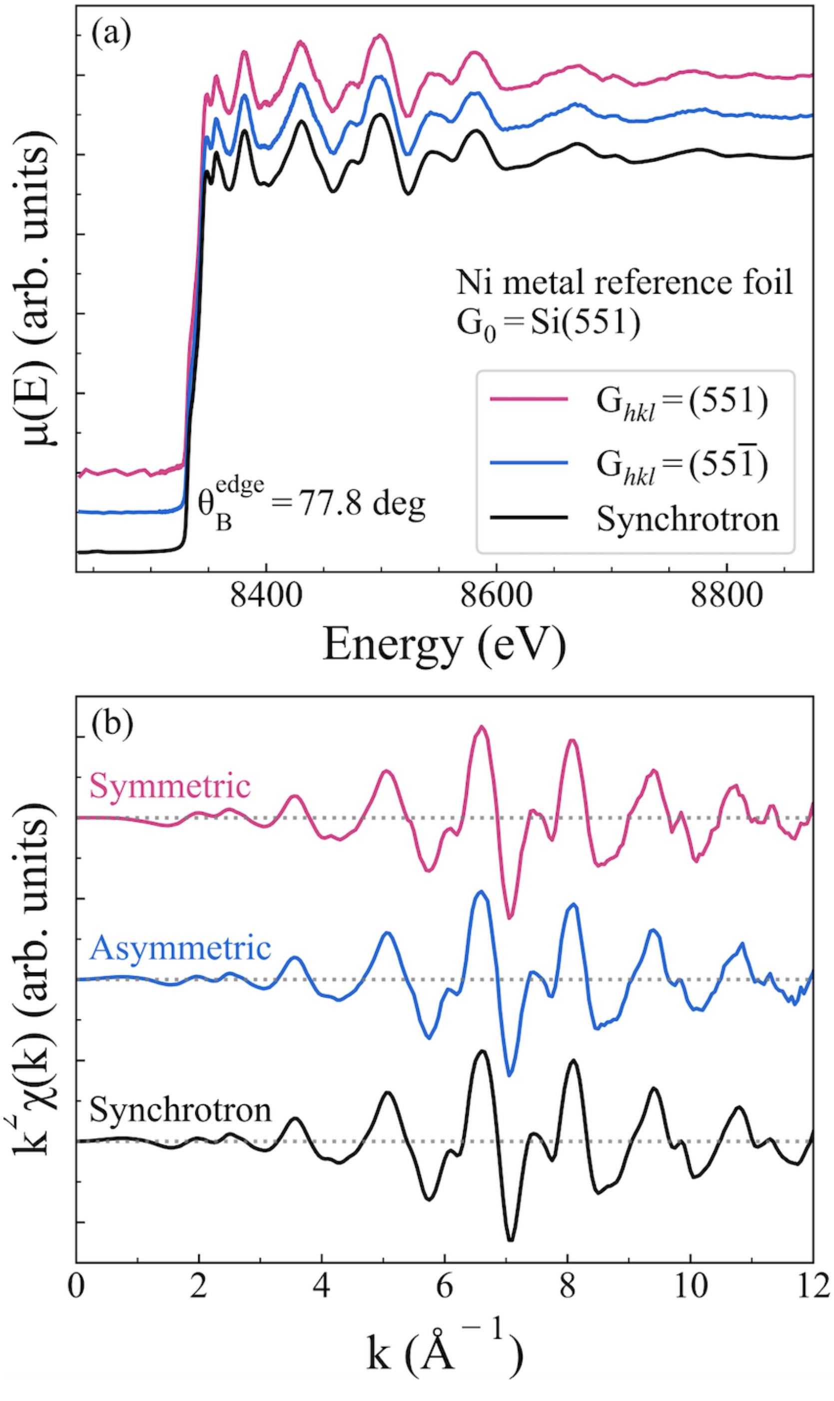

Figure 13: Ni K XAFS measured using a Si(551) analyzer symmetrically and with the $\mathbf{G}_{hkl} = (55\bar{1})$ reflection asymmetrically, compared to synchrotron results. Both spectra show agreement with synchrotron data. Spectra are offset for clarity of presentation.

case of the Zn measurement was 0.6 eV, compared to 4.6 eV in the symmetric case. The broadening in the asymmetric case is largely from source size effects.

To further investigate energy resolution effects, we performed transmission mode XANES and EXAFS studies on metal reference foils in symmetric and asymmetric SBCA configurations. Fig. 12 shows Cu XANES, selected for the well-known shoulder feature in its rising edge, measured symmetrically and asymmetrically with and without analyzer masking and compared to synchrotron data. Johann error both broadens and shifts the spectra, as shown in the unmasked symmetric case having $\theta_B = \theta_M = 65.2$ deg at the absorption edge, and analyzer masking improves the energy resolution of the symmetric data. However, the asymmetric spectra are unaffected by analyzer masking as Johann error is eliminated in the optical configuration with $\theta_B = 77.5$ and $\theta_M = 92.5$ deg, and the asymmetric spectra shows superb energy resolution with no loss of information compared to the synchrotron reference data.

Next, the Ni K-edge EXAFS was measured symmetrically and asymmetrically using the Si(551) analyzer and reflections $\mathbf{G}_0 = (551)$ and $\mathbf{G}_{hkl} = (55\bar{1})$ and compared to synchrotron data. The raw EXAFS and $\chi(k)$ are shown in Fig. 13 (a) and (b). There is again no loss in information between synchrotron and laboratory XAFS. The symmetric and asymmetric results are identical here because the Johann broadening in the symmetric case has little effect for spectrally broad features over the large energy range studied.

4.2 Synchrotron Measurements

Having demonstrated some benefits of asymmetric Rowland geometry in laboratory x-ray spectroscopy, we extend the discussion to synchrotron x-ray measurements. Fig. 14 shows the asymmetric Rowland geometry of the monochromator for a HERFD-XANES measurement, tuned to the Zn Kα_1 emission energy for a study of a ZnO thin film. Note that while Si(642) is the preferred symmetric analyzer, it is an uncommon SBCA and in our case did not exist at any of the several beamlines performing XES or HERFD at our synchrotron, whereas the Si(211) is relatively common for its (422) reflection to study XES for vanadium. Fig. 15 shows the HERFD-XANES collected using the asymmetric $\mathbf{G}_{hkl}$ = (642) reflection of a Si(211) SBCA compared to total fluorescence yield (TFY) results, and shows significant suppression of the Zn

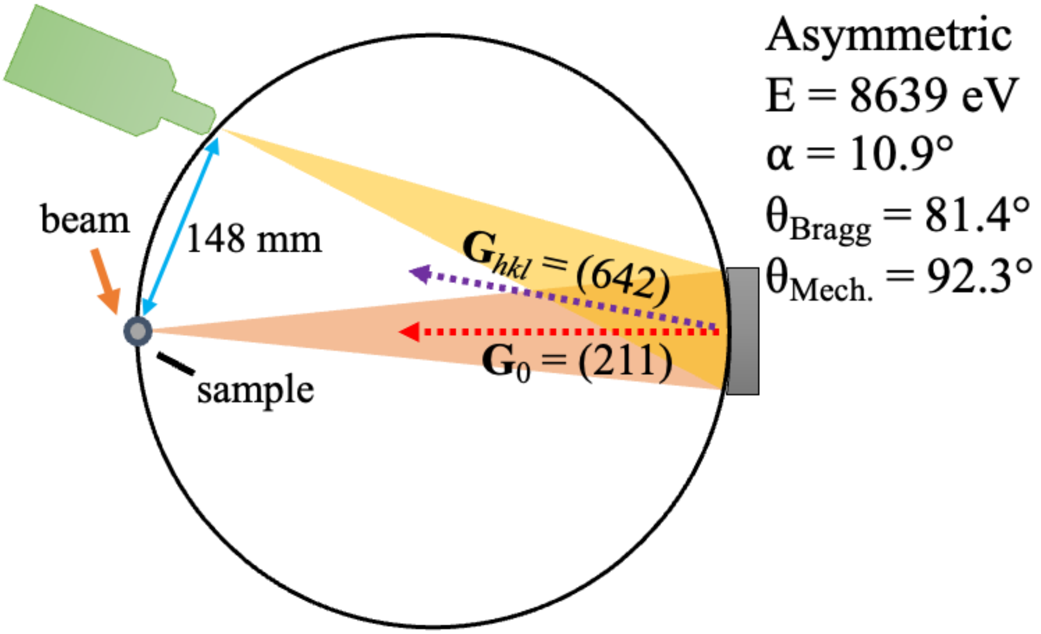

Figure 14: The asymmetric configuration implemented for HERFD-XANES measurements. Note the longer source-detector chord length (blue arrows), allowing greater flexibility in special sample environments and less size constraints than a symmetric counterpart.

K-shell lifetime broadening This result supports the use of asymmetric configurations for HERFD and XES at synchrotron light sources. The addition of ‘clock angle’ degrees of freedom to the common designs for multi-SBCA arrays for HERFD[45,46] would therefore allow *hkl*-hopping with increased user convenience, i.e., when a single analyzer is favorable for all user-desired emission lines in a given study, jumping between the different energy ranges would not require changing the SBCA and retuning.

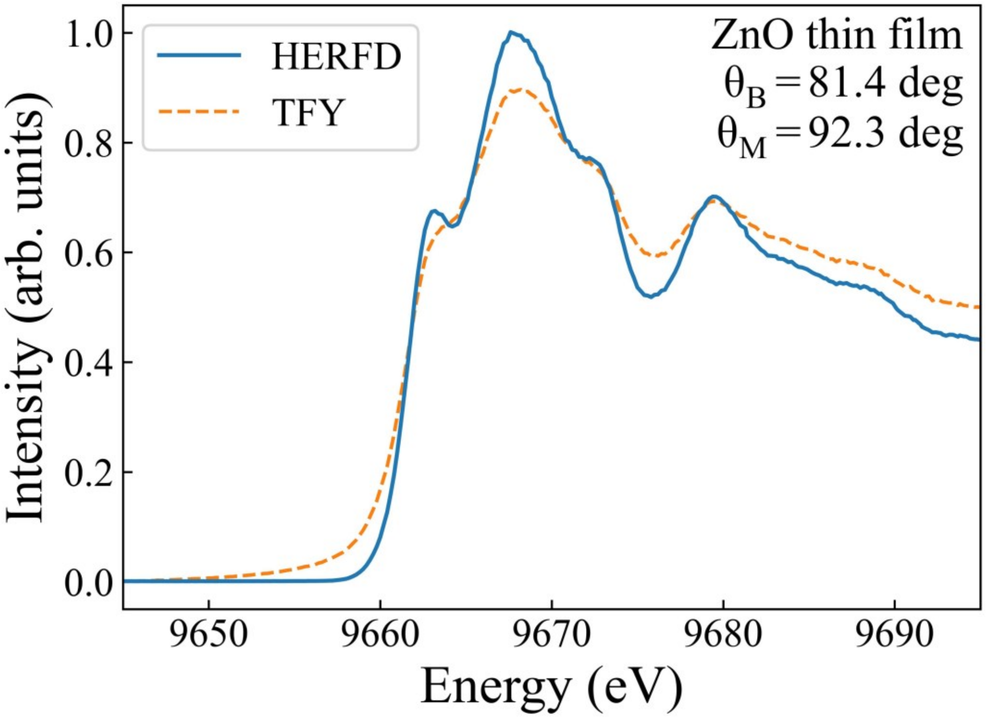

Figure 15: Zn HERFD-XANES measured with $\mathbf{G}_{hkl}$ = (642) of a Si(211) SBCA.

We now move to our last study, a demonstration of XRS with an SBCA in an asymmetric configuration. Here we again used the Si(211) analyzer asymmetrically accessing the $\mathbf{G}_{hkl}$ = (642) reflection, approximately satisfying the condition $\theta_B + \alpha = \theta_M = 90$ deg at 8702.9 eV. The elastic line, measured by scanning the Si(111) double crystal monochromator, is shown in Fig. 16. The shape and (near) symmetry of the elastic peak illustrates a favorable energy response function for the experimental realization. The FWHM is 1.25 eV, which is comparable to the expected resolution of the Si(111) double crystal monochromator without second-crystal detuning, i.e., the analyzer is adding little broadening in this configuration. In addition, the source/sample-detector chord length of ~150 mm is quite large compared to that for synchrotron XRS spectrometers. This is beneficial due to the easier rejection of stray scatter and the larger

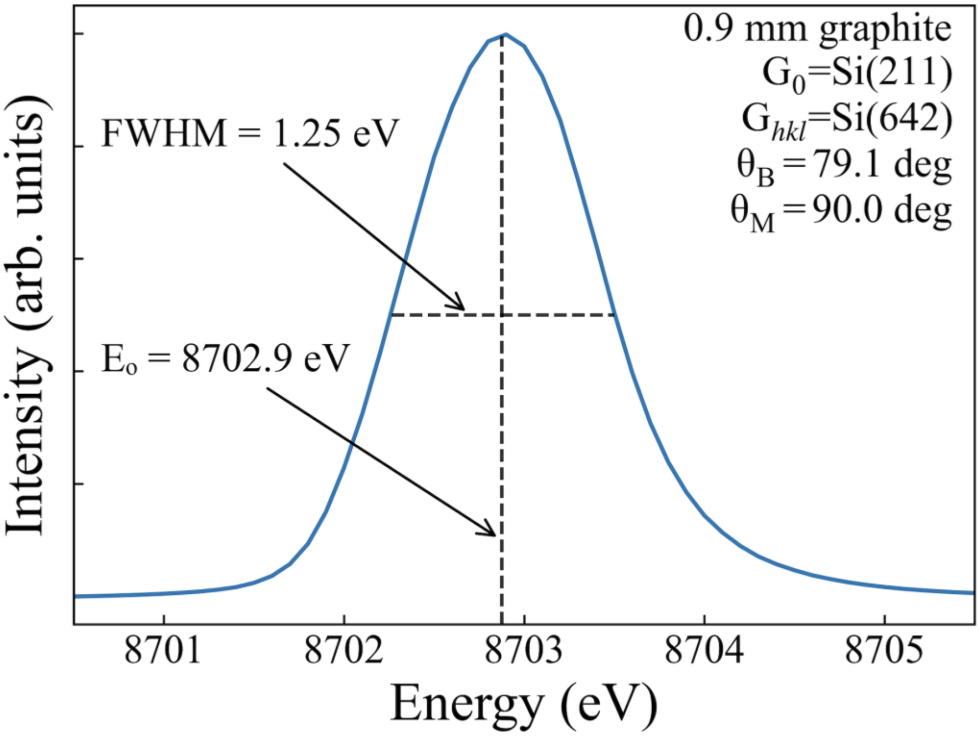

Figure 16: Elastic lines measured using a Si(211) analyzer asymmetrically $\mathbf{G}_{hkl}$ = (642), demonstrating Johann error elimination and narrowing of the analyzer response function when operated asymmetrically.

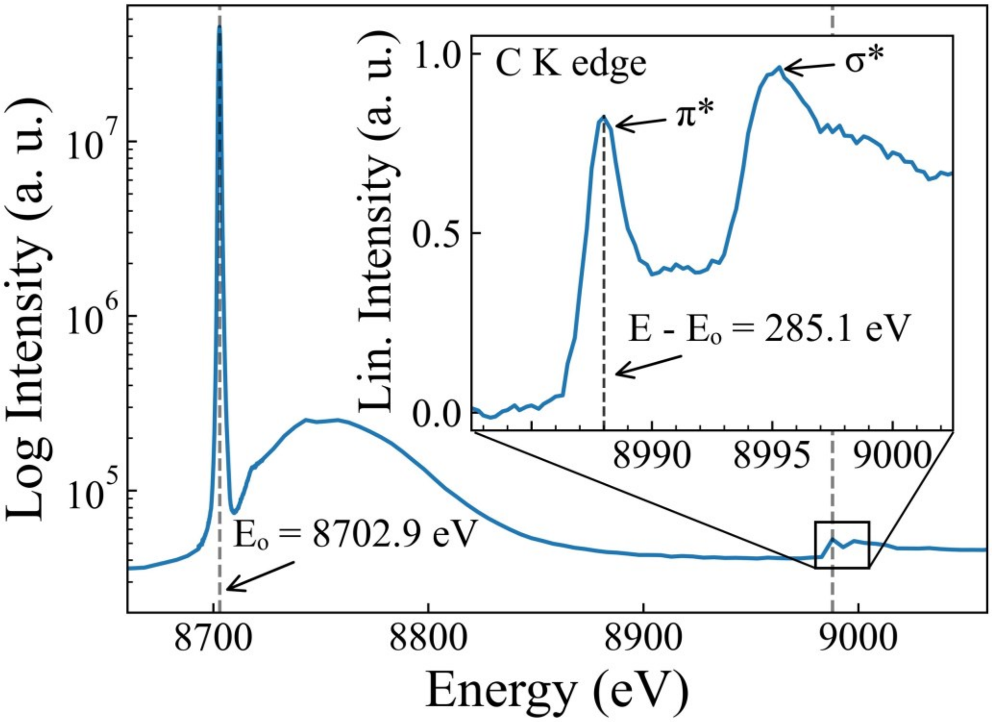

Figure 17: XRS of graphite showing elastic, inelastic, and XRS features of C K-edge. Measured with Si(211) using $\mathbf{G}_{hkl}$ = (642). The analyzer was mechanically at backscatter with a Bragg angle of 79.1 deg. The elastic peak FWHM is approximately 1.3 eV.

clearance for special sample environments. This configuration is best used with a focused beam to avoid source broadening, given the ~81 deg Bragg angle. We note that asymmetric operation of curved analyzers have been used before to accommodate unequal source-analyzer and analyzer-detector chords required by ancillary equipment.[35,47] However, here we make use of asymmetric operation to get high energy resolution and large analyzer solid angle together with good sample-to-detector clearance. Similar resolutions are reported in a prior XRS study using the von Hamos (non-Rowland) configuration[48], but it should be noted that contemporary XRS end stations overwhelmingly use arrays of SBCAs.[12,14,17,18] The resulting wide energy scan of the inelastic x-ray scattering and the C K-edge XRS itself are shown in Fig. 17, main panel and inset, respectively. The results indeed agree with the well-known spectrum for graphite. While these results are preliminary, they build on the strength of the prior demonstrations in this paper and strongly suggest the use of 0.5-m radius SBCA in XRS measurement, especially when a study requires focusing and thus makes source broadening irrelevant.

We note one detail missing from our present study: 0.5-m SBCA are typically sliced for strain relief which raises the question of whether the XRS imaging modality that is now is common use[49,50] may exhibit some degradation. This is an important topic for further study.

5. Conclusions

We investigate the merits of asymmetric Rowland geometries of spherically bent crystal analyzers (SBCAs) for laboratory based XAFS and XES as well as for synchrotron studies of high energy resolution fluorescence detection (HERFD) and x-ray Raman scattering (XRS). Several benefits of asymmetric operation are demonstrated. First, a single SBCA employed asymmetrically can use *hkl* hopping to access a large range of crystal planes and corresponding *d*-spacings, greatly extending the useful energy range with fine energy resolution compared to conventional symmetric operation. Second, by satisfying the condition that the source be at least relatively near to the SBCA sphere center, asymmetric Rowland geometries can mitigate or eliminate Johann error. Third, asymmetric Rowland geometries can significantly increase the clearance between sample and detector when the nominally perfect sphere-center geometry can be used. The combination of suppressed Johann error, larger solid angle (by use of the 0.5-m SBCA enabled by the elimination of Johann error), and large source-detector distance makes asymmetric operation an especially appealing paradigm for the design of future XRS endstations.

Acknowledgements

This work is supported by funding from the U.S. Department of Energy in the Nuclear Energy University Program under Contract No. DE-NE0009158. This research used resources of the Advanced Photon Source, a U.S. Department of Energy (DOE) Office of Science user facility operated for the DOE Office of Science by Argonne National Laboratory under Contract No. DE-AC02-06CH11357. We thank each of Mali Balasubramanian and Pieter Glatzel for useful discussions, Shelly Kelly and Chengjun Sun for beamline assistance, and Abdullah Ceylan and Abdul Rumaiz for providing the thin film sample studied by HERFD XAS.

References

1 H. H. Johann, *Z. Für Phys.*, 1931, **69**, 185–206.

2 W. M. Holden, O. R. Hoidn, A. S. Ditter, G. T. Seidler, J. Kas, J. L. Stein, B. M. Cossairt, S. A. Kozimor, J. Guo, Y. Ye, M. A. Marcus and S. Fakra, *Rev. Sci. Instrum.*, 2017, **88**, 073904.

3 G. T. Seidler, D. R. Mortensen, A. J. Remesnik, J. I. Pacold, N. A. Ball, N. Barry, M. Styczinski and O. R. Hoidn, *Rev. Sci. Instrum.*, 2014, **85**, 113906.

4 G. T. Seidler, D. R. Mortensen, A. S. Ditter, N. A. Ball and A. J. Remesnik, *J. Phys. Conf. Ser.*, 2016, **712**, 012015.

5 M. E. Mundy, D. Ung, N. L. Lai, E. P. Jahrman, G. T. Seidler and B. M. Cossairt, *Chem. Mater.*, 2018, **30**, 5373–5379.

6 E. P. Jahrman, W. M. Holden, A. S. Ditter, D. R. Mortensen, G. T. Seidler, T. T. Fister, S. A. Kozimor, L. F. J. Piper, J. Rana, N. C. Hyatt and M. C. Stennett, *Rev. Sci. Instrum.*, 2019, **90**, 024106.

7 D. R. Mortensen, G. T. Seidler, J. J. Kas, N. Govind, C. P. Schwartz, S. Pemmaraju and D. G. Prendergast, *Phys. Rev. B*, 2017, **96**, 125136.

8 D. R. Mortensen, G. T. Seidler, A. S. Ditter and P. Glatzel, *J. Phys. Conf. Ser.*, 2016, **712**, 012036.

9 R. A. Valenza, E. P. Jahrman, J. J. Kas and G. T. Seidler, *Phys. Rev. A*, 2017, **96**, 032504.

10 W. M. Holden, G. T. Seidler and S. Cheah, *J. Phys. Chem. A*, 2018, **122**, 5153–5161.

11 D. Sokaras, D. Nordlund, T.-C. Weng, R. A. Mori, P. Velikov, D. Wenger, A. Garachtchenko, M. George, V. Borzenets, B. Johnson, Q. Qian, T. Rabedeau and U. Bergmann, *Rev. Sci. Instrum.*, 2012, **83**, 043112.

12 M. Moretti Sala, K. Martel, C. Henriquet, A. Al Zein, L. Simonelli, C. Sahle, H. Gonzalez, M.-C. Lagier, C. Ponchut, S. Huotari, R. Verbeni, M. Krisch and G. Monaco, *J. Synchrotron Radiat.*, 2018, **25**, 580–591.

13 S. Huotari, C. J. Sahle, C. Henriquet, A. Al-Zein, K. Martel, L. Simonelli, R. Verbeni, H. Gonzalez, M.-C. Lagier, C. Ponchut, M. Moretti Sala, M. Krisch and G. Monaco, *J. Synchrotron Radiat.*, 2017, **24**, 521–530.

14 D. Sokaras, T.-C. Weng, D. Nordlund, R. Alonso-Mori, P. Velikov, D. Wenger, A. Garachtchenko, M. George, V. Borzenets, B. Johnson, T. Rabedeau and U. Bergmann, *Rev. Sci. Instrum.*, 2013, **84**, 053102.

15 E. Kleymenov, J. A. van Bokhoven, C. David, P. Glatzel, M. Janousch, R. Alonso-Mori, M. Studer, M. Willimann, A. Bergamaschi, B. Henrich and M. Nachtegaal, *Rev. Sci. Instrum.*, 2011, **82**, 065107.

16 I. Llorens, E. Lahera, W. Delnet, O. Proux, A. Braillard, J.-L. Hazemann, A. Prat, D. Testemale, Q. Dermigny, F. Gelebart, M. Morand, A. Shukla, N. Bardou, O. Ulrich, S. Arnaud, J.-F. Berar, N. Boudet, B. Caillot, P. Chaurand, J. Rose, E. Doelsch, P. Martin and P. L. Solari, *Rev. Sci. Instrum.*, 2012, **83**, 063104.

17 T. T. Fister, G. T. Seidler, L. Wharton, A. R. Battle, T. B. Ellis, J. O. Cross, A. T. Macrander, W. T. Elam, T. A. Tyson and Q. Qian, *Rev. Sci. Instrum.*, 2006, **77**, 063901.

18 R. Verbeni, T. Pylkkänen, S. Huotari, L. Simonelli, G. Vankó, K. Martel, C. Henriquet and G. Monaco, *J. Synchrotron Radiat.*, 2009, **16**, 469–476.

19 J. F. Seely, E. Galtier, L. T. Hudson, A. Henins and U. Feldman, *Appl. Opt.*, 2019, **58**, 5225–5232.

20 A. Bordage, M. Pápai, N. S. Sas, J. Szlachetko, M. Nachtegaal and G. Vankó, *Phys. Chem. Chem. Phys.*, 2013, **15**, 11088–11098.

21 P. Suortti, T. Buslaps, P. Fajardo, V. Honkimäki, M. Kretzschmer, U. Lienert, J. E. McCarthy, M. Renier, A. Shukla, T. Tschentscher and T. Meinander, *J. Synchrotron Radiat.*, 1999, **6**, 69–80.

22 P. Suortti, U. Lienert and C. Schulze, *Nucl. Instrum. Methods Phys. Res. Sect. Accel. Spectrometers Detect. Assoc. Equip.*, 1994, **338**, 27–32.

23 L. Simonelli, C. Marini, L. Ribo, R. Homs, J. Avila, D. Heinis, I. Preda and K. Klementiev, *J. Synchrotron Radiat.*, 2023, **30**, 235–241.

24 P. Suortti and W. Thomlinson, *Nucl. Instrum. Methods Phys. Res. Sect. Accel. Spectrometers Detect. Assoc. Equip.*, 1988, **269**, 639–648.

25 P. Suortti, P. Pattison and W. Weyrich, *J. Appl. Crystallogr.*, 1986, **19**, 336–342.

26 P. Suortti, P. Pattison and W. Weyrich, *J. Appl. Crystallogr.*, 1986, **19**, 343–352.

27 P. Pattison, P. Suortti and W. Weyrich, *J. Appl. Crystallogr.*, 1986, **19**, 353–363.

28 P. Suortti, U. Lienert and C. Schulze, *AIP Conf. Proc.*, 1997, **389**, 175–192.

29 P. Suortti, D. Chapman, J. R. Schneider and T. Tschentscher, *J. Appl. Crystallogr.*, 1992, **25**, 432–438.

30 E. Erola, V. Eteläniemi, P. Suortti, P. Pattison and W. Thomlinson, *J. Appl. Crystallogr.*, 1990, **23**, 35–42.

31 T. Matsushita and U. Kaminaga, *J. Appl. Crystallogr.*, 1980, **13**, 465–471.

32 A. Boeuf, S. Lagomarsino, S. Mazkedian, S. Melone, P. Puliti and F. Rustichelli, *J. Appl. Crystallogr.*, 1978, **11**, 442–449.

33 R. Caciuffo, S. Melone, F. Rustichelli and A. Boeuf, *Phys. Rep.*, 1987, **152**, 1–71.

34 S. G. Podorov, O. Renner, O. Wehrhan and E. Förster, *J. Phys. Appl. Phys.*, 2001, **34**, 2363.

35 R. Bartiromo, F. Bombarda and R. Giannella, *Nucl. Instrum. Methods Phys. Res.*, 1984, **221**, 453–459.

36 M. Moretti Sala, K. Martel, C. Henriquet, A. Al Zein, L. Simonelli, C. Sahle, H. Gonzalez, M.-C. Lagier, C. Ponchut, S. Huotari, R. Verbeni, M. Krisch and G. Monaco, *J. Synchrotron Radiat.*, 2018, **25**, 580–591.

37 D. Sokaras, D. Nordlund, T.-C. Weng, R. A. Mori, P. Velikov, D. Wenger, A. Garachtchenko, M. George, V. Borzenets, B. Johnson, Q. Qian, T. Rabedeau and U. Bergmann, *Rev. Sci. Instrum.*, 2012, **83**, 043112.

38 D. Sokaras, T.-C. Weng, D. Nordlund, R. Alonso-Mori, P. Velikov, D. Wenger, A. Garachtchenko, M. George, V. Borzenets, B. Johnson, T. Rabedeau and U. Bergmann, *Rev. Sci. Instrum.*, 2013, **84**, 053102.

39 Y. M. Xiao, P. Chow, G. Boman, L. G. Bai, E. Rod, A. Bommannavar, C. Kenney-Benson, S. Sinogeikin and G. Y. Shen, *Rev. Sci. Instrum.*, 2015, **86**, 072206.

40 Y. Q. Cai, P. Chow, C. C. Chen, H. Ishii, K. L. Tsang, C. C. Kao, K. S. Liang and C. T. Chen, *AIP Conf. Proc.*, 2004, **705**, 340–343.

41 J. M. Ablett, D. Prieur, D. Céolin, B. Lassalle-Kaiser, B. Lebert, M. Sauvage, T. Moreno, S. Bac, V. Balédent, A. Ovono, M. M, F. Gélebart, A. Shukla and J.-P. Rueff, *J. Synchrotron Radiat.*, 2019, **26**, 263–271.

42 D. R. Mortensen and G. T. Seidler, *J. Electron Spectrosc. Relat. Phenom.*, 2017, **215**, 8–15.
43 K. Klementiev and R. Chernikov, in *Advances in Computational Methods for X-Ray Optics III*, SPIE, 2014, vol. 9209, pp. 60–75.
44 A. Ceylan, A. K. Rumaiz, D. Caliskan, S. Ozcan, E. Ozbay and J. C. Woicik, *J. Appl. Phys.*, 2015, **117**, 105303.
45 N. P. Edwards, J. R. Bargar, D. van Campen, A. van Veelen, D. Sokaras, U. Bergmann and S. M. Webb, *Rev. Sci. Instrum.*, 2022, **93**, 083101.
46 P. Glatzel, A. Harris, P. Marion, M. Sikora, T.-C. Weng, C. Guilloud, S. Lafuerza, M. Rovezzi, B. Detlefs and L. Ducotté, *J. Synchrotron Radiat.*, 2021, **28**, 362–371.
47 P. Jagodziński, D. Banaś, M. Pajek, A. Kubala-Kukuś, Ł. Jabłoński, I. Stabrawa, K. Szary, D. Sobota, A. Warczak, A. Gumberidze, H. F. Beyer, M. Lestinsky, G. Weber, T. Stöhlker and M. Trassinelli, *J. Instrum.*, 2023, **18**, P11002.
48 N. Watanabe, H. Hayashi, Y. Udagawa, K. Takeshita and H. Kawata, *Appl. Phys. Lett.*, 1996, **69**, 1370–1372.
49 C. J. Sahle, A. D. Rosa, M. Rossi, V. Cerantola, G. Spiekermann, S. Petitgirard, J. Jacobs, S. Huotari, M. Moretti Sala and A. Mirone, *J. Synchrotron Radiat.*, 2017, **24**, 269–275.
50 C. J. Sahle, A. Mirone, T. Vincent, A. Kallonen and S. Huotari, *J. Synchrotron Radiat.*, 2017, **24**, 476–481.

Chapter 8 - `hklhop` a Selection Tool for Asymmetric Reflections of Spherically Bent Crystal Analyzers for High Resolution X-ray Spectroscopy

Originally published as: J. Abramson, Y. Chen, G. T. Seidler. *Journal of Analytical Atomic Spectrometry* 2025 Vol. 40 Page 817-824. J. Abramson wrote and conducted the majority of this work.

High resolution, hard x-ray spectroscopy at synchrotron x-ray light sources commonly uses spherically bent crystal analyzers (SBCAs) formed by shaping a single crystal wafer to a spherical backing. These Rowland circle optics are almost always used in 'symmetric' (or nearly symmetric) configurations wherein the reciprocal lattice vector used for energy selectivity via diffraction is coincident with the normal vector to the curved wafer surface. However, Gironda, et al., recently proposed that asymmetric operation of SBCA, wherein the reciprocal lattice vector is no longer normal to the wafer surface, has significant operational benefits and has been an underutilized opportunity. First, those authors find improved energy resolution through decreased Johann error, or equivalently find increased solid angle at a chosen experimental tolerance for energy broadening. Second, they find productive, high-resolution use of a large number of reciprocal lattice vectors from a single SBCA, thus enabling operation over a wide energy range without need to exchange SBCA upon making large changes in desired photon energy. These observations hold the potential to improve

performance, increase flexibility and decrease cost for both laboratory and synchrotron applications. Given these motivations, we report an open-source software package, hklhop, that enables exploration of the complex space of analyzer wafer choice, experimental energy range or ranges, and desired suppression of Johann error. This package can guide both the design and the day-to-day operations of Rowland spectrometers enabled for asymmetric use.

1. Introduction

Johann-style spherically bent crystal analyzers (SBCAs) have seen extensive use at synchrotron facilities for photon-in photon-out spectroscopies[1-8] and in laboratory spectrometers for x-ray absorption fine structure and x-ray emission spectroscopy[2, 9-18]. With rare exceptions at synchrotron facilities[19], and excluding the small adjustments made for wafer miscut in laboratory instruments[20], the SBCAs are operated with the diffracting plane that provides energy resolution nominally coincident with the curved crystal surface. This 'symmetric' configuration has the source and detector at equal angles with respect to the cylindrical axis of the SBCA. However, the Rowland circle equally supports asymmetric operation, a fact previously commented on by several groups, albeit infrequently used[19, 21-23]. In asymmetric operation the diffracting crystal planes are offset by an angle α in the Rowland circle plane (henceforth 'Rowland plane') from the wafer surface, see Fig. 1. Note the need to introduce a distinction between the Bragg angle θ_B, angle between the diffracting crystal plane and incoming x-rays, and the spectrometer or 'mechanical' angle θ_M, angle between the normal crystal plane and incoming x-rays.

Recently, Gironda et. al.[24], reported the development of an SBCA-based Rowland spectrometer that is optimized for investigation of asymmetric operation, having both the necessary mechanical freedom for asymmetric source and detector positions and also a new 'clock angle', or φ, degree of freedom that rotates the SBCA about its cylindrical axis. The importance of such a rotation for bringing a desired reciprocal lattice vector into the Rowland plane was previously noted by Mortensen, et al.[20], as a one-time manual adjustment to adapt to modest wafer miscuts and thus remove the need for two-axis tilt stages for orientation of

SBCAs. Gironda, et al.[24] motorize this degree of freedom enabling precise and repeatable rotations to bring any reciprocal lattice vector into the Rowland plane. For means of illustration, consider the pole plot for Si (211), Fig. 2, with α and φ being the radial and azimuthal directions, respectively.

While symmetric operation of such an analyzer would, allowing for harmonics, enable high resolution study of a few ~1-keV wide energy regions, there would be large gaps that in present symmetric practice would require physical exchange of SBCAs to obtain different *d*-spacings. However, as shown in Fig. 2, there are numerous reciprocal lattice vectors corresponding to different *d*-spacings within a reasonable asymmetric tilt (α) from, for example, the Si (211) diffraction plane. Using the φ degree of freedom the accessible energy range of the Si (211) SBCA is greatly increased.

Gironda, et al., find two general advantages in this extended perspective on the Rowland spectrometer. First, in accordance with prior observations[25-29], but few prior implementations[30-35], they observe suppression of Johann broadening when θ_M is kept relatively near to 90 deg, even at Bragg angles where symmetric operation would require analyzer masking to prevent significantly degraded energy resolution. For example, in Fig. 3 we show both a symmetric and an asymmetric spectrometer configuration with the same SBCA that are tuned to the same energy, 8905 eV for the Cu Kb$_{1,3}$ emission line. However, the anticipated energy resolutions are not the same: symmetric operation will have large broadening from Johann error while asymmetric operation, which is close to the 'Johann normal alignment' (JNA)[36] where θ_M=90 deg, will be largely immune from Johann broadening. Second, Gironda, et al.[24], in fact do find that the many reciprocal lattice vectors available from a single SBCA can often span all, or very nearly all, of the hard x-ray range where SBCAs are used. Hence, the common use of suites of SBCA to cover many different emission lines or absorption edges might be replaced with a much smaller number of SBCA, perhaps even just one, combined with the new φ degree of freedom resulting in cost savings and in simplified operations.

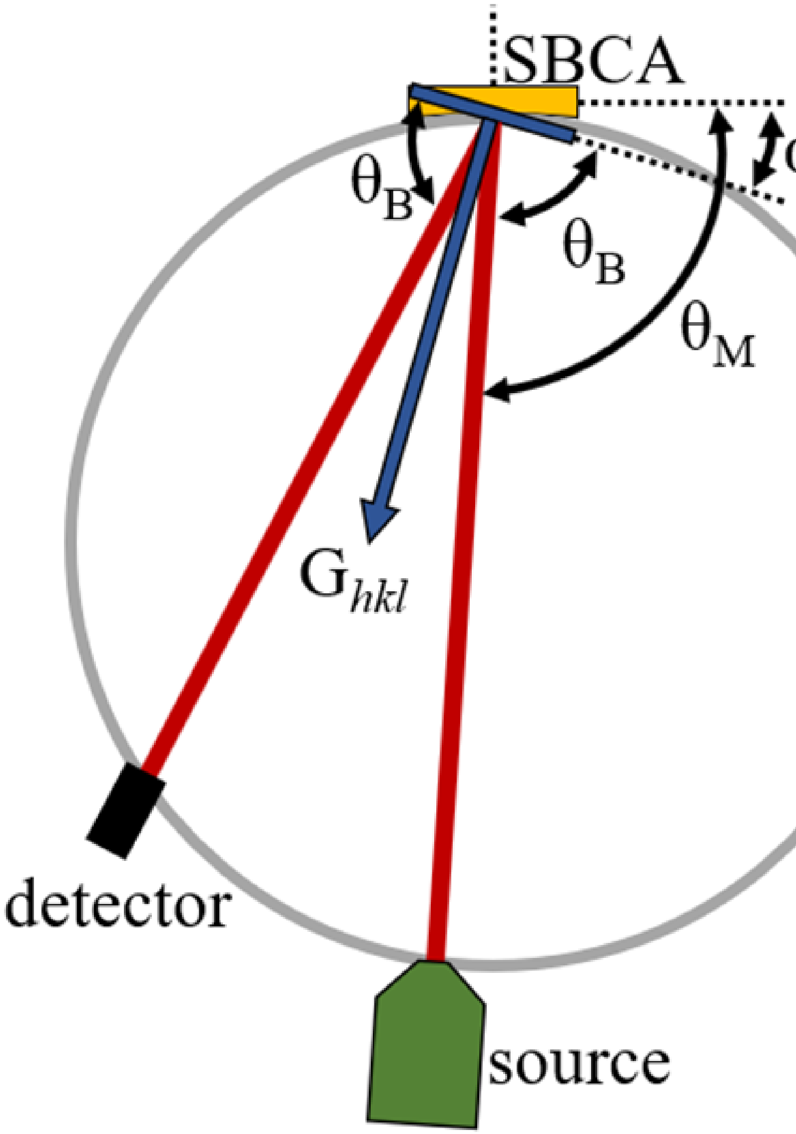

Figure 1 Diagram of asymmetric operation from the reference frame of the SBCA. θ_B is the Bragg angle, α is the angle between the crystal plane normal to the SBCA surface (which reflection the crystal was cut for, G0) and the reflection plane being used for asymmetric operation, Ghkl, and θ_M is the angle between the SBCA surface and the incident X-rays.

The above proposal to centralize asymmetric configurations in future spectrometer design and operations, however, comes with at least two limitations. First, asymmetry degrades the in-plane focus of the analyzed radiation on the detector plane and also disadvantageously increases the sagittal defocusing due to the shorter analyzer-to-detector chord[36], possibly resulting in lost detection efficiency due to finite detector size. This issue and the quantitative benefits in suppressing Johann error are addressed in the recent ray-tracing study of Chen, et al.[36] [36]Second, the considerable freedom of asymmetric operation comes with a need to fully explore the combined space of analyzer wafer selection, spectroscopic reflection selection, energy ranges dictated by experiment design, and energy resolution (meaning suppression of Johann error). We report here an open-source software package, `hklhop`, for this purpose.

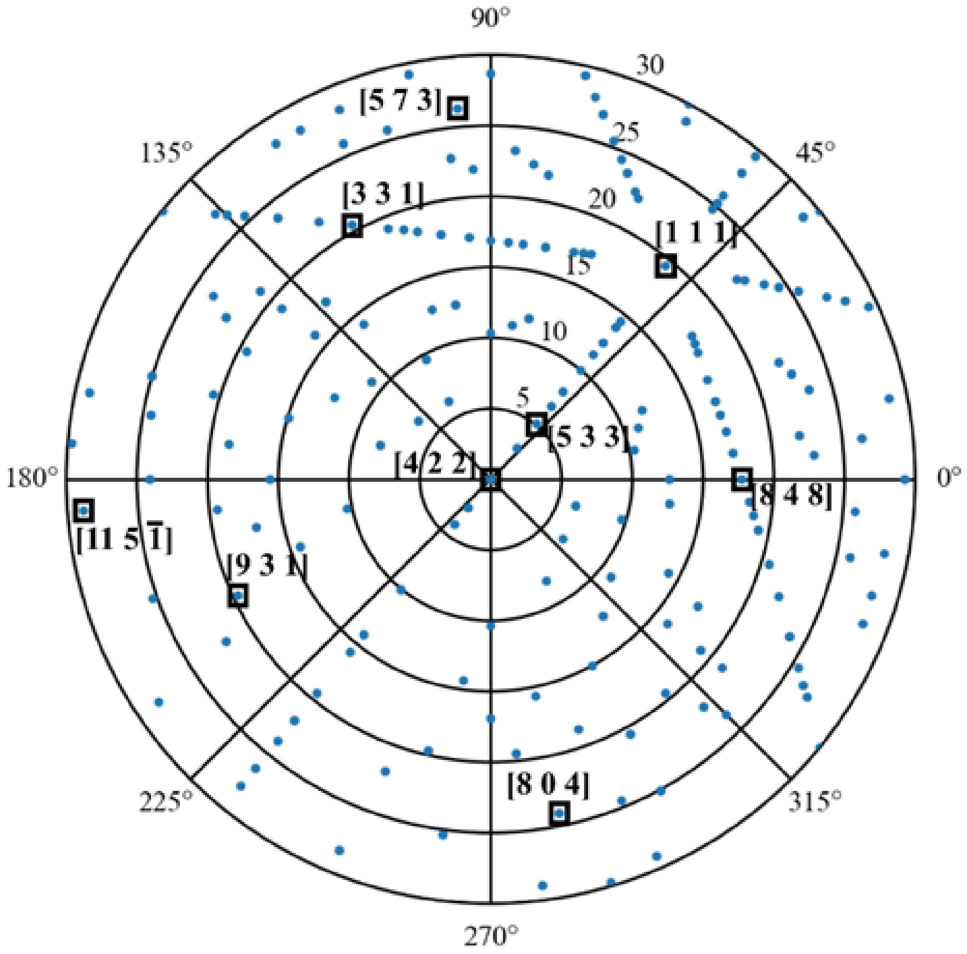

Figure 2 Pole plot demonstrating other reciprocal lattice vectors, G ⃗_hkl, available from the Si (211) SBCA. The radial direction is α, the angle of the reciprocal lattice vector with respect to [211], and the azimuthal direction is φ, the rotation angle of the system about the [211] direction. We show G ⃗_hkl with Miller indices in the range ±12, with only selected points labeled for clarity of presentation.

2. Methods

The package `hklhop` is implemented in a Jupyter Notebook. It is available as an open source code on Github^{37}. Ray tracing calculations are geometrical, with no allowance for strain effects^{2}, using the xrt package ^{38} and following the methods of Chen et. al.^{36}

3. Results and Discussion

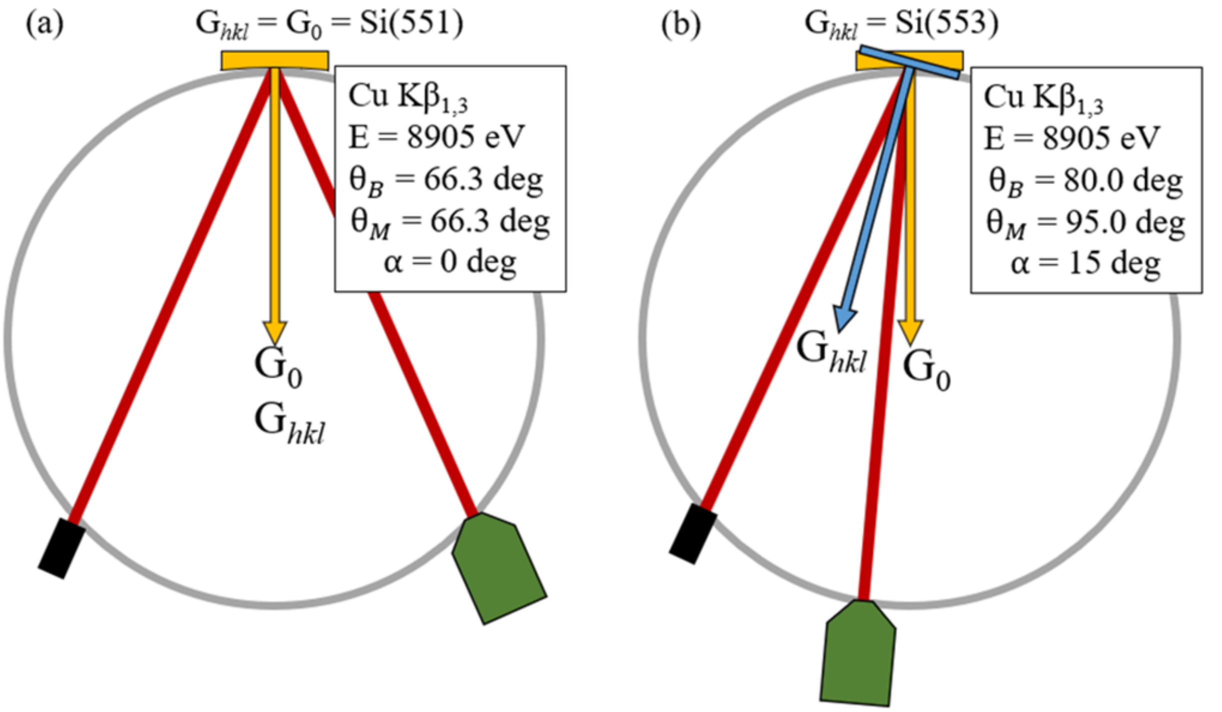

Figure 3 Two options for studying the Cu Kβ1,3 fluorescence. (a) Symmetric operation of a Si (551) SBCA; (b) Asymmetric operation of a Si (551) SBCA using the Si (553) diffraction plane.

The package, schematically shown in Fig. 4, was developed with one main function, `hkl_selection`, for investigating the possible *hkl* space of specified SBCAs and energies and another function, `sbca_selection`, for investigating the possible *hkl* space when only an energy is specified (no limit to SBCA wafer orientation). Here we consider five workflows that follow from realistic experimental needs: the user has a single SBCA and target energy to study (Case I); the user has a single SBCA and multiple energies to study (Case II); the user has multiple SBCAs and a single energy to study (Case III); the user has multiple SBCAs and multiple energies to study (Case IV); and the user has just an energy to study with no restriction on SBCA (Case V), see Figure 4. For Case I-IV the user must input a list of SBCAs (presently restricted to Si or Ge), a list of target energies, spectrometer specifications, and constraints on possible asymmetric orientations. These restrictions include the maximum index of the diffracting plane, the θ_B range, the θ_M range, and the necessary energy range above and below the target energy. For Case V the user instead inputs the maximum index of possible SBCA options, a target energy and the same restrictions as for Case I-IV. Below, we provide representative studies for each of the five workflows.

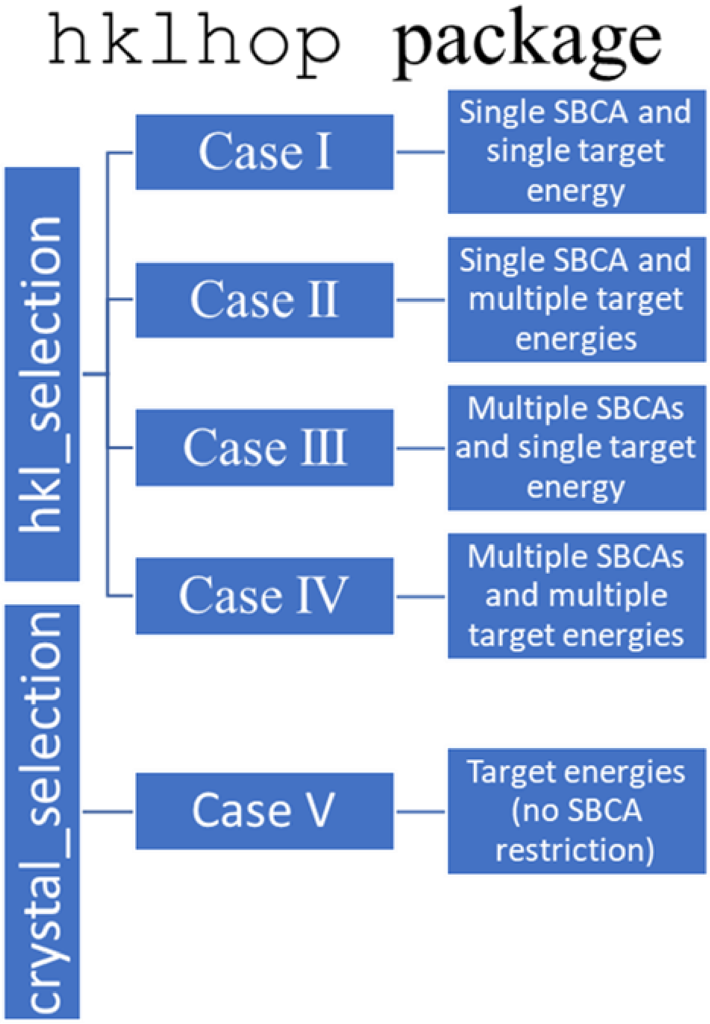

Figure 4 Descriptions of the five main use cases for the hklhop package. The two main functions in the package are `hkl_selection` and `crystal_selection`.

For Case I, where the user has a single SBCA and single energy to study, Table 1 shows the output with a Si (551) SBCA to isolate Zn Kα at 8639 eV, such as is needed for a high-energy resolution fluorescence detection (HERFD) study[39, 40]. Generally, Si (642) G_{hkl} is ideal for symmetric operation for Zn Kα as it has the best θ_B= 81.48 deg; given symmetric operation, $\theta_M = \theta_B$. While 81 deg is generally favorable, accessing the (642) crystal plane asymmetrically from the Si (551) SBCA results in the same Bragg angle but θ_M is now 94.82 deg, closer to the JNA and consequently leading to better energy resolution via decreased Johann error. This is further demonstrated by comparing the (642) and (64-2) G_{hkl} from Table 1. In Fig. 5 we show ray tracing results for the energy response function mapped across the face of the SBCA for these reflections. Note that the symmetric Si (642) shows 1- eV error at the SBCA edge while the asymmetric Si (642) shows 0.5-eV error and the asymmetric Si (64-2) shows 2-eV error. This difference between the three diffraction planes leads to a choice of the asymmetric (642) G_{hkl} over the symmetric (642) and asymmetric (64-2) G_{hkl} reflections.

	G_0	G_{hkl}	θ_B (deg)	α (deg)	θ_M (deg)	$G_{\Phi=0}$	Φ (deg)	CE (%)	SCE (%)
0	Si [5 5 1]	[6 4 2]	81.5	13.3	94.8	[1 0 0]	43.0	80.3	100.0
1	Si [5 5 1]	[6 4 -2]	81.5	26.1	107.6	[1 0 0]	-56.6	32.2	100.0
2	Si [5 5 1]	[5 5 1]	70.7	0.0	70.7	[1 0 0]	22.0	56.1	56.1
3	Si [5 5 1]	[5 5 -1]	70.7	16.1	86.8	[1 0 0]	-82.0	37.1	56.1
4	Si [5 5 1]	[7 1 1]	70.7	36.5	107.2	[1 0 0]	10.6	17.8	56.1
5	Si [5 5 1]	[4 4 4]	66.3	27.2	93.5	[1 0 0]	98.0	21.0	38.7
6	Si [5 5 1]	[4 4 -4]	66.3	43.3	109.6	[1 0 0]	-82.0	14.7	38.7

Table 1 Output from the `hkl_selection` function for Case I, having a single SBCA and single target energy, studying Zn Kα with a Si (551) SBCA. The green box has been added for indication of the optimal reciprocal lattice vector option.

The choice of which G_{hkl} to use depends largely on experimental constraints but typically the most important criteria is θ_B, with larger angles being favorable having less source size broadening[25-29]. Note that source size broadening is generic across symmetric and asymmetric operation as it is due to the source spanning multiple Bragg angles. This is followed in importance by θ_M, picking the reflection closest to JNA, and with no other considerations besides energy resolution the (642) G_{hkl} with the Si (551) SBCA would be the best choice for studying Zn Kα in a laboratory setting, see the green box in Table 1.

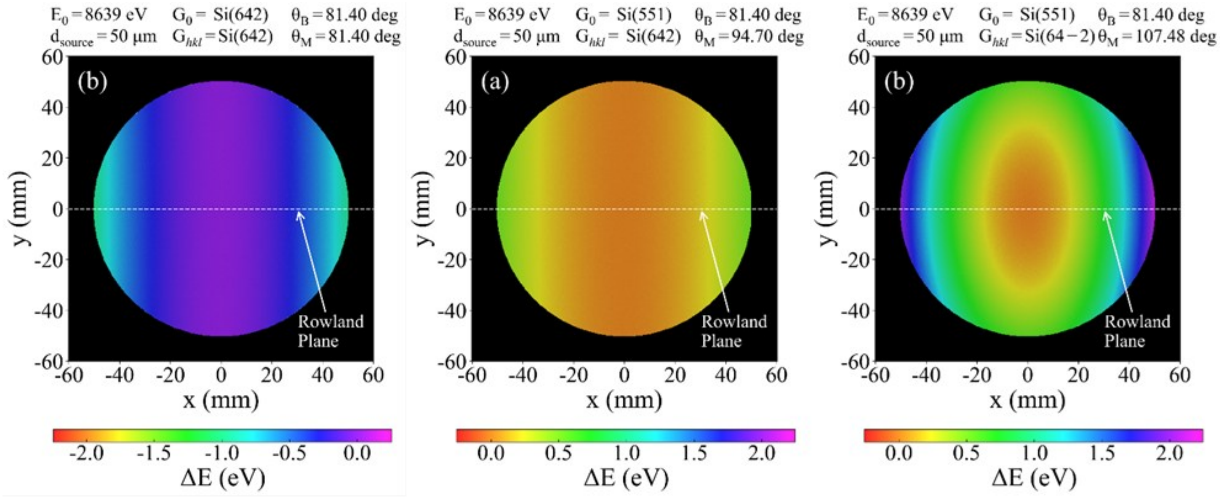

Figure 5 Predicted energy dispersion across the SBCA face for Si (642) reflections from symmetric and two asymmetric configurations: (a) using the (642) G*hkl* symmetrically having θ_B and θ_M of 81.40 deg (b) using the (642) G*hkl* from a Si (551) SBCA having θ_B of 81.40 deg and θ_M of 94.70 deg (c) using the (64-2) G*hkl* from a Si (551) SBCA having θ_B of 81.40 deg and θ_M of 107.48 deg. The larger broadening seen for the (642) symmetric and (64-2) asymmetric configuration is due to the inferior θ_M.

One such consideration is efficiency, where the dominant effect is from the often-large beam height at the detection plane when operating asymmetrically. This is considered in detail in Chen, et al.[36], whose work serves as the basis for the collection efficiency given in the `hkl_selection` output, CE. This is an estimate of the percentage of the total intensity collected on the detection plane for a given detector height. For context, symmetric collection efficiency for the same height detector is also given in the `hkl_selection` output, SCE, as even for symmetric operation the Rowland circle with a SBCA has a point-to-line-focus character. Details are case specific and therefore collection efficiency is not addressed further, but there is seldom greater than 50% relative decrease in collection efficiency between the symmetric and asymmetric cases due to increased focal height at the detector plane. Collection efficiencies presented in this manuscript are calculated with a 10-cm SBCA, 1-m Rowland Circle, and 6-mm detector height. There is also a generic but small loss in reflection efficiency due to the asymmetry itself [41]. While this is a large effect for strongly asymmetric diffraction geometries, it is typically a 10% or smaller contribution here.

Table for target energy of 5899 eV

	G_0	G_{hkl}	θ_B (deg)	α (deg)	θ_M (deg)	$G_{\Phi=0}$	Φ (deg)	CE (%)	SCE (%)
0	Ge [6 2 0]	[5 1 1]	74.8	13.2	88.0	[1 0 0]	57.7	33.3	53.8
1	Ge [6 2 0]	[5 1 -1]	74.8	13.2	88.0	[1 0 0]	-57.7	33.3	53.8
2	Ge [6 2 0]	[5 -1 -1]	74.8	31.6	106.4	[1 0 0]	-21.6	13.3	53.8
3	Ge [6 2 0]	[4 2 2]	65.5	25.4	90.8	[1 0 0]	107.5	13.0	22.1
4	Ge [6 2 0]	[4 2 -2]	65.5	25.4	90.8	[1 0 0]	-107.5	13.0	22.1

Table for target energy of 6930 eV

	G_0	G_{hkl}	θ_B (deg)	α (deg)	θ_M (deg)	$G_{\Phi=0}$	Φ (deg)	CE (%)	SCE (%)
0	Ge [6 2 0]	[5 3 1]	69.3	15.8	85.1	[1 0 0]	141.7	21.2	30.2
1	Ge [6 2 0]	[5 3 -1]	69.3	15.8	85.1	[1 0 0]	-141.7	21.2	30.2
2	Ge [6 2 0]	[5 1 -3]	69.3	31.2	100.5	[1 0 0]	-78.1	12.1	30.2

Table for target energy of 7478 eV

	G_0	G_{hkl}	θ_B (deg)	α (deg)	θ_M (deg)	$G_{\Phi=0}$	Φ (deg)	CE (%)	SCE (%)
0	Ge [6 2 0]	[5 3 3]	73.9	29.8	103.7	[1 0 0]	112.9	14.0	48.3
1	Ge [6 2 0]	[5 3 -3]	73.9	29.8	103.7	[1 0 0]	-112.9	14.0	48.3
2	Ge [6 2 0]	[6 0 -2]	67.9	25.8	93.8	[1 0 0]	-46.5	13.8	26.8

Table 2 Output from hkl_selection function for Case II, having a single SBCA and multiple target energies, studying Ni Kα, Mn Kα, and Co Kα all with a Ge (620) SBCA. The green boxes have been added to indicate the optimal choice of reciprocal lattice vector. The case shows the ability of a single SBCA to cover a range of energies.

Next, in Case II the user has a single SBCA and multiple energies to study. An example output is displayed in Table 2 for a Ge (620) SBCA being used to study the Mn Kα (5899 eV), Co Kα (6930 eV), and Ni Kα (7478 eV) fluorescence. The tables, generated separately for each energy, demonstrate the flexibility of working asymmetrically in allowing one SBCA to access multiple energies while retaining good resolution. Using the same diffraction plane selection method as for Case I we see that Ge (511) or (55-1), Ge (531) or (53-1), and Ge (533) or (53-3) reflection planes will be used, respectively, for Mn Kα, Co Kα, and Ni Kα fluorescence, see the green boxes in Table 2.

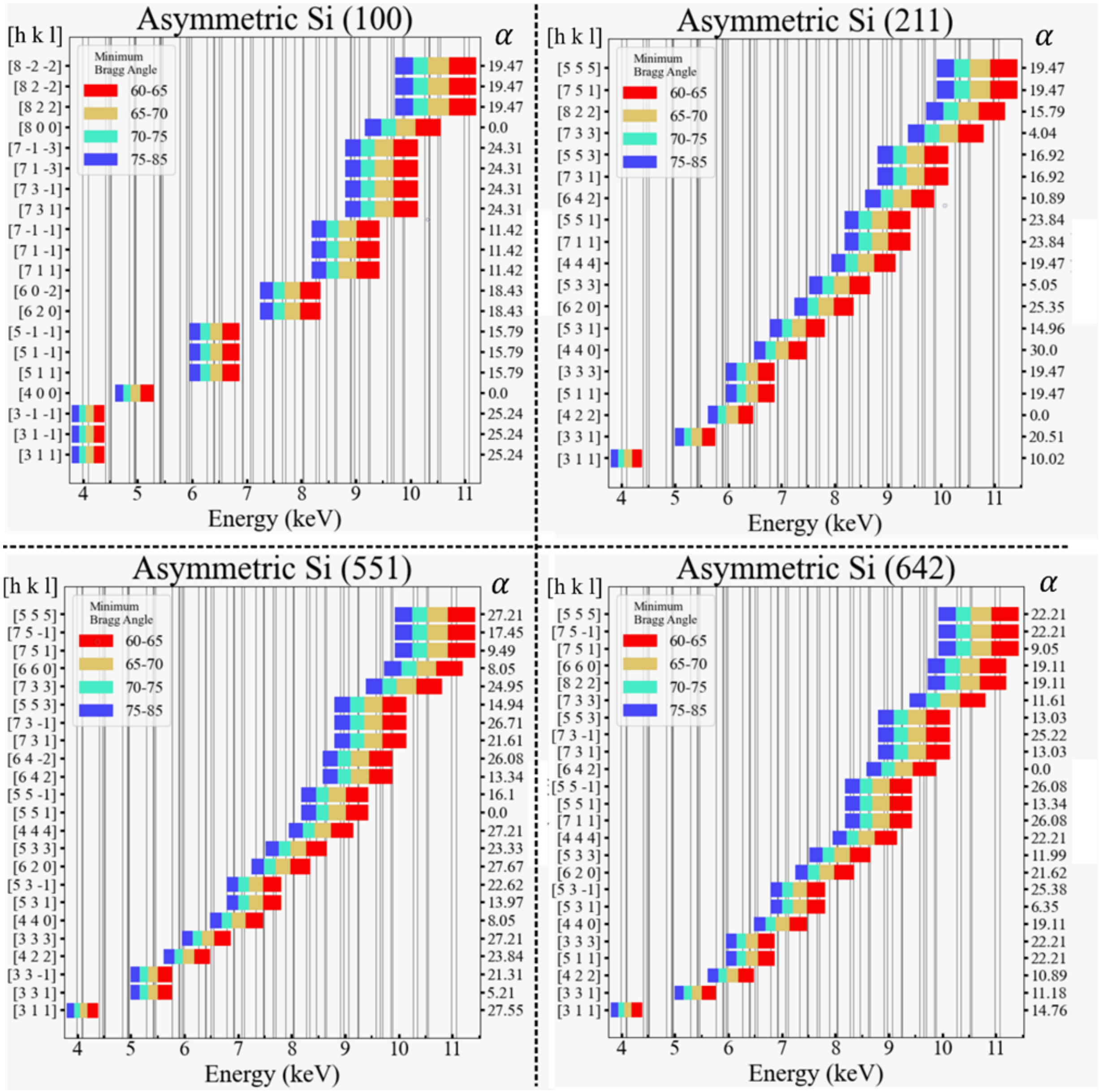

Figure 1 Bar charts generated by an auxiliary function of the package, bar_chart, displaying the energy ranges of the Si (100), Si (211), Si (551), and Si (642) SBCAs when used asymmetrically. The y-axis of each graph shows accessible crystal planes for ~4-10 keV.

To further examine the flexibility of working asymmetrically, Fig. 6 shows the full coverage of unique asymmetric reflections (those that do not access the exact same energy range) from Si (100), Si (211), Si (551), and Si (642) SBCAs within an energy range of 3750 to 10000 eV. These plots are generated by an auxiliary function of the package, `bar_chart`. Due to the higher symmetry for the Si (100) SBCA there are fewer crystal planes with unique *d*-spacing within reasonable α values, leading to poorer energy range coverage and therefore a preference for low symmetry SBCAs for asymmetric operation. At lower energies there are fewer crystal planes with correct *d*-spacings, leading to sparser energy range coverage for all SBCAs, high or low symmetry.

Table for target energy of 11,070 eV									
	G_0	**G_{hkl}**	**θ_B (deg)**	**α (deg)**	**θ_M (deg)**	**$G_{\Phi=0}$**	**Φ (deg)**	**CE (%)**	**SCE (%)**
0	Si [6 4 2]	[9 3 1]	79.7	17.7	97.4	[1 0 0]	-8.9	32.3	98.0
1	Si [2 1 1]	[9 3 1]	79.7	19.7	99.4	[1 0 0]	-26.1	28.0	98.0
2	Si [6 4 2]	[9 3 -1]	79.7	26.3	106.0	[1 0 0]	-31.9	18.6	98.0
3	Si [1 1 1]	[6 6 4]	75.4	10.0	85.4	[1 0 0]	-60.0	41.7	57.4
4	Si [6 4 2]	[6 6 4]	75.4	14.4	89.7	[1 0 0]	157.4	32.1	57.4
5	Si [2 1 1]	[6 6 4]	75.4	16.8	92.1	[1 0 0]	-148.5	27.7	57.4
6	Si [6 4 2]	[7 5 3]	70.0	4.1	74.1	[1 0 0]	136.9	32.2	32.2
7	Si [2 1 1]	[7 5 3]	70.0	9.7	79.6	[1 0 0]	-112.2	28.0	32.2
8	Si [1 1 1]	[7 5 3]	70.0	18.1	88.1	[1 0 0]	-30.0	19.9	32.2
9	Si [2 1 1]	[9 1 1]	70.0	26.3	96.3	[1 0 0]	0.0	14.4	32.2
10	Si [6 4 2]	[9 1 1]	70.0	28.3	98.3	[1 0 0]	5.9	13.4	32.2
11	Si [6 4 2]	[9 1 -1]	70.0	34.8	104.8	[1 0 0]	-15.0	11.0	32.2
12	Si [6 4 2]	[7 5 -3]	70.0	34.8	104.8	[1 0 0]	-71.2	11.0	32.2
13	Si [2 1 1]	[9 1 -1]	70.0	36.2	106.2	[1 0 0]	-15.2	10.6	32.2
14	Si [6 4 2]	[8 4 0]	67.3	17.0	84.3	[1 0 0]	-43.1	18.4	25.4
15	Si [2 1 1]	[8 4 0]	67.3	24.1	91.4	[1 0 0]	-50.8	14.3	25.4
16	Si [1 1 1]	[8 4 0]	67.3	39.2	106.5	[1 0 0]	-30.0	9.6	25.4

Table 3 Output from hkl_selection function for Case III, having multiple SBCAs and a single target energy, studying Pt VtC fluorescence with a Si (111), Si (211), or Si (642) SBCA. The blue and green boxes have been added to highlight the optimal choices of reciprocal lattice vector. The green box is for a large source size spectrometer, e.g. laboratory, where θ_B is the most important parameter for resolution, whereas the blue box is for a small source size spectrometer, e.g. micro-focused beamline, where θ_M is the most important parameter for resolution.

For Case III with a single energy and multiple SBCAs, Table 3 gives output for the energy of the Pt valence-to-core (VtC) fluorescence with either a Si (111), Si (211), or Si (642) SBCA. Comparing G_{hkl} across all three SCBAs the optimal configuration to study Pt VtC can be chosen as before: the [931] reciprocal lattice vector accessed with the Si (642) SBCA has θ_M closest to JNA for the options with the best θ_B, see the green box in Table 3. One common experimental constraint that will change this choice is having a small source size, such as from a micro-focused synchrotron beam. For small source sizes, the value of θ_M controls analyzer selection over θ_B because energy broadening becomes dominated by Johann error rather than source size, with the caveat that a good θ_B is still beneficial to minimize the consequences of off-circle alignment. Hence, for a small source size the [664] reciprocal lattice vector accessed with the Si (642) SBCA is preferred, see the blue box in Table 3.

Table for target energy of 5463 eV									
	G_0	G_{hkl}	θ_B (deg)	α (deg)	θ_M (deg)	$G_{\Phi=0}$	Φ(deg)	CE(%)	SCE (%)
0	Si [5 3 3]	[3 3 1]	65.6	19.2	84.8	[1 0 0]	-98.7	15.9	22.3
1	Si [3 1 1]	[3 3 1]	65.6	25.9	91.6	[1 0 0]	-132.1	12.9	22.3
2	Si [3 1 1]	[3 3 -1]	65.6	40.5	106.1	[1 0 0]	-90.0	9.2	22.3
3	Si [5 3 3]	[3 3 -1]	65.6	42.7	108.4	[1 0 0]	-73.0	8.8	22.3

Table for target energy of 7058 eV									
	G_0	G_{hkl}	θ_B (deg)	α (deg)	θ_M (deg)	$G_{\Phi=0}$	Φ(deg)	CE(%)	SCE (%)
0	Si [3 1 1]	[5 3 1]	73.1	14.5	87.6	[1 0 0]	-106.8	27.9	44.4
1	Si [5 3 3]	[5 3 1]	73.1	17.5	90.6	[1 0 0]	-52.7	23.8	44.4
2	Si [3 1 1]	[5 3 -1]	73.1	30.0	103.1	[1 0 0]	-73.2	13.7	44.4
3	Si [1 0 0]	[5 3 1]	73.1	32.3	105.4	[0 0 1]	71.6	12.6	44.4
4	Si [1 0 0]	[5 3 -1]	73.1	32.3	105.4	[0 0 1]	108.4	12.6	44.4
5	Si [1 0 0]	[5 1 -3]	73.1	32.3	105.4	[0 0 1]	161.6	12.6	44.4
6	Si [1 0 0]	[5 -1 -3]	73.1	32.3	105.4	[0 0 1]	-161.6	12.6	44.4
7	Si [5 3 3]	[4 4 0]	66.2	30.4	96.6	[1 0 0]	-81.3	11.5	23.3
8	Si [3 1 1]	[4 4 0]	66.2	31.5	97.7	[1 0 0]	-106.8	11.2	23.3

Table 4 Output from hkl_selection function for Case IV, having multiple SBCAs and multiple target energies. Here V VtC and Fe Kβ fluorescence is being studied by a Si (100), Si (311), or Si (533) SBCA. The green boxes have been added to indicate the optimal choice of reciprocal lattice vector for each energy.

For Case IV, investigating the use of multiple SBCAs to study multiple energies, Table 4 considers measurement of V VtC and Fe Kβ fluorescence using either a Si (100), Si (311), or Si (533) SBCA. By combining the multiple target energies and multiple SBCA options from Case II and Case III the user can investigate the full range of options available to them and choose the best SCBA and G_{hkl} combination at each energy or choose the best single SBCA that can study all the energies having G_{hkl} options for each. In this limited example of three SBCAs and two energies, all SBCAs can reach reciprocal lattice vectors with the largest θ_B possible for each energy, but having different α, and therefore differing θ_M. Optimizing θ_M while maintaining the largest θ_B leads to a choice of Si (311) SBCA accessing [331] for V VtC

(5463eV) and Si (533) SBCA accessing [531] for Fe Kβ (7058eV), boxed in green in Table 4. This choice uses a different SBCA for each energy, but if instead a single SBCA was desired to measure both V VtC and Fe Kβ then the Si (331) SBCA would be selected as it has the smallest deviation of θ_M from JNA across both energies.

	E (eV)	G_{hkl}	θ_B **(deg)**	G_0	**α (deg)**	θ_M **(deg)**
0	13615	[11 3 3]	81.4	[3 1 1]	4.1	85.5
1	13615	[11 3 3]	81.4	[5 1 1]	5.3	86.7
2	13615	[9 7 3]	81.4	[3 3 1]	7.1	88.4
3	13615	[9 7 3]	81.4	[5 3 1]	8.4	89.8
4	13615	[9 7 3]	81.4	[5 5 1]	9.7	91.0
5	13615	[9 7 3]	81.4	[5 5 3]	10.6	92.0
6	13615	[10 6 0]	77.9	[5 3 -1]	9.7	87.7
7	13615	[10 6 0]	77.9	[5 3 1]	9.7	87.7
8	13615	[10 6 0]	77.9	[2 2 0]	14.0	92.0
9	13615	[10 6 0]	77.9	[5 5 -1]	16.1	94.1
10	13615	[10 6 0]	77.9	[5 5 1]	16.1	94.1
11	13615	[8 6 6]	77.9	[1 1 1]	8.0	86.0
12	13615	[8 6 6]	77.9	[5 5 3]	10.8	88.7
13	13615	[8 6 6]	77.9	[4 2 2]	11.4	89.4

Table 5 Output from sbca_selection function for Case V, having just a target energy, 13,615 eV for U Lα_1. The function finds all reciprocal lattice vectors, G_{hkl}, that access the energy above a certain θ_B and find the SBCA reciprocal lattice vectors, G_0, that reach it and the associated α and θ_M.

Finally, for Case V, where the user has selected an energy but is open to all SBCA choices, we consider U Lα_1 in Table 5 which demonstrates typical output of the `sbca_`selection function. From this table an SBCA can be chosen to study a fluorescence line at an optimal configuration, see the green box in Table 5 for this example. While only one energy is shown in Table 5 the `sbca_selection` function accepts input of a list of energies, making a table for each one. This can help plan experiments where the number of SBCA changes can be minimized.

Presently, we have only addressed asymmetric operation of SBCAs, but these ideas may, with difficulty, generalize to von Hamos geometry[42-44] with a cylindrical analyzer. In that case the full flexibility of selecting an *hkl* would be reduced but a precise orientation of a cylindrically curved wafer would allow access to some asymmetric reflections. This could result in an increase in accessible energy range at high Bragg angles but will still be reduced compared to the SBCA case.

4. Conclusions

Asymmetric Rowland circle geometries greatly improve the energy range of SBCAs while also decreasing Johann error but have been historically underutilized due to lack of spectrometer capability, knowledge of the benefits, and guidance on how to operate asymmetrically. The `hklhop` package provides users with the missing guidance with tools to choose the best combinations of analyzer and reflection for any given experiment. Taking input tailored to a specific experimental set up, users are provided with tables of analyzers, reflections, and important parameters which aid in the choice and implementation of asymmetric operation. While the package is currently limited to Si and Ge SBCA, other analyzer materials can be easily added.

Acknowledgements

The project was supported by U.S. Department of Energy in the Nuclear Energy University Program under Contract No. DE-NE0009158

References

1. T. T. Fister, G. T. Seidler, L. Wharton, A. R. Battle, T. B. Ellis, J. O. Cross, A. T. Macrander, W. T. Elam, T. A. Tyson and Q. Qian, *Review of Scientific Instruments*, 2006, **77**, 063901.
2. S. Huotari, C. J. Sahle, C. Henriquet, A. Al-Zein, K. Martel, L. Simonelli, R. Verbeni, H. Gonzalez, M. C. Lagier, C. Ponchut, M. M. Sala, M. Krisch and G. Monaco, *Journal of Synchrotron Radiation*, 2017, **24**, 521-530.
3. E. Kleymenov, J. A. van Bokhoven, C. David, P. Glatzel, M. Janousch, R. Alonso-Mori, M. Studer, M. Willimann, A. Bergamaschi, B. Henrich and M. Nachtegaal, *Review of Scientific Instruments*, 2011, **82**, 065107.
4. I. Llorens, E. Lahera, W. Delnet, O. Proux, A. Braillard, J. L. Hazemann, A. Prat, D. Testemale, Q. Dermigny, F. Gelebart, M. Morand, A. Shukla, N. Bardou, O. Ulrich, S. Arnaud, J. F. Berar, N. Boudet, B. Caillot, P. Chaurand, J. Rose, E. Doelsch, P. Martin and P. L. Solari, *Review of Scientific Instruments*, 2012, **83**, 063104.
5. M. M. Sala, K. Martel, C. Henriquet, A. Al Zein, L. Simonelli, C. J. Sahle, H. Gonzalez, M. C. Lagier, C. Ponchut, S. Huotari, R. Verbeni, M. Krisch and G. Monaco, *Journal of Synchrotron Radiation*, 2018, **25**, 580-591.
6. D. Sokaras, D. Nordlund, T. C. Weng, R. A. Mori, P. Velikov, D. Wenger, A. Garachtchenko, M. George, V. Borzenets, B. Johnson, Q. Qian, T. Rabedeau and U. Bergmann, *Review of Scientific Instruments*, 2012, **83**, 043112.
7. D. Sokaras, T. C. Weng, D. Nordlund, R. Alonso-Mori, P. Velikov, D. Wenger, A. Garachtchenko, M. George, V. Borzenets, B. Johnson, T. Rabedeau and U. Bergmann, *Review of Scientific Instruments*, 2013, **84**, 053102.
8. R. Verbeni, T. Pylkkänen, S. Huotari, L. Simonelli, G. Vankó, K. Martel, C. Henriquet and G. Monaco, *Journal of Synchrotron Radiation*, 2009, **16**, 469-476.
9. W. M. Holden, O. R. Hoidn, A. S. Ditter, G. T. Seidler, J. Kas, J. L. Stein, B. M. Cossairt, S. A. Kozimor, J. H. Guo, Y. F. Ye, M. A. Marcus and S. Fakra, *Review of Scientific Instruments*, 2017, **88**, 073904.
10. W. M. Holden, G. T. Seidler and S. Cheah, *Journal of Physical Chemistry A*, 2018, **122**, 5153-5161.
11. E. P. Jahrman, W. M. Holden, A. S. Ditter, D. R. Mortensen, G. T. Seidler, T. T. Fister, S. A. Kozimor, L. F. J. Piper, J. Rana, N. C. Hyatt and M. C. Stennett, *Review of Scientific Instruments*, 2019, **90**, 024106.
12. D. R. Mortensen, G. T. Seidler, J. J. Kas, N. Govind, C. P. Schwartz, S. Pemmaraju and D. G. Prendergast, *Physical Review B*, 2017, **96**, 125136.
13. M. E. Mundy, D. Ung, N. L. Lai, E. P. Jahrman, G. T. Seidler and B. M. Cossairt, *Chemistry of Materials*, 2018, **30**, 5373-5379.
14. G. T. Seidler, D. R. Mortensen, A. J. Remesnik, J. I. Pacold, N. A. Ball, N. Barry, M. Styczinski and O. R. Hoidn, *Review of Scientific Instruments*, 2014, **85**, 113906.
15. R. A. Valenza, E. P. Jahrman, J. J. Kas and G. T. Seidler, *Physical Review A*, 2017, **96**, 032504.
16. N. S. Genz, A. J. Kallio, R. Oord, F. Krumeich, A. Pokle, O. Prytz, U. Olsbye, F. Meirer, S. Huotari and B. M. Weckhuysen, *Angewandte Chemie-International Edition*, 2022, **61**, e202209334.

17. A. P. Honkanen, S. Ollikkala, T. Ahopelto, A. J. Kallio, M. Blomberg and S. Huotari, *Review of Scientific Instruments*, 2019, **90**, 033107.
18. A. J. Kallio, A. Weiss, R. Bes, M. J. Heikkilä, M. Ritala, M. Kemell and S. Huotari, *Dalton Transactions*, 2022, **51**, 18593-18602.
19. A. Bordage, M. Pápai, N. S. Sas, J. Szlachetko, M. Nachtegaal and G. Vankó, *Physical Chemistry Chemical Physics*, 2013, **15**, 11088-11098.
20. D. R. Mortensen and G. T. Seidler, *Journal of Electron Spectroscopy and Related Phenomena*, 2017, **215**, 8-15.
21. J. F. Seely, E. Galtier, L. T. Hudson, A. Henins and U. Feldman, *Applied Optics*, 2019, **58**, 5225-5232.
22. P. Suortti, T. Buslaps, P. Fajardo, V. Honkimäki, M. Kretzschmer, U. Lienert, J. E. McCarthy, M. Renier, A. Shukla, T. Tschentscher and T. Meinander, *Journal of Synchrotron Radiation*, 1999, **6**, 69-80.
23. P. Suortti, U. Lienert and C. Schulze, *Nuclear Instruments & Methods in Physics Research Section a-Accelerators Spectrometers Detectors and Associated Equipment*, 1994, **338**, 27-32.
24. A. J. Gironda, J. E. Abramson, Y. Chen, M. Solovyev, G. E. Sterbinsky and G. T. Seidler, *Journal of Analytical Atomic Spectrometry*, 2024, **39**, 1375-1387.
25. A. Boeuf, S. Lagomarsino, S. Mazkedian, S. Melone, P. Puliti and F. Rustichelli, *Journal of Applied Crystallography*, 1978, **11**, 442-449.
26. R. Caciuffo, S. Melone, F. Rustichelli and A. Boeuf, *Physics Reports-Review Section of Physics Letters*, 1987, **152**, 1-71.
27. E. Erola, V. Etelaniemi, P. Suortti, P. Pattison and W. Thomlinson, *Journal of Applied Crystallography*, 1990, **23**, 35-42.
28. P. Jagodzinski, M. Pajek, D. Banas, H. F. Beyer, M. Trassinelli and T. Stöhlker, *Nuclear Instruments & Methods in Physics Research Section a-Accelerators Spectrometers Detectors and Associated Equipment*, 2014, **753**, 121-130.
29. T. Matsushita and U. Kaminaga, *Journal of Applied Crystallography*, 1980, **13**, 465-471.
30. P. Pattison, P. Suortti and W. Weyrich, *Journal of Applied Crystallography*, 1986, **19**, 353-363.
31. S. G. Podorov, O. Renner, O. Wehrhan and E. Förster, *Journal of Physics D-Applied Physics*, 2001, **34**, 2363-2368.
32. P. Suortti, D. Chapman, J. R. Schneider and T. Tschentscher, *Journal of Applied Crystallography*, 1992, **25**, 432-438.
33. P. Suortti, P. Pattison and W. Weyrich, *Journal of Applied Crystallography*, 1986, **19**, 336-342.
34. P. Suortti, P. Pattison and W. Weyrich, *Journal of Applied Crystallography*, 1986, **19**, 343-352.
35. P. Suortti and W. Thomlinson, *Nuclear Instruments & Methods in Physics Research Section a-Accelerators Spectrometers Detectors and Associated Equipment*, 1988, **269**, 639-648.
36. Y. Chen and G. T. Seidler, unpublished work.

37. J. E. Abramson and Y. Chen. *hklhop*. 2024: GitHub repository. Available from: https://github.com/Seidler-Lab/hklhop.git.
38. K. Klementiev and R. Chernikov, *Advances in Computational Methods for X-ray Optics III*, 2014, DOI: 10.1117/12.2061400.
39. S. Hayama, R. Boada, J. Chaboy, A. Birt, G. Duller, L. Cahill, A. Freeman, M. Amboage, L. Keenan and S. Diaz-Moreno, *Journal of Physics-Condensed Matter*, 2021, **33**, 284003.
40. I. A. Pankin, O. E. Polozhentsev, M. A. Soldatov, A. L. Bugaev, A. Tsaturyan, K. A. Lomachenko, A. A. Guda, A. P. Budnyk, C. Lamberti and A. V. Soldatov, *Journal of Solid State Chemistry*, 2018, **262**, 264-272.
41. M. D. Als-Nielsen J., in *Elements of Modern X-ray Physics*, 2011, DOI: https://doi.org/10.1002/9781119998365.ch6, ch. Diffraction by perfect crystals, pp. 207-238.
42. P. Jagodzinski, D. Banas, M. Pajek, A. Kubala-Kukus, L. Jablonski, I. Stabrawa, K. Szary, D. Sobota, A. Warczak, A. Gumberidze, H. F. Beyer, M. Lestinsky, G. Weber, T. Stöhlker and M. Trassinelli, *Journal of Instrumentation*, 2023, **18**.
43. Z. Németh, J. Szlachetko, E. G. Bajnóczi and G. Vankó, *Review of Scientific Instruments*, 2016, **87**.
44. J. Szlachetko, M. Nachtegaal, E. de Boni, M. Willimann, O. Safonova, J. Sa, G. Smolentsev, M. Szlachetko, J. A. van Bokhoven, J. C. Dousse, J. Hoszowska, Y. Kayser, P. Jagodzinski, A. Bergamaschi, B. Schmitt, C. David and A. Lücke, *Review of Scientific Instruments*, 2012, **83**.

Chapter 9 - X-ray Emission Spectropolarimetry of Strongly Anisotropic Single Crystal Systems using a Rowland Circle Geometry

Manuscript by J. Abramson, C. Cardot, J. Kas, J. Rehr, W. Kaminsky, H. Michor, P. Becker, G. T. Seidler.

J. Abramson performed all the experimental work and collaborated with C. Cardot to perform analysis and write the majority of this work.

Polarization dependence has historically seen extensive use in x-ray spectroscopy to determine magnetic and local geometric properties, but more broadly as a way to gain extra sensitivity to electronic structure at the level of individual magnetic orbitals. This is often done in the context of x-ray absorption through techniques like x-ray magnetic circular dichroism or x-ray linear dichroism, but it has seen little application to x-ray emission. Here we explore the information contained in the polarized emission of two 3d transition metal systems across both core-to-core (CtC) and valence-to-core emission (VtC) lines. We demonstrate how the Rowland circle geometry can be used as a spectropolarimeter, and apply it to the x-ray emission spectroscopy of spin-1/2 Cu(II) and spin-0 Ni(II) ions in $LiVCuO_4$ *and* $DyNiC_2$*, respectively. From this we explore how the polarized XES provides a reflection of the occupied density of states at the valence level, either as a second order effect through Coulomb exchange (CtC x-ray emission) or by direct transitions (VtC x-ray emission). Finally, we highlight how the individually polarized dipole emission spectra can be extracted from an orthogonal suite of directed*

emission spectra, allowing for polarized measurements at high Bragg angle with lower experimental broadening.

1. Introduction

X-ray emission spectroscopy (XES) is an element-specific probe of the occupied density of states [1]. It can be performed on a wide range of sample types, including under *in situ* conditions, which has led to its growing use for probing valence level electronic structure, chemical bonding, oxidation state, and ligand field effects [2]. However, analysis with XES is limited to only probing the occupied orbitals and therefore, when relevant, it is used in complement with x-ray absorption spectroscopy (XAS) which probes the unoccupied orbitals. This complementary nature has emerged as a powerful characterization pathway and been utilized to determine the structure of nitrogenase [3], the redox chemistry of lithium ion batteries [4], and the catalytic process of transition metal catalysts [5].

Many new materials such as superconducting cuprates, layered perovskites, or quasi-1D materials have anisotropic electronic structure [6, 7] which is ideal for study by x-ray spectroscopic techniques. In particular, polarized XAS and XES exploit selection rules governing electronic transitions to study the directional dependence of the local electronic environment [8].

Indeed polarized XAS is used frequently in techniques such as x-ray magnetic circular dichroism (XMCD) [9, 10], x-ray magnetic linear dichroism (XMLD) [11], angle-resolved photoemission spectroscopy (ARPES) [12–16], and resonant inelastic x-ray scattering (RIXS) [17–21] to study the directional dependence of the local electronic environment. For example, polarized RIXS has proven to be a powerful technique through its ability to naturally disentangle the symmetry of intermediate excitations via polarization analysis, and can probe *dd* and charge transfer excitations in strongly correlated materials [20, 22–25].

Alternatively, polarized non-resonant XES has seen little study due to the difficulty involved in measuring the polarization of a photon from low brilliance sources, i.e. fluorescence. Studies by Drager and Czolbe [26, 27] showed there were¨ polarization effects in XES which reflected the *m*-resolved density of states, but these developments were hampered due to optical constraints and detector efficiency. More recently Bergmann and co-workers [28] demonstrated how electronic anisotropy from different ligand species can produce a polarization dependence in the $K\beta''$ peak of Mn VtC-XES from $[Rh(en)_3][Mn(N)(CN)_5]\cdot H_2O$ single crystals.

To further investigate the application of polarized XES, both individually and in complement with XAS, we present two case studies on single crystal systems, $LiVCuO_4$ and $DyNiC_2$. We directly measure polarized XES using a spectropolarimeter design similar to the one developed by Drager¨ *et al.* [29] but with improved energy resolution, and indirectly by a new technique to extract the polarized spectra from a set of linearly independent, unpolarized XES spectra. We employ multiplet and real space Green's function calculations to interpret the electronic structure information from polarized CtC and VtC XES techniques. Finally we propose future developments using asymmetric Rowland operation [30] to achieve better resolution and polarization sensitivity in spectropolarimetry, which would push the analytical capabilities of polarized XES into being a proper complement to polarized XAS.

1.1 Manuscript Overview

The manuscript proceeds as follows. Section 2 describes the relevant terminology, a framework of XES and corresponding toy model, and the single crystal systems we study. In Section 3 we describe the experimental and computational methods. Special attention will be paid to the experimental setup and data processing to confirm that we perform a comparison of different polarizations on a consistent energy scale. In Section 4 we present a polarization analysis of the CtC Kβ XES and VtC-XES for both materials. Finally, in Section 5 we summarize our results and conclude.

2. Background

2.1 Terminology

Here we explicitly define the terminology regarding directed and polarized spectra used throughout this manuscript. Spectra measured at high Bragg angle will contain approximately equal contributions from in-plane (p) and out-of-plane (s) polarizations, and will therefore be refereed to as *unpolarized*. Spectra measured at low Bragg angle will be dominated by the out-of-plane polarization, and therefore we will refer to these as *partially polarized*. Further details will be provided in Section 3.1.

A key note is that both of these are considered *directed* spectra, where the specified axis refers to the direction of photon propagation, denoted as I_x, I_y, or I_z. However, the *partially polarized* spectra are dominated by a specific polarization component that is perpendicular to the propagation direction, and are therefore denoted with both the polarization axis and propagation axis specified (ex: σ_x, I_z). In contrast, *polarized* spectra refer to emission resulting from a dipole transition along a specific axis, denoted purely as σ_x, σ_y, or σ_z. All polarized spectra presented in this work are either extracted from experiment following Section 3.4.3 or directly calculated from theory. The terminology is summarized in Table 1.

Term	Definition
Unpolarized	High Bragg Angle
Partially Polarized	Low Bragg Angle
σ_x	x-polarized spectrum
σ_y	y-polarized spectrum
σ_z	z-polarized spectrum
Ix	x-directed spectrum
I_y	y-directed spectrum
I_z	z-directed spectrum

Table 1: Terminology and symbol definitions used in this work.

2.2 X-ray Emission Spectroscopy

X-ray emission is the fine energy resolution study of the fluorescence given off when an atom radiatively decays to fill a core hole left behind from an absorption event [2]. For 3*d* transition metal (TM) systems, the Kβ XES involves filling a 1*s* core hole from the 3*p* orbital, and known as a core-to-core (CtC) transition. CtC Kβ XES has two main spectral features: K$\beta_{1,3}$ and Kβ'. The K$\beta_{1,3}$ is defined by transitions from the spin-orbit split $3p_{1/2}$ or $3p_{3/2}$ orbitals filling the 1*s* hole. The Kβ' satellite line originates from the exchange interaction between the 3*p* core hole and unpaired 3*d* electrons in the valence shell. The strength of the satellite is strongly dependent on the 3*d* spin state, growing for higher spin systems [2].

When the transition is from the valence levels, which have a mix of 3*d* and ligand character, to 1*s* core hole the process is known as a valence-to-core (VtC) transition. 3*d* TMs VtC-XES also has two main spectral features; a main K$\beta_{2,5}$ spectral region coming from molecular orbitals with metal 3*d*, metal 4*p*, metal 4*s*, and ligand 2*p* character, and a Kβ'' satellite from ligand 2*s* electrons filling the metal 1*s* hole. As such VtC-XES is highly depend on local environment with the K$\beta_{2,5}$ peak changing due to bonding and 3*d* electron configuration and the Kβ'' peak energy and intensity being dependent on ligand speciation and bond length [31].

2.3 Electric Dipole Polarization Dependence

The x-ray emission intensity from a given initial state *i* is expressed in Eq. 1. The total spectrum comes from the sum over Fermi's golden rule for all final states *f* [32]. The energy $\hbar\omega$ is the energy of the radiation, *m* is the mass of the electron, $\vec{r}$ is the spatial coordinate vector, and $\vec{k}$ ($|\vec{k}| = 2\pi/\lambda$) is the propagation vector of the photon [32–34]. The orientation of the emitted radiation is entirely described by $\vec{k}$ and the polarization unit vector $\hat{\epsilon}$, which is orthogonal to $\vec{k}$.

$$\sigma = \frac{\omega e^2}{hm^2c^3} \sum_f \left| \langle f | \exp(i\vec{k} \cdot \vec{r})\, \hat{\epsilon} \cdot \vec{r} | i \rangle \right|^2 \times \delta(E_f - E_i + \hbar\omega) \tag{1}$$

If we approximate the wavelength of the photon, λ, to be much larger than the size of the 1*s* shell, $\lambda \gg r$, we arrive at the dipole approximation in Eq. 2. The dipole transition operator is given by $\sum_\alpha \hat{\epsilon}_\alpha \cdot \vec{r}$. The isotropic spectrum is equivalent to taking the average of the trace of the polarization tensor.

$$\begin{aligned} \sigma^{\text{dip}} &\propto \sum_f |\langle f| \sum_\alpha \hat{\epsilon}_\alpha \cdot \vec{r} |i\rangle|^2 \delta(E_f - E_i + \hbar\omega) \\ &\propto \sum_f |\langle f|\, \epsilon_x \hat{x} + \epsilon_y \hat{y} + \epsilon_z \hat{z}\, |i\rangle|^2\, \delta(E_f - E_i + \hbar\omega) \\ &= \sigma_x + \sigma_y + \sigma_z \end{aligned} \tag{2}$$

We refer to the observables σ_x, σ_y, and σ_z as the polarized spectra. They represent the emission intensity as a function of energy for a dipole transition along a given axis, and they are the quantity that polarization analysis of a single-crystal XES study seeks to determine. The dipole selection rules restrict transitions to be between orbitals that are related by $\Delta l = \pm 1$, which follows from the fact that the position operators x, y, and z transform as components of a spherical tensor of rank 1 and thus only connect states whose angular momenta differ by one unit [35].

The spectrum corresponding to a photon with wave vector $\vec{k}$ will have a polarization perpendicular to the direction of propagation [36]. The intensity of the emitted photon is symmetric azimuthally about the dipole transition moment axis (see Appendix A), which means that the measured emission along a given axis is composed of an equal mixing of the two signals with polarization perpendicular to the direction of propagation. The system of equations which gives the unpolarized intensity measured from a photon propagating in a given direction (I_x, I_y, and I_z) is shown in Eq. 3, where σ_x, σ_y, and σ_z correspond to the spectra from the x, y, and z dipole transition operators respectively.

$$\vec{I}_{\text{dir}} = \begin{bmatrix} I_x \\ I_y \\ I_z \end{bmatrix} \propto \frac{1}{2} \begin{bmatrix} 0 & 1 & 1 \\ 1 & 0 & 1 \\ 1 & 1 & 0 \end{bmatrix} \begin{bmatrix} \sigma_x \\ \sigma_y \\ \sigma_z \end{bmatrix} \qquad (3)$$

2.4 Toy Model of CtC-XES

Local anisotropy is often reflected in the (projected) electronic density of states of the valence shell of metal ions. For the purpose of demonstrating the origin of polarization effects in CtC-XES, we investigate how anisotropy in the valence level electron configuration is transferred to other levels via the the electron-electron Coulomb interaction. We start with a toy system of one d electron and one p electron, fixing the d electron to be spin down in the d_{xy} orbital. The choice of d_{xy} for this example is arbitrary, but in a real system will be determined by valence level splitting from crystal field effects. The Coulomb Hamiltonian is given in second quantization in Eq 4, where $\tau = \sigma, m, l, n$ denotes the spin and orbital degrees of freedom. The two particle Coulomb operator between the *p* and *d* orbitals can be split into spherical and radial components, and further split into the ‘direct’ (F0, F2) and ‘exchange’ (G1, G3) terms [37]. The coefficients κ_i set the scale of the individual Slater-Condon terms. For the toy Hamiltonian, we set the coefficients $\vec{\kappa} = [1.2, 8.0, 8.0, 5.0]$ to approximate the interaction between the 3*p* and 3*d* orbitals in the final state of a Kβ XES process.

$$H_{\text{toy}}^{C} = \sum_{\tau_1\tau_2\tau_3\tau_4} U_{\tau_1\tau_2\tau_3\tau_4}\, a^{\dagger}_{\tau_1} a^{\dagger}_{\tau_2} a_{\tau_4} a_{\tau_3} \tag{4a}$$

$$\begin{aligned} U_{\tau_1\tau_2\tau_3\tau_4} &= -\frac{1}{2}\delta_{\sigma_1,\sigma_3}\delta_{\sigma_2,\sigma_4}\sum_{k=0}^{\infty}\frac{4\pi}{2k+1} \\ &\times \langle Y^{(l_1)}_{m_1}|\, Y^{(k)}_{m_1-m_3}\, |Y^{(l_3)}_{m_3}\rangle \langle Y^{(l_4)}_{m_4}|\, Y^{(k)}_{m_4-m_2}\, |Y^{(l_2)}_{m_2}\rangle \\ &\times R^{k}[\tau_1\tau_2\tau_3\tau_4] \end{aligned} \tag{4b}$$

$$\begin{aligned} U_{\tau_1\tau_2\tau_3\tau_4} &= \kappa_0\, \mathrm{F0}_{\mathrm{pd}} + \kappa_1\, \mathrm{F2}_{\mathrm{pd}} \\ &+ \kappa_2\, \mathrm{G1}_{\mathrm{pd}} + \kappa_3\, \mathrm{G3}_{\mathrm{pd}} \end{aligned} \tag{4c}$$

d-Orbital	*d*-Spin	*p*-Orbital	*p*-Spin	Spin Aligned?	$\langle H_{\text{toy}}^{C} \rangle$	$\langle \mathrm{F0}_{\mathrm{pd}} \rangle$	$\langle \mathrm{F2}_{\mathrm{pd}} \rangle$	$\langle \mathrm{G1}_{\mathrm{pd}} \rangle$	$\langle \mathrm{G3}_{\mathrm{pd}} \rangle$
dxy	down	p_x	down	yes	-0.885	0.748	0.457	-1.600	-0.490
dxy	down	p_x	up	no	1.205	0.748	0.457	0.000	0.000
dxy	down	p_y	down	yes	-0.885	0.748	0.457	-1.600	-0.490
dxy	down	p_y	up	no	1.205	0.748	0.457	0.000	0.000
dxy	down	p_z	down	yes	-0.473	0.748	-0.914	0.000	-0.306
dxy	down	p_z	up	no	-0.167	0.748	-0.914	0.000	0.000

Table 2: Table of Coulombic *d*-orbital and *p*-orbital interactions for a system with one *d* electron constrained in the spin down d_{xy} fermionic mode and one *p* electron.

Table 2 shows the contributions to the total energy $\langle H_{\text{toy}}{}^{C}\rangle$ for different p, d configurations. These were calculated using the many-body second quantization code Quanty to encode the toy Hamiltonian [38]. The direct terms $F0_{pd}$ and $F2_{pd}$ are always non-zero, with the $F0_{pd}$ term corresponding to a spherically symmetric constant contribution and the $F2_{pd}$ changing signs and magnitude according to whether the occupied orbitals have overlapping symmetry. This behavior is effectively an inter-orbital Hund's rule [39]; when the d and p electrons have overlapping symmetry (ex: d_{xy} and p_x) the energy of that configuration is raised compared to when their symmetries do not overlap (ex: d_{xy} and p_z).

The exchange terms $G1_{pd}$ and $G3_{pd}$ come from the fermionic behavior of electrons which energetically split spin-aligned configurations from spin-opposed. Hund's principle of maximum multiplicity leads to systems with aligned spins having lower energy than when spins are opposed. The exchange terms behave similarly to the direct terms in that the magnitude of the interaction is larger when the symmetries of the two occupied orbitals are overlapping, but the contribution to the total energy is always negative. The behavior of the exchange Coulomb terms is what gives sensitivity to spin in CtC-XES, where for example the $K\beta'$ peak changes depending on whether a system is in a high spin or low spin configuration [2].

We demonstrate how this behavior in Fig. 1 combines with the difference in Coulomb interaction based on symmetry overlap to give polarized spectra. Starting from an initial state with 6 p electrons and an s core hole, we use the x, y, and z dipole transition operators to control where the unpaired electron in the p orbital ends up in the final state. The final state is constrained to have the single d electron in the d_{xy} orbital, meaning that our final states are analogous to the six rows shown in Table 2 (up to an overall shift).

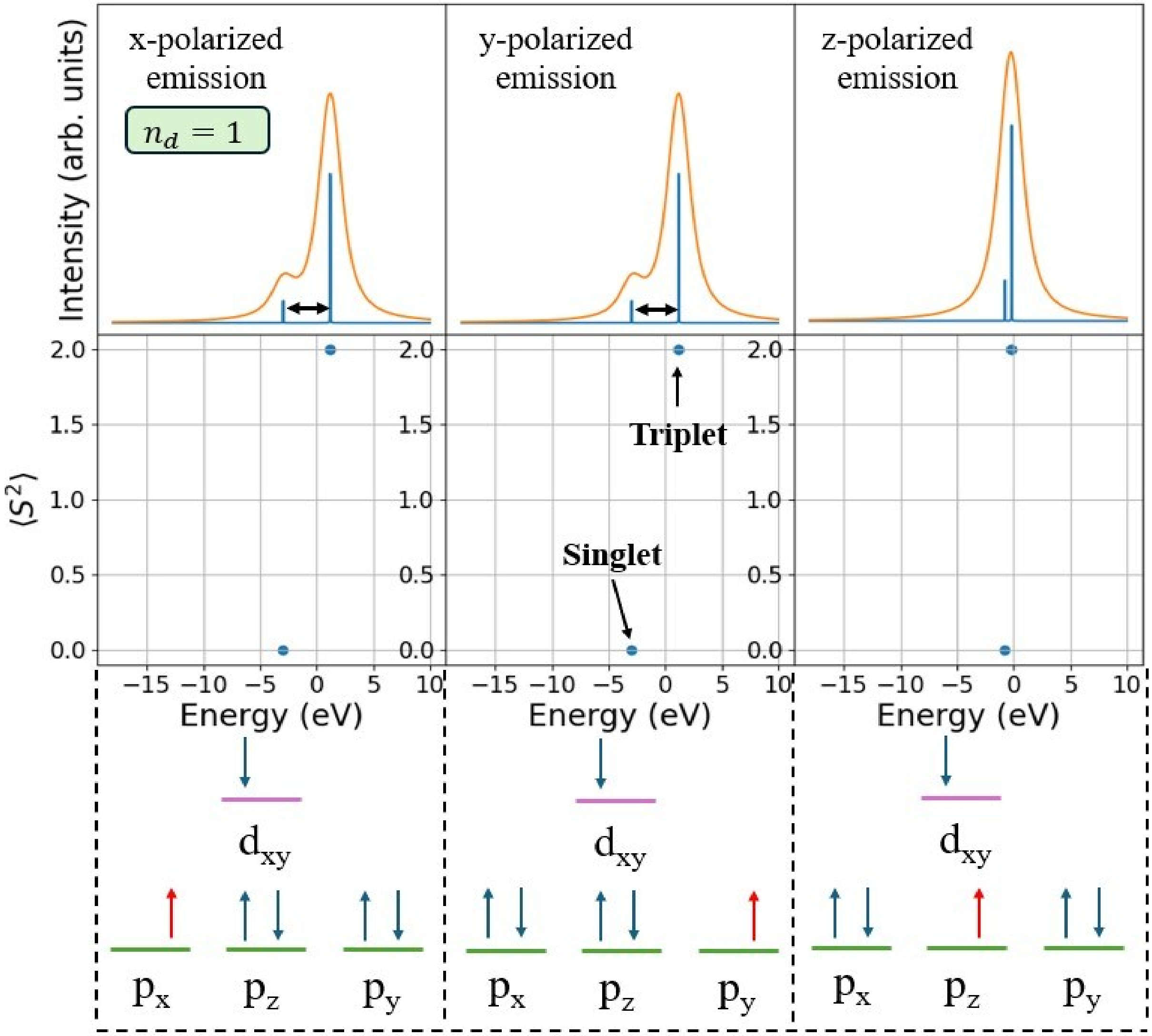

Figure 1: The polarized dipole $p \rightarrow s$ emission spectra and final states of our toy system described by Eq. 4. Only final state configurations with a spin down electron in the d_{xy} orbital are calculated. The top row shows the spectra for different dipole transition operators (x, y, and z). The middle row shows the expectation value of the total system $\langle S^2 \rangle$ operator for the final states. The last row shows the singlet configuration corresponding to the p core hole created by each of the dipole transition operators.

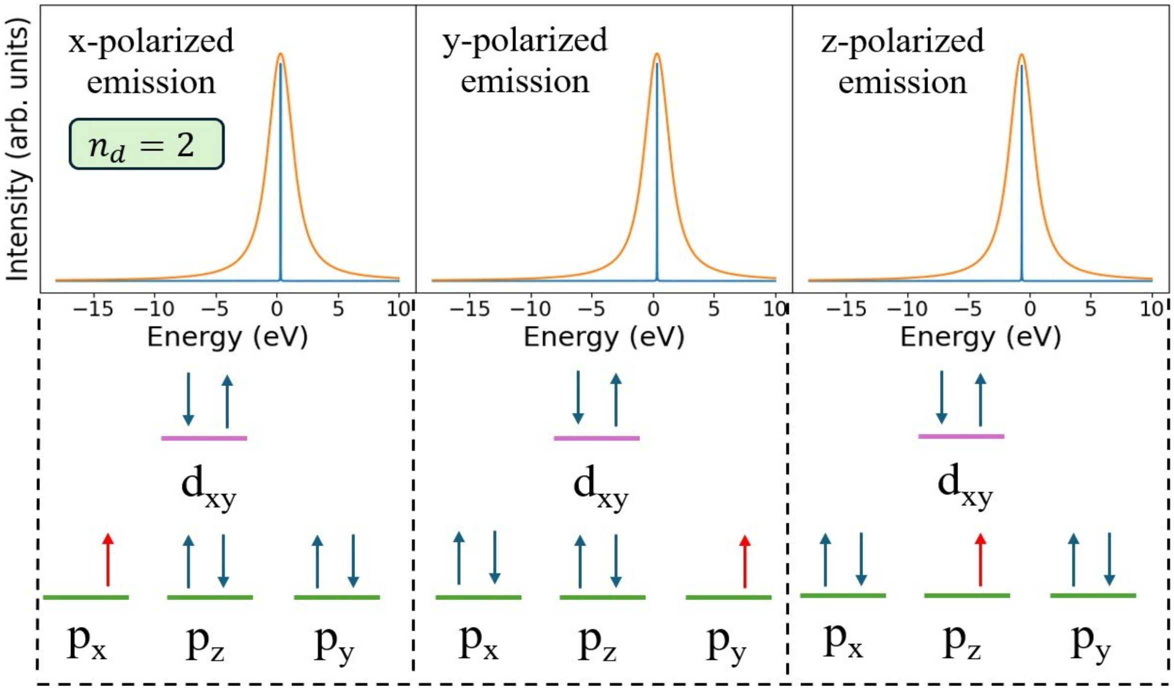

Figure 2: The polarized dipole $p \rightarrow s$ emission spectra for a final state described by Eq. 4, but with two electrons pinned into the same d_{xy} orbital. The top row shows the emission spectra for each polarization and the bottom row shows the singlet configuration of each final state.

Quanty was used to calculate the $p \rightarrow s$ polarized dipole emission spectra. The first row in Fig. 1 shows x, y, and z polarized emission spectra. We note that the x and y polarized emission are identical with a large splitting between the singlet and triplet states, while the z polarized emission has a much smaller splitting. An important note is that because we are neglecting spin-orbit splitting in this toy model the multiplicity of the entire system $\langle S^2 \rangle$ is a good quantum number, and it allows us to distinguish the configurations as seen in the second row. The singlet configuration for each final state is shown in the last row. For more information about the quantitative behavior of the splitting between the singlet and triplet states we refer readers to the theory discussion in Lafuerza *et al.* [1]. The splitting between these configurations is the same mechanism that underpins the spin-dependence of the Kβ' peak in 3p

→ 1*s* XES. The behavior of this toy system highlights a key result, namely that the intensity and position of the K*β*' in polarized emission can be a reflection of orbital occupation as well as the spin state.

A simpler, but equally useful result comes from adding a second electron into the d_{xy} orbital, see Fig. 2. The addition of a second electron takes the system from a spin-1/2 to spin-0 configuration and removes the split singlet-triplet behavior. While the final states of the non-degenerate polarizations will still experience an overall shift in energy, the effective anisotropy in the spectra becomes much weaker.

The model here is simple, but the results are generic. We have demonstrated how the polarized emission of CtC-XES is sensitive to the occupation of the valence orbitals via the Coulomb exchange interaction. Consequently, any symmetry breaking perturbations (crystal field, charge transfer) will also be reflected in the spectra. This is distinct from the polarization sensitivity observed in absorption techniques like $L_{2,3}$ XLD or XMCD, where the electron transitions from *p* into *d* provide a direct probe of the unoccupied density of states in the presence of a core hole.

2.5 Crystal Systems

We study two transition metal compounds: $LiVCuO_4$ and $DyNiC_2$. The crystal structure of $LiVCuO_4$ is shown in Fig. 3. CuO_4 ladders run through the *ab* plane, and have a nearly perfect square planar bond orientation with a small rhomboidal distortion, giving the Cu-O cluster a point group of D_{2h}. The Cu(II) ion leaves the system with $n_d = 9$. The crystal field splitting for the local cluster around the Cu leaves a single unpaired *d*-electron and a spin-1/2 system [40].

The $DyNiC_2$ structure is shown in Fig. 4 and has a structure of alternating Ni-C and Dy sheets in the *bc*-plane. The local Ni-C cluster is a strongly distorted square planar structure with a point group C_{2v}. The Ni(II) ion has $n_d = 8$. Low symmetry clusters, like $DyNiC_2$, experience spin-quenching when the crystal field split levels all lose their degeneracy [41], hence the $n_d = 8$ configuration here is fully spin-paired, leading to a spin-0 system.

Both systems have orthorhombic unit cells and therefore the crystal axes are orthogonal. For describing the direction of propagation and polarization of the x-ray emission we will use the *x*, *y*, *z* coordinate convention with the obvious mapping to the *a*, *b*, *c* crystal axes.

3. Methods

3.1 Experimental Setup

All XES measurements were performed on a laboratory spectrometer described in Jahrman et al. [42], using a 100W x-ray source with a Pd anode, 10-cm diameter spherically bent crystal analyzer (SBCA), and an Amptek X-123 silicon drift detector on a 1-m Rowland circle. The x-ray tube was held at 2.8 mA current and 35 kV accelerating potential. A 1-mm entrance slit and an SBCA mask that covers the outer 30 mm on either side of the SBCA were used to reduce the experimental broadening. Measurements were made with 0.25 eV steps around the features of interest and 1 eV steps outside this region for background determination. Each spectrum was collected over multiple scans, with the specific number of scans chosen to obtain a total of at least 10,000 counts for the $K\beta_{1,3}$ peak and ~1000 counts for the $K\beta_{2,5}$ peak. The first and last few scans were compared and showed no evidence of beam damage.

As shown in Fig. 5, two spectrometer geometries were used to obtain the unpolarized and partially polarized XES measurements, using high and low Bragg angles, respectively. Specific

Bragg angles are shown in Table 3. The experimental broadening is ~3-eV greater for the low Bragg angle geometry compared to the high Bragg angle, shown for reference spectra in Fig. 6, due to source size and Johann error broadening being worse for smaller Bragg angles[43–45].

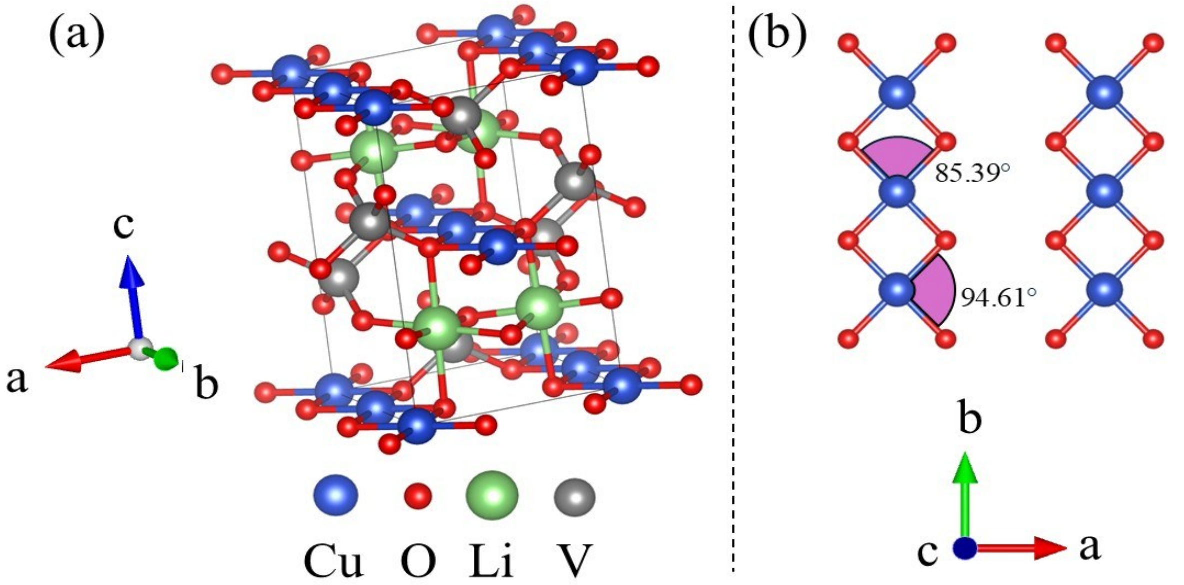

Figure 3: (a) $LiVCuO_4$ crystal structure. (b) Face down view on the a-b plane of square planar Cu-O chains.

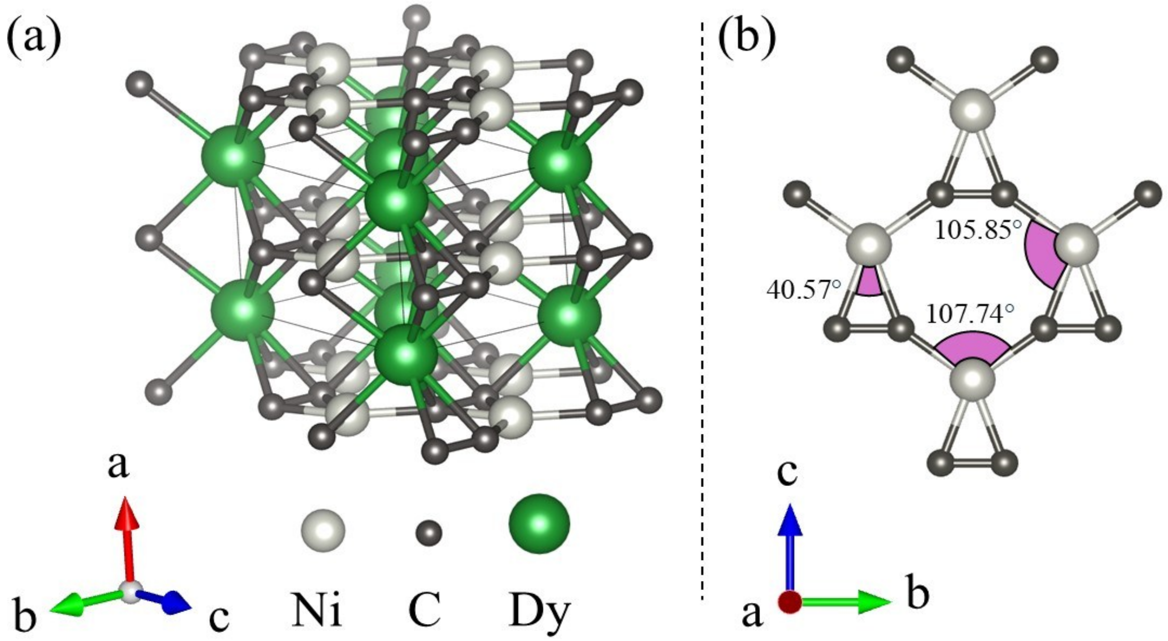

Figure 4: (a) $DyNiC_2$ crystal structure. (b) Face down view on the b-c plane of distorted square planar Ni-C chains.

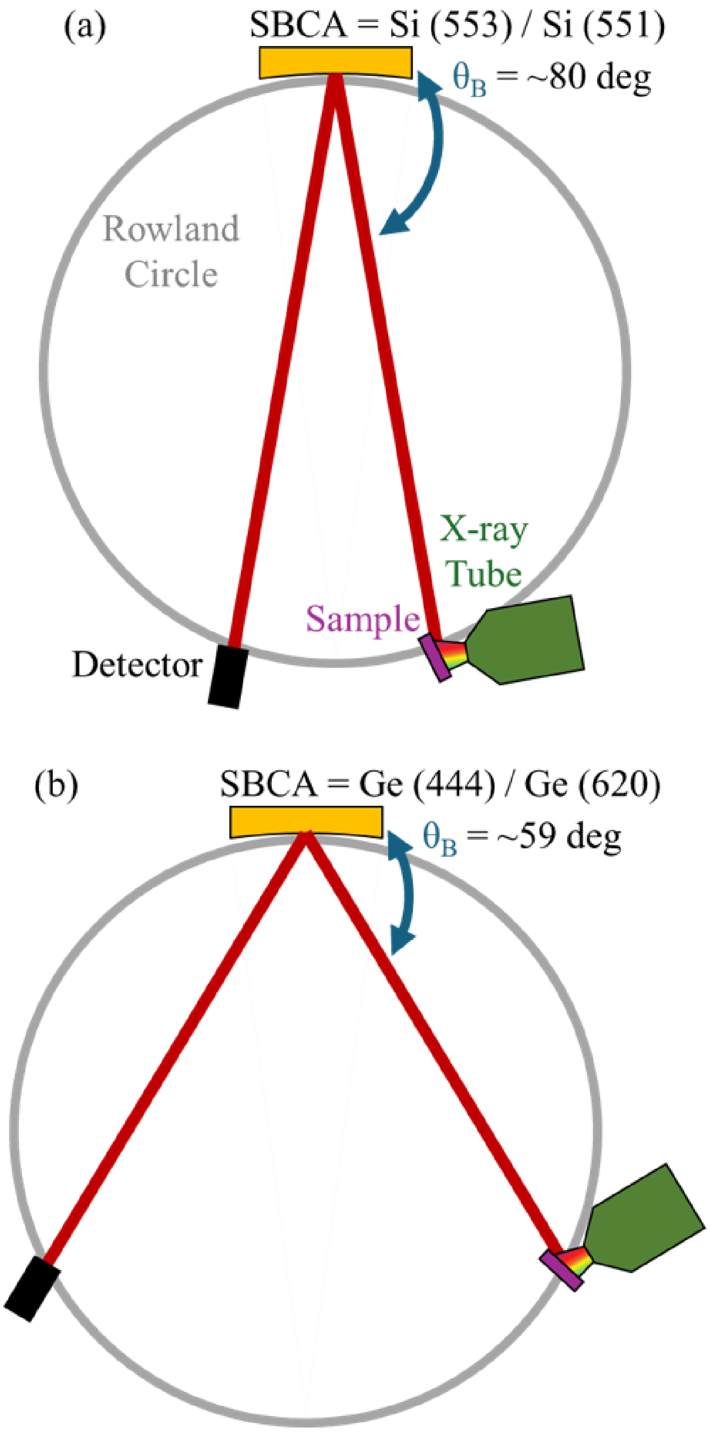

Figure 5: Rowland Circle geometry for unpolarized, (a), and partially polarized, (b), CtC and VtC Kβ XES measurements. For each geometry the first SBCA is for Cu measurements and the second is for Ni measurements.

Emission		Spectrometer		
Emission Line	Polarized	SBCA	θ_B (deg.)	Pol. Factor
Cu Kβ	No	Si (553)	80	0.88
Cu Kβ	Partial	Ge (444)	58	0.19
Cu VtC	No	Si (553)	78	0.84
Cu VtC	Partial	Ge (444)	58	0.19
Ni Kβ	No	Si (551)	81	0.91
Ni Kβ	Partial	Ge (620)	57	0.17
Ni VtC	No	Si (551)	80	0.88
Ni VtC	Partial	Ge (620)	57	0.17

Table 3: Emission line, polarization classification, analyzer, Bragg angle, and polarization factor (R_p/R_s) for all data presented in this work. See Fig.5 for graphical representations.

Polarization control was achieved by exploiting the difference in reflectivity of emission from photons polarized perpendicular (s-polarized) versus parallel (p-polarized) to the reflection plane, see Fig. 7. The reflectivity of these two polarizations is calculated with Fresnel's equations [46] using the index of refraction for Si or Ge at x-ray energies. This gives a ratio of emission reflecting off the SBCA with polarization parallel (R_p) versus perpendicular (R_s) to the Rowland plane of ~0.2 for low Bragg angles and ~0.85 for high Bragg angles. Therefore using the spectrometer geometry at low Bragg angles achieves selection of x-rays that are primarily polarized perpendicular to the Rowland plane, meaning that we detect a partially polarized spectra. By orienting the emitting sample with one crystallographic axis perpendicular to the Rowland plane the partially polarized spectra show the transition intensity along the specific axis.

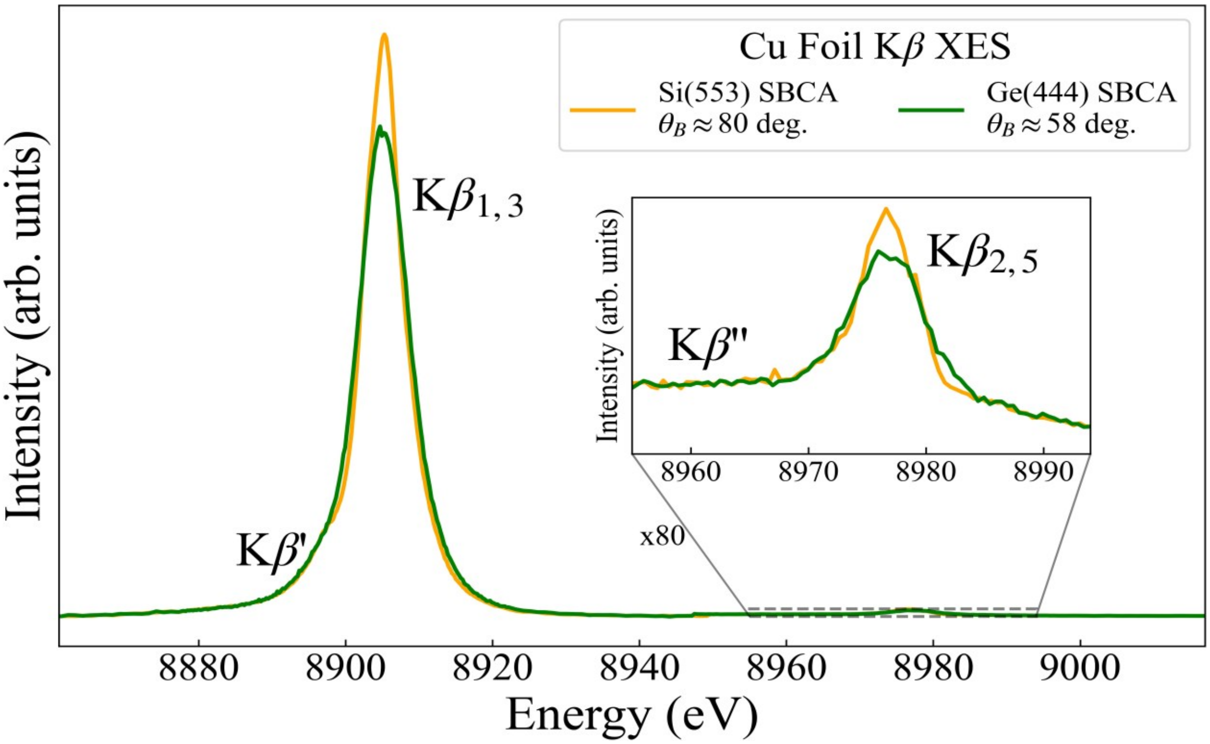

Figure 6: Cu foil Kβ x-ray emission spectra taken at high (orange) and low (green) Bragg angle.

3.2 Samples and Sample Orientation

Photographs of the two samples are shown in Fig. 8 (a) and (b). Both samples are plate-like having 4-mm to 8-mm spatial extent in their planar directions and are thinner (∼1-mm) in the perpendicular direction. The $LiVCuO_4$ crystal was grown from $LiVO_3$ flux cooled by 0.1K/hr from ∼880K as described in Grams *et al.* [47]. Single crystal X-ray diffraction was performed to confirm the structure and to orient the crystal. The $DyNiC_2$ crystal was grown and characterized following the procedure described in Roman *et al.* [48]. The crystal was synthesized using pure elements and the floating zone technique. It was oriented with Laue method and then characterized by scanning electron microscopy, powder x-ray diffraction to confirm crystal growth and homogeneity.

The samples were oriented in the spectrometer on a custom 3D printed mount for each measurement so one crystallographic axis is perpendicular to the Rowland plane and another is 15 degrees from the emission direction. An example of this mounting is given in Fig.8 (c). The 15 degree offset allows for a much higher count rate with a small correctable loss of directionality along the in-plane crystal axis, discussed in Section 3.4.3.

Reference Cu and Ni foils that were used during the calibration process were procured from ESPI metals being 99.995% elemental pure.

3.3 VtC-XES Computational Details

To calculate the K$\beta_{2,5}$ XES and the *l*,*m* projected density of states (DOS) we use the real-space Green's function code FEFF10 [49] which calculates a single-particle Green's function where many-body interactions are approximated via the LDA exchange-correlation potential. This is sufficient for valence level spectroscopies due to the more delocalized nature of the orbitals involved in bonding, and has been demonstrated to perform similarly to time-dependent DFT approaches for VtC-XES [50]. The x, y, and z polarizations are calculated using the POLARIZATION card and we include both electric dipole and quadrupole transitions with the MULTIPOLE card. While the main contribution to the VtC-XES of 3*d* transition metals comes from the *p* DOS from the dipole transition, roughly 10% of the intensity comes from quadrupole transitions from the *s* and *d* DOS, as demonstrated in Mortensen *et al.* [51].

The potentials and densities were calculated with the self-consistent field (SCF) approach and an SCF radius of 5.0 around the emitting atom and the spectra were calculated with a full multiple scattering (FMS) radius of 7.0-Å. The XES was calculated using the standard practice of omitting the core hole in accordance with the final state rule. The lifetime

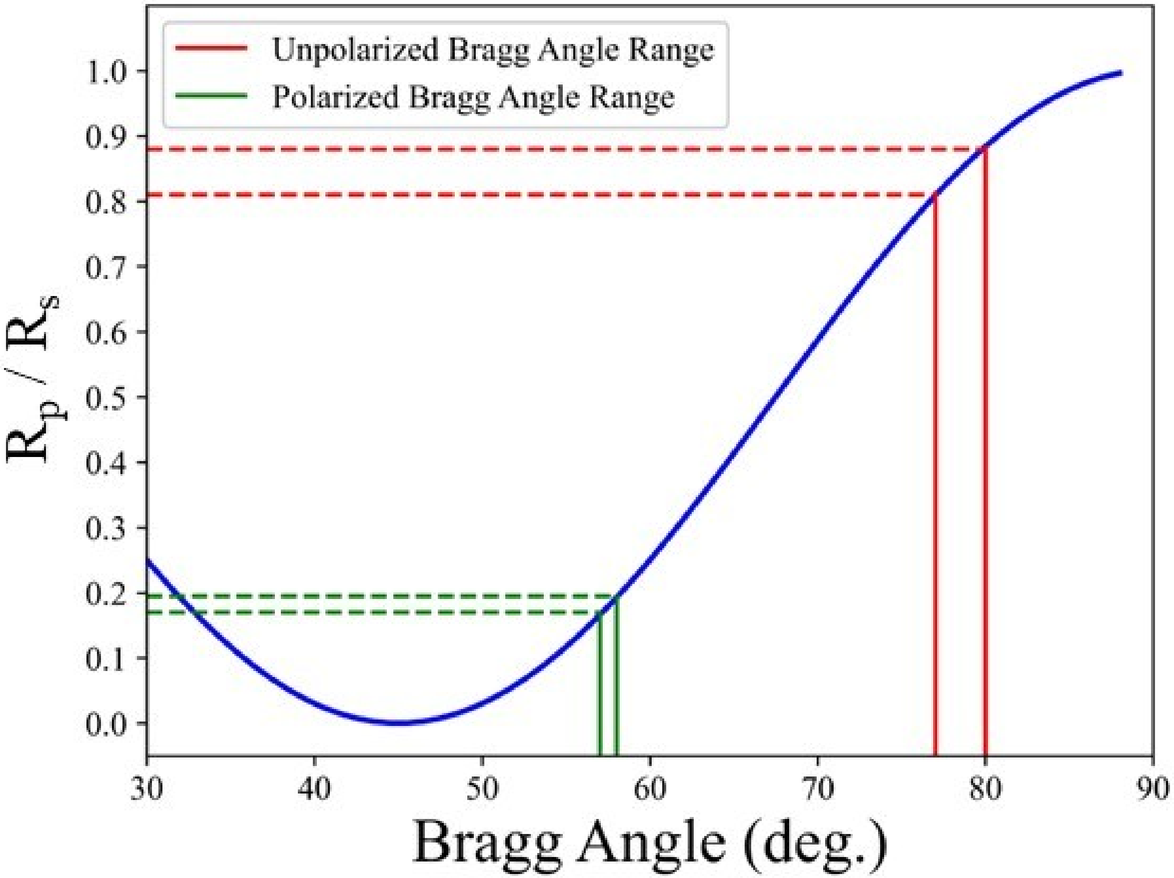

Figure 7: The calculated ratio of reflectance of x-rays with polarization parallel to the Rowland plane (R_p) verse perpendicular to the Rowland plane (R_s) as a function of Bragg angle for the SBCA. The minimum and maximum Bragg angles for the unpolarized (red) and partially polarized (green) XES spectra are marked.

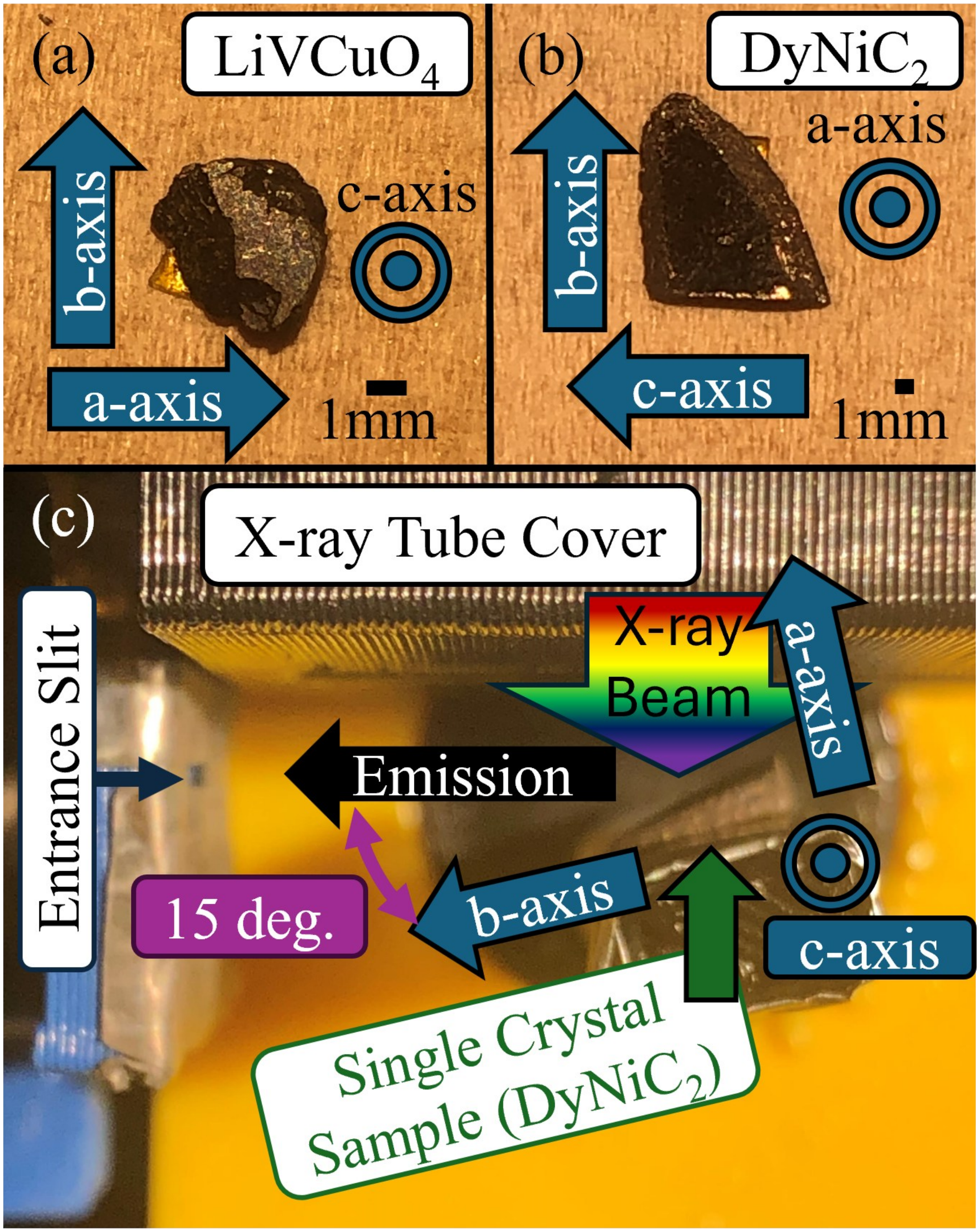

Figure 8: (a) $LiVCuO_4$ single crystal sample. (b) $DyNiC_2$ single crystal sample. (c) $DyNiC_2$ sample shown positioned in the spectrometer sample environment for *z*-polarized, *y*-directed (σ_z, I_y) XES spectra.

broadening from the core hole is already included within FEFF spectra, and a 1.0 eV FWHM Gaussian broadening was convolved with the spectra for comparison with experiment. Spectra were shifted independently to align with experiment, which is necessary to account for limitations from the muffin-tin potentials used within FEFF [51]. An extended version of the FEFF code was use to calculate the real spherical harmonic projected density of states, which can be directly compared to the x, y, z polarized spectra.

3.4 Data Processing Procedure

3.4.1 K*β*-XES

The Kβ spectra were processed by first averaging all spectra for one sample orientation. A background subtraction calculated from the first and last 5 eV of the spectrum was applied, followed by an integral normalization over the background subtracted spectrum. A unique Bragg angle correction is applied to the spectrum to position it in energy relative to a foil reference spectra. This is necessary because of the sensitivity of the energy scale to the sample position's relative to the entrance slit when the sample is not large enough to fully illuminate the entrance slit, a limitation that is related to the issue addressed in Abramson et al. [52]. Following that work, we find that summing a series of alignment scans as the sample steps across the entrance slit creates an effectively-large sample spectrum that fully illuminates the entrance slit. This set of scans can be used to finely calibrate the energy scale for the final measurement with a stationary, small sample - see Fig. 9. The calibration procedure involves comparing the resulting effectively-large sample spectrum's and the normalized, background subtracted spectrum's K$\beta_{1,3}$ energy to find the Bragg angle offset that corrects for the actual illumination of the entrance slit. This step is followed by the usual Bragg angle correction applied equally to all reference and sample spectra to align the Cu and Ni foil reference K$\beta_{1,3}$ energy with their published, standard values. This process aligns both the partially polarized and unpolarized spectra on the same energy scale for comparison.

3.4.2 VtC-XES

VtC-XES spectra were processed by summing all scans for one orientation then subtracting a constant background calculated by averaging the highest 5 eV of data. This was followed by normalization of the VtC region with the integral of the K$\beta_{1,3}$ and Kβ' features to bring the VtC spectra to a consistent molar scale [53]. The Bragg angle corrections determined by the Kβ XES are similarly applied to the VtC-XES.

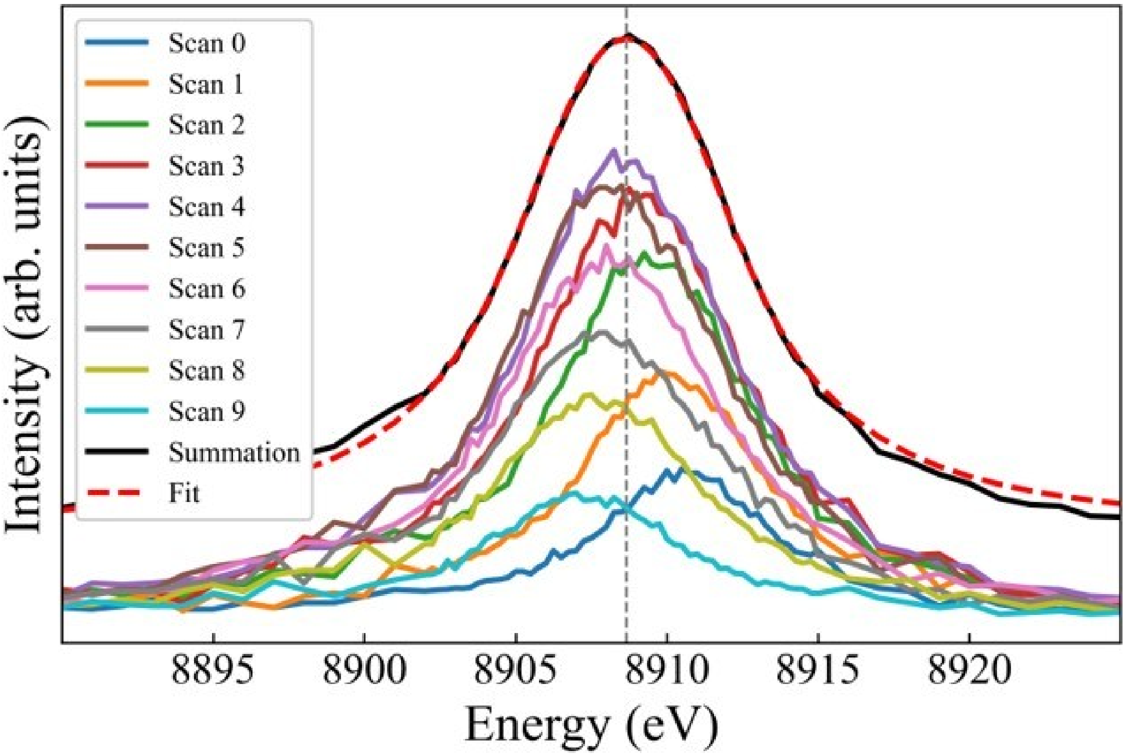

Figure 9: Kβ XES scans of the $LiVCuO_4$ single crystal sample as it is stepped across the entrance slit and the summation of these scans. A vertical gray dashed line marks the center position of the K$\beta_{1,3}$ peak, found by a fit to the summation. This energy is used to apply a Bragg angle correction to the sample spectra, positioning it correctly in energy relative to a Cu foil reference spectra.

3.4.3 Polarized Spectra Extraction

As described in Section 2.3, dipole x-ray emission propagating in a particular direction (ex: z) is a combination of emission from dipole transitions in the plane perpendicular to this direction of propagation (x and y). For the Rowland circle spectrometer, the direction of propagation is towards the SBCA, and the two polarizations which can reach the detector are orthogonal to the propagation direction: in the Rowland plane (p) and perpendicular to the Rowland plane (s). The ratio of s and p polarizations which reach the detector depend on the Bragg angle, laid out in Fig. 7. Due to the 15 degree difference between crystallographic axis and emission direction in the Rowland plane (Section 2.5) the p-polarization has contribution from polarized spectra along two crystallographic axis while s-polarization is only from the polarized spectra of the out of plane axis, example shown in 8(c). By measuring the emission spectra from a sample along three linearly independent directions, a system of equations is created where each directed spectra is an linear combination of the underlying polarized spectra. The relationship between measured intensities and the underlying polarized emission along the x-, y-, and z- directions is given in Eq. 5. The linear combination coefficients, A, have a geometric component due to the 15 degree difference between crystallographic axis and emission direction in the Rowland plane (Section 2.5) and a reflectivity component due to the R_p/R_s ratio of the Rowland circle geometry. A in Eq. 5b is given for $DyNiC_2$ with the second row matching the sample orientation shown in Fig. 8(c). With A being known, we extract extract the polarized spectra by matrix inversion.

At high Bragg angle, R_p/R_s is ~0.85, requiring the extraction procedure of Eq. 5 to infer the polarized spectra from the measured unpolarized directional spectra. At low Bragg angle

R_p/R_s is ~0.2 which heavily favors the out of plane polarization. Performing the dipole extraction on the measured partially polarized directional spectra changes the integral intensity by ~5 percent, meaning that the measured partially polarized directional spectra are approximately equal to the polarized spectra. An important note here is that this extraction procedure will only be exact for dipole transition spectra. Because the spectra we study in this work are all highly dipole dominated (see Appendix B), we will only consider the previously mentioned extraction procedure.

$$\begin{bmatrix} I_x \\ I_y \\ I_z \end{bmatrix} = A \begin{bmatrix} \sigma_x \\ \sigma_y \\ \sigma_z \end{bmatrix} \tag{5a}$$

$$A = \begin{bmatrix} R_p \sin 15^\circ & R_s & R_p \cos 15^\circ \\ R_p \cos 15^\circ & R_p \sin 15^\circ & R_s \\ R_s & R_p \cos 15^\circ & R_p \cos 15^\circ \end{bmatrix} \tag{5b}$$

4. Results and Discussion

4.1 CtC-XES

We expect core-to-core transitions to demonstrate relatively weak polarization sensitivity given that local environmental effects are only reflected through a coupling between the core hole and valence level, as we discussed in Section 2.4. The size of the effect is demonstrated through experimental spectra in Fig. 10. The left and right columns show the Kβ emission from $LiVCuO_4$ and $DyNiC_2$ respectively. The top (a, b) row shows the unpolarized spectra and the bottom (c, d) row shows the extracted polarized spectra along the crystallographic directions using the procedure laid out in Section 3.4.3.

While the overall anisotropic signals in both Kβ spectra are weak, one key observation is the polarization dependence of the Kβ' feature. The spin-1/2 Cu in $LiVCuO_4$ shows a significant difference between the σ_z spectrum and the σ_x/σ_y spectra. This, along with knowledge of the crystal field symmetry from the C_{2v} Cu cluster, allows us to determine that the unpaired electron lies in the d_{xy} orbital (using the crystal axes as a basis). When the polarization vector is in the *xy*-plane, the interaction between the newly unpaired 3*p* electron and the unpaired $3d_{xy}$ electron produces an energy difference between the spin-aligned (triplet) and spin-opposed (singlet) configurations, leading to a more prominent $K\beta'$ satellite. Conversely, when the polarization vector of the emission is along the *z*-axis, the symmetry of the core hole and the unpaired valence electron do not match and the interaction is weaker, leading to a less prominent $K\beta'$ feature and a larger $K\beta$ main peak for the *z*-polarized spectra in Fig. 10 (c).

The Ni in the $DyNiC_2$ system is spin-0 and therefore produces no $K\beta'$ feature. The absence of a singlet-triplet splitting interaction limits the anisotropic signal to small changes in the energy and intensity of the $K\beta_{1,3}$ main peak. This is similar to what we observe in Fig. 2 of the toy model, where having a spin-0 valence suppresses anisotropy in the polarized spectra. The overall weak polarization dependence of the main $K\beta$ is not unexpected given it is a second-order property transferred to the core level through the core-valence Coulomb interaction.

We expect to see much stronger polarization dependence when we probe the valence levels directly in the VtC-XES presented in the following section.

4.2 VtC-XES

The Cu and Ni VtC emission from $LiVCuO_4$ and $DyNiC_2$ are shown in Fig. 11. Unpolarized (high Bragg angle) and partially polarized (low Bragg angle) are shown in subplots (a, b) and (c, d) respectively. The extracted polarization spectra in subplots (e, f) are calculated from combinations of the directional spectra, as described in the system of equations given in Section 3.4.3. The theory spectra in subplots (g, h) are calculated according to Section 3.3, and follow the exact same extraction procedure for the purpose of comparison.

The directed emission spectra (a, b) show weakly anisotropic behavior, which is expected given that they are averages of two polarization contributions. The partially polarized spectra in (c, d) qualitatively match with the polarized spectra (e, f) and the calculated polarized spectra (g, h). They show clear polarization differences, such as the ability to distinguish which polarized spectra are most contributing to the Kβ'' ligand peak or K$\beta_{2,5}$ feature, indicating the usefulness of these spectropolarimeter measurements. But the ∼20 percent contribution of in-plane polarized spectra, Fig. 7, and the lower resolution, Fig. 6, for the partially polarized measurements restricts its quantitative analysis.

For $LiVCuO_4$ the nearly square planar CuO_4 structure means the Cu-O bonds lie in the xy-plane. This geometry means that the Cu d_z2 orbital lacks suitable ligand orbitals to form σ bonds, leading to reduced electron density along the z-axis and, consequently, weaker z-polarized (σ_z) emission compared to the x and y polarizations. The unpolarized I_z emission in (a) is therefore stronger than the I_x and I_y signals, as it averages over stronger in-plane transitions. Similarly, the partially polarized and extracted polarized spectra in (c) and (e) show suppressed σ_z contributions, while σ_x and σ_y remain strong and nearly identical due to the symmetry of the in-plane bonding environment. This also accounts for the presence of the Kβ'' ligand peak at 8958 eV in both σ_x and σ_y.

For $DyNiC_2$, the distorted planar structure leads to highly anisotropic emission, with the σ_y spectrum being the strongest, followed by σ_z, and then σ_x, which is the weakest due to the absence of a Ni–C bond along the *x*-direction. This is analogous to the lack of Cu-O bonding along the *z*-axis in $LiVCuO_4$. The distortion of the NiC_4 cluster results in nonequivalent σ_y and σ_z spectra. The differences are consistent with the Ni–C bond angles in the *bc*-plane: an average of 42.78° relative to the *b*/*y*-axis and 37.08° relative to the *c*/*z*-axis. This slight compression along the *z*-axis manifests in the spectra as a ~3 eV energy shift of the σ_z $K\beta_{2,5}$ emission peak compared to the σ_y one, and a more intense C ligand peak at 8316 eV in the *z*-polarization.

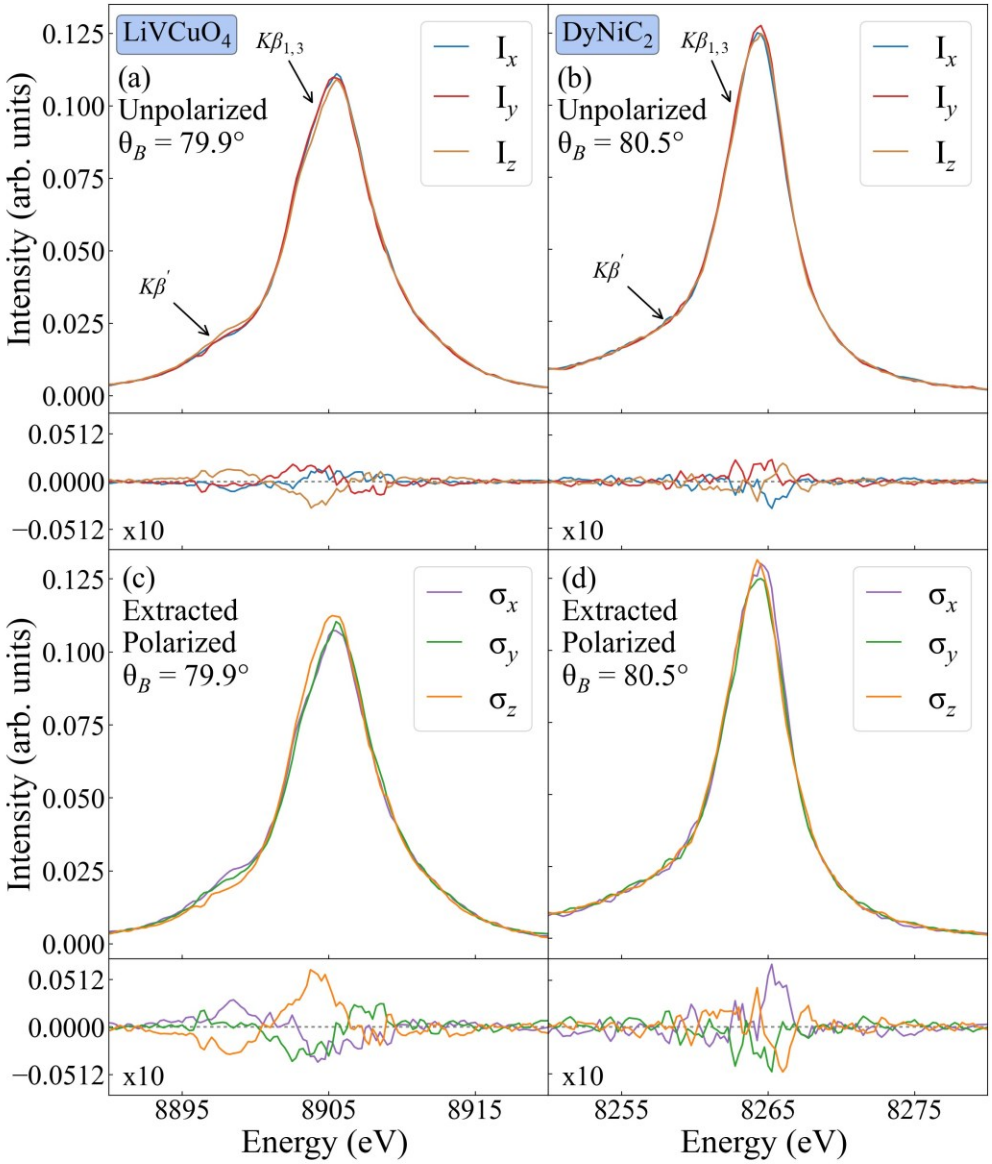

Figure 10: (left) LiVCuO$_4$ Cu and (right) DyNiC$_2$ Ni Kβ CtC-XES. (a, b) Unpolarized emission at high Bragg angle from radiation propagating along the *x* (blue), *y* (red), and *z* (brown) directions. (c, d) polarized spectra extracted from the directional spectra in (a, b) with polarizations along the *x* (purple), *y* (green), and *z* (orange) directions. Difference plots are shown at the bottom of each subplot and are calculated by subtracting the average spectra from each curve. Note the polarization dependence in the Kβ' feature for LiVCuO$_4$.

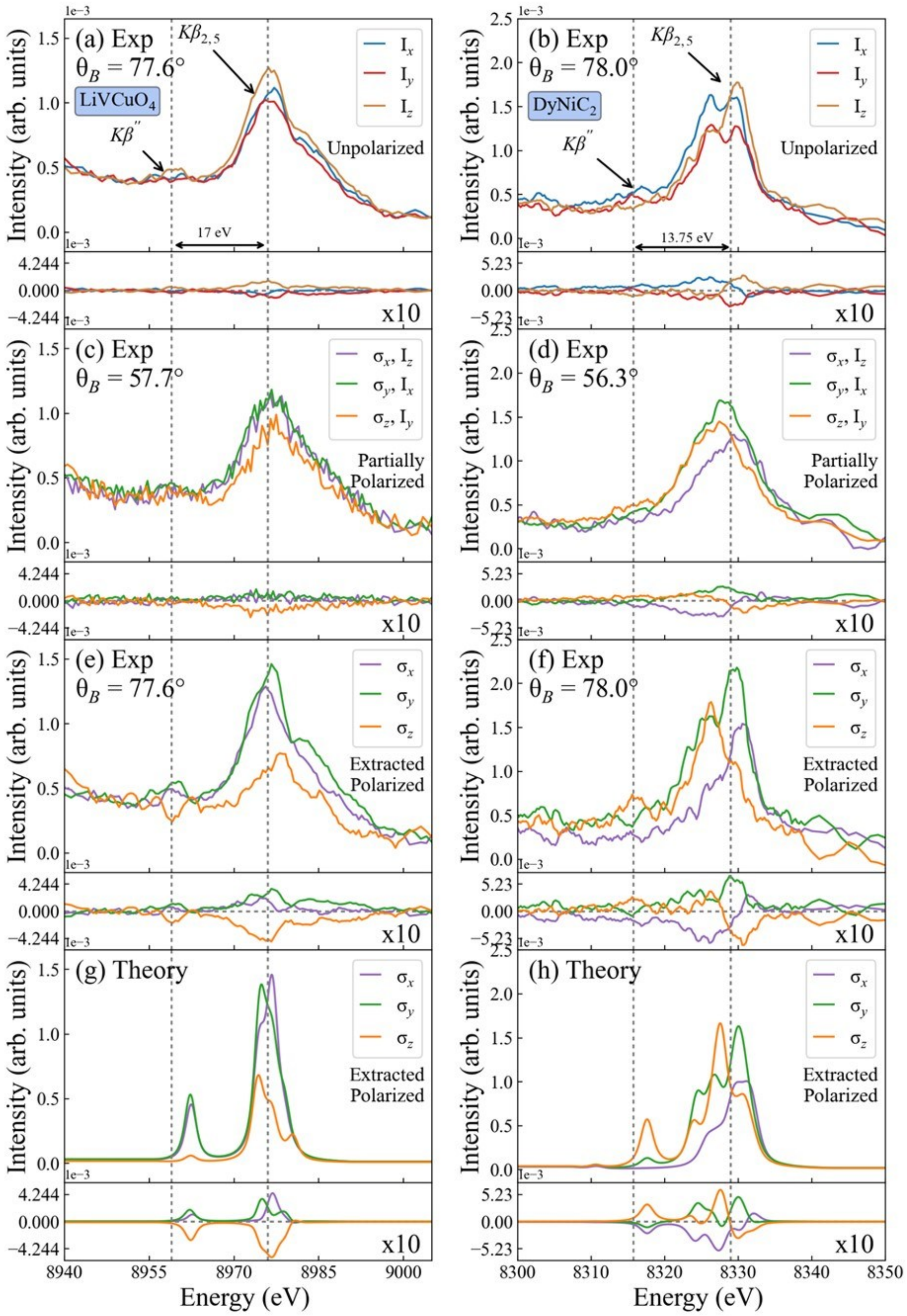

Figure 11: (left) LiVCuO$_4$ Cu and (right) DyNiC$_2$ Ni VtC-XES. (a, b) Measured unpolarized emission from radiation propagating along the *x*, *y*, and *z* directions as defined by the coordinate systems in Section 2.5. (c, d) Measured partially polarized emission, where each spectrum is dominated by a single polarization axis, albeit with poorer energy resolution. (e, f) Extracted polarized spectra. (g, h) Calculated polarized emission, including both electric dipole and quadrupole components.

In both $DyNiC_2$ and LiVCuO4, the $K\beta''$ satellite is relatively weak compared to the main $K\beta 2,5$ peak, a trend attributable to the long metal–ligand bond distances—1.96 A° for Ni–C bonds in $DyNiC_2$ and 2.14 A° for Cu–O bonds in LiVCuO4 [31]. This reduces the hybridization between the ligand 2*s* and metal valence orbitals, thereby suppressing the weak $K\beta''$ feature. Additionally, the $K\beta''$–$K\beta_{2,5}$ energy separation is roughly 5 eV greater in $LiVCuO_4$ than in $DyNiC_2$, reflecting the difference in 2*s* binding energies between O and C ligands [54].

The extracted polarization spectra in subplots (e, f) match well with the calculated polarized spectra in subplots (g, h), and their residuals. However, one important difference between the calculated and extracted is that the position of the $K\beta''$ peak is too high in energy by about 2 eV. This is likely due to limitations imposed by the use of muffin-tin potentials within the FEFF code to approximate the scattering potential, which tend to underestimate the anisotropy of the electron density in the interstitial regions. As a result, the hybridization between the transition metal 3*d* and ligand 2*p* states may be overestimated, artificially shifting the energy position of the $K\beta''$ peak.

4.3 Future Directions

The spectropolarimetry to directly measure the polarized spectra (low Bragg angle) suffered as a analytical measurement from low resolution and only partial polarization sensitivity. Both factors can be greatly improved upon by working in an asymmetric Rowland configuration [30], allowing for a selection of reflection geometry with near 45 degree Bragg angle for perfect polarization sensitivity with emission incident perpendicular to the SBCA face reducing one of two main broadening mechanisms, Johann error [43]. If the spectropolarimetry measurements were performed with asymmetric Rowland geometry and with micro-focused synchrotron radiation the other main broadening mechanism, source size error, could be eliminated resulting in a direct, high-fidelity measurement of polarized spectra.

An additional benefit of performing the direct polarized measurements at a synchrotron source is the increased flux which allows for resolving weaker spectral features such as quadrupole transitions, which depend on both the direction of propagation and the polarization axis, adding an extra layer of complexity. Because quadrupole transitions are much weaker than the dominant dipole transitions (see Appendix B), their detection requires careful analysis of intensity variations with crystal orientation. Achieving lower experimental broadening and increased flux would make it significantly easier to isolate and identify these subtle features.

5. Conclusion

We have shown that single crystals with local asymmetry around the a 3d transition metal reflect the anisotropy in the polarized emission spectra for both the CtC and VtC-XES. The polarized emission along a specific crystallographic direction is obtained directly with partially polarized measurements obtained with laboratory single crystal spectropolarimetry and indirectly with a new technique to extract polarized spectra from unpolarized emission. With the polarized emission we obtained information about the local electronic structure, particularly the anisotropic distribution of unoccupied states.

The CtC $K\beta$ features showed clear polarization dependence for Cu in LiVCuO4, which can be attributed to the spin-1/2 nature of Cu^{2+}. This allows for Coulomb coupling between the $3p$ and $3d$ orbitals. The emission weight shifts toward the $K\beta'$ feature when the polarization is in the ligand plane and toward the $K\beta1,3$ feature when it is perpendicular to the plane. In contrast, $DyNiC_2$ contains Ni^{2+} in a spin-0 configuration, and its CtC spectrum showed little to no polarization dependence. This contrasting behavior is consistent with predictions from a simple toy model.

In the VtC region, both systems exhibited strong polarization effects. The Kβ'' and K$\beta_{2,5}$ features became more intense when the polarization aligned with metal-ligand bond directions, consistent with expectations based on orbital occupation. Additionally, the Kβ'' peak entirely disappeared for out-of-plane polarizations, further emphasizing the directional nature of the metal-ligand bonding. These trends were qualitatively reproduced by FEFF calculations, reinforcing the interpretation that VtC-XES is sensitive to directional bonding and orbital interactions [50].

Overall, these results establish polarization-resolved XES as a valuable tool for probing anisotropic electronic environments in transition metal systems. This technique provides access to subtle variations in chemical bonding and orbital character, which could be further leveraged in future studies to resolve weak quadrupole transitions, characterize ligand field asymmetry, and investigate site-specific electronic structure in more complex systems.

6. Acknowledgments

JJK and JJR acknowledge support from the Theory Center for Materials and Energy Spectroscopies (TIMES) at SLAC funded by DOE BSE Contract DE-AC02-76SF00515. CAC was supported by the National Science Foundation Graduate Research Fellowship Program under Grant No. DGE-2140004. GTS and JEA were supported by funding from the U.S. Department of Energy in the Nuclear Energy University Program under Contract No. DE-NE0009158. Any opinions, findings, and conclusions or recommendations expressed in this material are those of the author(s) and do not necessarily reflect the views of the National Science Foundation or the U.S. Department of Energy.

7. Appendix

A Directional Dependence of Dipole Radiation

The radiation pattern of any dipole or quadrupole transition element between two hydrogenic orbitals can be calculated by directly integrating the matrix elements from Eq 2 (dipole) and Eq 6 (quadrupole) for an arbitrary $\vec{k}$. The propagation vector $\vec{k}$ and polarization vector $\vec{\epsilon}$ are given in Eq 7, where δ is the angle $\vec{\epsilon}$ makes in the plane perpendicular to $\vec{k}$ which will be integrated out. This follows the same convention established in [33].

$$\sigma^{\text{quad}} \propto \sum_{f} \left| \left\langle f \left| (\hat{\epsilon} \cdot \vec{r})(\vec{k} \cdot \vec{r}) \right| i \right\rangle \right|^2 \delta(E_f - E_i + \hbar\omega) \quad (6)$$

$$\vec{k}(\theta, \phi) = \begin{bmatrix} \sin\theta\cos\phi \\ \sin\theta\sin\phi \\ \cos\theta \end{bmatrix} \quad (7a)$$

$$\vec{\epsilon}(\theta, \phi, \delta) = \begin{bmatrix} \cos\theta\cos\phi\cos\delta - \sin\phi\sin\delta \\ \cos\theta\sin\phi\cos\delta - \cos\omega\sin\delta \\ -\sin\theta\cos\delta \end{bmatrix} \quad (7b)$$

For example, the angular component of a dipole transition from a p_z orbital to a s orbital is written out in Eq 8, where θ, ϕ, and δ are as defined in equation 7, and ρ and ω are dummy variables used for evaluating the matrix element. The matrix element ends up simply as $\langle s| \vec{\epsilon} \cdot \vec{r} |p_z\rangle \propto \sin\theta$, and the radiation pattern is given by $(\sin\theta)^2$, as is shown in Fig. 12 (a). We also show examples for the $p_x \rightarrow s$, $d_{z2} \rightarrow s$, and $d_{xy} \rightarrow s$. The surface of the radiation pattern gives a qualitative measure of how much radiation is emitted in a particular direction from a given dipole transition element. Given the generalized definitions of $\vec{k}$ and $\vec{\epsilon}$, it's possible to invert them and derive the 'polarization' pattern for a fixed polarization direction and a propagation vector integrated over a plane (δ), which of course produces the exact same patterns but with a different interpretation.

$$
\begin{aligned}
\langle s|\,\vec{\epsilon}\cdot\vec{r}\,|p_z\rangle = \Bigg[\int_0^{2\pi}\int_0^{2\pi}\int_0^{\pi} & \qquad\qquad (8) \\
\Big((\cos\theta\cos\phi\cos\delta - \sin\phi\sin\delta)\sin\rho\cos\omega\Big) & \\
\Big((\cos\theta\sin\phi\cos\delta - \cos\omega\sin\delta)\sin\rho\sin\omega\Big) & \\
\Big((-\sin\theta\cos\delta)\cos\rho\Big)(\sin\rho\cos\rho)\;d\rho\,d\omega\,d\delta\Bigg] & \\
\propto \sin\theta &
\end{aligned}
$$

B Additional FEFF calculations

X-ray emission is often interpreted as a reflection of the occupied density of states [1, 2, 55] in the presence of a core hole. We see this represented in figures 13 and 14 which show how the polarized VtC-XES in subplot (a) matches up almost exactly with the p-projected DOS in subplot (c). We also note that the quadrupole contribution shown in subplot (b) is relatively weak, with it making up only 10% and 3% of the total spectral intensity for $LiVCuO_4$ and $DyNiC_2$ respectively. This supports the approximation made when extracting the polarizations from the directional spectra. The main contribution to the quadrupole transition is the *d*-projected DOS which is much larger (in units of electron/eV) than the p-DOS. The overall weak contribution to the total spectra is due to the additional $\vec{k}$ term in the quadrupole matrix element and the small overlap between the metal 3*d* orbital and 1*s* orbital.

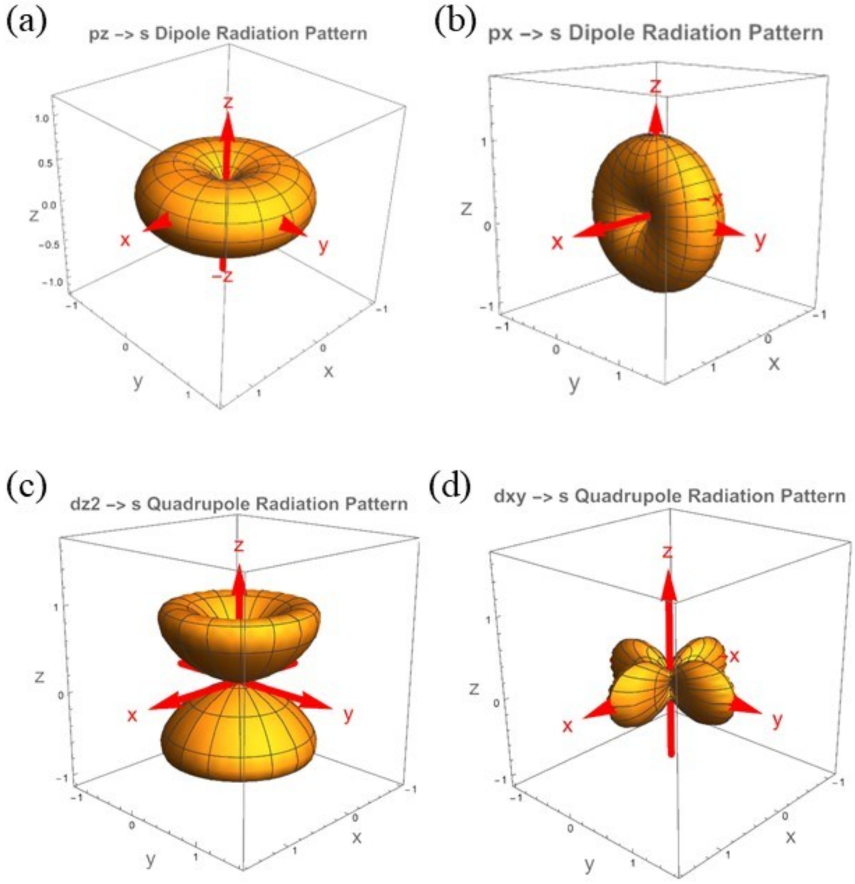

Figure 12: Radiation pattern of dipole and quadrupole transitions between different *l*, *m* orbitals. (a) and (b) show dipole transitions from the p_z and p_x to *s* orbitals respectively while (c) and (d) show quadrupole transition from the d_{z2} and d_{xy} to *s* orbitals. The shape of the radiation patterns are equivalent to oscillating charges with spatial distributions that are consistent with the lobes of positive and negative phases from each atomic orbital.

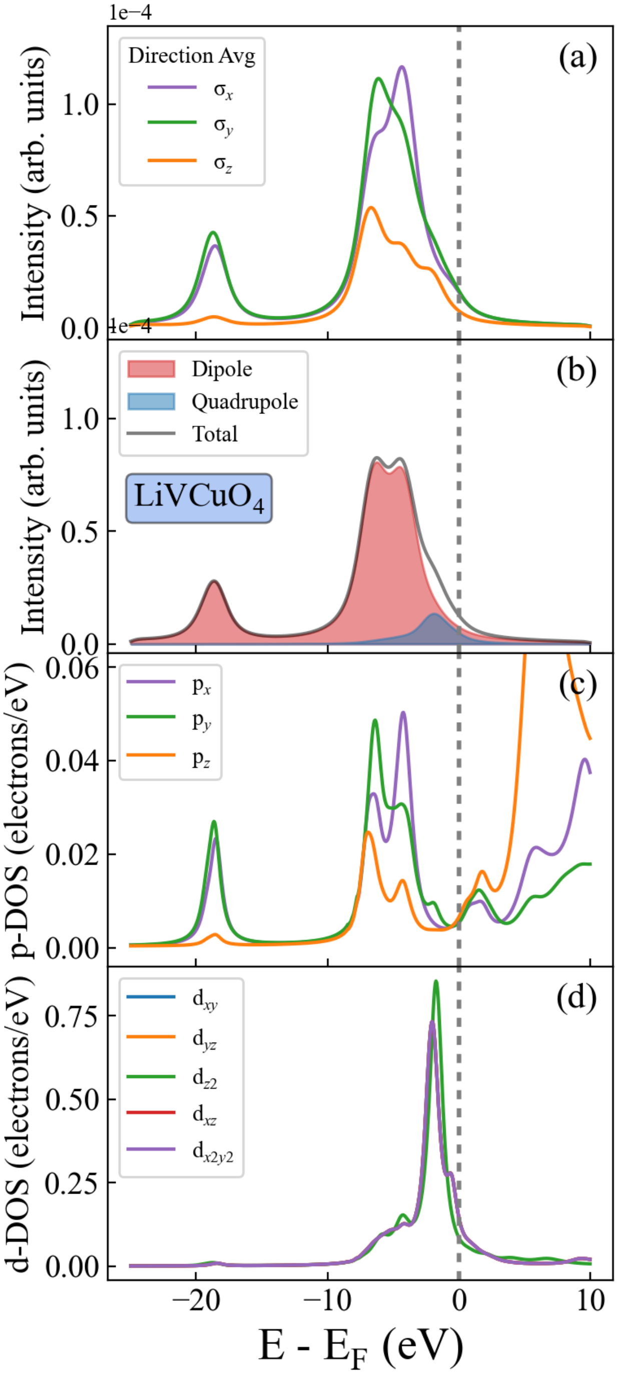

Figure 13: FEFF calculated Cu VtC spectra and DOS from LiVCuO4. (a) Polarized x-ray emission with the quadrupole component averaged over directions perpendicular to the polarization axes. (b) Isotropic emission separated into dipole (red) and quadrupole (blue) components. (c) The p-projected density of states. (d) The d-projected density of states.

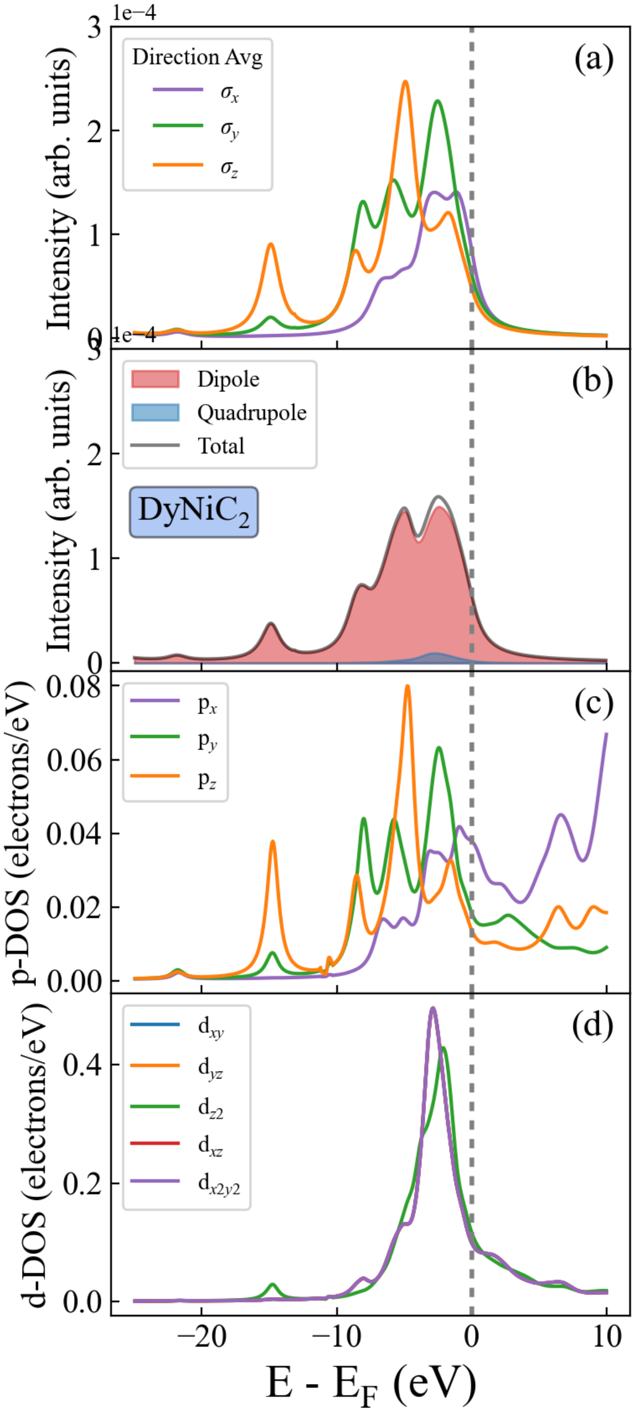

Figure 14: FEFF calculated Ni VtC spectra and DOS from DyNiC2. (a) Polarized x-ray emission with the quadrupole component averaged over directions perpendicular to the polarization axes. (b) Isotropic emission separated into dipole (red) and quadrupole (blue) components. (c) The p-projected density of states. (d) The d-projected density of states.

References

[1] Sara Lafuerza, Andrea Carlantuono, Marius Retegan, and Pieter Glatzel. Chemical Sensitivity of K and K X-ray Emission from a Systematic Investigation of Iron Compounds. *Inorganic Chemistry*, 59(17):12518–12535, 2020.

[2] Pieter Glatzel and Uwe Bergmann. High resolution 1s core hole X-ray spectroscopy in 3d transition metal complexes—electronic and structural information. *Coordination Chemistry Reviews*, 249(1-2):65–95, 2004.

[3] Joanna Kowalska and Serena DeBeer. The role of x-ray spectroscopy in understanding the geometric and electronic structure of nitrogenase. *Biochimica et Biophysica Acta (BBA) - Molecular Cell Research*, 1853(6):1406–1415, 2015.

[4] Abiram Krishnan, Dong-Chan Lee, Ian Slagle, Sumaiyatul Ahsan, Samantha Mitra, Ethan Read, and Faisal M. Alamgir. Monitoring redox processes in lithium-ion batteries by laboratory-scale operando x-ray emission spectroscopy. *ACS Applied Materials & Interfaces*, 16(13):16096–16105, 2024.

[5] Filippo Giordanino, Elisa Borfecchia, Kirill A. Lomachenko, Andrea Lazzarini, Giovanni Agostini, Erik Gallo, Alexander V. Soldatov, Pablo Beato, Silvia Bordiga, and Carlo Lamberti. Interaction of nh3 with cu-ssz-13 catalyst: A complementary ftir, xanes, and xes study. *The Journal of Physical Chemistry Letters*, 5(9):1552–1559, 2014.

[6] H. A. Evans, L. Mao, R. Seshadri, and A. K. Cheetham. Layered double perovskites. *Annual Review of Materials Research*, 51:351–380, 2021.

[7] J. Schlappa, K. Wohlfeld, K. J. Zhou, M. Mourigal, M. W. Haverkort, V. N. Strocov, C. Monney, T. Hunt, J. Stahler,¨ H. M. Ronnow, et al. Spin–orbital separation in the quasi-one-dimensional mott insulator sr_2cuo_3. *Nature*, 485(7396):82–85, 2012.

[8] S.H. Southworth, D.W. Lindle, R. Mayer, and P.L. Cowan. Anisotropy of polarized x-ray emission from molecules. *Physical Review Letters*, 67(1):1098–1101, 1991.

[9] J. Stohr. X-ray magnetic circular dichroism spectroscopy of transition metal thin films.¨ *Journal of Electron Spectroscopy and Related Phenomena*, 75:253–272, 1995.

[10] Gerrit Van Der Laan and Adriana I. Figueroa. X-ray magnetic circular dichroism—A versatile tool to study magnetism. *Coordination Chemistry Reviews*, 277-278:95–129, 2014.

[11] E. Heppell, F. Maccherozzi, L. S. I. Veiga, S. Langridge, G. Van Der Laan, T. Hesjedal, and D. Backes. Handle on the antiferromagnetic spin structure of NiO using a ferromagnetic adlayer. *Physical Review Materials*, 9(1):014408, 2025.

[12] Jonathan A. Sobota, Yu He, and Zhi-Xun Shen. Angle-resolved photoemission studies of quantum materials. *Reviews of Modern Physics*, 93(2):025006, 2021.

[13] Elliott Rosenberg, Jonathan M. DeStefano, Yucheng Guo, Ji Seop Oh, Makoto Hashimoto, Donghui Lu, Robert J. Birgeneau, Yongbin Lee, Liqin Ke, Ming Yi, and Jiun-Haw Chu. Uniaxial ferromagnetism in the kagome metal TbV6Sn6. *Physical Review B*, 106(11):115139, 2022.

[14] Derek Bergner, Tai Kong, Ping Ai, Daniel Eilbott, Claudia Fatuzzo, Samuel Ciocys, Nicholas Dale, Conrad Stansbury, Drew W. Latzke, Everardo Molina, Ryan Reno, Robert J. Cava, Alessandra Lanzara, and Claudia Ojeda-Aristizabal. Polarization dependent

photoemission as a probe of the magnetic ground state in the van der Waals ferromagnet VI3. *Applied Physics Letters*, 121(18):183104, 2022.

[15] M. C. Falub, M. Shi, P. R. Willmott, J. Krempasky, S. G. Chiuzbaian, K. Hricovini, and L. Patthey. Polarization dependent angle-resolved photoemission spectroscopy study ofLa1xSrxMnO3. *Physical Review B*, 72(5):05444, 2005.

[16] T Hajiri, R Niwa, T Ito, M Matsunami, B H Min, S Kimura, and Y S Kwon. Polarization-dependent three-dimensional angle-resolved photoemission study on LiFeAs. *Journal of Physics Conference Series*, 391:012125, 2012.

[17] Luuk J. P. Ament, Michel Van Veenendaal, Thomas P. Devereaux, John P. Hill, and Jeroen Van Den Brink. Resonant inelastic x-ray scattering studies of elementary excitations. *Reviews of Modern Physics*, 83(2):705–767, 2011.

[18] C. Ulrich, L. J. P. Ament, G. Ghiringhelli, L. Braicovich, M. Moretti Sala, N. Pezzotta, T. Schmitt, G. Khaliullin, J. Van Den Brink, H. Roth, T. Lorenz, and B. Keimer. Momentum dependence of orbital excitations in Mott-Insulating titanates. *Physical Review Letters*, 103(10):107205, 2009.

[19] Yoshihisa Harada, Kozo Okada, Ritsuko Eguchi, Akio Kotani, Hidenori Takagi, Tomoyuki Takeuchi, and Shik Shin. Unique identification of Zhang-Rice singlet excitation inSr2CuO2Cl. *Physical review. B, Condensed matter*, 66(16):165104, 2002.

[20] M Moretti Sala, V Bisogni, C Aruta, G Balestrino, H Berger, N B Brookes, G M De Luca, D Di Castro, M Grioni,
M Guarise, P G Medaglia, F Miletto Granozio, M Minola, P Perna, M Radovic, M Salluzzo, T Schmitt, K J Zhou, L Braicovich, and G Ghiringhelli. Energy and symmetry of dd excitations in undoped layered cuprates measured by CuL3resonant inelastic x-ray scattering. *New Journal of Physics*, 13(4):043026, 2011.

[21] Michel Van Veenendaal. Polarization dependence of L- and M-Edge resonant inelastic X-Ray scattering in Transition Metal compounds. *Physical Review Letters*, 96(11):117404, 2006.

[22] R. Fumagalli, L. Braicovich, M. Minola, Y. Y. Peng, K. Kummer, D. Betto, M. Rossi, E. Lefranc¸ois, C. Morawe, M. Salluzzo, H. Suzuki, F. Yakhou, M. Le Tacon, B. Keimer, N. B. Brookes, M. Moretti Sala, and G. Ghiringhelli. Polarization-resolved Cu L3 -edge resonant inelastic x-ray scattering of orbital and spin excitations in NdBa2Cu3O7. *Physical review. B./Physical review. B*, 99(13):134517, 2019.

[23] M. R. Norman, A. S. Botana, J. Karp, A. Hampel, H. LaBollita, A. J. Millis, G. Fabbris, Y. Shen, and M. P. M. Dean. Orbital polarization, charge transfer, and fluorescence in reduced-valence nickelates. *Physical review. B./Physical review. B*, 107(16):165124, 2023.

[24] K. Ham¨ al¨ ainen, J. P. Hill, S. Huotari, C.-c. Kao, L. E. Berman, A. Kotani, T. Id¨ e, J. L. Peng, and R. L. Greene.´ Polarization and momentum dependence of a charge-transfer excitation inNd2CuO4. *Physical review. B, Condensed matter*, 61(3):1836–1840, 2000.

[25] J. A. Carlisle, Eric L. Shirley, E. A. Hudson, L. J. Terminello, T. A. Callcott, J. J. Jia, D. L. Ederer, R. C. C. Perera, and F. J. Himpsel. Probing the Graphite Band Structure with Resonant Soft-X-Ray Fluorescence. *Physical Review Letters*, 74(7):1234–1237, 1995.

[26] G. Drager and O. Br¨ ummer. Polarized X-Ray emission spectra of single crystals.¨ *physica status solidi (b)*, 124(1):11– 28, 1984.

[27] W. Czolbe, U. Dick, G. Drager, and K. Fischer. The electronic structure of single crystal YBa2Cu3O7– studied by¨ polarized Cu K2,5 X-ray emission. *physica status solidi (b)*, 174(1):91–98, 1992.
[28] U. Bergmann, J. Bendix, P. Glatzel, H. B. Gray, and S. P. Cramer. Anisotropic valence→core x-ray fluorescence from a [Rh(en)3][Mn(N)(CN)5]H2O single crystal: Experimental results and density functional calculations. *The Journal of Chemical Physics*, 116(5):2011–2015, 2002.
[29] G. Drager and O. Br¨ ummer. X-ray spectroscopic investigation of beryllium by polarized K-emission valence bands.¨ *physica status solidi (b)*, 78(2):729–735, 1976.
[30] Anthony J. Gironda, Jared E. Abramson, Yeu Chen, Mikhail Solovyev, George E. Sterbinsky, and Gerald T. Seidler. Asymmetric Rowland circle geometries for spherically bent crystal analyzers in laboratory and synchrotron applications. *Journal of Analytical Atomic Spectrometry*, 39(5):1375–1387, 2024.
[31] U. Bergmann, C.R. Horne, T.J. Collins, J.M. Workman, and S.P. Cramer. Chemical dependence of interatomic x-ray transition energies and intensities – a study of mn k and k2,5 spectra. *Chemical Physics Letters*, 302(1):119–124, 1999.
[32] Frank De Groot and Akio Kotani. *Core Level Spectroscopy of Solids*. CRC Press, 1st edition, 2008.
[33] R. Laihia, K. Kokko, W. Hergert, and J. A. Leiro. K-emission spectra of Zn, ZnS, and ZnSe within dipole and quadrupole approximations. *Physical review. B, Condensed matter*, 58(3):1272–1278, 1998.
[34] H. Ogasawara, K. Fukui, and M. Matsubara. Polarization dependence of X-ray emission spectroscopy. *Journal of Electron Spectroscopy and Related Phenomena*, 136(1-2):161–166, 2004.
[35] J. J. Sakurai and Jim Napolitano. *Modern Quantum Mechanics*. Cambridge University Press, 3rd edition, 2020.
[36] David J. Griffiths. *Introduction to Electrodynamics*. Cambridge University Press, 4th edition, 2017.
[37] John Clarke Slater. *Quantum Theory of Atomic Structure*. McGraw-Hill, 1st edition, 1960.
[38] M. W. Haverkort, M. Zwierzycki, and O. K. Andersen. Multiplet ligand-field theory using Wannier orbitals. *Physical Review B*, 85(16):165113, 2012.
[39] Y. Sajeev, M. Sindelka, and N. Moiseyev. Hund's multiplicity rule: From atoms to quantum dots. *The Journal of Chemical Physics*, 128(6):061101, 2008.
[40] Hiroshi Watanabe. *Operator methods in ligand field theory*. Prentice-Hall, 1st edition, 1966.
[41] Gianfranco Pacchioni and Piercarlo Fantucci. Spin states and quenching of magnetism in naked and carbonylated nickel clusters. *Chemical Physics Letters*, 134(5):407–412, 1987.
[42] Evan P. Jahrman, William M. Holden, Alexander S. Ditter, Devon R. Mortensen, Gerald T. Seidler, Timothy T. Fister, Stosh A. Kozimor, Louis F. J. Piper, Jatinkumar Rana, Neil C. Hyatt, and Martin C. Stennett. An improved laboratory-based x-ray absorption fine structure and x-ray emission spectrometer for analytical applications in materials chemistry research. *Review of Scientific Instruments*, 90(2):024106, 2019.

[43] Yeu Chen, Anthony J. Gironda, Yaxin Shen, Andre D. Taylor, and Gerald T. Seidler. A ray tracing survey of asymmet-´ ric operation of the x-ray rowland circle using spherically bent crystal analyzers. *J. Anal. At. Spectrom.*, 40:836–847, 2025.

[44] Uwe Bergmann and Stephen P. Cramer. High-resolution large-acceptance analyzer for x-ray fluorescence and Raman spectroscopy. In Albert T. Macrander, Andreas K. Freund, Tetsuya Ishikawa, and Dennis M. Mills, editors, *Crystal and Multilayer Optics*, volume 3448, pages 198 – 209. International Society for Optics and Photonics, SPIE, 1998.

[45] Mauro Rovezzi, Christophe Lapras, Alain Manceau, Pieter Glatzel, and Roberto Verbeni. High energy-resolution x-ray spectroscopy at ultra-high dilution with spherically bent crystal analyzers of 0.5 m radius. *Review of Scientific Instruments*, 88(1):013108, 01 2017.

[46] Eugene Hecht. *Optics*. Pearson, 5th edition, 2016.

[47] Christoph P. Grams, Daniel Bruning, Severin Kopatz, Thomas Lorenz, Petra Becker, Ladislav Bohat¨ y, and Joachim´ Hemberger. Observation of chiral solitons in LiCuVO4. *Communications Physics*, 5(1):37, 2022.

[48] Marta Roman, Maria Fritthum, Berthold Stoger, Devashibhai T. Adroja, and Herwig Michor. Charge density wave¨ and crystalline electric field effects inTmNiC2. *Physical review. B./Physical review. B*, 107(12):125137, 2023.

[49] J. J. Kas, F. D. Vila, C. D. Pemmaraju, T. S. Tan, and J. J. Rehr. Advanced calculations of X-ray spectroscopies with FEFF10 and Corvus. *Journal of Synchrotron Radiation*, 28(6):1801–1810, 2021.

[50] Evan P. Jahrman, William M. Holden, Niranjan Govind, Joshua J. Kas, Jatinkumar Rana, Louis F. J. Piper, Carrie Siu, M. Stanley Whittingham, Timothy T. Fister, and Gerald T. Seidler. Valence-to-core X-ray emission spectroscopy of vanadium oxide and lithiated vanadyl phosphate materials. *Journal of Materials Chemistry A*, 8(32):16332–16344, 2020.

[51] D. R. Mortensen, G. T. Seidler, Joshua J. Kas, Niranjan Govind, Craig P. Schwartz, Sri Pemmaraju, and David G. Prendergast. Benchmark results and theoretical treatments for valence-to-core x-ray emission spectroscopy in transition metal compounds. *Physical review. B./Physical review. B*, 96(12):125136, 2017.

[52] Jared E. Abramson, Nancy M. Avalos, Agathe L. M. Bourchy, Sarah A. Saslow, and Gerald T. Seidler. An exploration of benchtop X-ray emission spectroscopy for precise characterization of the sulfur redox state in cementitious materials. *X-Ray Spectrometry*, 51(2):151–162, 2021.

[53] Diwash Dhakal, Darren M. Driscoll, Niranjan Govind, Andrew G. Stack, Nikhil Rampal, Gregory Schenter, Christopher J. Mundy, Timothy T. Fister, John L. Fulton, Mahalingam Balasubramanian, and Gerald T. Seidler. The evolution of solvation symmetry and composition in Zn halide aqueous solutions from dilute to extreme concentrations. *Physical Chemistry Chemical Physics*, 25(34):22650–22661, 2023.

[54] Luis Miaja-Avila, Galen C. O'Neil, Young Il Joe, Kelsey M. Morgan, Joseph W. Fowler, William B. Doriese, Brianna Ganly, Deyu Lu, Bruce Ravel, Daniel S. Swetz, and Joel N. Ullom. Valence-to-core X-ray emission spectroscopy of titanium compounds using energy dispersive detectors. *X-Ray Spectrometry*, 50(1):9–20, 2020.

[55] Samantha Tetef, Niranjan Govind, and Gerald T. Seidler. Unsupervised machine learning for unbiased chemical classification in X-ray absorption spectroscopy and X-ray emission spectroscopy. *Physical Chemistry Chemical Physics*, 23(41):23586–23601, 2021.